

THE UNIVERSITY OF NOTTINGHAM

Department of Electrical and Electronic Engineering

Faculty of Engineering

Design of High Speed Wound Field Synchronous Generators

Yinli Wang, B.Eng.(Hons.),

Submitted to the University of Nottingham for the degree of Doctor of Philosophy,

March 2021

Wound field synchronous generator has a long history for being implemented as power generation methods in power plants, standby power generation at 50 or 60 *Hz*. Recent demands for transportation electrification for automotive, marine and aerospace industry raise new requirements for power generation and traction applications. These new requirements includes high speed operation, increased power density and minimizing the cost. High speed and low weight requirements for a wound field synchronous generators result in a complex multi-physics analysis and iteration process. Nevertheless, no commercial tool is available to design a wound field synchronous generator from scratch with simple generator performance inputs and perform thermal and mechanical analysis. However, a parametrised multi-physics design tool for wound field synchronous generator should offer features as follows. First, individual physical field packaged modules for sizing and analysing a generator. Second, individual modules accepts identical generator data array as its inputs. Third, individual physical field analysing module can be upgraded within the modules without interfering other modules. Forth, additional modules can be easily integrated with the existing tools.

In this thesis, a commercially unavailable multi-physics objected oriented design tool dedicated for high speed wound field synchronous generators is developed for designing a wound field synchronous generator from scratch with simple design inputs such as power, speed, terminal voltage and the speed offering features listed above. The objected oriented design tool for a wound field synchronous generator

is able to design a generator via an analytical sizing script, analysing its thermal and mechanical performance. A feasible high speed wound field synchronous generator design option is finalized through multiple iteration processes using the objected oriented design tool proposed in this thesis. This objected oriented wound field synchronous generator design tool also offers features of individual optimization and upgrades of existing design modules integrated in the tool. In addition, since objected oriented architectures are adopted for this tool, other design or analysing modules related to wound field synchronous generator such as rotor dynamics, bearing life time, insulation type and thickness, etc. are able to be integrated with existing tool without interfering with existing modules.

In this thesis, M235-35A core is used to investigate the feasibility of low cost high speed wound field synchronous generators. Therefore, novel dovetails under each rotor pole are proposed to reduce the stress level so that a rotor core made of M235-35A is able to survive the high speed operation. Open slot configuration for damper cages are also proposed in this thesis to address the high stress concentrated at the surface of rotor pole. Integrated damper cages are proposed to resolve the complex copper damper cage assembly process and the stress concentration at rotor pole surface at the same time.

ACKNOWLEDGEMENTS

Many thanks to all of those who contributed in completing the Ph.D project presented in this thesis.

Great appreciation to my supervisor Prof. Michael Galea for his constant help, guidance and support, as well as Dr. Gaurang Vaki, Dr. Michele Degano, Dr. He Zhang and Prof. Chris Gerada for their intervention whenever needed.

Also many thanks to Dr. Stefano Nuzzo, Prof. Giampaolo Buticchi, Dr. Weiduo Zhao and Dr. Wei Dai for their generous help during this Ph.D project. Many thanks to all my colleagues and friends who helped me go through all the difficulties towards the completion of the Ph.D project.

I would like to express my sincere gratitude for a precious friend who turned up at the most desperate time in the middle of my Ph.D for illuminating the darkness around me.

TABLE OF CONTENTS

Abstract.....	ii
Acknowledgements.....	iv
Table of Contents.....	v
List of Figures.....	xi
List of Tables.....	xx
Acronyms.....	xxii
Glossary of Symbols.....	xxv
Chapter 1 Project introduction.....	1
1.1 Project description.....	5
1.2 Aims and objectives.....	6
1.3 Thesis outline.....	9
Chapter 2 Literature review.....	12
2.1 Introduction.....	13
2.2 Current Status of WFSGs Compared with PM, SR and Induction Generators as Individual Components.....	16
2.2.1 State of the art today – WFSG.....	18
2.2.2 Power density of the state of the art WFSG.....	20
2.2.3 Conclusive remark.....	20
2.3 Future Power Distribution Systems on Aircraft and Future Implemented Power Generation Methods.....	21
2.3.1 Constant speed power generation.....	21
2.3.2 Variable speed power generation.....	22

2.3.3 Advantages of variable speed systems	23
2.3.4 Efficiency of the Overall System	24
2.3.5 Reliability concerns.....	25
2.4 Challenges for WFSGs Achieving State of the Art Performance	28
2.4.1 Background for WFSGs.....	28
2.4.2 Thermal challenges for WFSGs implemented for variable speed systems	30
2.4.3 Mechanical challenges for WFSGs implemented for variable.....	31
2.4.4 Other challenges associated with variable speed systems for WFSGs.....	32
2.4.5 Summarizing remarks	32
2.5 Opportunities for WFSGs to Achieve State of the Art Performance	33
2.5.1 Thermal aspects – structure associated with WFSGs.....	34
2.5.2 Mechanical aspects – materials.....	36
2.5.3 Thermal aspects – materials.....	37
2.5.4 Extra functionalities	37
2.6 Conclusion	38
Chapter 3 Design methodologies for conventional wound field synchronous generators	40
3.1 General Theories for Wound Field Synchronous Generators	41
3.1.1 Steady state behaviour of WFSGs.....	41
3.1.2 Transient state behaviour of WFSGs	44
3.2 An Analytical Model for Wound Field Synchronous Generators	45
3.2.1 Analytical sizing equations and the logic flow of an analytical sizing script.....	46
3.2.2 Sizing validation of a WFSG sizing script.....	51
3.2.3 Performance validation of a WFSG sizing script.....	53

3.3 FE Models for Wound Field Synchronous Generators	53
3.3.1 FE model construction for WFSGs	55
3.3.2 Experimental Validation for electromagnetic FE models	57
3.4 Thermal models for a WFSG	59
3.4.1 A lumped parameter thermal network.....	59
3.4.2 A lumped parameter thermal network for a WFSG	62
3.4.3 Experimental validation for the lumped thermal network for an existing WFSG.....	70
3.5 Conclusion	73
Chapter 4 Design methodologies for high speed wound field synchronous generators.....	74
4.1 Trade-off study for high speed wound field synchronous generators	76
4.1.1 Design process for a high-speed wound field synchronous generator	76
4.1.2 Power quality considerations for WFSGs	88
4.1.3 Torque ripple consideration for WSFGs	99
4.2 Design methodologies for high speed wound field synchronous generators with high operating temperature	100
4.2.1 Design process of a high-speed wound field synchronous generator at higher coil operating temperature	101
4.2.2 Losses consideration for a high speed wound filed synchronous generator.....	108
4.2.3 Investigation of effects of length to radius ratio for wound field synchronous generators on maximum copper coil temperature.....	116
4.3 Conclusion	126
Chapter 5 Mechanical design and FE analysis.....	128
5.1 Mechanical design and FE analysis	129
5.1.1 Challenges for WFSGs from mechanical perspective.....	129

5.1.2 Von-Mises distribution analysis of WFSG rotor cores	131
5.2 Von-Mises distribution analysis of proposed stress reduction methods.....	144
5.2.1 Fillets sizing for corner 1 and 2.....	144
5.2.2 Increasing the thickness of the thin edges holding damper cages (damper edge 3).....	147
5.2.3 Open slot configuration for damper cages	149
5.2.4 Integrated damper cages designed for retaining copper wires and THD reduction.....	152
5.2.5 Deformation of rotor structure for WFSGs.....	167
5.3 Further considerations for improving the performance of a WFSG.....	169
5.3.1 Effects of air gap length on the overall WFSG performance	170
5.3.2 Methodologies for stress reduction at critical spots	173
5.3.3 Practical limitations for assembling a WFSG in house.....	177
5.3.4 Solidworks 3D explosive view.....	180
5.4 Conclusion	181
Chapter 6 Manufacturing and experimental validation of high speed wound field synchronous generators.....	185
6.1 Manufacturing of a main alternator.....	186
6.1.1 Basic characteristics.....	186
6.1.2 Presentation of the individual components	187
6.2 Assembly process of the WFSG	189
6.2.1 Stator assembly and thermal couples setup.....	189
6.2.2 Rotor core assembly process.....	190
6.2.3 Final complete assembly process	196
6.3 Experimental testing of the WFSG prototype	197

6.3.1 Open circuit and short circuit characteristics	199
6.3.2 Power quality results.....	202
6.3.4 Thermal performance of a WFSG prototype.....	206
6.4 Conclusion	212
Chapter 7 Updated design for wound field synchronous generators.....	214
7.1 Descriptions of high grade materials.....	216
7.2 CoFe based rotor core material – Vacodur S Plus.....	219
7.2.1 Stator core made of Vacoflux 48.....	219
7.2.2 Stator core made of 10JNEX900.....	222
7.2.3 Stator core made of 35HXT590T.....	226
7.3 SiFe based rotor core material – 35HXT590T	229
7.3.1 Stator core made of Vacoflux 48.....	229
7.3.2 Stator core made of 10JNEX900.....	232
7.3.3 Stator core made of 35HXT590T.....	234
7.4 SiFe based rotor core material – 35HXT680T	237
7.4.1 Stator core made of Vacoflux 48.....	238
7.4.2 Stator core made of 10JNEX900.....	240
7.4.3 Stator core made of 35HXT590T.....	243
7.5 SiFe based rotor core material – 35HXT780T	245
7.5.1 Stator core made of Vacoflux 48.....	246
7.5.2 Stator core made of 10JNEX900.....	248
7.5.3 Stator core made of 35HXT590T.....	250
7.6 Summary of the design considerations adopting high graded materials	252

Chapter 8 Conclusion.....	260
8.1 Object oriented analytical, electromagnetic FE, thermal and mechanical design tool for a WFSG	261
8.2 Integrated damper cages for THD improvements	263
8.3 Major contributions to research	263
8.4 Future work.....	264
Appendix A Modelling: Heat Transfer Coefficients Calculation.....	266
References.....	271

LIST OF FIGURES

Fig. 1 Evolution of electrical power systems.	15
Fig. 2 Generators designed and tested or implemented for aircraft power generation systems.	17
Fig. 3 Constant speed constant frequency systems.	21
Fig. 4 Variable speed power generation systems.	23
Fig. 5 Schematics of a 3-stage system comprising the PMG, the exciter, the diode rectifier and the WFSG.	29
Fig. 6 Rotor structure of a typical WFSG.	29
Fig. 7 alignment of rotating d-q axes and stationary a, b, c axes on the d-q plane and the voltage phasor V_s	41
Fig. 8 Generator action (a) under-excited (b) over-excited.....	43
Fig. 9 A typical three phase short circuit currents for a WFSG involves sub-transient, transient and steady state.....	45
Fig. 10 a) A quarter machine model b) flux density distribution in the air-gap for a single pole only	47
Fig. 11 Flow charts for sizing the main alternator of a WFSG	50
Fig. 12 Coupled WFSG OOD architectures.....	54
Fig. 13 a) field map for a full WFSG FE model b) field map for a quarter WFSG FE model.....	56
Fig. 14 Open circuit characteristics and short circuit characteristics for FE results of actual and analytical sizing model and experimental results.....	57
Fig. 15 Conceptual blueprint of a 2D LPTN for elements in one stator slot for a WFSG	64
Fig. 16 Conceptual blueprint of a 2D LPTN for elements in one rotor pole for a WFSG	64
Fig. 17 Conceptual blueprints for a 3D LPTN for an existing WFSG	69
Fig. 18 Experimental stator temperature rise measurements vs. Simulink LPTN simulation (An UoN existing WFSG)	71
Fig. 19 Experimental rotor temperature rise measurements vs. Simulink LPTN simulation (An UoN existing WFSG)	72

Fig. 20 Torque speed map for design requirements in chapter 1.2	77
Fig. 21 Weight information for 4 WFSG design options	80
Fig. 22 FE performance evaluations for 4 WFSG design options.....	81
Fig. 23 Maximum stator temperature during generation mode.....	82
Fig. 24 Maximum rotor temperature during generation mode.....	84
Fig. 25 Torque production for 3 WFSG design options.....	85
Fig. 26 Maximum stator temperature during starting mode.....	86
Fig. 27 Maximum rotor temperature during starting mode.....	87
Fig. 28 Rotor pole shaping methods a) exaggerated pole shaping methods explanation b) a pole shaping mode simulated in FE software c) zoomed in in-consistent air gap	88
Fig. 29 Sensitivity analysis of THD level with different pole shaping depth at various speeds	90
Fig. 30 No-load THD level in real value (not in percentage) at different generation speeds for 3 THD reduction techniques	92
Fig. 31 Maximum stator coil temperature for the original WFSG and WFSGs with THD reduction techniques implemented.....	93
Fig. 32 Maximum rotor coil temperature for the original WFSG and WFSGs with THD reduction techniques implemented.....	94
Fig. 33 Torque speed map for WFSGs with THD reduction features in Table 10.....	95
Fig. 34 Torque speed curve for two THD reduction techniques combined	96
Fig. 35 Maximum stator temperature for WFSG design options with two different THD reduction techniques	97
Fig. 36 Maximum rotor temperature for WFSG design options with two different THD reduction techniques	97
Fig. 37 Comparison of no-load THD level in real value for all the design cases been simulated....	98
Fig. 38 Comparison of full load THD level in real value for all the design cases been simulated..	99
Fig. 39 Torque ripple for WFSGs design options with THD reductions techniques	99
Fig. 40 Stator coil temperature of a WFSG with an electric loading of 30 <i>kA/m</i> during starting operation	102

Fig. 41 Stator coil temperature of a WFSG with an electric loading of 30 kA/m during generation operation	102
Fig. 42 Rotor coil temperature of a WFSG with an electric loading of 30 kA/m during starting operation	103
Fig. 43 Rotor coil temperature of a WFSG with an electric loading of 30 kA/m during generation operation	103
Fig. 44 Stator coil temperature of a WFSG with an electric loading of 50 kA/m during starting operation	104
Fig. 45 Stator coil temperature of a WFSG with an electric loading of 50 kA/m during generation operation	104
Fig. 46 Rotor coil temperature of a WFSG with an electric loading of 50 kA/m during starting operation	105
Fig. 47 Rotor coil temperature of a WFSG with an electric loading of 50 kA/m during generation operation	106
Fig. 48 Torque speed curve for WFSGs design with high temperature with 54 stator slots	107
Fig. 49 Torque ripple for a high temperature 54 slot WFSG	107
Fig. 50 Shaped compacted litz wire	109
Fig. 51 No load harmonic content for a high temperature WFSG design option for 2/3 short pitch stator winding and a skew process of one slot pitch	110
Fig. 52 Cross sectional view of commercial WFSGs implemented on aircraft.....	112
Fig. 53 Rectification circuit on the rotor.....	114
Fig. 54 DC current ripple after a six pulse rectifier with different load inductance.....	115
Fig. 55 Generator stator temperature (typical value)	116
Fig. 56 Maximum stator and rotor temperature for WFSGs designed with different length to diameter ratio	118
Fig. 57 Weight information for individual WFSGs designed with different L2D ratio	119
Fig. 58 Maximum rotor and stator coil temperature with increased field current density	123
Fig. 59 Weight comparison when the rotor current density is increased	124

Fig. 60 Rotor pole structure including rotor body, field coils and damper cages.....	132
Fig. 61 Von-Mises distribution for case 1 (rotor core only)	134
Fig. 62 Von-Mises distribution simulation setup for case 2 (rotor body and rotor copper coils)...	136
Fig. 63 Von-Mises distribution for case 2 (rotor core and field coils).....	137
Fig. 64 Von-Mises distribution simulation setup for case 3 (rotor body and damper cages).....	138
Fig. 65 Von-Mises distribution for case 3 (rotor core and damper cages)	138
Fig. 66 Von-Mises distribution simulation setup for case 4 (rotor body, field coils and damper cages)	139
Fig. 67 Von-Mises distribution for case 4 (rotor core, field coils and damper cages)	140
Fig. 68 Field distribution for a WFSG finalized in chapter 4.2 full load condition	144
Fig. 69 Von-Mises distribution for case 4 (rotor core, field coils and damper cages) with 3 mm and 5 mm fillets at corner 1 and 2 respectively.....	145
Fig. 70 A complete rotor core (Courtesy Cummins Generator Technologies).....	146
Fig. 71 Von-Mises distribution for case 4 (rotor core, field coils and damper cages) with 4 mm and 3 mm fillets at corner 1 and 2 respectively.....	147
Fig. 72 Von-Mises distribution for case 4 (rotor core, field coils and damper cages) with 4 mm and 3 mm fillets at corner 1 and 2 respectively the depth of damper edge 0.5 mm.....	148
Fig. 73 Harmonic contents for increased damper bar depth configuration at no-load (see Fig. 72) at 7,200 rpm, 9,000 rpm, 12,000 rpm and 16,000 rpm	149
Fig. 74 Von-Mises distribution for case 4 (rotor core, field coils and damper cages) with 4 mm and 3 mm fillets at corner 1 and 2 respectively damper bar slot opening is set as 1 mm	150
Fig. 75 Zoomed in damper edge 3 a) case 4 simulated in Fig. 69 b) case 4 simulated in Fig. 74..	151
Fig. 76 Harmonic contents for damper bars open slot configuration at no-load (case 4 in Fig. 74) at 7,200 rpm, 9,000 rpm, 12,000 rpm and 16,000 rpm	152
Fig. 77 End caps for retaining field windings (hatched region).....	153
Fig. 78 A WFSG equipped with different damper cage options a) conventional damper cage b) integrated damper cage made of copper c) integrated damper cage made of stainless steel.....	155
Fig. 79 No-load air gap flux density for three different damper cage options	156

Fig. 80 Harmonic contents for a WFSG without any THD reduction technique at 7,200 rpm, 9,000 rpm, 12,000 rpm and 16,000 rpm.....	157
Fig. 81 Harmonic contents for a WFSG with 17-4PH made integrated damper cages with no 2/3 short pitching and no skewing at 7,200 rpm, 9,000 rpm, 12,000 rpm and 16,000 rpm.....	158
Fig. 82 Harmonic contents for a WFSG with 17-4PH H900 made integrated damper cages and 2/3 short pitching at 7,200 rpm, 9,000 rpm, 12,000 rpm and 16,000 rpm.....	159
Fig. 83 Harmonic contents for a WFSG with 17-4PH made integrated damper cages, 2/3 short pitching and one stator slot pitch skew at 7,200 rpm, 9,000 rpm, 12,000 rpm and 16,000 rpm	161
Fig. 84 Harmonic contents for a WFSG with C18150 made integrated damper cages, 2/3 short pitching at 7,200 rpm, 9,000 rpm, 12,000 rpm and 16,000 rpm.....	162
Fig. 85 THD level for WFSG equipped with integrated damper cage made of 17-4PH and C18150	162
Fig. 86 Short circuit transient behaviour for a WFSG equipped with 17-4PH H900 made integrated damper cages.....	163
Fig. 87 B-H properties for A3 steel, 17-4PH with H900 heat treatments, 17-4PH with H1150 heat treatments and M235-35A	164
Fig. 88 Phase RMS voltage, no-load amper-turns and no-load THD for WFSGs equipped with integrated damper cages with different materials	165
Fig. 89 Von-Mises distribution for case 3 (rotor core and damper cages) with 4 mm and 3 mm fillets at corner 1 and 2 respectively	167
Fig. 90 Total deformation for a rotor core geometry for case 4 (rotor core, damper bars and field windings)	169
Fig. 91 Von-Mises distribution for case 4 (rotor core, field coils and damper cages) with 4 mm and 3 mm fillets at corner 1 and 2 respectively; a dovetail is added at the bottom of the rotor core	174
Fig. 92 Von-Mises distribution for case 4 (rotor core, field coils and damper cages) with 4 mm and 3 mm fillets at corner 1 and 2 respectively; a dovetail is added at the bottom of the rotor core with increased fillets	176
Fig. 93 a) Cummins generator winding process b) Rotor core wound by Alliance winding	177

Fig. 94 Von-Mises distribution of a separate rotor core at 6,800 rpm	178
Fig. 95 Von-Mises distribution of a separate rotor core at 7,200 rpm	179
Fig. 96 3D explosive view of a WFSG designed based on geometry in Fig. 95.....	180
Fig. 97 Cross sectional view of a WFSG designed based on geometry in Fig. 95.....	181
Fig. 98 a) A housing and end plates for the WFSG b) Front end plate quality check under coordinate measurements machine CMM	187
Fig. 99 a) A rotor core made by A b) A rotor core made by B c) A stator core made by C.....	188
Fig. 100 a) A slip ring b) SKF bearing 6211-2Z k.....	188
Fig. 101 A customized shaft for a WFSG designed in chapter 5.3.3	188
Fig. 102 a) axial position for 5 thermal couples b) radial location for thermal couples.....	190
Fig. 103 a) full stator assembly setup b) thermal couples assemblies inside stator coil.....	190
Fig. 104 a) first rotor core assembly b) modified winding process c) outcome of final rotor core outlook	191
Fig. 105 a) Position of two k type thermal couples on rotor axial direction b) position of two k type thermal couples on rotor radial direction	192
Fig. 106 a) A rotor core assemble with rotor coils ready b) 17-4PH integrated damper cage in place	194
Fig. 107 a) rotor balancing with SCHENCK balancing machine b) the entire rotor core after rotor balancing.....	195
Fig. 108 a) a rotor core been installed inside the stator housing b) a slip ring installation process	195
Fig. 109 The final assembly for a WFSG prototype	196
Fig. 110 An experimental rig setup for a WFSG testing.....	198
Fig. 111 Overall rig setup for a WFSG testing	199
Fig. 112 The flow rate of air from the outlet port of a generator	199
Fig. 113 Open circuit test for a WFSG prototype experiment (exp.) results vs FE simulation.....	200
Fig. 114 Short circuit test for a WFSG prototype experiment (exp.) results vs FE simulation.....	201
Fig. 115 FE no-load voltage waveform at different speeds a) 500 rpm b) 1,000 rpm c)1,500 rpm d) 3,000 rpm.....	202

Fig. 116 Harmonic contents for FE no-load terminal voltage waveform at 500 <i>rpm</i> , 1,000 <i>rpm</i> , 1,500 <i>rpm</i> and 3,000 <i>rpm</i>	203
Fig. 117 Experimental no-load voltage waveform at different speeds a) 500 <i>rpm</i> b) 1,000 <i>rpm</i> c)1,500 <i>rpm</i> d) 3,000 <i>rpm</i>	204
Fig. 118 Harmonic contents for experimental no-load terminal voltage waveform at 500 <i>rpm</i> , 1,000 <i>rpm</i> , 1,500 <i>rpm</i> and 3,000 <i>rpm</i>	205
Fig. 119 FE and experimental THD level for no-load terminal voltage at 500 <i>rpm</i> , 1,000 <i>rpm</i> , 1,500 <i>rpm</i> and 3,000 <i>rpm</i>	206
Fig. 120 Stator temperature rise at full load stator currents - experimental measurements versus a 3D LPTN simulation.....	207
Fig. 121 Rotor coil temperature rise maximum rotor currents - experimental measurements versus a 3D LPTN simulation.....	210
Fig. 122 Stator temperature rise at 1,500 <i>rpm</i> full load stator temperature measurements versus a LPTN simulation.....	211
Fig. 123 Rotor coil temperature rise at 1,500 <i>rpm</i> full load rotor temperature measurements versus a LPTN simulation.....	212
Fig. 124 Comparison of core losses and yield strength for different high performance electrical steels	216
Fig. 125 BH curve for representative materials such as 10JNEX900, CoFe and SiFe.....	218
Fig. 126 a) No-load field plot for WFSGs with rotor core made of Vacodur S Plus and stator core made of Vacoflux 48 at 7,200 <i>rpm</i> b) Von-Mises distribution of rotor geometry made of Vacodur S Plus with stator core made of Vacoflux 48 at 16,000 <i>rpm</i> c) Total deformation of rotor geometry made of Vacodur S Plus with stator core made of Vacoflux 48 at 16,000 <i>rpm</i>	221
Fig. 127 a) No-load field plot for WFSGs with rotor core made of Vacodur S Plus and stator core made of 10JNEX900 at 7,200 <i>rpm</i> b) Von-Mises distribution of rotor geometry made of Vacodur S Plus with stator core made of 10JNEX900 at 16,000 <i>rpm</i> c) Total deformation of rotor geometry made of Vacodur S Plus with stator core made of 10JNEX900 at 16,000 <i>rpm</i>	225

Fig. 128 a) No-load field plot for WFSGs with rotor core made of Vacodur S Plus and stator core made of 35HXT590T at 7,200 rpm b) Von-Mises distribution of rotor geometry made of Vacodur S Plus with stator core made of 35HXT590T at 16,000 rpm c) Total deformation of rotor geometry made of Vacodur S Plus with stator core made of 35HXT590T at 16,000 rpm 228

Fig. 129 a) No-load field plot for WFSGs with rotor core made of 35HXT590T and stator core made of Vacoflux 48 at 7,200 rpm b) Von-Mises distribution of rotor geometry made of 35HXT590T with stator core made of Vacoflux 48 at 16,000 rpm c) Total deformation of rotor geometry made of 35HXT590T with stator core made of Vacoflux 48 at 16,000 rpm 231

Fig. 130 a) No-load field plot for WFSGs with rotor core made of 35HXT590T and stator core made of 35HXT590T at 7,200 rpm b) Von-Mises distribution of rotor geometry made of 35HXT590T with stator core made of 35HXT590T at 16,000 rpm c) Total deformation of rotor geometry made of 35HXT590T with stator core made of 35HXT590T at 16,000 rpm..... 233

Fig. 131 a) No-load field plot for WFSGs with rotor core made of 35HXT590T and stator core made of 35HXT590T at 7,200 rpm b) Von-Mises distribution of rotor geometry made of 35HXT590T with stator core made of 35HXT590T at 16,000 rpm c) Total deformation of rotor geometry made of 35HXT590T with stator core made of 35HXT590T at 16,000 rpm..... 235

Fig. 132 a) No-load field plot for WFSGs with rotor core made of 35HXT680T and stator core made of Vacoflux 48 at 7,200 rpm b) Von-Mises distribution of rotor geometry made of 35HXT680T with stator core made of Vacoflux 48 at 16,000 rpm c) Total deformation of rotor geometry made of 35HXT680T with stator core made of Vacoflux 48 at 16,000 rpm 239

Fig. 133 a) No-load field plot for WFSGs with rotor core made of 35HXT680T and stator core made of 10JNEX900 at 7,200 rpm b) Von-Mises distribution of rotor geometry made of 35HXT680T with stator core made of 10JNEX900 at 16,000 rpm c) Total deformation of rotor geometry made of 35HXT680T with stator core made of 10JNEX900 at 16,000 rpm 241

Fig. 134 a) No-load field plot for WFSGs with rotor core made of 35HXT680T and stator core made of 35HXT590T at 7,200 rpm b) Von-Mises distribution of rotor geometry made of 35HXT680T with stator core made of 35HXT590T at 16,000 rpm c) Total deformation of rotor geometry made of 35HXT680T with stator core made of 35HXT590T at 16,000 rpm..... 244

Fig. 135 a) No-load field plot for WFSGs with rotor core made of 35HXT780T and stator core made of Vacoflux 48 at 7,200 rpm b) Von-Mises distribution of rotor geometry made of 35HXT780T with stator core made of Vacoflux 48 at 16,000 rpm c) Total deformation of rotor geometry made of 35HXT780T with stator core made of Vacoflux 48 at 16,000 rpm	247
Fig. 136 a) No-load field plot for WFSGs with rotor core made of 35HXT780T and stator core made of 10JNEX900 at 7,200 rpm b) Von-Mises distribution of rotor geometry made of 35HXT780T with stator core made of 10JNEX900 at 16,000 rpm c) Total deformation of rotor geometry made of 35HXT780T with stator core made of 10JNEX900 at 16,000 rpm	248
Fig. 137 a) No-load field plot for WFSGs with rotor core made of 35HXT780T and stator core made of 35HXT590T at 7200 rpm b) Von-Mises distribution of rotor geometry made of 35HXT780T with stator core made of 35HXT590T at 16,000 rpm c) Total deformation of rotor geometry made of 35HXT780T with stator core made of 35HXT590T at 16,000 rpm.....	251
Fig. 138 Total deformation and actual safety factor for WFSG with each combination of materials	253
Fig. 139 Maximum stator and rotor coil temperature for 12 different materials combinations	256
Fig. 140 Weight information for generator designed with these.....	257

LIST OF TABLES

Table 1 Efficiency comparison for various generator found in the literature	24
Table 2 Flux density required for the Cummins generator	52
Table 3 Comparison of an existing machine dimension and the analytical sizing script	52
Table 4 An analytical main alternator performance vs. an existing alternator performance.....	53
Table 5 Heat transfer coefficients obtained at critical points for the existing WFSG	67
Table 6 Comparison of inlet and outlet temperature at stator back iron, rotor windings and stator windings.....	70
Table 7 Analytical sizing dimensions of a WFSG	79
Table 8 Losses comparison of WFSGs with different slot combinations	81
Table 9 Tick marks for 3 deign WFSG design options.....	87
Table 10 Key dimensions for WFSGs with THD reduction methods applied	94
Table 11 Active weight of the different parts of the WFSG designed	108
Table 12 Key parameters for WFSGs designed in Fig. 56.....	120
Table 13 Key parameters for WFSGs designed in Fig. 59 with increased field current density....	125
Table 14 Sensitivity analysis of mesh refinement size versus stress level.....	133
Table 15 Key performance comparison of the state of art WFSG introduce lately	171
Table 16 MMF consumed by different part of a WFSG for case 4 geometry (see Fig. 71) with specific flux density	172
Table 17 Weight of different components and the overall weight	186
Table 18 full load performance of a WFSG designed with Vacodur S Plus and Vacoflux at 7,200 rpm	222
Table 19 full load performance of a WFSG designed with Vacodur S Plus and 10JNEX900 at 7,200 rpm.....	226
Table 20 full load performance of a WFSG designed with Vacodur S Plus and 10JNEX900 at 7,200 rpm.....	228
Table 21 full load performance of a WFSG designed with 35HXT590T and Vacoflux 48 at 7,200 rpm.....	232

Table 22 full load performance of a WFSG designed with 35HXT680T and 10JNEX900 48 at 7,200 rpm.....	234
Table 23 full load performance of a WFSG designed with 35HXT590T and 35HXT590T at 7,200 rpm.....	236
Table 24 full load performance of a WFSG designed with 35HXT680T and Vacoflux 48 at 7,200 rpm.....	240
Table 25 full load performance of a WFSG designed with 35HXT680T and 10JNEX900 48 at 7,200 rpm.....	242
Table 26 full load performance of a WFSG designed with 35HXT680T and 35HXT590T at 7,200 rpm.....	245
Table 27 full load performance of a WFSG designed with 35HXT780T and Vacoflux 48 at 7,200 rpm.....	247
Table 28 full load performance of a WFSG designed with 35HXT780T and 10JNEX900 at 7,200 rpm.....	249
Table 29 full load performance of a WFSG designed with 35HXT780T and 35HXT590T at 7,200 rpm.....	250

ACRONYMS

AC	Alternative current
AGD	Axial gear differential
APU	Auxiliary power unit
AVR	Automatic voltage regulator
CFD	Computational fluid dynamics
CMM	Coordinate measuring machine
CSCF	Constant speed constant frequency
CSD	Constant speed drive
DC	Direct current
FE	Finite element
GE	General electric
HTC	Heat transfer coefficients
HVDC	High voltage direct current
IDG	Integrated drive generator
IG	Induction generator
IM	Induction machine

LPTN	Lumped parameters thermal network
MEA	More electric aircraft
MMF	Magneto-motive-force
MTBF	Mean time between failures
OOD	Object oriented design
PE	Power electronics
PEC	Power electronic converters
PM	Permanent magnet
PMG	Permanent magnet generator
POR	Point of regulation
RMS	Root mean square
SiFe	Silicon iron
SR	Switched reluctance
THD	Total harmonic distortion
UoN	University of Nottingham
VPI	Vacuum pressure impregnation
VSCF	Variable speed constant frequency

VSVF Variable speed variable frequency

WFSG Wound field synchronous generator

GLOSSARY OF SYMBOLS

A	Linear current density or electric loading, [kA/m]
\hat{B}_δ	Peak air-gap flux density, [T]
\hat{B}_d'	Apparent flux density on the rotor pole, [T]
b_p	Width of rotor pole, [m]
\hat{H}_d	Magnetic field strength, [A/m]
J	current density, [A/m ²]
k_{Cs}	Rotor carter factor
k_{Fe}	Stacking factor of laminations
l	Axial length of the machine, [m]
l'	Equivalent length of the machine, [m]
$\hat{U}_{m,\delta e}$	Magnetic voltage consumed by the air-gap, [A]
V_s	Terminal voltage of a WFSG [V]
δ	Air-gap length, [m]
δ_{load}	load angle, [degree]
μ_0	Permeability of vacuum, $4\pi \cdot 10^{-7}$ [Vs/Am, H/m]
τ_p	Rotor pole pitch, [m]
τ_{pspan}	Rotor pole span

ω_c Synchronous speed, [rad/s]

Chapter 1

Project introduction

Policy makers around the world are issuing stringent requirements for greenhouse gas emission every year. These policies have huge impacts on daily transports as they contribute to significant amount of greenhouse gas emission. Automotive industry has already launched a few pure electric vehicles such as Tesla model S, Audi E-tron and Mercedes EQC. Therefore, the trend for replacing existing vehicles with electric vehicles is an inevitable path. Advantages such as better efficiency, lower maintenance cost offered by transportation electrification are appealing aspects to end users. Consequently, transportation electrification is becoming a hot research focus for transportation industry in the future.

Expanded demands for electrified public transports raise requirements for significant weight and volume reduction for machines used for power generation and powertrain. The advancements on power electronics (PE) has enabled the utility of various machine topologies such as permanent magnet (PM), switched reluctance (SR), induction and wound field machines under variable speed conditions. PM, SR and induction machine topologies offer a chance for higher power density and robustness at high operating speed. Therefore, automotive and aviation industry spend great efforts on investigating PM, SR and induction machine topologies. However, classical wound field synchronous machine topology is left behind since most wound field synchronous machines in the past are used as huge power

generators at fix speed to generate 50 Hz/60 Hz grid voltage. Despite the advantages offered by wound field synchronous generators (WFSG) such as field controllability, temperature independent performance, WFSG topologies are considered to have less chance to achieve the same high speed as PM, SR or inductions hence low power density.

In contrast, PM, SR and induction machine offers advantages such as higher efficiency, higher power density, cheaper cost and higher robustness. Nevertheless, these machine topologies also have inherent drawbacks. PM materials are highly temperature dependent. SR machines suffers from high torque ripple and induction machines in general have relatively low efficiency. As a result, aviation industry still implements WFSGs as main bus power source. The era of WFSGs dominates aircraft main power generation dates back to 1960 [1]. With more than 50 years of development and implementation, WFSGs are mature technologies can safely operate on board. In contrast, PM and SR power generation systems require more time to address the safety concerns raised by aviation industry and power system standard MIL-STD-704F. Therefore, WFSGs are still a preferable option for power generation methods for aviation industry. Even the latest introduced more electric aircraft (MEA) the Boeing 787 adopts WFSGs as its starter generator coupled with the main power distribution buses. In contrast, research efforts on PM and SR generators are a hot topic for aviation industry and academic field as well. An elaboration of this contradictory phenomenon between research streams and industry preference is presented in chapter 2.

The most appealing advantage offered by WFSGs is its field controllability. Therefore, WFSGs can be quickly de-excited when there is a fault in the terminal voltages. WFSGs does not have PM materials on which the electromagnetic performance is highly temperature sensitive and dependent. This implicates the performance of a WFSG is highly temperature independent. The third obvious advantage for WFSGs is its proven technologies and reliability in the past 50 years. These advantages are extremely attractive to safe critical applications such as aviation industry. Consequently, although PM and SR generators are considered to have better performance compared with WFSGs, the research and development efforts are still increasingly spent on WFSGs. A mighty breakthrough for WFSGs is achieved by Honeywell in 2013 [2].

Ideal more electric aircraft (MEA) concepts would replace mechanical, pneumatic and hydraulic power with electric power. The lately introduce MEA the Boeing 787 has replaced its pneumatic systems with electric powered systems [3]. The total installed electric capacity on board for the Boeing 787 has reached 1MW. Each power generation unit the Boeing 787 can deliver 250 kVA which is the highest power rated single power generation unit found on commercial aircraft. This trend to replace existing mechanical, pneumatic and hydraulic power sources results in a significantly increased demand for electric power. It can be perceived that the future MEA will likely have more than 1MW installed on board for large passage aircrafts. Therefore, increased electric capacity on board and strict weight requirements bring unprecedented challenges for design of WFSGs for future MEA.

Therefore, in the past decade, variable speed WFSGs with motoring functions is still a brand new field only favoured by aviation industry. Promisingly, automotive giants BMW and Renault are joining the crew developing classical WFSGs into variable speed machines that are able to operate both as motor and generator. BWM iX3 and Renault ZOE already implemented WFSG as the traction source for their electric vehicles. Therefore, the transport electrification stream still demands high speed WFSG as long as three major obstacles are addressed – high speed operation, power density and budget cost.

1.1 Project description

The key challenges for high speed, high power and high power density WFSGs are listed below.

- a) The nature of the shape of a rotor core of salient pole generators experience high stress level at high speed in general.
- b) Limited yield strength of soft magnetic core materials prevents salient pole machine from reaching high rotational speed.
- c) Significant amount of heat generated by the rotor coils of a WFSG increases the difficulties regarding to a rotor cooling.
- d) Extracting heat from a limited surface area inside a WFSG is difficult.

The design methodologies for WFSGs with high speed and high power density are the complex multi-discipline problems including electromagnetic, thermal and mechanical aspects. Since high power rating, high speed and high power density are all design objectives, the balance between these contradictory aspects becomes an extremely challenging task.

Therefore, bringing the power density of WFSGs to a completely new level requires an understanding of multi-discipline subjects such as material science, electromagnetic, thermal and mechanical aspects. Apart from the material science, a design tool is required to design and analyse the performance of a high speed. At the moment, market ready FE software is capable of analysing the electromagnetic, thermal and mechanical behaviour of an electric machine with a given geometry. However, no existing tool is available to design and analysis the performance of a

WFSG with given generator performance requirements such as rated power, speed and voltage etc. as input parameters from scratch.

1.2 Aims and objectives

The aim of this project is to develop an object oriented multi-physics design tool capable of designing, optimizing and analysing multi-physics phenomena of high speed WFSGs. Meanwhile, this object oriented design (OOD) tool is also designed with features such as continuous upgrades for existing design modules and further expansions for new design modules. Upgrades for existing design modules offer advantages of improving the accuracy and performance of existing design modules without affecting other modules. Further expansions of new design modules include program capable of analysing the bearing life time, vibration and noise level of a WFSG etc. without changing the rest of the modules. The design requirements for a high speed WFSG are listed as below.

- | | |
|--|------------------------------------|
| a) Rated power: | 250 <i>kVA</i> |
| b) Rated terminal voltage:
(POR) | 235 <i>Vac</i> Point of regulation |
| c) The number of pole pairs for the main alternator: | 3 |
| d) Power factor: | 0.75 – 1 lagging |
| e) Frequency range: | 360 ~ 800 <i>Hz</i> |
| f) DC link voltage: | 540 <i>Vdc</i> |
| g) Maximum allowable speed: | 18,000 <i>rpm</i> |
| h) Starting time: | 60s worst case scenario 120s |
| i) Starting torque: | 407 <i>Nm</i> |
| j) Weight | around 100 <i>kg</i> |
| k) Cooling capability | air |

In literatures, a high speed WFSG usually adopts cobalt iron (CoFe) as core materials [1] with high yield strength, but this sort of material is usually very expensive provided by selected suppliers such as Vacummschmelze. Due to limited budget, conventional silicon steel M235-35A is adopted as core materials, but this type of material only has half of the yield strength compared with CoFe. Several critical objectives are established to achieve the aim of developing an OOD tool to design and analyse the performance of a high speed WFSG.

First, an electromagnetic analytical sizing script is developed and validated against the actual dimensions of an existing WFSG available.

Second, a FE model is also developed to analyse the electromagnetic performance of a WFSG. Scripting commands are adopted to build this FE model in order to allow easy migration of different design modules. The dimensions of the FE WFSG model are controlled by the input dimensions to the FE scripts. The validity of the FE model is verified by comparing the electromagnetic simulation results against experimental results.

A thermal model based on lumped parameter circuits is developed to analyse the temperature behaviour of different sections of a WFSG is also developed as the third objective. This lumped parameters thermal network (LPTN) is validated by applying losses results from FE simulation and the initial heat transfer coefficients (HTC) based on empirical data. This verified thermal model is integrated into an OOD tools to analyse the temperature of WFSGs been designed.

At this stage, an OOD tool composes two validated design modules - an electromagnetic and a thermal module. This partially finished tool is used to design and analyse the electromagnetic and thermal behaviour of a high speed WFSG. The final WFSG is selected from a series of WFSG design options, which is passed to the next stage for mechanical analysis. This is considered as the fourth objective.

The fifth objective includes mechanical design and static structure simulation of the geometry designed according to the electromagnetic and thermal constraints. Some dimensions not affecting electromagnetic performance of a WFSG is adjusted based on Von-Mises analysis. This information is fed back to the electromagnetic sizing scripts to prevent critical sectors of a WFSG from exceeding the mechanical limitations.

Theoretical analysis of a multi-physic model for a WFSG is finished. Nevertheless, M235-35A is selected to be the core material for a high speed WFSG. This significantly limits the maximum peripheral speed that can be achieved compared with materials with high yield strength. Therefore, new mechanical geometry is investigated trying to allow silicon iron (SiFe) made core reaching targeted maximum operating speed.

Next objective is to verify this multi-physic model with a prototype built according to the final engineering design. With a multi-physic model been validated by a WFSG prototype, this OOD design tool can be used to design high speed WFSGs with relatively good accuracy. Meanwhile, object oriented features for this OOD tool also allow further upgrades with other analysis associated with WFSGs such as

bearing life time calculation, critical speed analysis and insulation life time study, etc.

1.3 Thesis outline

The structure of this thesis is presented in a way to elaborate each step and process to establish a multi-physic design tool to design and analyse high speed WFSGs.

Chapter 1 introduces the backgrounds for WFSGs implemented for aviation industry and identifies the challenges for variable high speed synchronous machines. The aim and objectives for designing high speed WFSGs is elaborated. Chapter 2 gives a thorough review on the design choices of a machine under different power rating and speed. In the review, it is concluded that classical WFSGs is still capable of competing against other more advanced machine topologies. Challenges and opportunities to achieve a high-power density machine are also discussed and presented.

Chapter 3 presents the background operating theory of a WFSG. A detailed explanation of an analytical sizing process based on electromagnetic model for a WFSG is presented and validated. A 3D LPTN model is also established and validated to analyse the temperature behaviour of a WFSG at different sections.

The design process and trade off studies for an optimum WFSG design option with M235-35A are presented in chapter 4. Both low and high temperature wires are considered as designed options to ensure minimum weight is achieved. Power quality, torque ripple and AC losses are also been analysed for WFSGs designed in chapter 4. Different length to diameter ratios are considered to understand how this

critical design parameter can affect the weight of a generator with same power rating and cooling capability.

Chapter 5 performs the static structure (Von-Mises distribution) analysis of a WFSG designed and finalized in chapter 4. Compromise between core stress and the available rotor winding area (rotor coil temperature) is considered. Options for stress reduction at critical rotor spots are analysed in chapter 5. At the end, air gap length reduction and dovetail structures at the bottom of the core are considered as very effective methods of improving the performance of a WFSG without changing core material to high grade soft-magnetic cores. A complete Solidworks 3D model including non-active components (e.g. a shaft, bearings and accessories) and active parts (e.g. stator and rotor cores) is presented for later engineering process (engineering drawings and manufacturing).

Chapter 6 includes the manufacturing aspects of the WFSG finalized in chapter 5. The assembly process of the WFSG is well presented. The experimental validation of the proposed multi-physics design tools is presented.

Chapter 7 implements the validated multi-physics design tool to design and analyse a WFSG adopting advanced CoFe and SiFe based materials to investigate if further weight reduction can be achieved. Meanwhile, an objective of high speed, low cost, relative low mass WFSG is also considered adopting less expensive SiFe materials in this chapter to expand the possible utility application fields such as automotive, marine and renewable energy generation industry for a WFSG.

Chapter 8 summarizes the key concepts of multi-physics design tool and imperative achievements of this thesis.

Chapter 2

Literature review

With the advent of enabling technologies such as power electronics, fast computational resources and new materials, modern permanent magnet and switched reluctance drives are perceived to achieve much higher performances than the traditional wound field synchronous generators. Yet, the aviation industry still implements the classical wound field synchronous generators even on the latest platform - Boeing 787.

This chapter focuses on investigating this particular trend by presenting a detailed overview of historical generation systems on board aircraft. This analysis compares the current state of the art of wound field machines with other generator families. The results of this analysis are then projected into the needs of electrical power generation and distribution systems on aircraft. While power density is a major objective for any aerospace application, however the extra benefits associated with wound field systems are still essential even in today's era of modern technologies.

Later chapter then focuses on the main challenges for improving power density of wound field machines. Recommendations, opportunities and improvements related to wound field machines are discussed. In conclusion, if robust designs for higher speed wound field generators are consolidated, it is very probably that these classical machines might still be implemented on future MEA platforms.

2.1 Introduction

As the aircraft industry keeps moving toward greener and more electric solutions [4] [5], electrical power generation in aircraft will continue to play an ever-more important role. The push towards ‘bigger and better’ power generation on board today becomes more and more important. However, the truth is that on board power systems have been continuously evolving since the start of manned flight.

Before the 1950s, electric loads on aircraft were limited to very basic functions such as flight controls, lighting and heating. To accomplish these tasks, small DC generators were typically enough [6]. After the 1950s, more electric loads, such as de-icing, environmental control and flight control, etc. started to be introduced, resulting in heavier power requirements. Fig. 1 summarizes the evolution of the most important power systems which have been implemented on board aircraft since the 1950. As can be observed in Fig. 1, various power system configurations have been proposed and investigated to accommodate the progressively increasing electric loadings. Early configurations included higher voltage DC systems, such as the 112V DC bus adopted by the Vickers Valiant V Bomber [7]. Later on, DC distribution systems started to be replaced by AC systems coupled with constant speed drives (CSDs), thus resulting in constant speed constant frequency (CSCF i.e. 400Hz) distribution systems. Such CSDs were available in two variants, namely axial gear differentials (AGDs) in the early 1960s [1] or integrated drive generators (IDG) [1]. Typical examples include the DC-9 in 1963 [1] and the Boeing 777 which is still operational today [8].

The CSCF systems were a common choice for more than 60 years. However, the limitation of such a system related to the required fixed ‘input’ speed implying the need for heavy, mechanical gearboxes [9] nudged the aircraft industry to start looking toward more feasible and modern alternatives. Thus, the era of the variable speed, power distribution system was launched and today, such VSVF systems can be found on various modern aircraft such as Boeing 787 and Airbus A380.

In all the above, a component that is critical for all power generation and distribution system is the electrical machine responsible for generating the demanded power on board. Typically, this will be an electrical machine, being used in generating mode, whose main shaft is attached to a prime-mover. Various types of electrical machines have been proposed and implemented throughout the years, but the most commonly and extensively used machine is and remains the wound field synchronous generator (WFSG) [10]. The WFSG is a consolidated, well-proven, and reliable technology that has served as the main on board energy source for decades. Its key features include the following.

- 1) Complete field controllability, a feature that is highly desirable for the aviation industry, as it gives an excellent fault mitigation capability.
- 2) Very simple and practically autonomous control schemes are required for operation.
- 3) High flexibility in terms of general scheme and architecture configuration, leading to various operations being achieved, for example, starter generators, three stage starter-generator.

Even considering these advantages, the advances in power electronics (PE) and

computational capabilities of the last decades enabled the toughest competition among WFSGs, switched reluctance (SR) and permanent magnet (PM) machines.

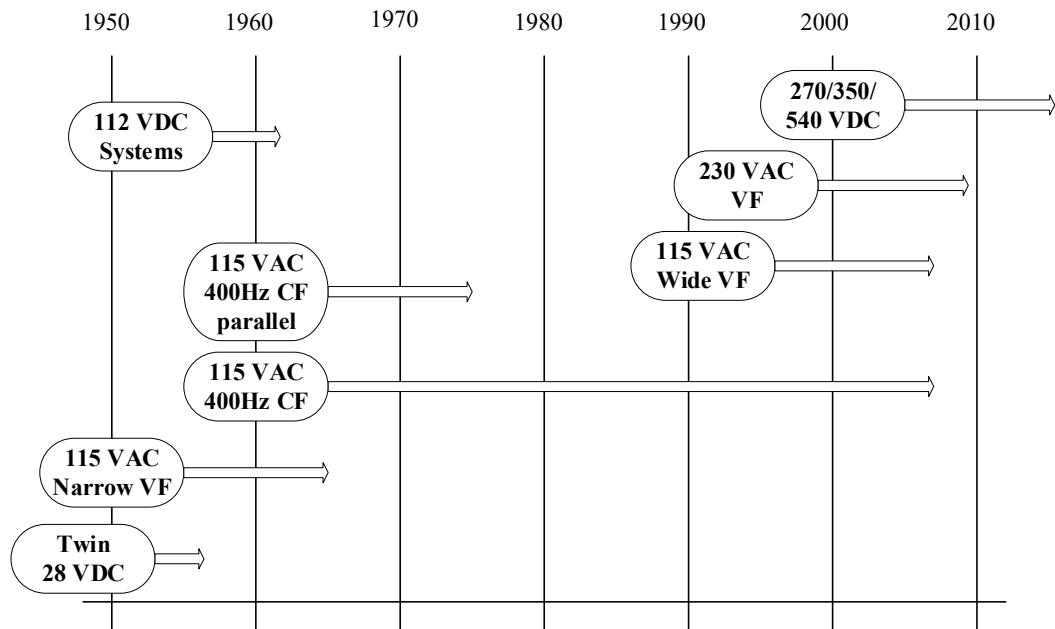


Fig. 1 Evolution of electrical power systems.

Riding on the step-changing advances in new materials such as wide bandgap semiconductors [11], new packaging and manufacturing approaches and thermal management techniques, the field of PE plays an ever-increasing role in the aviation industry [12] [13]. This, in turn, has allowed the PM machine to become a feasible and attractive contender for all areas of the industry.

With the assistance of PE, SR and PM generators have become potential candidates for power generation on modern aircraft. The higher power density and efficiency offered by PM generators and the inherently robust nature of SR machines are very attractive features. These are, therefore, opening up debates about their supposed superiority over the WFSG for power generation.

On the other hand, although both these technologies have been extensively proposed

in literature [14] [15], however, no known commercial aircraft has until now implemented PM or SR generator, as the main electrical source, despite the perceived advantages offered by these technologies.

In light of all the above, this paper therefore aims to investigate and report on the real situation with power generation machines seen today in the aerospace field. To do this, this paper first compiles a relatively detailed literature review of the various alternators and their associated systems to be found on aircraft. This is visually represented by one of the major outcomes of this paper, which is a comprehensive figure of all known generating aerospace machines. The article then analyses more deeply a small number of the better performing machine systems, identified in the review process. The identified WFSG systems for aircraft applications are highlighted. All this is then projected into a discussion about the role of this machine in the aircraft industry and how this classical but ever-evolving machine is and will be still relevant to the modern aircraft industry in the near future.

2.2 Current Status of WFSGs Compared with PM, SR and Induction Generators as Individual Components

Despite the advantages, mentioned in chapter 2.1, offered by the WFSGs, SR and PM generators are also very appealing to the aviation industry and research institutes [16] [17] due to their robust high-speed characteristics, high power densities and system efficiencies [18] [19]. This chapter investigates the status of aircraft primary power generation methods implemented on aircraft by studying the various topologies implemented or designed as engine driven main bus generators. The results are compiled on a dynamic speed map. The parameter termed as dynamic

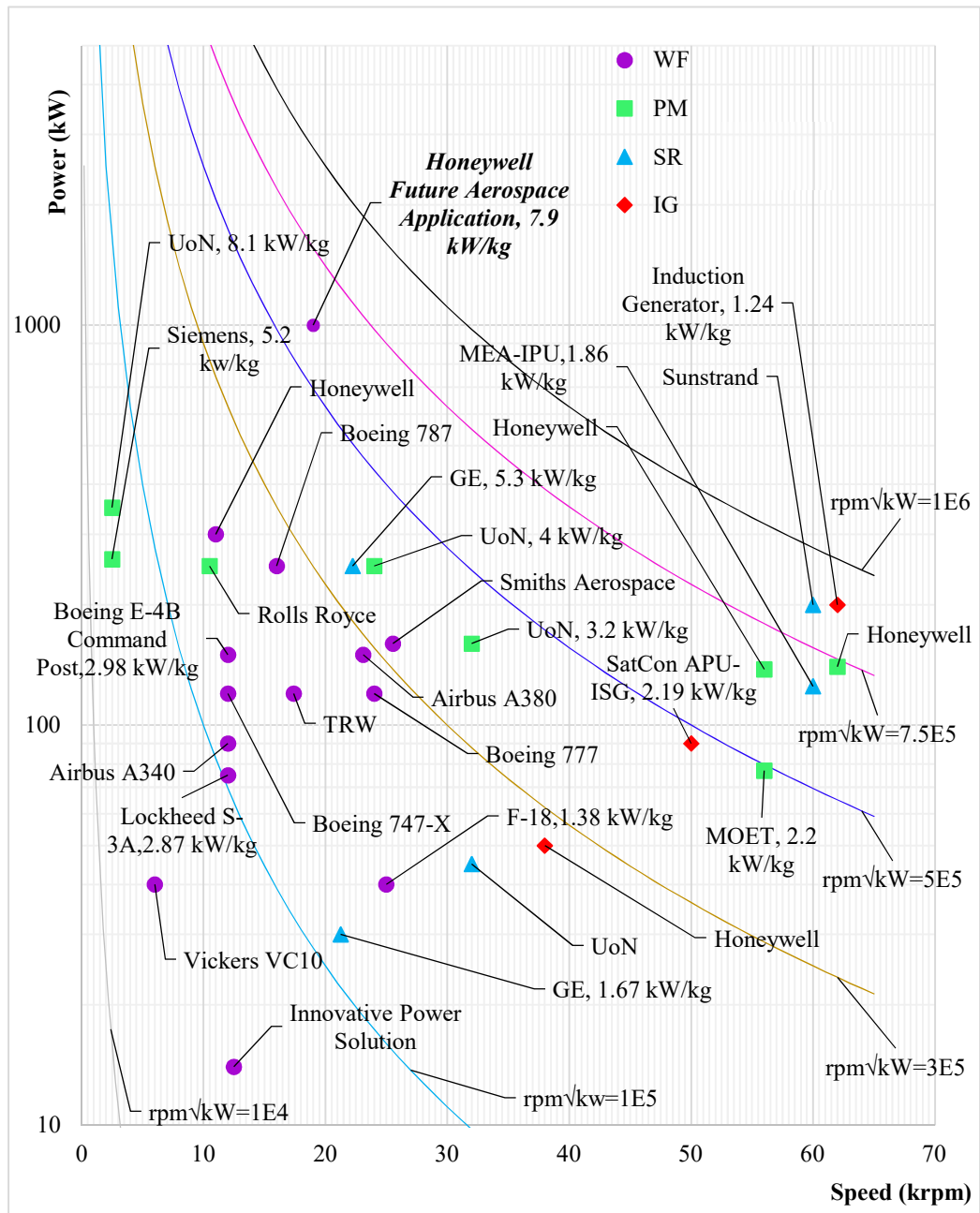


Fig. 2 Generators designed and tested or implemented for aircraft power generation systems
 speed can be defined as a value that is able to define the “goodness” in terms of power capability and operational robustness of rotating bodies. It was first proposed in [20] and its unity of measure “rpm √ kW” is its defining parameter, used to

evaluate the severity of dynamic issues such as critical speed, peripheral speed, and stress [20].

2.2.1 State of the art today – WFSG

Considering that lightweight is always a critical key factor in the aviation industry, an appropriate parameter for power density improvements is the machine speed. Fig. 2 [1, 2, 6, 21-38] collects the dynamic speed information of four types of generators topologies, aimed for aircraft main power generation, from which the power density (kW/kg) can be easily derived.

By comparing machines at a similar dynamic speed (e.g., $\text{rpm} \sqrt{kW} = 100,000$) in Fig. 2, the PM machine developed by University of Nottingham (UoN), Nottingham, U.K., achieves the highest power density (8.1 kW/kg) among all the candidates.

From Fig. 2, one can easily observe how classical WFSGs are typically found in the lower speed ranges of approximately 10 to 25 krpm. However, it can also be easily observed how the top part of Fig. 2 is dominated by PM machine designs [30] [39]. In addition, on the right-hand side of Fig. 2 (i.e. the higher speed ranges) is the realm of the one-body rotor machines such as SR machines and induction machines (IMs) [27] [31]. In the 250 kW range, two channel SR generators developed by General Electric (GE) demonstrate a competitive power density, even against a modern advanced Siemens machines [38].

The main outcome of Fig. 2 is that it allows to visually perceive that for higher power densities, performance developers are actually opting to investigate newer configurations such as PM machines. Higher performance and highly optimized SR

machines are also an interesting concept. In Fig. 2, PM machines, SR generators and induction generator (IG) families can be observed to cover a significant amount of the high speed region, where the design and manufacturing of any machine is particularly challenging. In contrast, WFSGs are typically found for lower speeds regions. The inherent difficulty of implementing WFSGs for higher speeds and by progression their lower power densities relative to PM or SR generators can thus be perceived.

It is the potential for higher power densities (through higher speeds) that makes PM machines and potentially SR machines so attractive for the aviation industry. A comprehensive study in [40] has shown that power density does not always increase with an increase in machine speeds. High speeds usually result in high frequency iron losses and AC copper losses which have a negative impact on further reduction of machine weight and size. It must be clearly stated that till now, it is still 'just' a research and development interest. The only know aircraft that implements SR generators is the F-22 [6] in 2001. No commercial aircraft has so far been equipped with any of the more 'fancy' machines. Even the most more-electric of them all, that is, Boeing 787 in 2009 has WFSGs as main engine driven starter generators. This clearly indicates that although weight is so important in the aerospace agenda, however, there are other important factors, such as the direct control of the field option, the small component count, which still prompts aircraft manufactures to choose the WFSG for power generation in aircraft.

2.2.2 Power density of the state of the art WFSG

In the world of electrical machines, speed is proportional to power, so with some generalization and by considering a few assumptions, then one can safely argue that higher speeds practically mean higher power densities. The highest speed WFSG that could be found in available literature was in [41], which reports a generator tested up to 28 *krpm* without failure in 1981. This machine was reported to achieve a power density at this speed of 2.47 kW/kg.

Although this is the best figure found in the literature, advancements in design tools, new materials and new manufacturing techniques, much better performances and higher speed WFSGs can be achieved. Even so, no evidence exists so far that any implemented WFSG has achieved a dramatic increase in power density that makes the WFSG able to compete against a PM machine.

It is, however, very important to mention one of the most exciting WFSG ever unveiled. In 2013, Honeywell demonstrated its dual three phase aerospace WFSG prototype that is claimed to be basically ‘playing in the same league’ as the most advanced PM and SR generators with an overall power density of 7.9 kW/kg [2]. Could this be the real major breakthrough for WFSGs?

2.2.3 Conclusive remark

The unveiling of Honeywell’s revolutionary WFSG closed the gap in terms of high power density between PM and WFSG generators, stepping up competition among WFSG, PM and SR platforms, especially for future MEA applications. Apart from power density, WFSGs still possess numerous advantages compared with PM and SR generators, such as easy control of the field, no need for active PEs. Compared

with PM and SR generators, advantages for WFSGs mentioned above contributes to less components count, no permanent excitation field, thus more reliable system favoured by the aviation industry. Therefore, these will be considered in light of the system level design for WFSGs.

2.3 Future Power Distribution Systems on Aircraft and Future Implemented Power Generation Methods

Although weight minimization is always the main objective for the aviation industry, other factors such as safety, reliability and availability are also essential. Thus, apart from the generator itself, the selectin of the power generation method on board is also driven by the system architecture and its associated efficiency and reliability. This chapter will discuss different power generation architectures on board and associated aspects, such as efficiency and reliability challenges [42]. The likely future power generation methods will also be mentioned in this chapter.

2.3.1 Constant speed power generation

Constant speed power generation systems include a CSD between a turbine or a turboprop engine [10] and a generator for conventional aircraft as shown in Fig. 3.

Modern aircraft adopts AC systems operating at 115V and 400 Hz.

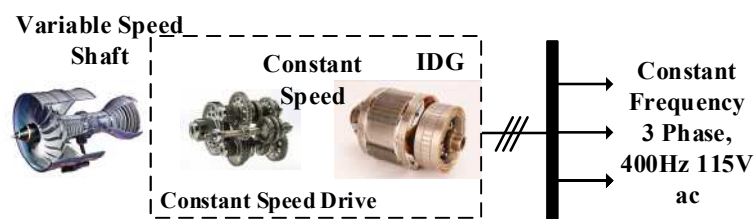


Fig. 3 Constant speed constant frequency systems.

The primary AC power systems on board are three phase configurations with a neutral terminal available [43]. The four-wire layout allows single phase line-to-

neutral, single phase line-to-line or three-phase loads to be connected to the power distribution system. This flexibility creates its own downside for having unbalanced load even though aircraft loads are designed to be balanced. The unbalanced loaded conditions result from duty cycles and schedule of different loads.

2.3.2 Variable speed power generation

Variable speed power generation systems are implemented on Boeing 787 and Airbus A380. These eliminate the need of a CSD due to mechanical wear out [41] coupled between a turbine and a generator as shown in Fig. 4.

Variable speed power generation can be achieved adopting one of the four options as shown in Fig. 4. The first variable speed constant frequency (VSCF) option comprises cycloconverters directly coupled to the outputs terminals of the generator [44]. The F-18 is an example adopting this system [45] which requires that all the electric power is processed by a PE converter (PEC) connected to the main bus bar. Another VSCF option is the DC link method [46] implemented on the Boeing 777 as backup generator [8], which has a diode bridge rectifier, DC link capacitors and an inverter. Both these methods produce constant voltage and constant frequency output. The third VS VF system includes bus bars directly connected to the terminals of the generator, which is widely adopted by the latest power distribution architectures implemented onto Airbus A380 and Boeing 787 [10]. The last method is high voltage DC distribution system, which is a concept raised more than 60 years ago [47] but studied and investigated recently [48] [49]. However, apart from F-22 and F-35, no known civilian aircraft implements such a type of system [6] [50].

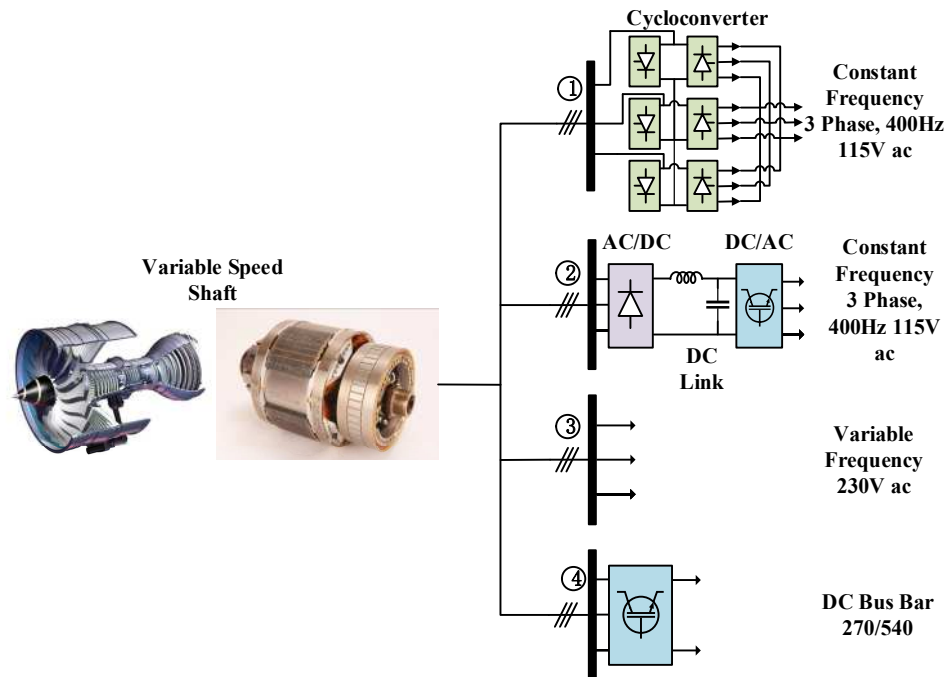


Fig. 4 Variable speed power generation systems.

2.3.3 Advantages of variable speed systems

Boeing 787 is considered today as the most advanced commercial MEA that exists from a technological point of view implementing VSVF systems. It replaces the consumption of pneumatic power with electric power (no-bleed systems) [51]. This increases the on board load dramatically up to $1MW$ and requires a generator with higher capacity (i.e. 250 kVA) [23] compared with generators (i.e. 150 kVA) [52] installed on A380.

The system architecture for Boeing 787 has offered significant amount of improvements such as a 50% reduction of mechanical system complexities compared to the Boeing 767 (constant speed power systems) [3], since no bleed systems are implemented. At the same time, mean time between failures (MTBF), defined in (1), has a 300% percent increment for Boeing 787 compared to Boeing

767. This changes the aircraft availability, which makes the Boeing 787 highly preferable for revenue services.

$$MTBF = \frac{\sum(\text{start of downtime} - \text{start of uptime})}{\text{Number of failures}} \quad (1)$$

The advantages gained by implementing MEA (variable speed power systems) proven by Boeing 787 indicate that future aircraft adopting MEA concepts are the way forward [53]. Typical examples of this future trend of MEA [54] are Boeing 737 next generation auxiliary power unit (APU) [3] and the Airbus A350 which adopt VSVF systems as their power generation methods. Although four different types of power generation and distribution systems do exist, VSVF and DC systems are considered the most promising options for future MEA.

2.3.4 Efficiency of the Overall System

Table 1 Efficiency comparison for various generator found in the literature

Source	Topologies	Power system	Rating(kVA)	Effi.	Ref.
F-18	WFSG	VSCF	40	78%-80%	[45]
V22	WFSG	CSCF&VSVF	40-50	74% 80%	[55]
Honeywell	WFSG	600VDC	1000	97%	[2]
GE	SR	270VDC	250	90.8%-93.1%	[56]
UoN	PM	270VDC	45	65%	[30]

The overall efficiency is one of the critical factors to evaluate the performance of an electrical system. Table 1 compares various generator technologies under different power system architecture. Typically, WFSGs demonstrate the lowest efficiency among all types of generators. In general, it is clear that PM generators have the highest efficiency compared with WFSG and SR generators. The efficiency of SR generators is better than WFSGs but lower than PM generators, in general. However,

it is very important to note that the lately introduced Honeywell mega-watt class WFSG [2] features an almost comparable system efficiency of around 97%.

2.3.5 Reliability concerns

Future MEA aircraft will most likely adopt VSVF or DC power distribution systems as the primary buses. This requires all three types of generators, considered in this paper, to install a fully or over rated PECs to condition the output power. The fully rated power conditioning device not only contributes to the overall weight of the power generation systems, but also raises issues related to reliability, such as component count, which is a major concern for aviation industry [57].

1) PECs implemented on the main bus power distribution:

PECs are subject to four failure factors: thermal shock, over voltage, mechanical forces and environmental effects [58]. Till now the failure mechanisms due to those four factors are still not comprehensively understood. Thus, this situation results in unpredictable lifetime of PECs implemented on the primary bus bars. Power loss on the main bus bars would be an unacceptable and catastrophic failure for aircraft.

In [59], an authoritative survey on reliability issues for PE systems designed for applications such as variable speed drives, electric vehicles, renewable energy systems and MEA is presented. This was conducted by the consultation of various leading researchers in the field of reliability for PE systems. The key aim of this survey was to investigate the industrial challenges on reliability issues for future application specific PE systems.

87% of the consulted industry experts believe that the current focus and quantity of research on reliability of PECs are insufficient. Semiconductor modules and capacitors are aspects of PECs subject to most failures [59]. Nearly 66% of the specialists agree that reliability of power modules and capacitors is imperative [59]. Due to the emerging demands for high reliable PECs from industry, an increasing research efforts is being conducted with the aim of further the understanding of physical failure mechanisms, online monitoring and lifetime prediction techniques [60]. However, more than half of the industry participants considered that current research efforts are not enough for aircraft industry [59].

2) Reliability issues for diode bridges:

WFSGs are already been implemented for VSVF power distribution systems (Boeing 787). As for DC power distribution systems, WFSGs can be equipped with a diode rectifier or PECs to provide constant DC voltage on the primary buses. It is reported that diodes have only 25% of the failure rate compared to active switches [58]. Therefore, three phase diode bridges are more likely to be implemented on the main bus for aircraft power systems compared with active rectifiers.

3) Fault conditions for PM generators

According to MIL-STD-704F, the loss of one of the phases should not cause hazards or damage to utilization equipment. In addition, a main challenge with PM machines directly connected to prime movers is the risk of an uncontrollable fault sequence which might result in damage to the PEC itself (the DC link capacitor) [39]. To address this issue, fault-tolerant PM machines developed by Honeywell [61] and very advanced fault detection and health monitoring techniques [62] are also

investigated with promising outcomes being achieved. However, these techniques do not actually clear the fault condition but are only able to control the fault when this is within a limited range. Therefore, turn to turn short circuit fault is a risk for PM generators not passing the aviation electrical power system standard. High speed PM generators are often equipped with sleeves made of carbon fibre or Inconel [63] which are prone to fail if not well designed.

4) Conclusive remarks:

At system level, PECs that make PM and SR generators competitive candidates in MEA power generator systems are also the bottleneck for PM and SR generators to be implemented soon on commercial flights at current stage. This is due to the fact that justifying the reliability of PECs might take a relative long time. In contrast, WFSGs are much more flexible in terms of adapting to VSVF or DC power systems without the assistance of PECs. Meanwhile, the efficiency of Honeywell's WFSG is dramatically increased.

The primary buses on commercial aircraft must have the highest reliability compared with another level of distribution buses. Therefore, it is impractical to implement PECs on the primary buses of commercial aircraft without a comprehensive understanding of the reliability and lifetime of PECs. Therefore, the implementation of PM and SR generators on DC primary distribution buses would have to wait until the reliability of PECs is justified. As for VSVF distribution systems, neither one of PM or SR generators are able to provide constant voltage variable frequency output without PECs.

In conclusion, PECs prevent PM and SR generators to be implemented as main bus generators on MEA at the moment. Meanwhile, WFSGs can be integrated into VSVF and DC systems by adopting nothing or diode rectifiers that is much more reliable than PECs. Therefore, WFSGs will have a higher chance to be implemented for future MEA before the reliability issue for PECs are justified compared with PM and SR generators.

2.4 Challenges for WFSGs Achieving State of the Art Performance

The power density of the highest performance WFSGs ever-recorded, namely the one demonstrated by Honeywell [2] is very competitive against that of PM and SR generators as individual components. Although very little information is available on how Honeywell's state of the art generator is achieved, however it is very clear that, to obtain that level of power density, then all the aspects of the WFSG must be pushed beyond the standard boundaries. This requires a full understanding of each individual component in a WFSG from electromagnetic, thermal and mechanical aspects. This chapter, therefore, recalls the basic structure and make-up of a WFSG including how all its components and sub-assemblies fit together. Finally, challenges arising from electromagnetic, thermal and mechanical aspects are identified.

2.4.1 Background for WFSGs

Fig. 5 depicts a schematic of the most common configuration for a WFSG (i.e., three machines on the same shaft) system for aviation industry. Its system comprises a WFSG, a main exciter, a permanent magnet generator (PMG) and an automatic voltage regulator (AVR) [64]. The AVR controls the WFSG output voltage by

feeding the exciter field winding. The exciter armature winding, in turn, is connected to a rotating diode rectifier whose output DC terminals are directly linked to the main alternator field winding. The PMG ensures a reliable power supply for the AVR.

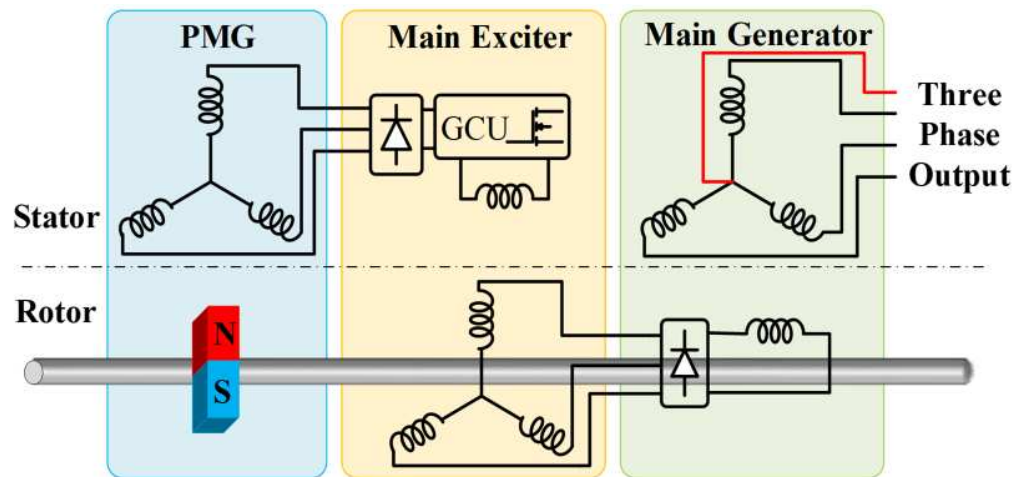


Fig. 5 Schematics of a 3-stage system comprising the PMG, the exciter, the diode rectifier and the WFSG.

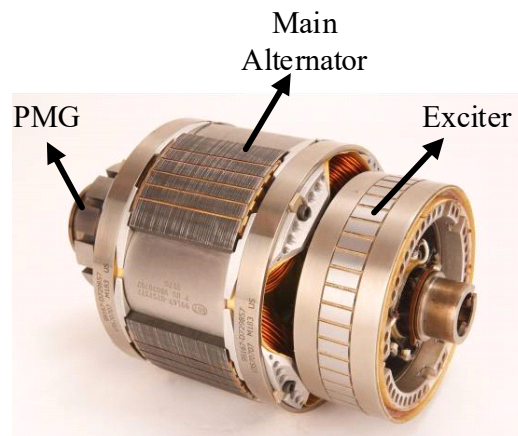


Fig. 6 Rotor structure of a typical WFSG.

Fig. 6 presents a typical rotor structure of WFSGs. Major challenges for WFSGs designed for aviation industry involve thermal [65] [66] and mechanical aspects. In addition, in the context of aerospace applications, where the power-to-weight ratio

is a critical factor, the traditional machine limits need to be improved and this is usually done by addressing materials [67], cooling capabilities [68] [69] and structural mechanical design and analysis [70].

2.4.2 Thermal challenges for WFSGs implemented for variable speed systems

Effective cooling methods can improve the weight reduction for WFSGs [71].

WFSGs has two major heat sources on the rotor which are difficult to implemented effective cooling systems: rotor field winding and the damper cage.

The field winding on the rotor is used to provide the excitation field for the main alternator. The loss from this winding is of course dissipated as heat. Considering the difficulty of heat extraction from a rotating body, this can become a limit on the actual size of the rotor.

The electrical frequency for WFSGs implemented for variable speed systems is typically 360 - 800Hz. This results in higher order harmonics in the air gap, thus, induced high frequency currents in the damper cage are observable. In Fig. 6, damper cages are embedded into the inter-pole gaps and into the rotor slots. In addition, the high electric frequency of the magnetic field also results in high losses and temperature increase in the magnetic core and stator windings [72].

In general, forced air and oil cooling are commonly seen on aircraft cooling systems. Oil cooled generators are preferable in CSCF system since oil circuits are already available within the mechanical gearbox or IDGs. However, with variable frequency generators, no existing oil cooling units are available. This leads to the need of extra cooling circuits, pumps and gauges directly mounted onto the WFSG, which

contributes to weight and complexity increase of the overall system. In [41], it is reported that the cooling oil might not even be available to a generator at certain flight mission cycle if shared lubrication oil is implemented as a system cooling agent. Therefore, an important potential challenge for the design of variable frequency systems is the trade-off needed to maximize power density and minimize system complexity and weight, both for generators and periphery accessories.

2.4.3 Mechanical challenges for WFSGs implemented for variable

In Fig. 2, the typical operating speed for WFSGs are 10 krpm to 25 krpm. High speeds with large power demands imply high peripheral speeds at the rotor surfaces, which can easily cause mechanical fatigue or damage.

Apart from speed and volume, an inherent mechanical challenge is that WFSGs have a field winding on its salient-pole as shown in Fig. 6. Pole tips are typically used as mechanical structures to withstand centrifuge forces caused by field windings. Therefore, very high mechanical stress levels can be registered at the rotor bore and pole tips [73].

Another challenging aspect of WFSGs relates to the damper cage that is located on the surface of rotor poles, as depicted in Fig. 6. Hollow structures on the surface of rotor poles designed to accommodate the damper cage potentially weaken the structure of rotor pole at high-speed operation. The thermal expansion of the damping bars may worsen the case to a certain degree.

In addition, due to the mechanical vibrations and centrifuge forces, field windings need to be retained by extra mechanical structures such as retaining rings for end

windings [1] [74] as indicated in Fig. 6. Equation (2) can be used to roughly estimate the highest stress (τ_{mech}) found on a rotor core. C' is the Poisson's ratio relate parameter, ρ is the mass density of the core materials, r is the radius of the machine and Ω is the angular speed.

$$\tau_{\text{mech}} = C' \rho r^2 \Omega^2 \quad (2)$$

2.4.4 Other challenges associated with variable speed systems for WFSGs

Another important challenge of variable frequency generators is whether starting capability of turbine is required, such as for Boeing 787, where electric starting capabilities for WFSGs are necessary for a successful implementation of the Boeing 787's 'no-bleed' system. This requires field windings to be fed by a standstill main exciter. The key challenge for this auxiliary machine during system start-up is to supply the field winding with adequate DC currents [75] without oversizing. Therefore, the key objective function here is the maximization of kVA input to kW output ratio.

2.4.5 Summarizing remarks

In chapter 2.4, the challenges associated with WFSGs at machine and at system-level have been highlighted. The key challenges of such a system can be summarized as follows.

1. Mechanical aspects:
 - a) Stress concentration at the corner of rotor bore and of rotor pole shoe.
 - b) Stress concentration on the rotor iron bridges between damper bars and main air gap.

- c) Structures required preventing end winding from falling apart.
 - d) Structural failures associated with rotating diodes.
 - e) Rotor dynamic issues and vibrations.
2. Thermal aspects:
- a) Effective stator and, most critically, rotor coil cooling methods.
 - b) Iron losses both in stator and rotor cores.
 - c) AC losses resulting from stator coils.
 - d) Selection of cooling type.
3. Power quality aspects:
- a) Stringent requirements for AC power systems [76] [77].
 - b) Ripple [78] requirements for DC power system.
4. Extra functionalities:
- a) Exciter design and criticalities at start-up.
 - b) kVA input to kW output ratio during starting.

The main important point to consider here is that for real breakthrough in terms of WFSG performance, these challenges cannot be considered individually. A step change in terms of performance would require interlinked multi-disciplinary approaches. Novel modelling a design techniques that can help addressing these challenges are required.

2.5 Opportunities for WFSGs to Achieve State of the Art Performance

In chapter 2.4, the challenges for designing WFSGs are identified. This chapter will discuss what has been ‘tried’ to achieve optimal performance by addressing the challenges raised above.

2.5.1 Thermal aspects – structure associated with WFSGs

In a VSVF system, WFSGs equipped with damper cages [72, 79, 80] are required due to following reasons [81] [82].

- 1) Suppressing hunting oscillation.
- 2) Damping oscillations resulting from short circuits or switching.
- 3) Preventing voltage distortions caused by unbalanced loads.
- 4) Balancing the terminal voltage due to unbalanced loads.

A recent study [82] reveals that damper cage design has an influence on mutually affective parameters, namely losses and power quality. For AC generation and distribution systems, conventional techniques at the machine level for reducing the THD include the following three aspects [83] [84]:

- 1) Pole shaping.
- 2) Short pitching.
- 3) Skewing of stator cores.

The THD of any generic function $a(t)$ is defined as in (3), where A_n is the rms value of the n th harmonic and A_1 is that of the fundamental component. The THD levels can be maintained within the requirements by adopting the conventional techniques listed above but usually at the cost of reducing the fundamental component [77]. To compensate for such side effects, the field current is boosted; however, rotor cooling can become ever more challenging

$$THD = \frac{\sqrt{\sum_{n=2}^{\infty} A_n^2}}{A_1} \quad (3)$$

An advanced technique named damper cage modulation has recently shown a great potential in improving the output waveforms' quality, while minimizing damper cage losses [82] and in enabling the removal of stator skew [79], while not compromising the fundamental components of the output quantities, thus no boosting of the field current is necessary.

Apart from VSVF systems, all the systems shown in Fig. 4 need PECs on board to condition the output power, which decouples the bus bar voltage from the generator outputs [45] [85]. Therefore, the unbalanced loads that are decoupled from the output terminals of WFSGs will potentially no longer be an issue and the need of damper cages will also be removed. Salient-pole WFSGs with no damper cages offer several advantages both mechanically and thermally.

In [86], the optimal losses distribution is as equally important as losses reduction from electromagnetic design perspective. With damper cages eliminated from WFSGs, one of the heat sources especially acting during any unbalanced operation is removed from the rotor. This leads to an improved thermal management of machine.

Advanced harmonics or losses reduction methods also exists using active devices such as active power filters [87], active rectifiers [88] for WFSGs. However, as mentioned earlier, the reliability for active devices are still a major concern for aviation industry. Therefore, those advanced techniques may not be implemented on aircraft that soon.

Aerospace oriented WFSGs often adopt oil-spray cooling at their effective cooling methods [89] [90]. However, to bring power density of WFSGs to a different level, thorough studies of spray cooling methods are required.

2.5.2 Mechanical aspects – materials

One of the key factors limiting rotating machines to achieve high peripheral speeds is the relatively low yield strength (460MPa) featured by the common ferromagnetic materials typically employed for the rotor core. The increased power demand for MEA requires WFSGs to be designed with larger rotor radii. This leads to the implementation of high-grade materials such as CoFe.

Commonly known developments in CoFe achieve high yield strengths in the range of 800MPa (Vacodur S Plus). Other recently developed materials like JNEX900, JNHF600 [67] and 2605SA1 [91] are all having relatively high yield strength. The lately introduced material 35HXT780T can achieve a maximum yield strength of 860MPa [92]. Far more advancements in materials' technologies are expected in the future.

High strength material may address the challenges in salient-pole WFSGs related to local stress concentration raised in chapter 2.4. Apart from the local stress concentration, end windings deformations due to centrifugal forces must also be considered. WFSGs implemented on board use retaining metallic rings to prevent rotor end windings from bending outwards touching the stator [74]. Carbon fibre or high strength sleeves can be used for retaining the field coils in WFSGs as shown in Fig. 6, as similarly done for the PMs for PMSMs [93] [94].

2.5.3 Thermal aspects – materials

Variable speed power generation concepts increase the maximum operating frequency for WFSGs up to 800 Hz. Therefore, high-speed power dense generators suffer from high surface losses due to high frequency harmonics. CoFe materials presents advantages of achieving high magnetic loading but an associated downside is that they feature high hysteresis and eddy current losses. In contrast, special SiFe steel has relatively low magnetic loading but significant lower losses. Studies elaborate that the power density of a PM starter generator adopting CoFe (high core losses material) and high silicon content steels (low core losses materials) remains the same at relatively high-speed level [95] [96]. Therefore, low losses materials are potential candidates for high power density and cost effective WFSGs for high-speed applications.

Ceramic material with high thermal conductive (230W/mK) are widely investigated by material scientists [97]. Ceramic materials also feature high dielectric strength allowing them to be considered as insulation materials in electric machines. Therefore, adopting ceramic materials can potentially reduce the thermal resistance from a heat source to ambient.

2.5.4 Extra functionalities

Emergent MEA concepts require WFSGs to start the turbine. This extra functionality introduces challenges in the design of the exciters of such generators. Various methods have been proposed for new topologies and can be summarized as follows: single phase, dual, three phase and two windings exciters [98-100]. Dual and three phase exciters have demonstrated significant improvements of kVA input

to kW output ratios. This increases the exciter power density, but at the cost of increasing the control complexity. Apart from developing topologies achieving high kVA input to kW output ratio exciter, advanced control algorithm are developed by Honeywell to achieve the same goal [101].

Investigations on how to improve the efficiency of a generation system by acting on the exciters of WFSGs have been described in [64] [102]. Capacitive couplings and rotating transformers are considered as alternatives replacing traditional exciters due to less speed dependent and efficient power transfer features [103]. A capacitive coupled SG via journal bearings has demonstrated weight, volume and efficiency improvements of 80%, 54% and 31%, respectively, compared with an existing exciter [104]. Therefore, capacitive power transfer has great potential to improve system weight and efficiency with the potential advancements in materials science in the future.

2.6 Conclusion

This chapter has tried to investigate why the aerospace industry still favours the classical WFSG as the main source of electrical power generation on board aircraft. Following a detailed review of existing materials, this paper has shown how the direct controllability of the field for a WFSG, its robustness and the inherent reliability bottleneck of more advanced machine (PM, SR) drive families have all contributed to this trend.

Following this, this article then focused on highlighting the main challenge faced by such WFSG systems, i.e. their inherent low, system-level power density. The traditionally low operating speeds associated with WFSGs need to be increased by

significant orders, even when considering the mechanical challenges associated with such rotating field systems. The current state of the art WFSG that exceeds all other systems is the generator developed and demonstrated by Honeywell that can achieve 7.9kW/kg at a rotor speed of 19,000 rpm. This demonstrator has shown that by overcoming the mechanical challenges associated with higher speeds, then a WFSG can achieve comparable power density levels to those coming from more advanced technologies such as PM and SR drives. Upon combining this improvement in power density with the traditional benefits of wound field systems (controllability, reliability and robustness), then it can be clearly perceived that the WFSG still has a lot to offer even in such harsh and demanding environments such as that of the aerospace industry.

Chapter 3

Design methodologies for conventional wound field synchronous generators

Previous chapter gives a relatively comprehensive literature review on high speed WFSGs and their competitors implemented or proposed for MEA applications. However, according to the challenges listed in chapter 2, designing a high speed WFSG requires multi-physics understanding of a WFSG, including electro-magnetism, thermal, mechanics and material science, etc. A multi-physics model able to analysis a high speed WFSG is difficult. Therefore, models are built and validated as an individual component and coupled together later to analyse complex physical behaviour of a high speed WFSG. This chapter focuses on introducing a coupled analytical and finite element (FE) electro-magnetic design methodologies for conventional WFSGs and validates its performance against experimental results.

3.1 General Theories for Wound Field Synchronous Generators

Chapter 2 briefly introduces the operational principles and physical layouts of a 3-stage WFSG. This section expands the background theories for WFSGs in more details. Both steady-state and transient behaviour of WFSGs are introduced in this chapter.

3.1.1 Steady state behaviour of WFSGs

Park transformation can be used to convert three phase quantities into d-q form. This transformation can be applied to establish the fundamental methods to analysis the steady state, transient and fault behaviour. This chapter concentrates on analysing steady state operation of WFSGs using d-q-n quantities. The connection between a three phase frame and d-q axis is denoted in Fig. 7. D-q axes rotates at speed of ω_e aligned with rotor pole axes. Phasor V_s is the amplitude of three phase terminal voltage. δ_{load} is the load angle a WFSG.

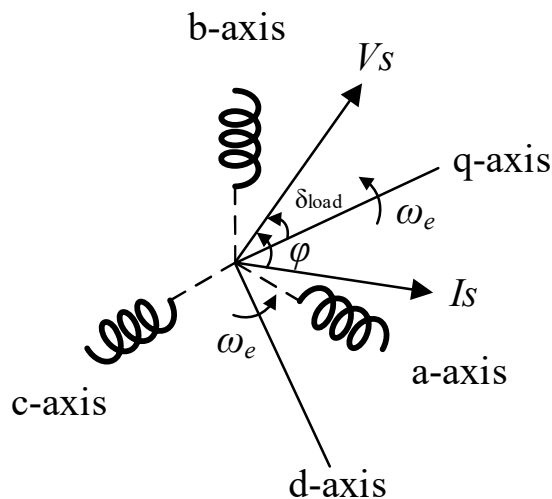


Fig. 7 alignment of rotating d-q axes and stationary a, b, c axes on the d-q plane and the voltage phasor V_s .

D-axis depicted in Fig. 7 is aligned with a rotor pole instantaneously to simplify the analysis of such d-q-n rotating reference frame. Therefore, d-axis rotates synchronously with a rotor pole at a speed of ω_e . Three phase quantities can be expressed as functions of times as equation (4) to (6).

$$V_a = V_s \cos(\omega_e t + \delta_{load}) \quad (4)$$

$$V_b = V_s \cos\left(\omega_e t + \delta_{load} - \frac{2\pi}{3}\right) \quad (5)$$

$$V_c = V_s \cos\left(\omega_e t + \delta_{load} + \frac{2\pi}{3}\right) \quad (6)$$

These three quantities can be projected onto the d-q-n rotating reference frame resulting in d-q-n quantities derived as equation (7).

$$\begin{bmatrix} V_{ds} \\ V_{qs} \\ V_{ns} \end{bmatrix} = \frac{2}{3} \begin{bmatrix} \sin(\omega_e t) & \sin(\omega_e t - \frac{2\pi}{3}) & \sin(\omega_e t + \frac{2\pi}{3}) \\ \cos(\omega_e t) & \cos(\omega_e t - \frac{2\pi}{3}) & \cos(\omega_e t + \frac{2\pi}{3}) \\ \frac{1}{\sqrt{2}} & \frac{1}{\sqrt{2}} & \frac{1}{\sqrt{2}} \end{bmatrix} V_s \quad (7)$$

Quantities on the n-axis are shown as equation (7). Based on the knowledge of trigonometry, the quantities on the n-axis presented in equation (7) equals to zero. In this case, rotational vectors plotted in a d-q plane are adequate to analysis a three phase network.

Fig. 8 plots the graphical interpretation of rotation phasors for WFSGs operating under over- and under-excited condition. With the assistance of this d-q plane, the connection between three phase currents and currents in d-q plane is expressed as equation (8) to (10).

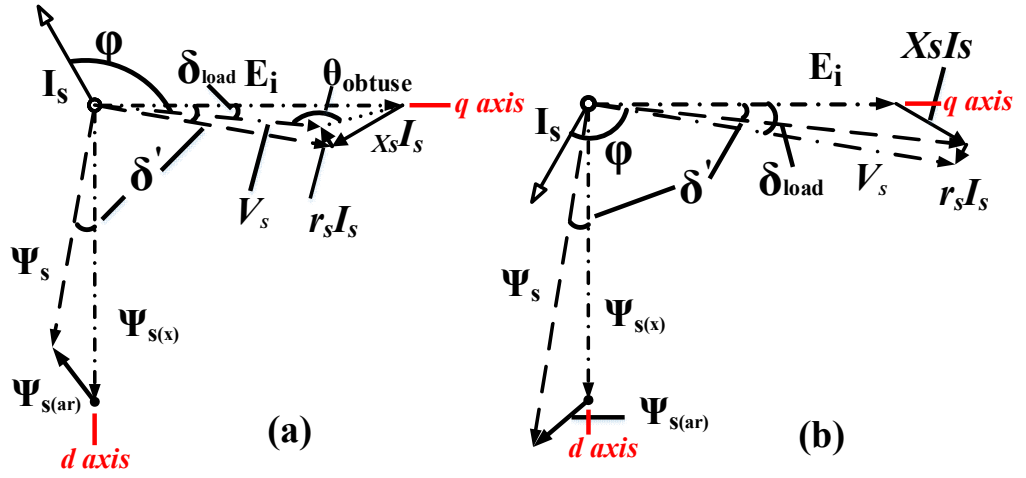


Fig. 8 Generator action (a) under-excited (b) over-excited

$$I_{as} = I_{ds} \sin(\omega_e t) + I_{qs} \cos(\omega_e t) \quad (8)$$

$$I_{bs} = I_{ds} \cos\left(\omega_e t - \frac{2\pi}{3}\right) + I_{qs} \sin\left(\omega_e t - \frac{2\pi}{3}\right) \quad (9)$$

$$I_{cs} = I_{ds} \cos\left(\omega_e t + \frac{2\pi}{3}\right) + I_{qs} \sin\left(\omega_e t + \frac{2\pi}{3}\right) \quad (10)$$

According to Fig. 8, the three phase currents can be derived as equation (11) to (13) linking stator current vector I_s shown in Fig. 8, hence linking with current in d-q frame.

$$I_{as} = I_s \cos(\omega_e t + \delta + \phi) \quad (11)$$

$$I_{bs} = I_s \cos\left(\omega_e t + \delta + \phi - \frac{2\pi}{3}\right) \quad (12)$$

$$I_{cs} = I_s \cos\left(\omega_e t + \delta + \phi + \frac{2\pi}{3}\right) \quad (13)$$

A power equation of a WFSG at steady state derived based on information in Fig. 8 is presented as equation (17).

$$P_e = V_s^2 \left(\frac{x_{ds} - x_{qs}}{2x_{ds}x_{qs}} \right) \sin 2\delta \quad (14)$$

Chapter 3.1.1 completes a general overview of methods used to analyse the performance of a WFSG under steady state. For any WFSG, transient state operations are also critical for a WFSG. Therefore, next chapter focuses on elaborating the operating principle of a WFSG at transient state.

3.1.2 Transient state behaviour of WFSGs

Transient state behaviour for a WFSG is also critical as it determines the stability of a given machine. However, analysis of the transient behaviour of WFSGs is intractable unless certain assumptions are made. One of the most important theory is the constant flux linkage theorem [105] while analysing the transient behaviour of a WFSG. For example, during a sudden short circuit fault at time instant t_2 and the instant right before the short circuit fault t_1 ($t_2 > t_1$), the total flux linkage remains to be a constant value at time instant t_1 and t_2 . With these assumptions been made, d-q transient currents can be presented as (15) and (16).

$$I_{ds}(t) \cong -\frac{E_i}{x_{ds}} - E_i \left(\frac{1}{x'_d} - \frac{1}{x_{ds}} \right) e^{-\frac{t}{T'_d}} - E_i \left(\frac{1}{x''_d} - \frac{1}{x'_d} \right) e^{-\frac{t}{T''_d}} + \frac{E_i}{x''_d} e^{-\frac{t}{T_a}} \cos(\omega_e t) \quad (15)$$

$$I_{qs} \cong -\frac{E_i}{x''_q} e^{-\frac{t}{T_a}} \sin(\omega_e t) \quad (16)$$

E_i is the no-load terminal voltage; x_{ds} is the steady state d-axis synchronous reactance; x'_d is the transient d-axis reactance; x''_d is the sub-transient reactance; T_a is the steady state time constants; T'_d is the transient time constants; T''_d is the sub-transient time constants; x''_q is the q-axis sub-transient reactance. By substituting (15) and (16) into (8) to (10), the resultant three phase currents can be plotted as shown in Fig. 9. During the sub-transient state (first 10 to 20 cycles in Fig. 9), flux created

by armature short circuit current and leakage flux penetrates through air gap linking field coils and damper circuits. The induced current in damper cages damps the short circuit current. While damper currents and rotor surface current decay to small steady value, leakage flux and armature flux passing field coils becomes dominate. Short circuit currents are damped by field generator by field coils, leakage flux and armature flux until steady state is reached. Terminal short circuit behaviour introduced above are the most important factor for determining the stability of a WFSG. Other short circuit transients such as phase to earth, phase to phase short is not covered in this chapter.

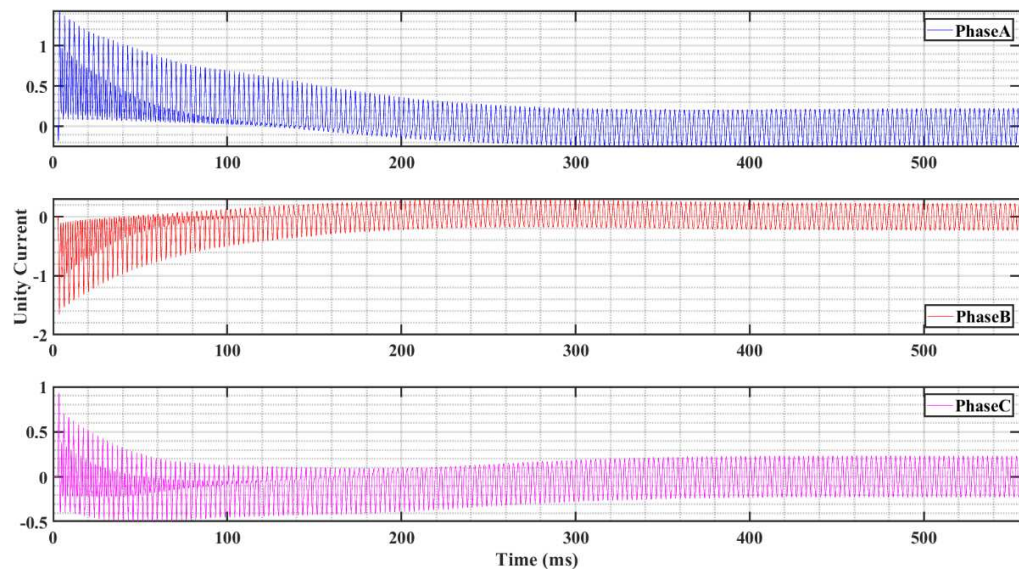


Fig. 9 A typical three phase short circuit currents for a WFSG involves sub-transient, transient and steady state

3.2 An Analytical Model for Wound Field Synchronous Generators

For conventional grid connected WFSGs (50 Hz – 60 Hz) ranging from a few hundred kilo-watts have less constraints in terms of thermal, mechanical and weight issues. As for those applications, budget for WFSGs is critical. Therefore, industry

grade materials are adopted such as M700-65A and 150 °C grade insulated copper windings.

3.2.1 Analytical sizing equations and the logic flow of an analytical sizing script

Standard analytical sizing equations introduced in [106] are adopted to size the stator core. However, sizing equations for determining dimensions of rotor structures require certain amount of modifications. In Fig. 10 b), the flux seldom traveling through the inter-pole region shown in Fig. 10 a). Thus, the equation proposed in [106] calculating teeth width is adjusted as in (17) and (18) to solve the rotor body width. By combining (17) and (18), rotor width b_p can be easily solved.

$$\hat{B}_d = \hat{B}'_d - \left(\frac{l' \tau_p \tau_{pspan}}{k_{Fe} l b_p} - 1 \right) \mu_0 \hat{H}_d \quad (17)$$

$$\hat{B}'_d = \frac{l' \tau_p \tau_{pspan}}{k_{Fe} l b_p} \hat{B}_\delta \quad (18)$$

$$\hat{U}_{m,\delta} = \frac{\hat{B}_\delta k_{Cs} \delta}{\mu_0} \quad (19)$$

Due to the presence of slot openings, the flux density crossing the air-gap drops by a small amount shown in Fig. 10 b). Therefore, the length of the air-gap seen by the current linkage produced by the rotor field windings is longer than its physical length δ . Thus, the Carter factor k_{Cs} is used to estimate the effective air-gap length [106] accounting slot opening effects for both stator and rotor. However, for WFSGs in Fig. 10 a) inter-pole area for rotor is not the path for the main flux travelling through. Therefore, overall Carter factor does not need to take rotor slot opening space into account.

An analytical sizing script for a main alternator is programmed following the logic as shown in flow chart Fig. 11 based on the knowledge of sizing equations presented in chapter 3.2.1. The initial state of variables defined in Fig. 11 such as magnetic loading and electric loading are selected based on the BH property of magnetic steel and empirical experience data presented in [106] respectively. The saturation point for SiFe steel used for an existing WFSG is close to 1.6T. Therefore, the peak flux density in the air gap is selected to be in a range of 0.8-0.9T. Flux traveling through one pole pitch is calculated based on an assumption that the initial state of flux density presented in the air gap is purely sinusoidal and the peak value is within the range of 0.8-0.9T.

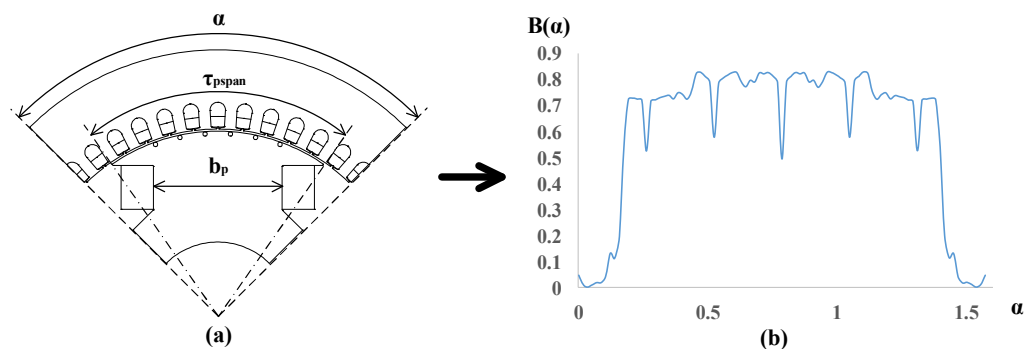


Fig. 10 a) A quarter machine model b) flux density distribution in the air-gap for a single pole only

In Fig. 11, the ratio between the axial length of the machine and the diameter of the rotor core is defined as length to diameter ratio. The program following the logic presented in Fig. 11 is programmed to locate a ratio when the peak air gap flux density falls into the range of 0.8-0.9T. To maximize the utility of the soft-magnetic material, the flux density on the iron core such as rotor yoke, stator teeth and stator

back iron shown in Fig. 10 a) is chosen to be at the knee point on a BH curve of the material used. For SiFe steel, this value is selected from a range of 1.4-1.8T.

With the knowledge of above information as design inputs, the rest dimensions such as stator slot depth, thickness of stator back iron and the width of the stator teeth presented in Fig. 10 a) are calculated using equations proposed in [106] [107]. The next step is to obtain the magneto-motive force (MMF) to establish the required magnetic field for no-load operation with key machine dimensions calculated.

A complete magnetic circuit in a WFSG has different level of saturation at different position. Consequently, taking the saturation effects of SiFe steel into design consideration is inevitable during no-load operation. In order to calculate the overall MMF, a line integral alongside the magnetic circuit is performed. However, in a simplified analytical model the geometrical information is not as detailed as that in FE software. The sum of the MMF over several segments of magnetic path assuming the magnetic field strength is a constant is more feasible to achieve.

In this case, an entire magnetic circuit travelling through neighbouring poles is divided into rotor core, air gap, stator teeth and stator back iron where dimensional information is a known factor. Following equations presented in [106], the total MMF required to establish the magnetic field for no-load operation can be determined. The number of turns for the field winding can be easily settled by determine the wire gauge.

Till this stage, an entire process for determining key machine parameters is completed. However, at this stage, the analytical process does not reflect the actual

machine performance. The initial state of flux density in the air gap for first round calculation of this analytical script is assumed to be sinusoidal. The actual existing waveform for the flux density in the air gap for a WFSG is close to the one presented in Fig. 10 b). The presence of harmonic contents in the waveform of air gap flux density is due to the saturation of the core materials and the space harmonics caused by stator teeth. The more MMF been applied to the magnetic circuit, the more saturation and hence the more harmonic contents presented in the flux density waveform in the air gap is. Therefore, a flattened sinusoidal or a trapezoidal waveform presented in Fig. 10 b) is much closer to the actual air gap flux density waveform in a machine. In order to obtain a more accurate analytical modelling tool for a WFSG, saturation factor presented in (20) and (21) is introduced to quantify this phenomenon [106].

$$\alpha_i = \frac{1.24k_{sat} + 1}{1.42k_{sat} + 1.57} \quad (20)$$

$$k_{sat} = \frac{\hat{U}_{m,ds} + \hat{U}_{m,dr}}{\hat{U}_{m,\delta}} \quad (21)$$

A coefficient α_i in (20) is used to alter the magnetic loading according to the saturation level been calculated using (21) where $\hat{U}_{m,ds}$ is the MMF consumed by the stator teeth; $\hat{U}_{m,dr}$ is the MMF applied to the rotor pole body; $\hat{U}_{m,\delta}$ is the MMF consumed by the air gap. In Fig. 11, iterations of the machine sizing process explained is automatically started until the convergence of saturation factor is met.

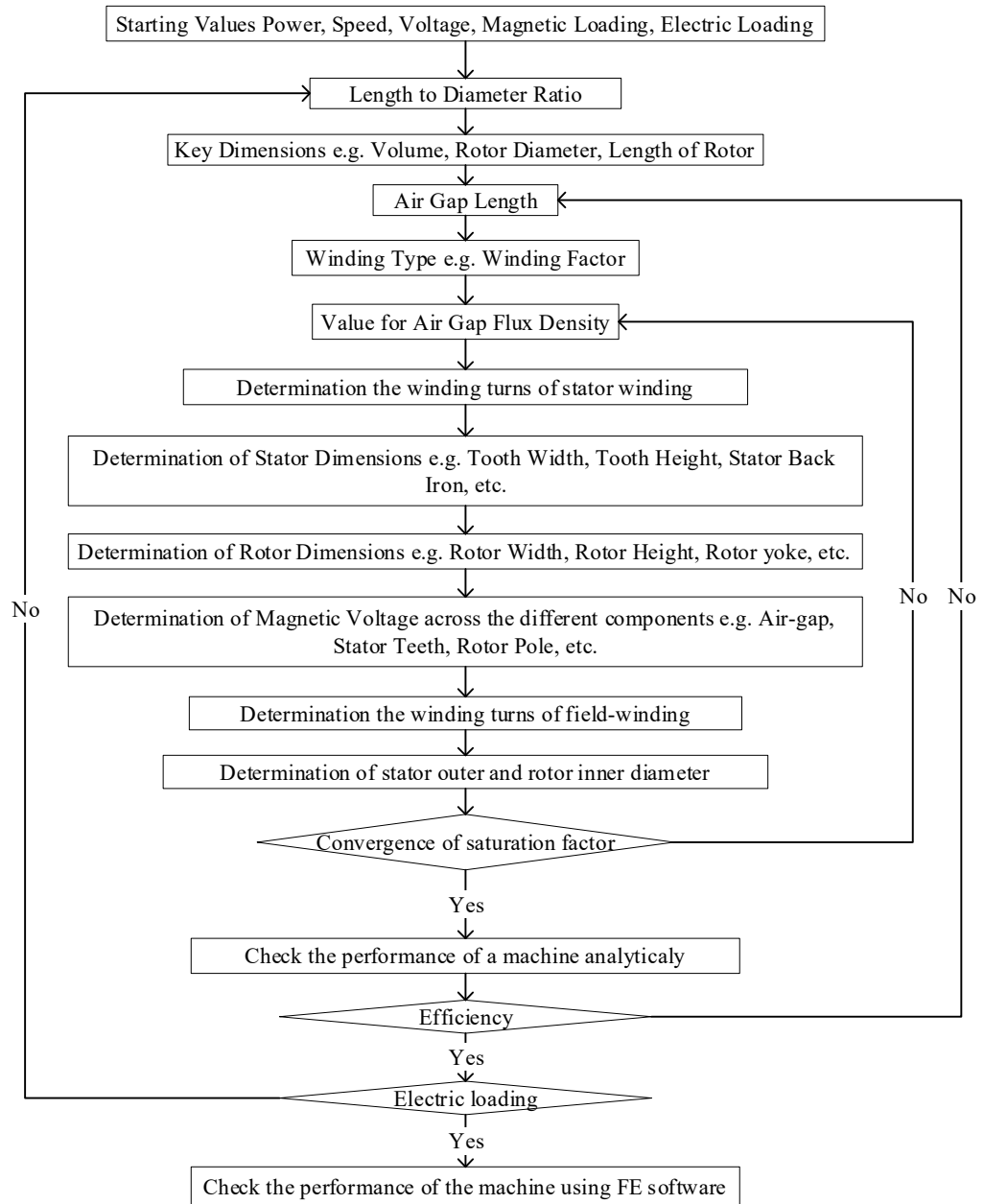


Fig. 11 Flow charts for sizing the main alternator of a WFSG

During the iteration, design requirements such as electric loading, peak air gap flux density are carefully monitored in order to ensure that the design requirements are met. However, not all the design inputs such as flux density at different parts of the machine and electric loading are reasonable design choices. The final output values of those variables (flux density, electric loading etc.) slightly differs from the initial

design choices at the end of the iteration of machine sizing process. The difference is regulated in a predefined range according to the accuracy required. There are also conditions where the final output values of those variables (air gap flux density, electric loading etc.) exceed constraints been applied to the sizing program. In this case, the initial design choices for those variables (flux density, electric loading, etc.) must be re-evaluated. New design choices are applied to the same analytical sizing script until the value for all the variables (flux density, electric loading, etc.) falls within the required range.

After machine dimensions are determined, machine performance is re-determined by resultant generator dimensions. These machine performances such as power, efficiency and electric loading etc. are compared against design requirements. If these criteria are not met, iterations of the same process following Fig. 11 are ran altering dimension sensitive parameters such as air gap length, air gap flux density and axial length to rotor diameter ratio until machine design objectives are met.

3.2.2 Sizing validation of a WFSG sizing script

Chapter 3.2.1 demonstrates a process of an analytical sizing script for designing a WFSG from scratch. The dimension of an existing WFSG is used to validate the analytical sizing script been programmed. An off-the-shelf WFSG is rated at 400 kVA, 50 Hz, 400 V. M700-65A has material properties that is similar to an off-the-shelf WFSG. The analytical sizing script takes those machine performance parameters as design requirements and the properties of M700-65A to determine the size and performance of a WFSG. Table 2 presents the flux density for the Cummins generator designed in this chapter. The leakage flux coefficients can be obtained

from [106]. Table 3 compares the key dimensions of an existing WFSG such as diameter of a stator core and rotor core, slot depth, width of stator teeth and rotor body with the outputs of the analytical sizing script. The comparison results shown in Table 3 demonstrate a very good match in terms of those essential dimensions. The deviation for majority of the key sizing dimensions in Table 3 is less than 3%. For some less important dimensions such as rotor inner diameter, the difference is a little bit bigger. The maximum difference in Table 3 exists for the number of turns for field windings, which is around 10%. In conclusion, the analytical sizing script is accurate enough to compute the size and the magnetic-motive-force (MMF) also known as current linkage.

Table 2 Flux density required for the Cummins generator

	Stator Back Iron	Stator Teeth	Rotor Body	Rotor Bore
Flux Density (T)	1.7	1.8	1.6	1.5

Table 3 Comparison of an existing machine dimension and the analytical sizing script

	Existing machine	Analytical sizing	Error
Stator Outer Diameter (mm)	500	496.8	0.64%
Stator Inner Diameter (mm)	349	345.7	0.95%
Rotor Outer Diameter (mm)	345	341.7	0.96%
Rotor Inner Diameter (mm)	115	109.8	4.52%
Depth of stator slots (mm)	26.52	26.8	1.06%
Width of the stator tooth (mm)	10.2	10.7	4.90%
Height of rotor pole (mm)	83.9	88.3	5.24%
Rotor pole width (mm)	118	119	0.85%
Height of stator back iron (mm)	48.98	48.8	0.37%
Height of rotor yoke (mm)	42.5	43.6	2.59%
Number of turns for stator coils	2	2	0.00%
Number of turns for rotor coils	125	138	10.40%

3.2.3 Performance validation of a WFSG sizing script

The performance of a main alternator sized using analytical script is compared with existing measurement results of an existing WFSG listed in Table 4. The maximum difference between key machine performance such as output power, terminal voltage and efficiency are all less than 5%. In conclusion, it is clear that the analytical sizing model designed for WFSGs achieve relative accurate sizing results for a low speed WFSG.

Table 4 An analytical main alternator performance vs. an existing alternator performance

	Existing machine	Analytical output	Error
Output power (kVA)	400	412.5	3.13%
Terminal voltage (V)	400	398.4	0.40%
Efficiency	95.03%	96.50%	1.55%

However, this analytical sizing script is designed at no-load operation point based on simplified machine geometry and a single operating point. Under this circumstance, space and time harmonics for a main alternator cannot be easily evaluated by analytical equations. Therefore, FE analysis methods are used to perform detailed electromagnetic analysis on the machine behaviours in much more accurate ways.

3.3 FE Models for Wound Field Synchronous Generators

Section 3.2.1 demonstrates the process of how an analytical script designs a main wound field alternator from scratch. The accuracy of this initial analytical sizing script is also validated. This section focuses on establishing a FE model using dimensions calculated by the analytical sizing script in section 3.2.1. The FE model

for WFSGs is built using embedded scripting commands provided by the FE software.

To be able to couple FE scripts with existing analytical scripts, objected oriented design (OOD) concepts is chosen to program FE scripts for FE WFSG models, which can be further expanded with thermal and mechanical design module. Better encapsulations, data protection and code recyclability features offered by OOD concepts allow analytical sizing scripts and FE scripts to be individually optimized, upgraded and coupled together without unpredictable alteration and usage of data by different call for functions.

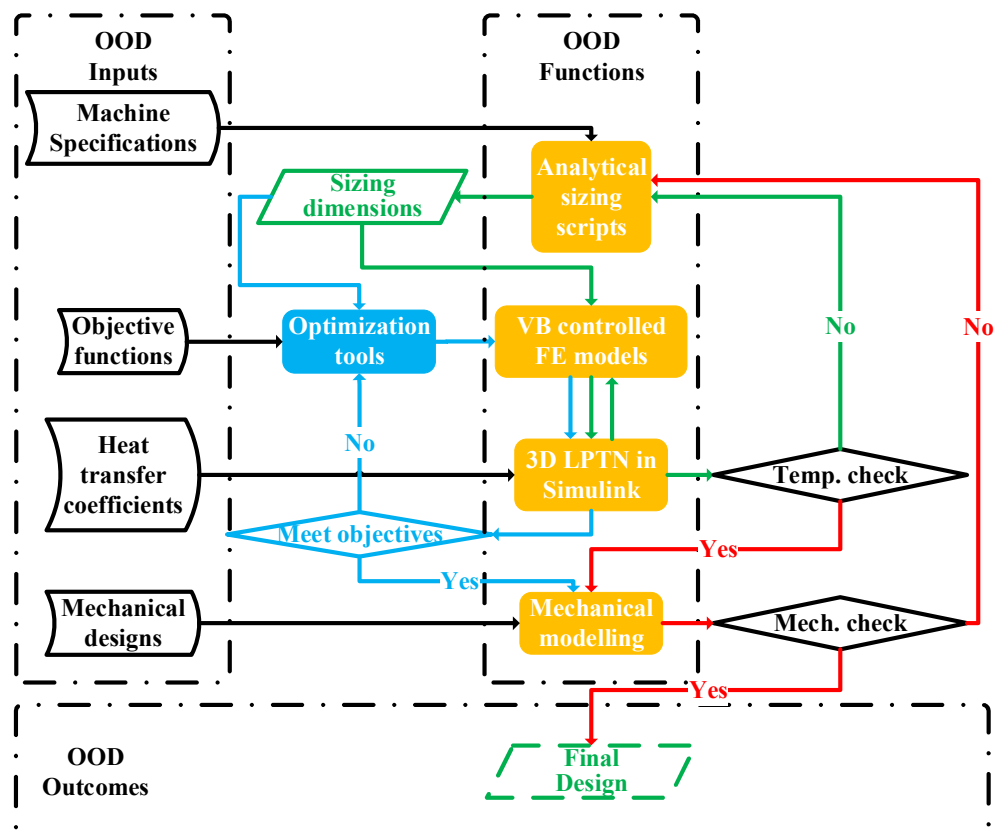


Fig. 12 Coupled WFSG OOD architectures

Fig. 12 indicates the OOD architectures for design tools customized for WFSGs with features discussed above. This design tool includes protected input parameters (a private structure array) such as machine performance requirements for analytical sizing scripts, objective functions for FE scripts, heat transfer coefficients (HTC) for lumped parameter models and mechanical constraints for mechanical models. Arrow paths in Fig. 12 are defined data bus containing read only data structure to be assigned to a next OOD function. Commencing from machine performance requirements in Fig. 12 following the green path a number of preliminary WFSG designs can be proposed. With certain knowledge of how different WFSGs behaves under the same design constraint, optimization procedures are initiated to locate an ideal design point constrained by thermal and mechanical performance. Most importantly, the architecture in Fig. 12 can also be further developed by coupling OOD modules relating to WFSG performance characterization such as bearing life calculation, vibration and noise analysis, etc. Individual modules in Fig. 12 can also be upgraded if faster or more accurate methods for analytical sizing, FE model setups, thermal models and mechanical models are proposed as long as input and output data ports for each module is able to read and write to a predefined data structure.

3.3.1 FE model construction for WFSGs

As OOD concepts are adopted, FE scripts for constructing FE model (Infolytica MagNet) take a structure output containing pre-defined machine dimensions from an analytical sizing script as a structure input. This input is assigned to structure variables in FE scripts. Under this circumstance, structure variables in FE scripts

prevents original structure input dimensions from analytical sizing scripts been unpredictably changed by functions in FE scripts. The rest of dimensions required to build a FE WFSG model are calculated based on the input dimensions.

Fig. 13 a) illustrates full 2D FE models built and simulated using the FE scripts based on dimensions and pole-slot combinations from analytical sizing input. The accuracy of 2D FE electromagnetic model is enough unless complex electromagnetic behaviour are critical [108]. Due to the limitation of computing resources, boundary conditions are applied to 2D FE model to reduce the time consumptions [108] as shown in Fig. 13 b). In addition, the behaviour of damper cage should be carefully considered as damper cages are shorted in different kinds of methods [81]. In a reduce FE WFSG model, with all damper cages shorted with a single ring an extra short circuit path is necessary to be provided allowing damper currents channelled through neighbouring poles [108].

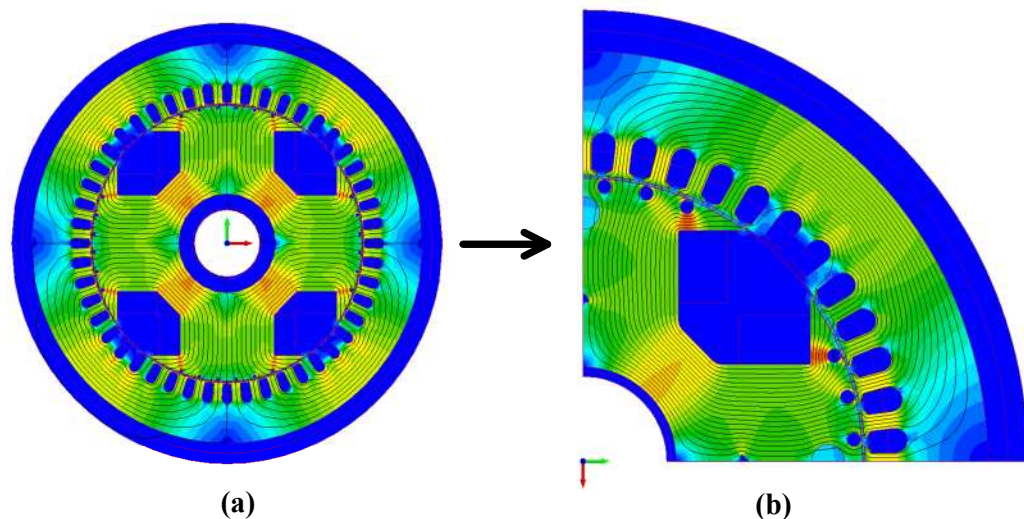


Fig. 13 a) field map for a full WFSG FE model b) field map for a quarter WFSG FE model

After the initial design dimensions are determined by analytical scripts, optimization of input dimensions to FE scripts can be carried out by decoupling the connection between analytical and FE scripts. The objective functions of machine performance can be defined within the optimization tools been chosen, which is coupled to the FE scripts as the blue paths shown in Fig. 12.

3.3.2 Experimental Validation for electromagnetic FE models

In the section 3.3.1, an electromagnetic FE script is programmed to setup a WFSG FE model in a software based on pre-defined structure data array containing critical machine dimensions. This section mainly focuses on validating the accuracy and the validity of FE scripts. Meanwhile, the validity of a coupled analytical sizing – FE model design process is also checked in this chapter. The comparison is planned as follows. First, FE analysis based on actual generator size is compared with experimental measurements. Second, FE analysis of a coupled analytical sizing – FE model design process is also compared with the experimental measurements.

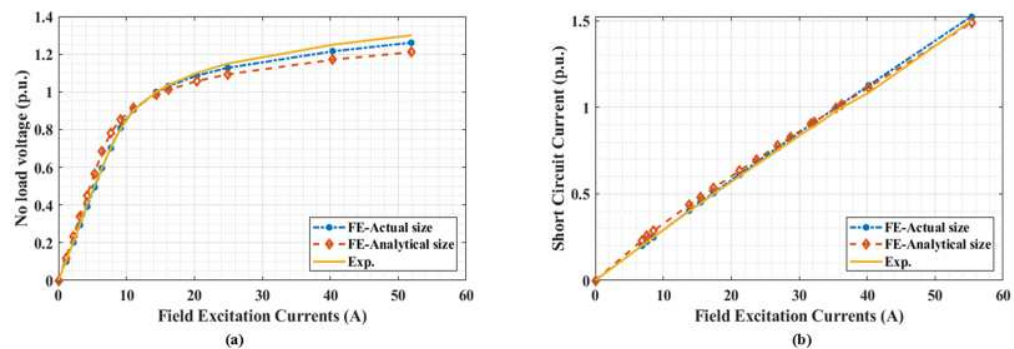


Fig. 14 Open circuit characteristics and short circuit characteristics for FE results of actual and analytical sizing model and experimental results

In Fig. 14(a), open circuit characteristics for electromagnetic FE models built by an actual WFSG size and analytically arithmetic size are compared with an existing

WFSG experimental results. Actual size based electromagnetic FE simulation results marked in blue dotted dash line matches experimental measurements marked in solid yellow line. In Fig. 14(b), short circuit characteristics are also compared for above mentioned two cases. A good match between FE actual size model and experimental results can be found. This indicates that the electromagnetic FE model is capable of analysing electromagnetic behaviour of a WFSG correctly. FE results for an analytically sized WFSG (design inputs comes from the tag on an existing generator) is compared with the experimental measurements. Fig. 14 demonstrated a fairly good match between analytical size base FE results (dash red diamond line) and experimental data (solid yellow line).

Apart from the comparison of those basic characteristics proposed in literature, losses characteristics obtained from FE simulation results are compared against the experimental measurements. A few issues have to be clarified before losses data can be compared with the experimental results. First issue is the copper wire modelled in MagNet is stranded coils. Under this circumstance, AC losses are not considered in the FE model. An existing WFSG is rated at 50Hz and the ac losses is insignificant compared with the dc losses but counts for a small fractional amount of totally losses practically. Second, the 2D electromagnetic FE model in chapter 3.3.1 does not take end windings into consideration. Thus, copper losses extracted from the FE model are multiplied by a factor that counts end winding length. Third, copper losses calculated in FE model is under 20°C. Thermal coefficients are used to correct the simulated losses in FE software at 20°C to that under steady state temperature for an existing WFSG.

Iron losses induced in the machine is always a troublesome issue. Both analytical and FE methods are proposed in literature [106] [108] to analyse hysteresis and eddy current losses. However, till now those proposed methods require several practical coefficients to correct them so that arithmetical losses are similar to experimental measure ones.

3.4 Thermal models for a WFSG

An electromagnetic sizing and FE analysis process presented in chapter 3.3 and 3.4 have demonstrated its accuracy in terms of electromagnetic performance such as torque, voltage and flux density, etc. Thermal behaviour are also an important factor in electrical machine design process. Computational fluid dynamics (CFD) is the most complicated but most accurate temperature analysing tool [109]. However, a complete CFD model requires a comprehensive understanding of fluid dynamics, thermal dynamics and knowledge on other discipline such as mathematics. Therefore, a LPTN is considered to analyse the temperature behaviour for this PhD thesis. Chapter 3.4 focuses on the process of establishing a LPTN module integrated into the OOD tool.

3.4.1 A lumped parameter thermal network

In Fig. 11, electric loading is one of the design inputs related to thermal aspects of an electric machine sizing process. Current density selected for determine the slot area or copper area is also a parameter that affects the temperature behaviour of an electric machine. However, the above mentioned two parameters do not have an explicit indication in terms of hot spot temperature which is limited by the insulation grades of copper wires.

According to [106], the product of electric loading (A) and current density (J) has a more meaningful physical value, which is defined as AJ in this thesis. Based on the available cooling capacity, AJ can be used for fast determination whether this machine is feasible or not based on the experience in [106] for initial preliminary design. A LPTN accounting the geometry and the thermal properties of materials used for a WFSG is adopted to determine the maximum coil temperature. Electric loading and current density for coils are iterated based on the outcomes of the maximum coil temperature.

The setup of a LPTN requires the knowledge of the dimensions of a WFSG and appropriate discretization (the number of nodes) of the geometry. The more nodes a thermal network have, the more accuracy a thermal network is. However, more nodes result in a time consuming network setup and simulation process. Therefore, a thermal network being setup in this section tries to use minimum number of nodes to simulate the temperature behaviour of an existing WFSG in the lab with relatively good accuracy.

A LPTN is similar to an electric circuit, temperature, thermal resistance, thermal mass are analogized as voltage, electric resistance and electric capacitance respectively. Thermal resistance are defined according to the heat transfer methodologies within a given space, such as conduction, convection and radiation. Thermal resistance for each of this heat transfer methods are calculated as equations (22) to (24) [110].

$$R_{cond} = \frac{l_m}{A_{mcd} \times k} \quad (22)$$

$$R_{cov} = \frac{1}{A_{scv} \times h} \quad (23)$$

$$R_{rad} = \frac{1}{F_{\epsilon} \times F_G \times \sigma \times A_{sr}} \quad (24)$$

In (22), the R_{cond} is the thermal resistance for conduction; l_m is the length of the material (measured on a path parallel to the heat flow); k is the heat transfer coefficient of the material; A_{mcd} is the surface area perpendicular to the path of heat transfer.

In (23), R_{cov} is the thermal resistance for convection; A_{scv} is the contact area between fluids and solid body; h is the heat transfer coefficient.

In (24), R_{rad} is the thermal resistance for radiation; F_{ϵ} is the emissivity function; F_G is the geometric “view factor” function; σ is the Stefan-Boltzmann constant that is $5.669 \times 10^{-8} \text{ W/m}^2\text{K}^4$; A_{sr} is the area with radiation took place.

In addition, damper cages embedded inside the rotor body is a long cylindrical rod whose thermal resistance cannot be obtained by equation (22). The cylindrical shaped damper cages satisfy the condition that when the length to radius is sufficiently high, the temperature behaviour of such slim cylinder is a function of radius only according to [110] [69]. Therefore, equation (25) is used to determine the thermal resistance of a long cylinder.

$$R_{cyd} = \frac{r_{rod}^2}{4k} \quad (25)$$

For majority of the cases, conduction and convection counts for nearly all the heat been extracted from a machine. Therefore, a LPTN established for a given machine contains thermal path for conduction and convection is accurate enough except a

machine cooled by nature convection. The HTC for nature convection is within a range of 5-20 W/m^2K . This value is substantially smaller than HTC for forced air cooling (see Table 5) and water and oil cooling [90]. Therefore, heat taken away from a machine due to nature convection is comparable with radiation. A LPTN built for a natural cooled machine must include both natural convection and radiation for obtaining an accurate temperature results.

3.4.2 A lumped parameter thermal network for a WFSG

With a short introduction of the knowledge for a LPTN, a network designed to analyse the temperature of a WFSG is elaborated here. In Fig. 11, the thermal analysis of a WFSG is part of the OOD tool. In this case, the dimensions of a WFSG passed to a LPTN are defined in the same way as the FE electromagnetic model. Material properties such as thermal conductivity, heat transfer coefficients, mass of different materials and thermal coefficients etc. are defined as a structure array as well to protect data from unpredicted alteration during arithmetic process.

Fig. 15 a) and b) depicts a simple 2D LPTN for a stator slot and a rotor pole. Ideally, a complete 2D LPTN has to include all the geometrical information (all the slots and rotor poles) as shown in Fig. 13 a). Thus, a resultant LPTN for an existing WFSG is very bulky. This results in extensive efforts been spent on creating discrete nodes for a complete WFSG. Under this circumstance, a few assumptions are made to simplify the LPTN for a WFSG.

1. First assumption is that the loss generated during the operation at any time instants are evenly distributed.

2. Second, copper wires and resin in the stator and rotor coils are considered as isotropic materials, which has the same equivalent thermal conductivity.

Thus, a WFSG can be modelled by a rotor pole and the number of stator slots that fits into the one pole pitch. This can significantly reduce efforts spent on establishing a LPTN and simulation time. In [111], three nodes horizontally distributed in a stator slot achieve very good accuracy modelling the temperature in a slot for a water cooled PM machine adopting concentrated winding. Nevertheless, the number of nodes is affected by many factors. Since the existing WFSG available adopts air as its cooling agent, this potentially creates more unknown factors when building a LPTN. Complex rotor configurations for a WFSG (including field coils, damper cages) result in increased difficulties in terms of the modelling of rotor temperature. But, three nodes in stator and rotor winding are chosen as a starting point for establishing a 2D-LPTN for a WFSG.

With the number of nodes in a LPTN addressed, heat transfer coefficients are also essential for a LPTN, which is related to the cooling method available. The cooling method for an existing WFSG is forced air cooling via a fan coupled on the shaft. The air flow inside the existing WFSG is a complex fluid and thermal dynamic problem. An accurate air flow modelling requires comprehensive understanding of fluid and thermal dynamics. A complete and accurate WFSG CFD model is also required to correctly model intricate fluid and thermal dynamic problems [112].

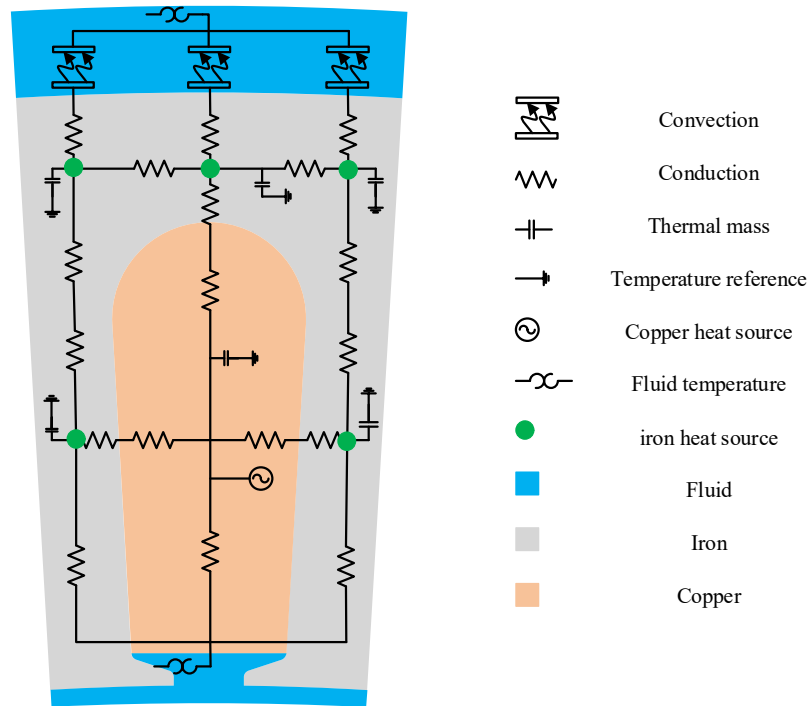


Fig. 15 Conceptual blueprint of a 2D LPTN for elements in one stator slot for a WFSG

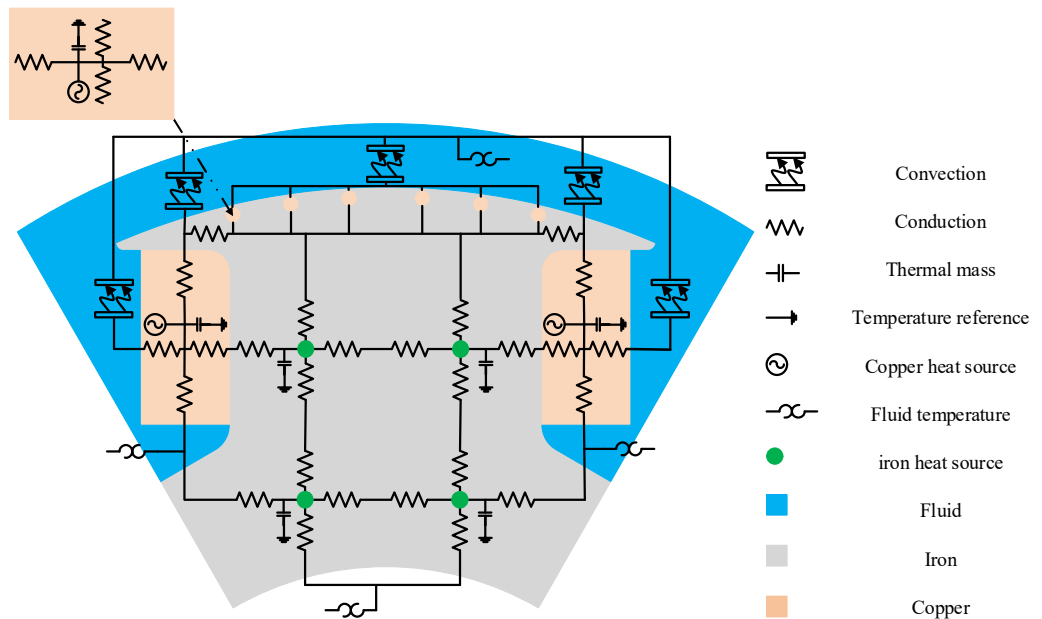


Fig. 16 Conceptual blueprint of a 2D LPTN for elements in one rotor pole for a WFSG

As mentioned at the beginning of the chapter 3.4, a CFD FE modelling of a WFSG is not covered in this thesis, but the heat transfer coefficients simulated in the past for an existing WFSG is used as initial inputs to a LPTN. Table 5 compiles the heat transfer coefficients at different parts of the existing WFSG. Consequently, heat transfer coefficients are carefully chosen to correctly establish a LPTN to simulate the temperature behaviour of an existing WFSG.

With $0.48 \text{ m}^3/\text{s}$ blown through a generator via a fan achieving roughly 2 m/s of air flow, the heat transfer coefficients surrounding the rotor coils reach a range of 309-560 $\text{W}/\text{m}^2\text{K}$ summarized in Table 5. The analytical methods for the heat transfer coefficients are presented in Appendix A. A key point has to be addressed here is that the HTC obtained using empirical equations are subjected to a $\pm 15\%$ difference compared with practical results [110]. Meanwhile, air ducts are provided at the stator back iron to maximize the capability to extract as much heat from the iron core as possible. The HTC are given as $87 \text{ W}/\text{m}^2\text{K}$ as an average value.

In Table 5, HTC for the air gap region and air surrounding field coils are significantly different. Therefore, the cross-sectional area that has air passing through is divided into two parts – air gap and inter-pole area, which has different HTC. A 2D LPTN model is built for the existing WFSG according to the LPTN network in Fig. 15 and Fig. 16. However, three nodes do not given an accurate temperature simulation compared with experimental data. In quite a lot of literatures [113] [114], a 2D thermal network is enough to analyse the temperature behaviour for most electric machines. However, those 2D models are accurate enough to determine the maximum coil temperature of a liquid cooled machine. Under this

circumstances, more number of nodes in a stator slots are also been presented in literature [115] to obtain an accurate plot of stator slot temperature.

A 2D LPTN only simulates heat flow in radial and tangential directions. For an air cooled WFSG, the air flow through the axial direction of a WFSG is an intricate phenomenon not only for the active part, but also for the end windings. Consequently, the HTC are different through the entire axial length of the generator due to reduced air flow rate shown in Table 5. In order to build a LPTN capable of analysing temperature behaviour of end windings and active parts in an accurate way, a 3D LPTN [65] is adopted in this thesis to analyse the temperature behaviour of a WFSG. In the 3D LPTN model proposed in [65], an extra thermal resistance links copper wire in an axial direction, which allows heat flux travelling axially. The temperature of cooling fluid in the axial direction is assumed to be a constant. Although in [65] the temperature measurements complies with the 3D LPTN model, the assumption that cooling liquid temperature remains unchanged does not fit for an air cooled generator. The measured inlet and outlet air temperature change for an existing generator is close to 20 °C.

As a result, this chapter a new 3D LPTN model is proposed to simulate a generator whose axial cooling air temperature varies alongside the axial direction. At the beginning, five slices of a 2D LPTN are linked axially shown in Fig. 17 simulating the active part of a WFSG. Extra thermal resistance is added between two slices of 2D LPTN models until the ambient air region is reached as shown in Fig. 17. Most importantly, not all the materials can be connected in the axial direction. The laminations are insulated against each other to reduce eddy current loss. In this case,

an assumption is made that no heat flux in the SiFe steel is considered passing axially. The HTC for air gap and inter-pole region for each slice are given with different values to simulate dropped air speed in the axial direction.

Table 5 Heat transfer coefficients obtained at critical points for the existing WFSG

Axial length	Surface Heat Flux (W/m ²)	Surface Temperature (K)	Bulk Air Temperature (K)	HTC
Stator Air gap				
0-100 mm	10289	379	325	191
100-200 mm	6095	403	336	91
200-300 mm	5454	418	345	75
300-400 mm	4841	427	352	64
400-500 mm	4486	428	357	63
Rotor-Winding				
0-100 mm	6757	328	316	560
100-200 mm	5683	335	322	432
200-300 mm	5745	342	327	393
300-400 mm	5505	351	334	309
400-500 mm	5868	358	340	310
Stator Back Iron	7952	405	314	87
Rotor End windings Inlet	7529	322	306	451
Rotor End windings Outlet	4987	369	336	152
Stator End windings Inlet	7789	323	306	440
Stator End windings Outlet	7522	361	336	302

Another two slices modelling end winding region are added to each side of a 3D LTPN in Fig. 17. The air gap and inter-pole region at end winding slice are connected to ambient air to correctly model a scenario of an air cooled WFSG. The ambient temperature for the air gap and inter-pole region at each end is given by the measured inlet and outlet air temperature. The cross-sectional area for end windings and windings inside the stator slots is the same. The same number of nodes are

used to model the end winding. The overall 3D LPTN contains five slices modelling active region and two slices modelling end windings.

Design ideas of a 3D LPTN for a WFSG are all introduced. This section introduces the actual implementation of a 3D LPTN in Matlab and Simulink. A Matlab script is programmed to include material properties (thermal conductivity, mass), fluid properties (thermal conductivities, heat transfer coefficients) and portals that accept WFSGs dimensions and losses data. Meanwhile, discretization of a generator geometry (the number of nodes in iron core and copper wire; the number of slices in the axial direction) is kept as variables allowing flexible implementation for a WFSG with different methods of discretization. This Matlab script controls the parameters been sent to a 3D LPTN models in Simulink.

In Simulink, a small 2D LPTN for a single stator slot as shown in Fig. 15 is built and considered as a small module. The number of nodes designed to have for iron core and copper wires in this LPTN is already determined initially based on the accuracy that is needed which are kept as variables. A similar module for half of a rotor core is built in Simulink due to symmetry as shown in Fig. 16. HTC, thermal resistance and thermal masses in those 2D LPTN are parameterized according to Matlab script. A complete 2D LPTN for a WFSG whether it is half pole or full pole pitch can all be achieved by replicating single stator slot and half rotor pole LPTN. This forms a slice of a 2D LPTN. A 3D LPTN can also be replicated by linking multiple 2D slice together as shown in Fig. 17. By running the Matlab script, a 3D LPTN model automatically generates temperature behaviour of a WFSG ready for post processing including transient and steady state.

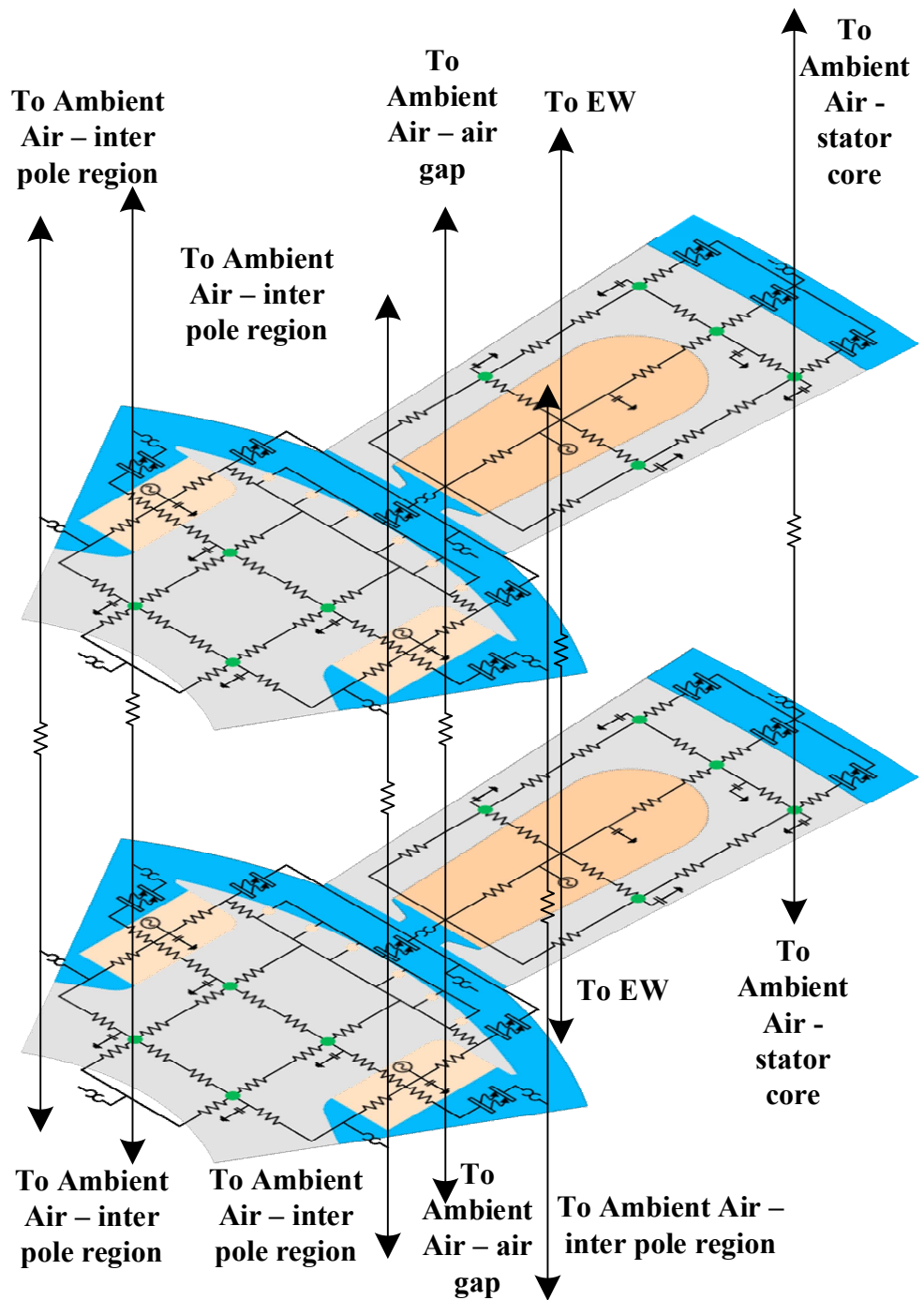


Fig. 17 Conceptual blueprints for a 3D LPTN for an existing WFSG

3.4.3 Experimental validation for the lumped thermal network for an existing WFSG

A 3D LPTN model is completed in chapter 3.4.2. This thermal network has considered sensitive factors such as the geometry for a WFSG, thermal conductivity and the HTC of coolants in different sections. However, this model still needs experimental validation to check whether the temperature behaviour of stator and rotor coils comply with the experimental measurements.

Table 6 compiles the inlet and outlet temperature near air gap and back iron for both simulation and experimental measurements. A relatively good match between simulated and practical results can be found. This indicates the made-up value for axial HTC are reasonable.

Table 6 Comparison of inlet and outlet temperature at stator back iron, rotor windings and stator windings

	Measured(°C)	Simulation(°C)	Error
Stator Back Iron	51	47	8%
Rotor End windings Inlet	57	51	11%
Rotor End windings Outlet	82	79	4%
Stator End windings Inlet	66	57	14%
Stator End windings Outlet	78	80	3%

Fig. 18 compares the hot spot temperature rise profile for stator slots simulated using the 3D LPTN and the UoN experimental measurements. Multiple temperature simulation points can be obtained from the 3D LPTN. The overall temperature profile from the simulation falls within the profile of the experimental measurements. Since manufacturer and UoN has a different ambient temperature setup, the steady state temperature for a hot spot in the stator slot does not reflect the validity for a 3D LPTN designed for a WFSG. Therefore, temperature rise data for both

manufacture and UoN is considered while validating the 3D LPTN. The manufacture of this WFSG also provide UoN with the hot spot temperature rise in the stator winding that is 73°C . Fig. 18 demonstrates the temperature rise for stator slot through the entire axial length falls within the region where UoN measurements are carried out. Only a single temperature measurements is shared by the manufacture, but this measurement can be done at any place in a stator slots. Comparing 73°C with data in Fig. 18, this value is not far away from UoN measurements. Therefore, it is still considered as a valid point for comparison.

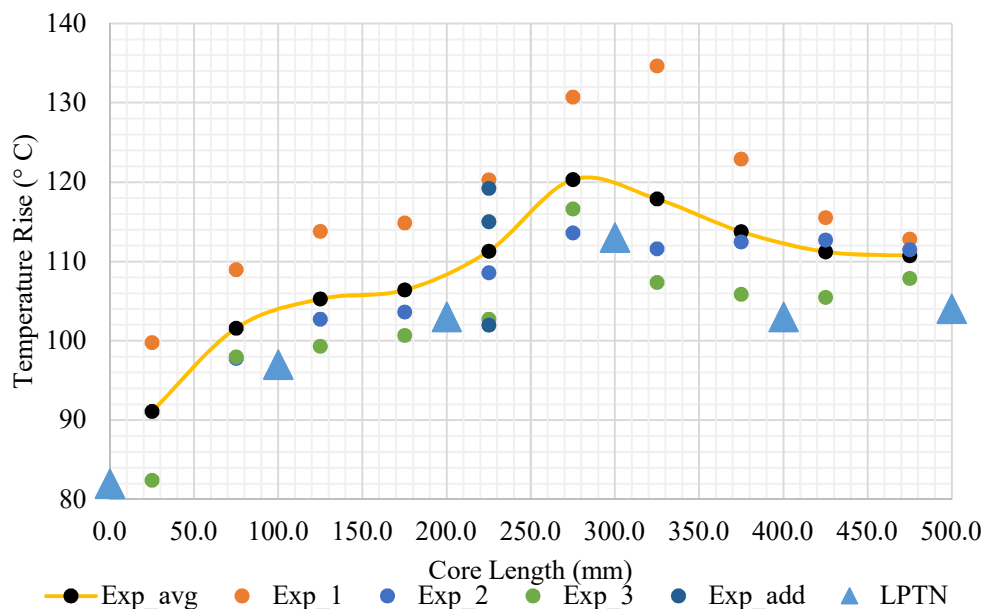


Fig. 18 Experimental stator temperature rise measurements vs. Simulink LPTN simulation (An UoN existing WFSG)

Fig. 19 collects the hot spot temperature profile for rotor windings simulated using the LPTN and the experimental results. The rotor temperature is hardest part to simulate as the fluid and thermal dynamic behaviour of air passing through rotor core are difficult to quantify. In Fig. 19, the LPTN rotor temperature profile lies above the profile of the UoN experimental measurements. The reference rotor temperature

rise from manufacture is 101°C . Average hottest rotor spot temperature rise simulated by the LPTN is 97°C close to 101°C .

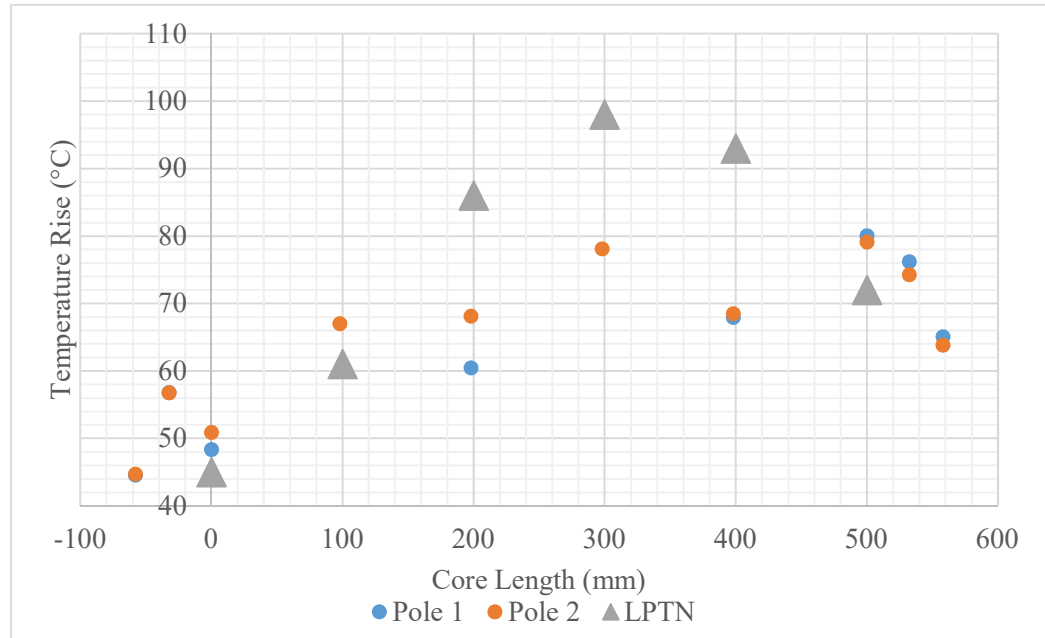


Fig. 19 Experimental rotor temperature rise measurements vs. Simulink LPTN simulation (An UoN existing WFSG)

In conclusion, a 3D LPTN established in this chapter for a WFSG is validated against experimental measurements. Relatively good simulation outcomes in terms of the temperature behaviour are found. Therefore, the 3D LPTN can be used to analyse the temperature behaviour of other WFSGs with similar cooling methods. If this tool is used to analyse temperature behaviour of WFSGs designed from scratch, adjustments of HTC in a reasonable range for a given cooling method are alternative methods to understand the temperature behaviour of a new generator. This gives a rough sizing recommendation for a WFSG prototype.

3.5 Conclusion

This chapter starts with an overview of the background theory for analysing a WFSG such as phasor diagrams and d-q plan quantities. The main focus for this chapter is to establish an analytical sizing script that is able to accurately determine key dimensions for a WFSG. This information is passed to a script controlled electromagnetic FE model to simulate the behaviour of a WFSG in details. The WFSG dimensional information and losses results are passed to a novel 3D LPTN to analyse the temperature behaviour of a WFSG. These three tools are all validated against an existing WFSG and integrated together in an OOD tool package. With a validated OOD tool ready for a WFSG, this tool can be used to design and analyse the performance of a new WFSG. However, due to the possible different regarding to the manufacturing process, the thermal performance can vary to a certain extent. If a new WFSG is designed using OOD tool with existing empirical parameters for example HTC and thermal conductivity, the finalized geometry is a reference point for this new WFSG with given manufacturing processes. Due to the advantages gained by applying OOD concepts when setting up the initial architecture, this partially finished multi-physics design tools for WFSGs can be further upgraded for better accuracy and enlarged thermal data base. For example, the empirical parameters such as equivalent thermal conductivity and HTC of copper wires are further improved by validating the simulated performance of a WFSG against its final prototype.

Chapter 4

Design methodologies for high speed wound field synchronous generators

In the previous chapter, electro-magnetic design methodologies for WFSGs are introduced. A 3D LPTN is validated to analyse the temperature behaviour of a WFSG. These models are developed based on a low speed WFSGs. This chapter mainly focuses on high speed WFSG design methodologies by utilizing and enhancing the OOD design tool developed in chapter 3.

However, high speed machines suffer from two major obstacles, high frequency harmonics associated losses and high centrifugal forces applied to the rotor body. These two factors raise necessities on comprehensive analysis on high frequency iron loss, AC losses in the stator windings, static structure and rotor dynamic analysis. Therefore, a multi-physics model covering issues raised above for a WFSG is further developed in this chapter.

This chapter further enhances an analytical electro-magnetic model built in the previous chapter to be capable of analysing high frequency losses behaviour for a WFSG. The partially finished OOD design tool developed in chapter 3 is utilized to design a high speed WFSG according to the design requirements listed in chapter 1.2. A 3D LPTN for WFSGs built in chapter 3 is implemented to determine the temperature behaviour of a given design option. A trade off study covering

electromagnetic and thermal performance of a WFSG is presented. The final design choice of a WFSG is analysed by mechanical design tools developed in chapter 5.

4.1 Trade-off study for high speed wound field synchronous generators

In chapter 1.2, the fundamental frequency of the WFSG required reaches 360Hz to 800Hz corresponding to 7,200rpm to 16,000rpm. This immediately raise two major concerns 1) losses induced by high fundamental frequency and its harmonics in copper winding and iron core materials; 2) whether soft-magnetic material can withstand high speed operation. The trade-off study utilizing OOD tool developed in chapter 3 considering electromagnetic and thermal performance is presented first.

4.1.1 Design process for a high-speed wound field synchronous generator

As mentioned in chapter 1.2, SiFe steel of grade M235-35A is selected due to concerns on budgets and the high risks of failure adopting high grade materials such as CoFe. Since cost is always an influential factor for any commercial industry, 150 (temperature limits) grade copper wires are selected for the first trade-off study. A required torque speed map is summarized in Fig. 20 based on the information given in chapter 1.2.

Design requirements for this WFSG are summarized as follows. This WFSG has to deliver 407Nm from 0 to 4,693 rpm and 200kW between 4,693 and 6,780 rpm hatched in blue in Fig. 20. This worst starting scenario must last for 2 minutes. Between 6,780 rpm and 7,200 rpm, this WFSG runs at idle waiting for the turbine to be ignited as shown in Fig. 20. After the engine is ignited, this WFSG must be able to deliver a maximum power of 250kVA between 7,200 rpm and 16,000 rpm as hatched in red region in Fig. 20. The power quality of the output voltage is required to be less than 5% according to MIL-STD-704F. Meanwhile, a WFSG has to achieve the lowest weight possible (close to 100 kg).

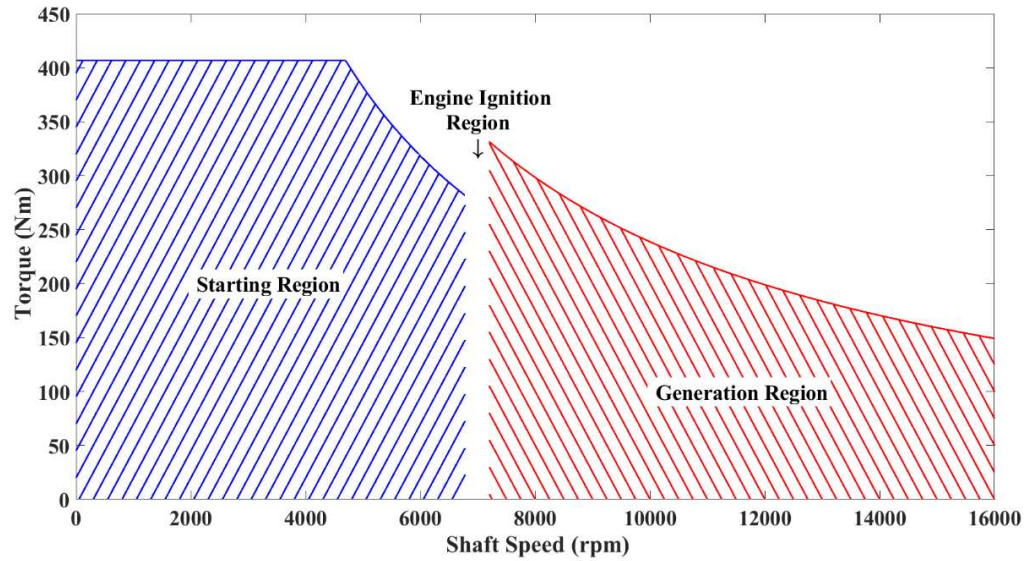


Fig. 20 Torque speed map for design requirements in chapter 1.2

According to literatures [1], integral slot winding for the stator core is often adopted for this sort application. The linear current density and current density for stator and rotor coils are selected as $25k/A/m$, $9A/mm^2$ and $6A/mm^2$ respectively. The flux density at the rotor pole, rotor bore, stator teeth and stator yoke are $1.5T$, $1.6T$, $1.8T$ and $1.6T$ respectively. The peak flux density in the air gap is $0.85T$ due to the saturation point for M235-35A is $1.6T$. For a WFSG, the air gap length is directly proportional to the field current. Due to limited space and cooling capability available, high speed WFSGs is designed with small air gap in general. Thus, the air gap length for this high speed WFSG is chosen as 1 mm . A WFSG has to deliver $250kVA$ at all the generation region hatch in red in Fig. 20 while achieving minimum weight. Therefore, a design point for this WFSG should be at $331Nm$, and $7,200\text{ rpm}$. The speeds chosen for power generation simulated in this thesis are $7,200\text{ rpm}$, $9,000\text{ rpm}$, $12,000\text{ rpm}$ and $16,000\text{ rpm}$. The torque required at those speeds are 331 Nm , 265 Nm , 199 Nm and 149 Nm . The power for all the simulation

conducted is all 250 kVA. The speeds chosen for generator starting simulated in this thesis are 2,000 *rpm*, 4,692 *rpm*, 5,500 *rpm* and 6,780 *rpm*. The torque required at those speeds are 407 *Nm*, 407 *Nm*, 347 *Nm* and 282 *Nm*. The power for starting at 2,000 *rpm* is 85 kW and 200 kW at 4,692 *rpm*, 5,500 *rpm* and 6,780 *rpm*. This information is used for all the simulation conducted in this thesis.

The design point on torque speed map and design requirements are clear. The operation points of this WFSG for temperature simulation using a 3D LPTN are discussed next. During power generation operation, theoretically, highest temperature for the generator can be found with full load and 0.75 power factor operating scenarios. While a WFSG operates under full power, field current is at its maximum value to overcome the armature reaction. While the power factor is at its minimum value lagging, excessive field current is needed to maintain terminal voltage at POR compared with that of unity power factor. In addition, while a WFSG operates at higher speed than the rated value, the ac losses caused by high frequency harmonics becomes more significant. Although field current is substantially reduce at higher operating speeds, increased losses due to various high frequency harmonics complicates the temperature behaviour of a WFSG. Without a thermal simulation, it is not easy to predict at which speed the maximum temperature occurs. Therefore, the full load, 0.75 power factor lagging operation following red envelop in Fig. 20 gives highest possible temperature rise for a WFSG at generation region. Operating scenarios at 7,200, 9,000, 12,000 and 16,000 *rpm* are selected for electromagnetic FE and a 3D LPTN simulation.

The maximum allowable peripheral speed for the rotor core is limited to 180 *m/s* according to [116] which limits the rotor radius of a generator. At the beginning, different pole slot combinations are studied to understand the effects of different number slots on the performance of WFSGs such as terminal voltage, torque, temperature and THD, etc. At this stage, integral slot winding and full pitch winding are chosen for initial generator design stage.

Table 7 Analytical sizing dimensions of a WFSG

Slot Number	25k A/m			
	18	36	54	72
Stator Outer Diameter (<i>mm</i>)	263.1	261.4	260.9	266.1
Stator Inner Diameter (<i>mm</i>)	199.3	199.3	199.3	199.3
Rotor Outer Diameter (<i>mm</i>)	197.3	197.3	197.3	197.3
Slot Depth (<i>mm</i>)	13.8	12.7	12.4	15.1
Tooth Width (<i>mm</i>)	18.5	9.3	6.2	4.7
Axial Length (<i>mm</i>)	394.6	394.6	394.6	394.6

Table 7 compiles 4 different WFSGs designed (different pole slot combinations) options using the OOD tool developed in chapter 3 with design inputs in chapter 4.1.1. Due to the mechanical constraint, the rotor diameter for all 4 WFSG options are kept the same - 197.3 *mm*. The outer envelope for all the design options are around 260 *mm* and the axial length is 394.6 *mm* for 4 different options in Table 7. In chapter 1.2, the number of poles are determined to be 6, and thus, only the slot number can be altered as design variables. Weight information for 4 different WFSG's combinations are plotted in Fig. 21. The key performance value such as no-load terminal voltage, no-load THD and efficiency 7,200*rpm* for 4 WFSG options are listed in Fig. 22.

In Fig. 21, weight information for 4 WFSG design options are given by the OOD tool at rated speed. The estimated weight for all slot pole combinations are similar. No combination has significant advantages over the rest options. For copper consumed in 4 different options, 72 slot option consumes more material on armature coils and both 18 and 72 slot machine used more copper for filed coils than 36 and 54 slot generator. In terms of stator and rotor iron, 36 and 54 slots generator need less iron than 18 and 72 slot options. In conclusion, 36 and 54 slot design options are about 6.7% lighter than the rest design options in terms of weight.

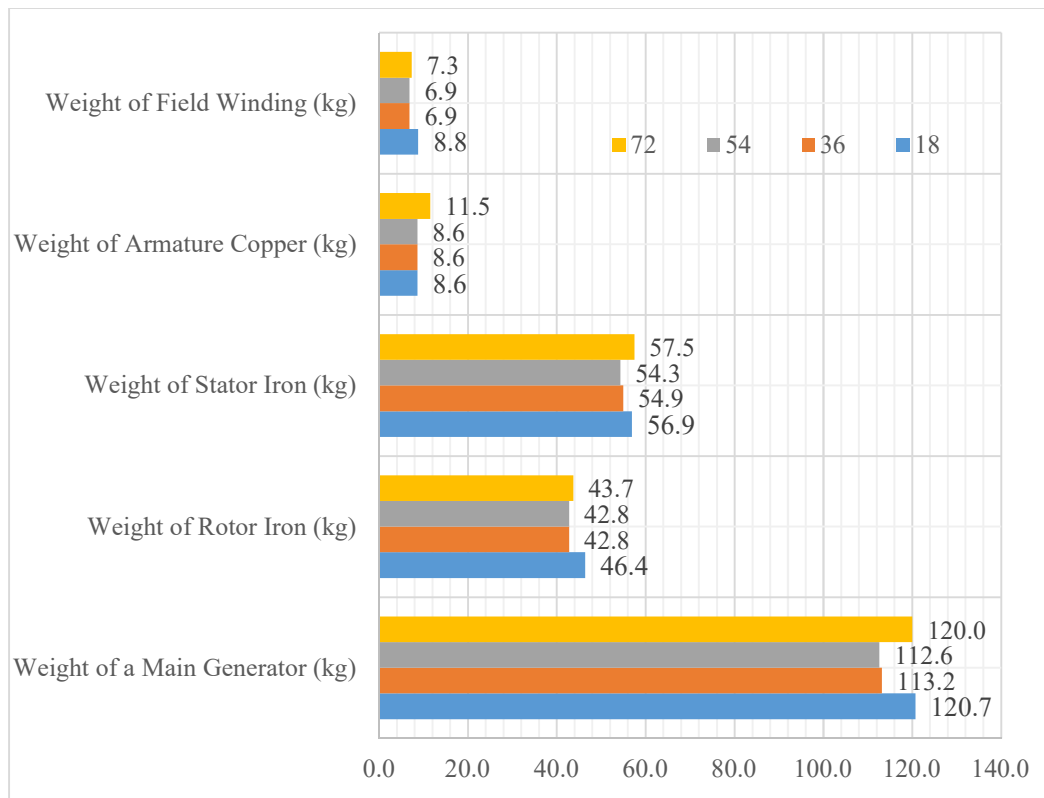


Fig. 21 Weight information for 4 WFSG design options

In Fig. 22, the performance of 4 different design options evaluated by the FE OOD module. A 54 slot WFSG has the lowest THD level compared with the rest of the design options. The no-load terminal voltage for 4 different design options has a

maximum 4.2% error compared with the POR 235Vac. For this criteria, all 4 different design options are not significantly different from each other. Efficiency is one of the most essential factors in generator design. In Fig. 22, the efficiency for 36, 54 and 72 slot design options is similar under worst operation scenarios and 12% higher than 18 slot design option. Based on the analysis above, 54 slot design option wins the competition at this stage.

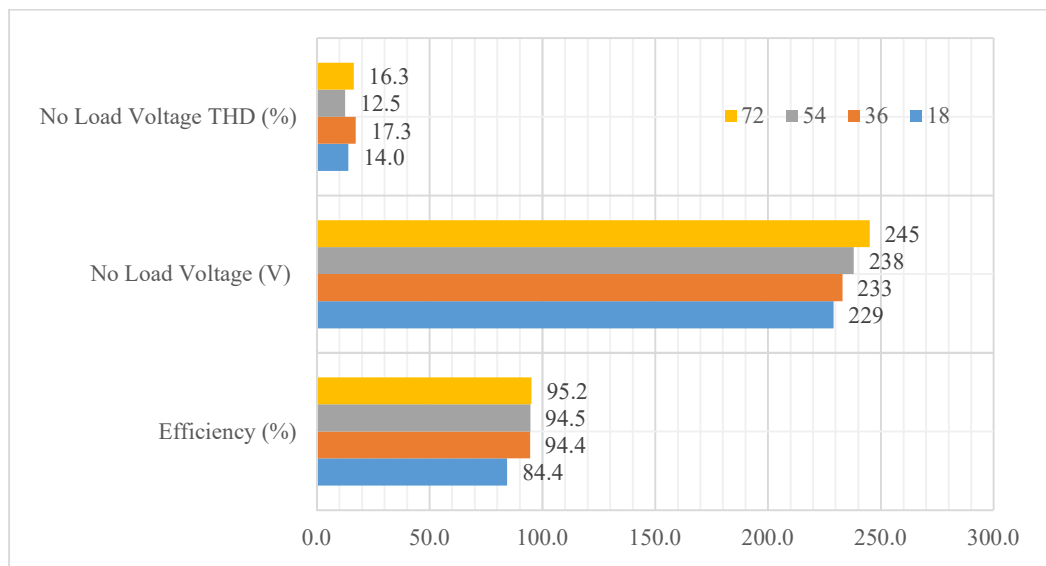


Fig. 22 FE performance evaluations for 4 WFSG design options

Table 8 Losses comparison of WFSGs with different slot combinations

	25k A/m			
	18	36	54	72
The number of slots	18	36	54	72
Armature Coils (kw)	1.027	1.121	1.358	1.18
Field Coils (kw)	2.014	1.605	1.613	1.613
Damper Coils (kw)	9.461	1.428	1.047	0.606
Rotor Iron (kw)	0.0509	0.0491	0.056	0.0706
Stator Iron (kw)	0.4178	0.4316	0.477	0.531

Table 8 compares the different losses of WFSGs with different slot numbers. It can be concluded that the efficiency of 36, 54 and 72 slots machine is similar. Under this circumstance, the temperature behavior of different design options is important.

Although a 54 slot WFSG is concluded to be the best design options among the rest of the choices, temperature limits are still a dominating factor to choose an appropriate pole slot combination. RL loads are connected in the external circuit to simulate an inductive load for a WFSG with 0.75 lagging power factor. Fig. 23 shows the hottest temperature in the stator coil at 7,200rpm, 9,000rpm, 12,000rpm and 16,000rpm for all four pole slot combinations. In general, with an increase of slot number, the highest temperature spot in the stator slot for a WFSG decreases (vertical comparison) at each speed simulated. The maximum stator slot temperature are all below 150 °C. Meanwhile, 54 slot option presents the lowest temperature among all the 4 options, but the advantages for 54 slot option over 72 slot are negligible. In summary, both 54 and 72 slot options are potential candidates for the best performing WFSG.

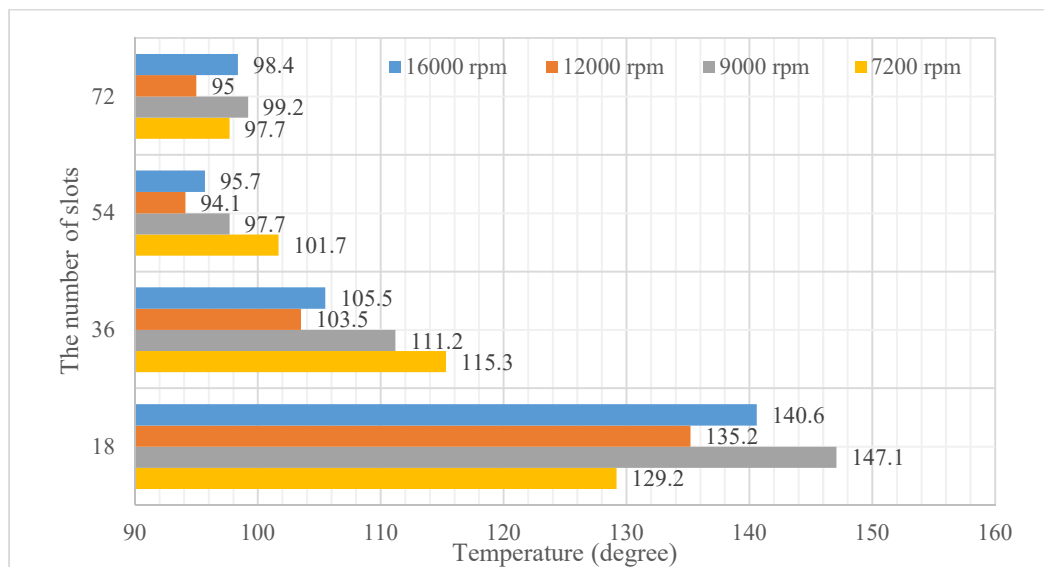


Fig. 23 Maximum stator temperature during generation mode

Fig. 24 shows the hottest temperature in the rotor coil at 7,200rpm, 9,000rpm, 12,000rpm and 16,000rpm for all four pole slot combinations. A similar trend for

temperature behaviour can be found for rotor temperature compared with Fig. 23. The highest rotor temperature spot in a WFSG decreases (vertical comparison) with an increased slot number at each speed simulated. An important issue can be found from Fig. 24 that the hottest temperature spot for 18 slot option exceeds the 150 °C which is the threshold temperature for such grade insulation material.

Copper operating temperature greater than the rated one degrades the lifetime of the insulation materials coated on copper wires. Therefore, a conclusion can be drawn from Fig. 24 that the 18 slot design configuration is ruled out from the design competition as the temperature for the rotor coils exceeds 150°C by quite a margin. Highest temperature spot for 36, 54 and 72 slots configurations on rotor and stator coils are less than 150 °C. By analysing both Fig. 23 and Fig. 24, the more slots a WFSG has, the lower the temperature in rotor and stator coils is. 54 and 72 slot WFSGs configurations are the two options that have the lowest coil temperature compared with the rest. The temperature difference for 54 and 72 slot WFSGs is very small. Therefore, further comparisons are required between 36, 54 and 72 slot options to determine which design option has the best performance.

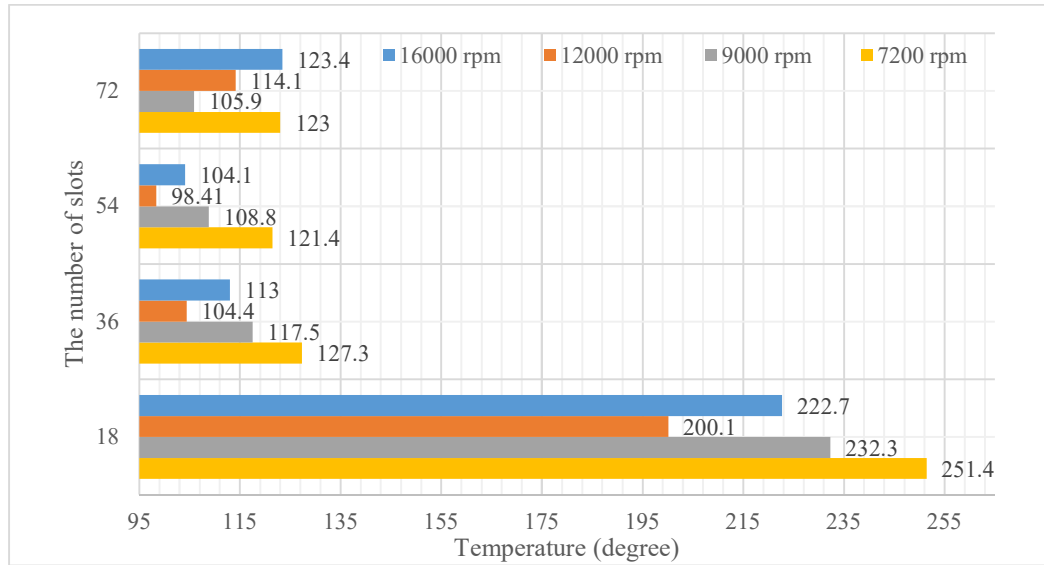


Fig. 24 Maximum rotor temperature during generation mode

The analysis for thermal behaviour during power generation region all the WFSG design options is finished. Next step is to analyse the temperature behaviour at starting region. Starting functionality is also one of the design requirements for a WFSG presented in chapter 1.2. A WFSG is required to deliver 407 Nm at low speed range as shown in Fig. 20. The starting torque (407 Nm) required from the WFSG is beyond the rated torque (331 Nm) for a WFSG at $7,200 \text{ rpm}$ in Fig. 20, which represents an overload operating condition for a WFSG. In this case, starting operation for a WFSG is a short duty operating scenario to keep the maximum coil temperature under $150 \text{ }^\circ\text{C}$. In chapter 1.2, the maximum operating time is 120 seconds. Therefore, transient temperature behaviour is investigated to understand whether the remaining 3 WFSG design options (36, 54 and 72 slot) can deliver required amount of starting torque. This also constrains the size and weight of WFSGs been designed.

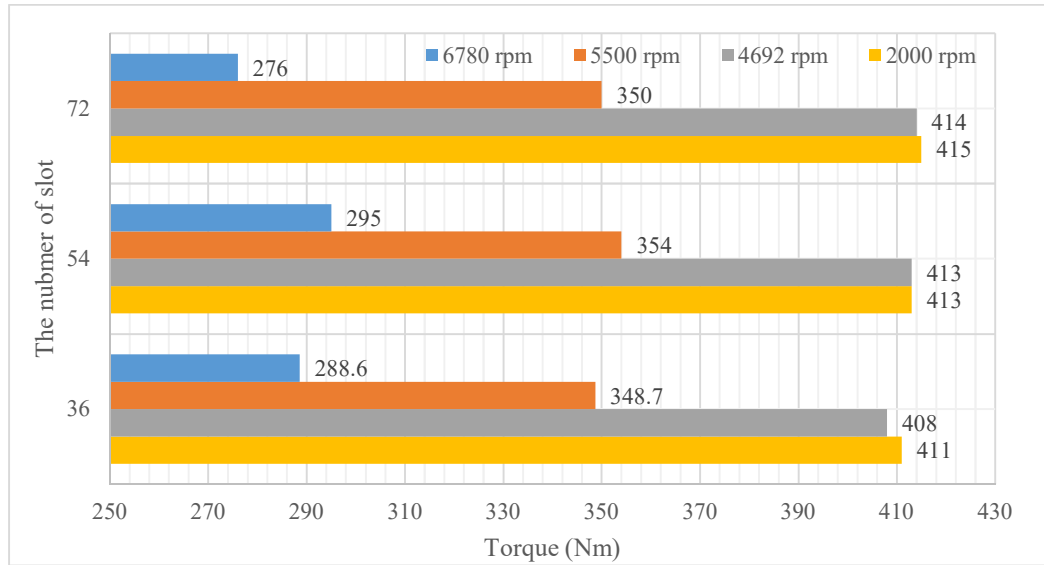


Fig. 25 Torque production for 3 WFSG design options

By examining Fig. 25, 3 WFSG design options all provides adequate torque at each speed been simulated by comparing against the red envelope in Fig. 20. To obtain the maximum torque from the WFSG, the field currents are applied with doubled no-load field current at 7,200 *rpm*. The stator currents are adjust to a value that can produce required torque at required speed. Next step is to check the highest transient temperature profile in 120 seconds using a 3D LPTN built in chapter 3.4. In the electromagnetic FE simulation, external current sources are connected to the three-phase winding.

Fig. 26 presents the maximum stator coil temperature for 3 WFSG design options at 2,000 *rpm*, 4,000 *rpm*, 5,000 *rpm* and 6,800 *rpm* in 120 seconds. 36 slot option achieves 144 °C close to the threshold value. In contrast, 54 and 72 slot design options achieved significant lower temperature compared with 36 slot option at given speeds. Thus, judging from maximum stator coil temperature, 54 and 72 slot WFSG design options presents better performance than 36 slot configuration.

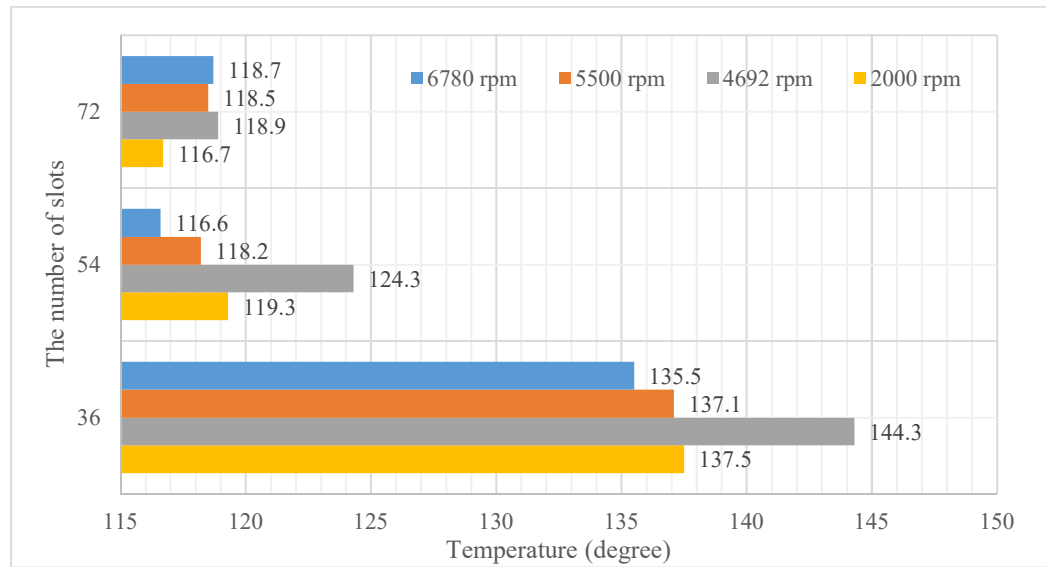


Fig. 26 Maximum stator temperature during starting mode

Fig. 27 presents the maximum rotor temperature during machine cranking period for 3 remaining WFSG design options. A 36 slot design option hits 160 °C that is beyond the threshold value. 54 and 72 slot WFSG design options have the lowest rotor coil temperature among all the WFSG design configurations. From an electromagnetic and thermal perspectives both 54 and 72 slot WFSGs can meet the demands. From rotor temperature perspective at crank start period, 72 slot design option is the best performing option and 54 slot design is the second best performing generator.

In summary, the selected WFSG design option has to satisfy both generation and motoring operation as required. The performance for power generation is given with more weight ratio compared with motoring operation when making a choice due to following reasons. Power generations is continues operating tasks. In contrast, motoring mode is a short time duty operation. Therefore, the performance of a

WFSG under power generation mode affects the overall performance in a greater extent than motoring mode.

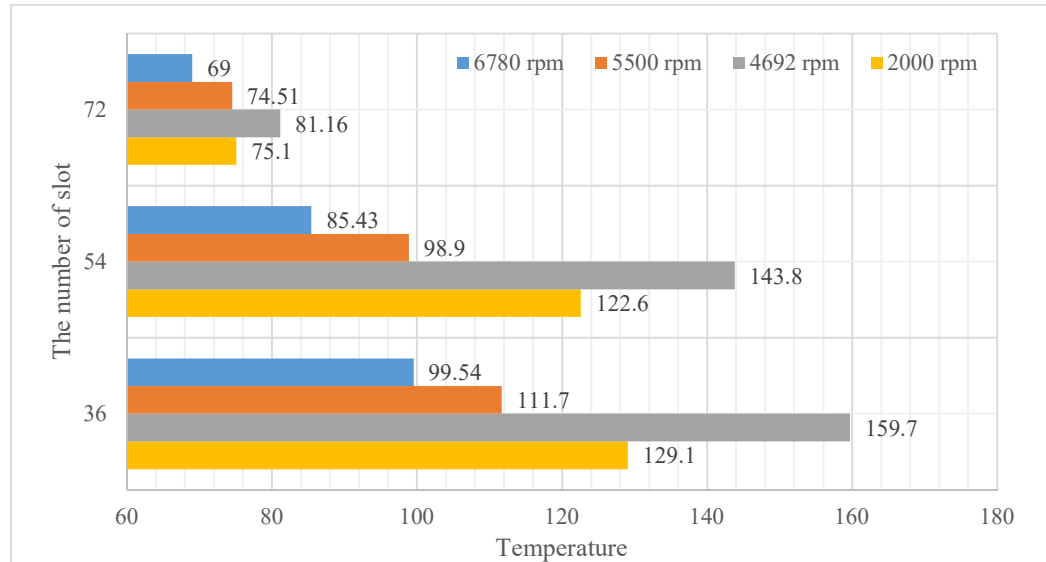


Fig. 27 Maximum rotor temperature during starting mode

Table 9 Tick marks for 3 design WFSG design options

	Generation		Motoring		Efficiency
	Stator Temp.	Rotor Temp.	Stator Temp.	Rotor Temp.	
36	✓	✓✓	✓	✓	✓
54	✓✓✓	✓✓✓	✓✓	✓✓	✓
72	✓✓	✓	✓✓✓	✓✓✓	✓

Table 9 summarizes the marks for temperature behaviour analysis based on information from Fig. 23 to Fig. 27. 54 slot design option is one point higher than 72 slot machine. The performance during generation is given with more weight ratio. Therefore, 54 slot WFSG design option is determined to have better performance under power generation mode without compromising the performance of motoring mode too much.

4.1.2 Power quality considerations for WFSGs

A 6 pole 54 slots WFSG configuration is concluded to be the best choice to go forward in chapter 4.1.1. Next step is to modify several dimensions to tune the electromagnetic performance such as THD and losses to desired value.

The power quality for the terminal voltage of a WFSG required is less 5%. In Fig. 22, the THD level for the output voltage for no-load operation is 12.5% that exceeds the required value. Thus, several techniques are investigated to reduce the THD level for a 6 pole 54 slot WFSG for further upgrades.

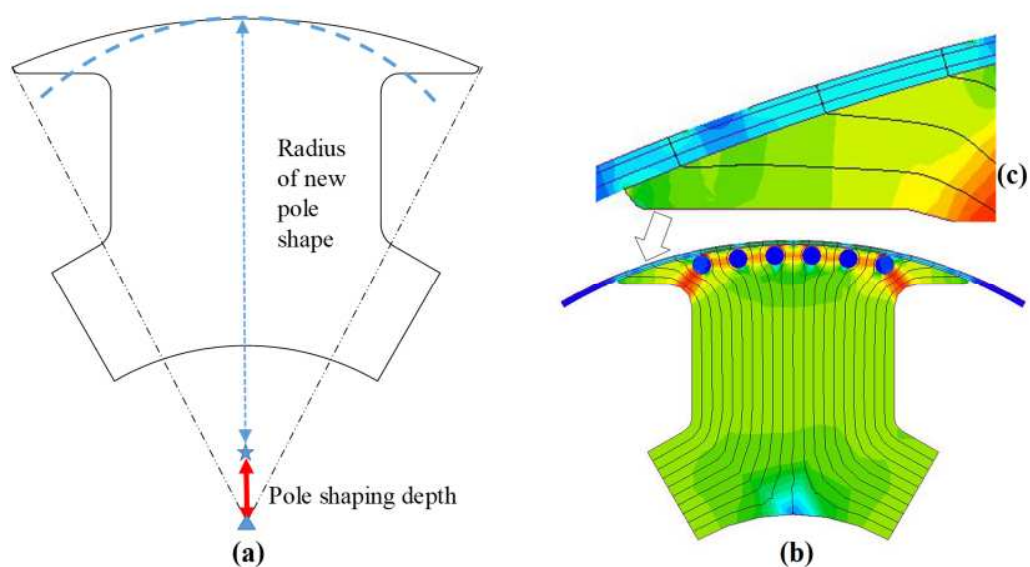


Fig. 28 Rotor pole shaping methods a) exaggerated pole shaping methods explanation b) a pole shaping mode simulated in FE software c) zoomed in inconsistent air gap

The techniques to reduce the THD of the output voltage are listed in chapter 2. These techniques include 1) pole shaping 2) short pitching 3) stator slot skewing. These are conventional techniques implemented in the past by industry. However, all these

techniques reduce the root mean square (RMS) value of the output voltage. This section uses these conventional techniques to see if the THD value can be reduced below 5%.

Pole shaping of rotor core is done as the way shown in Fig. 28. The blue triangle in Fig. 28 is the centre of the rotor pole in solid line (uniform air gap). A new centre (blue star) for a new pole shape is moved upwards for a distance named as pole shaping depth as a red arrow shown in Fig. 28 a). A new radius is given as the difference between original radius and the pole shaping depth shown as blue dashed arrow in Fig. 28 a). The targeted shape of a new rotor pole is also shown in an exaggerated way in Fig. 28 a) in dashed blue lines. The shortest distance between rotor pole and stator inner radius is still 1mm . Fig. 28 b) presents the shaped rotor pole simulated in FE software with a zoomed in pole tip figure in Fig. 28 c) showing the non-consistent air gap length. The presence of the harmonic contents in the output terminal voltage are not easily quantified by analytically equations [84]. In the electromagnetic FE simulation, a sensitivity analysis is performed to understand the relationship between the poles shaping depth and the THD value for the output terminal voltage at no-load conditions and the results are shown in Fig. 29. A 'V' shaped scatter figure is observed for THD level at different pole shaping depth and speed combinations. Pole shaping depth around 11 to 13 mm gives lowest no-load THD values for terminal voltage close to 5%. Thus, pole shaping depth at 11 mm is selected to analyse the WFSG performance characteristics at $7,200\text{rpm}$, $9,000\text{rpm}$, $12,000\text{rpm}$ and $16,000\text{rpm}$.

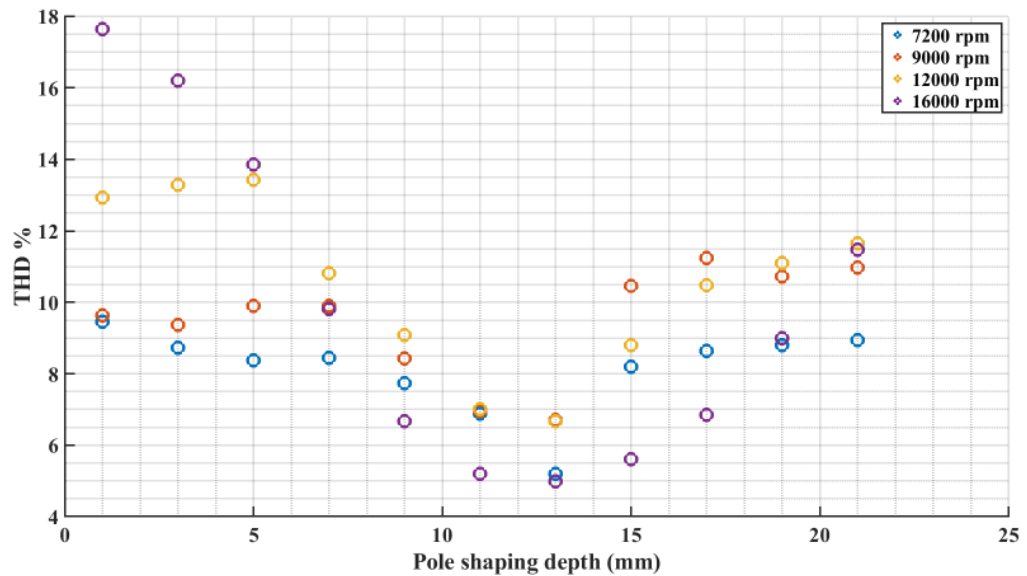


Fig. 29 Sensitivity analysis of THD level with different pole shaping depth at various speeds

The RMS values for the terminal voltage are reduced due to decreased magnetic loading caused by pole shaping. The axial length of a WFSG is increased to compensate the power lost by pole shaping so that the WFSG dimensions in the cross sectional view remain unchanged. A thermal analysis of this new pole shaped WFSG is necessary to determine the temperature utilizing the 3D LPTN developed in chapter 3.4. Fig. 29 collects the simulation results for THD value for no-load output voltages against pole shaping depth. Pole shaping depth around 11 mm leads to the lowest THD for the output no-load voltage.

Reduced end winding length and improved power quality are the major advantages offered by the short pitch technique. The disadvantage for short pitch is that this technique can only reduce specific harmonics by corresponding short pitch. For example, 5/6 short pitch can cancel 5th and 7th harmonics; 2/3 short pitch cancels 3rd harmonics. 2/3 short pitch is selected to achieve the minimum THD level within a

selected number of short pitch options available. Meanwhile, this technique reduces the RMS value of the terminal voltage based on pitch factor. Extending the axial length of the WFSG is also necessary to compensate the power been lost through short pitching. Temperature behaviour of this short pitched WFSG must be simulated to investigate whether the size of the machine is enough to deliver required power while keeping the temperature limits.

Stator skew is used to reduce the slot harmonics while 3rd harmonics cannot be cancelled by this technique. According to equation (26) [106], one slot pitch is implemented to cancel the higher order slot harmonics. The axial length of the WFSG is also adjusted to increase the power of the machine. At the same time, temperature behaviour of skewed WFSG is investigated.

$$k_{sqv} = \frac{\sin\left(v \frac{\pi}{2} \frac{S_{sp}}{mq}\right)}{v \frac{S}{\tau_p} \frac{S_{sp}}{mq}} \quad (26)$$

Fig. 30 summarizes the THD values obtained from the electromagnetic FE simulation at 7,200rpm, 9,000rpm, 12,000rpm and 16,000rpm by implementing single THD reduction technique on a WFSG. In Fig. 30, THD level gradually increases with an increase of the operation speeds. In contrast, pole shaping is the most effective method compared with rest of the techniques and achieves the lowest THD level among all the techniques introduced. However, none of the three techniques reduce the no-load THD level to 5% required by MIL-STD-704F.

Fig. 31 collects the hottest temperature spot value in a stator coil for WFSGs modified with above mentioned three THD reduction techniques. The stator coils

temperature sees a decrease with THD reduction techniques implemented in general. During generation region in Fig. 31 and Fig. 32, pole shaping technique achieves lowest stator coil temperature compared with the rest of the technique for most speed condition. During starting operation in Fig. 31 and Fig. 32, skew and pole shaping technique achieves lower stator coil temperature compared with short pitching technique for most operating speed. In conclusion, the maximum stator coil temperature does not exceed the 150 °C threshold.

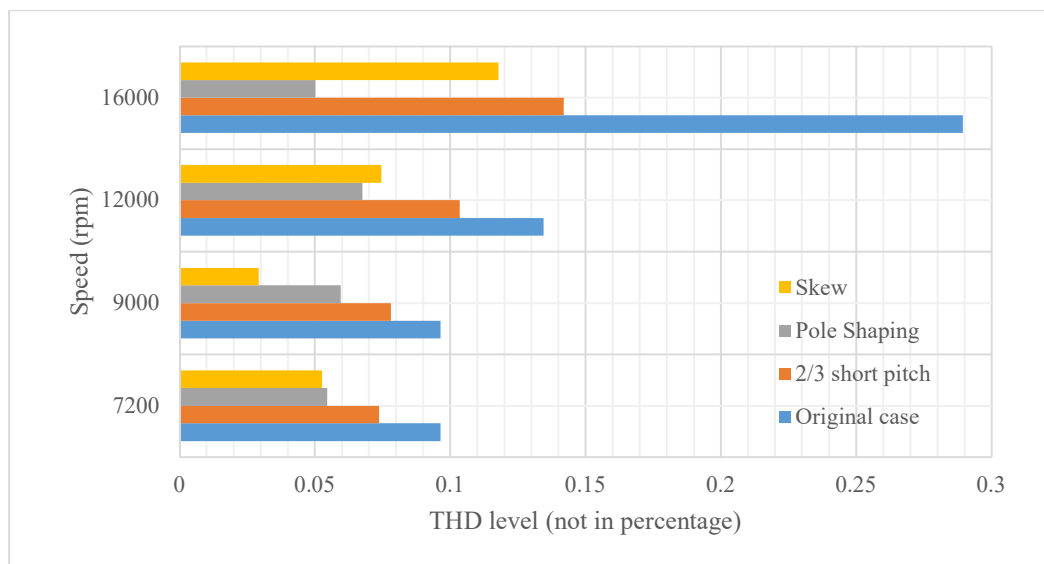


Fig. 30 No-load THD level in real value (not in percentage) at different generation speeds for 3 THD reduction techniques

Maximum rotor coil temperature is summarized in Fig. 32. An increase of coil temperature is observed for three THD reduction techniques during starting operation in general. WFSG design options for pole shaping and 2/3 short pitching techniques hit 160 °C exceeding 150 °C by 6% which is still acceptable for a short period duty cycle. During generation period, WFSG with THD reduction techniques at 7,200 rpm sees an increase of rotor temperature around 15% compared with

WFSG without any modifications hitting closely to the 150 °C threshold value. In contrast, the rest of generation region (speed region) for the WFSG designed sees a decrease of rotor temperature compared with the original case. In summary, WFSG design options with three THD reduction techniques satisfies the coil insulation limits.

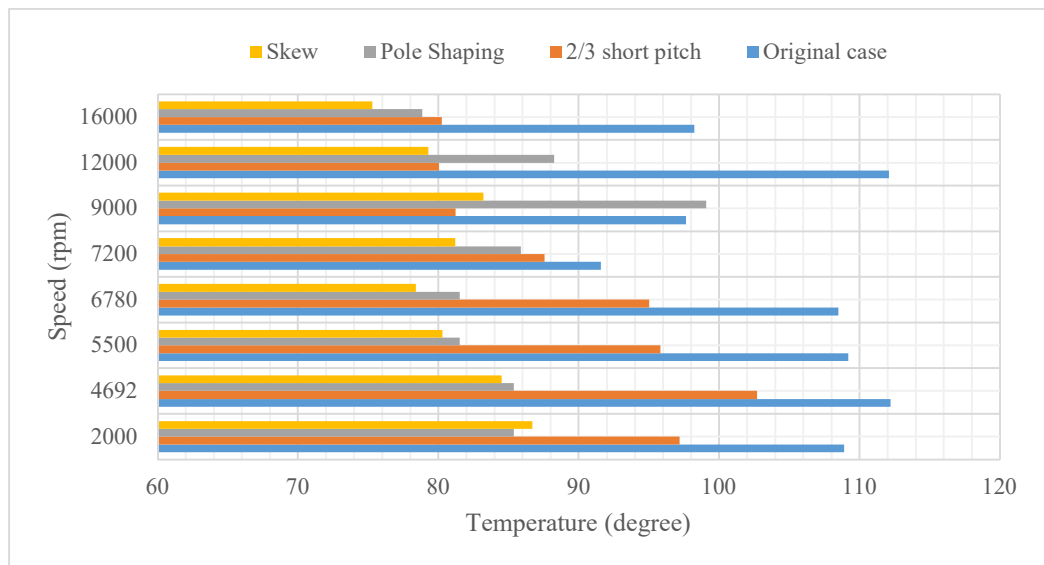


Fig. 31 Maximum stator coil temperature for the original WFSG and WFSGs with THD reduction techniques implemented

Although the temperature profile for all the WFSG design options with three THD satisfies the design threshold temperature 150 °C based on a 3D LPTN analysis. In addition to temperature analysis, the torque and weight of WFSGs analysed in Fig. 30 are also analysed to see if they fulfilled the design specifications. The axial length of the machine are increased till the point where maximum coil temperature for either stator or rotor reached 150 °C as shown in Fig. 31 and Fig. 32. Table 10 collects the key dimensional and the weight information of WFSGs been modified. It is clear from Table 10 that a 15 to 20 kg of weight is added to WFSG with THD

reduction techniques. Hence, the overall weight of WFSG designed is far away from the required values.

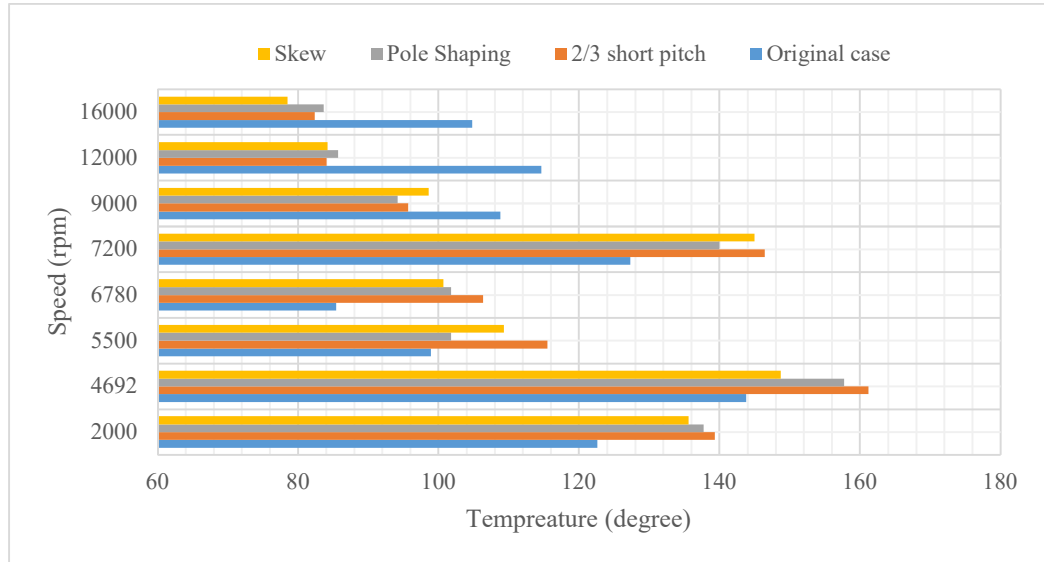


Fig. 32 Maximum rotor coil temperature for the original WFSG and WFSGs with THD reduction techniques implemented

Table 10 Key dimensions for WFSGs with THD reduction methods applied

	Original case	2/3 short pitch	Pole Shaping	Skew
Stator Outer Diameter (mm)	260.9	260.9	260.9	260.9
Stator Inner Diameter (mm)	199.3	199.3	199.3	199.3
Rotor Outer Diameter (mm)	197.3	197.3	197.3	197.3
Slot Depth (mm)	12.4	12.4	12.4	12.4
Tooth Width (mm)	6.2	6.2	6.2	6.2
Axial Length (mm)	394.6	453.79	418.3	394.6
Weight of a Main Generator (kg)	112.58	134.3	125.2	126.5

In Fig. 33, WFSGs modified with THD reduction features all deliver required torque at each speed simulated compared with requirements (blue solid line). With adequate torque been delivered, WFSGs with THD reduction features have all hit 150 °C as shown in Fig. 32. In this case, weight for WFSGs designed in Table 10 is already the minimum value under worst operating scenarios.

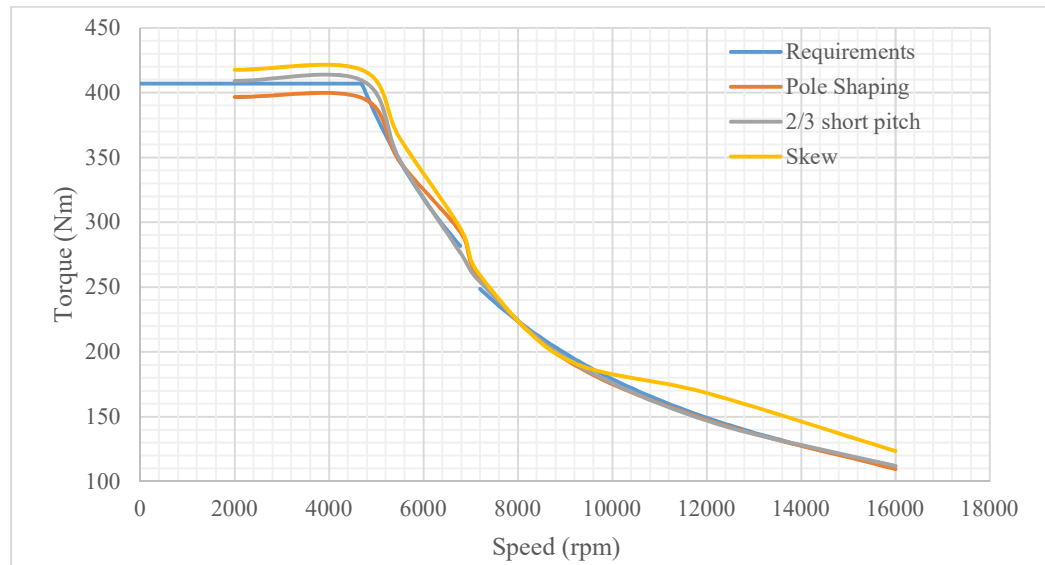


Fig. 33 Torque speed map for WFSGs with THD reduction features in Table 10

In summary, WFSGs with individual THD reduction technique implemented does not reduce the no-load THD level below 5% in Fig. 30. Therefore, a more aggressive approach by combining any two of these three techniques in order to reduce no-load THD level below 5%. In Fig. 5, a WFSG installed on the grid has 4 terminals (three phase terminals and a neutral terminal). A neutral terminal is used to service on board loads including single phase load [43], which promotes hazardous neutral currents in power distribution systems [117]. Therefore, 2/3 short pitch windings are used to cancel all triplen harmonics to prevent harmful triplen harmonics from load and source traveling through the neutral point. Consequently, pole shaping and stator slot skew combination is not considered as an option since this combination cannot fully eliminate 3rd harmonics which is harmful to power distribution systems. Short pitch and stator skew; pole shaping and short pitch are two combinations been investigated to understand their effects on THD level for output terminal voltages.

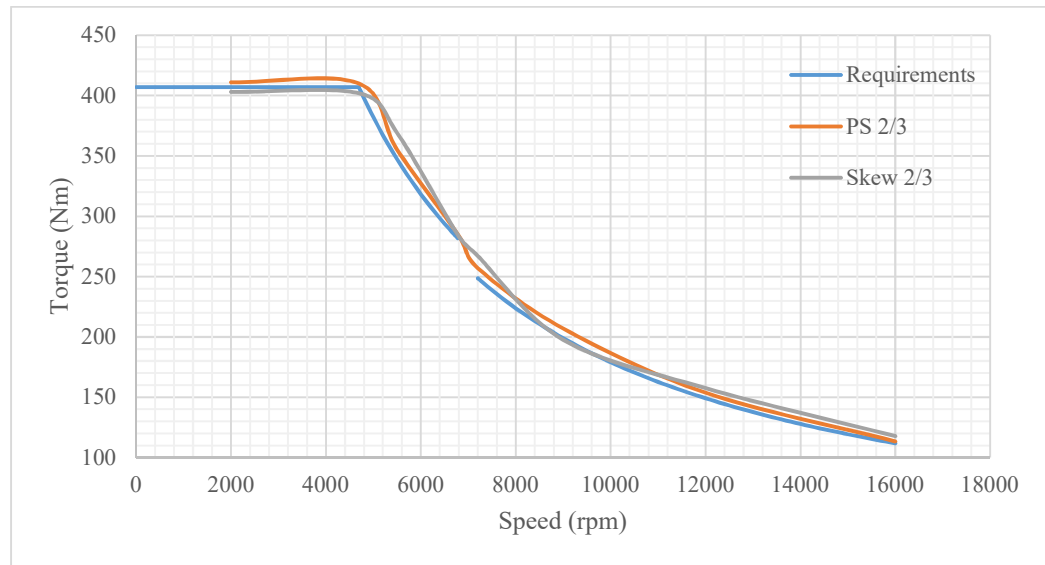


Fig. 34 Torque speed curve for two THD reduction techniques combined

Fig. 34 demonstrates the torque produced by the WFSGs modified with a combination of two THD reduction techniques. All the modified WFSGs in Fig. 34 are able to provide enough torque compared with the required torque speed map. Therefore, enough power is delivered or generated at starting and generation operating scenarios.

Fig. 35 and Fig. 36 shows the highest rotor and stator coil temperature under different operating scenarios. Under worst operating conditions, all the modified versions of WFSGs are designed to operate below 150°C . No significant advantage can be observed from hottest temperature perspective. In Fig. 37, the no-load THDs levels for WFSG options equipped with two THD reduction techniques are below 5%. A WFSG design option modified with 2/3 short pitching and skewed stator achieves the lowest no-load THD level among all the cases been simulated.

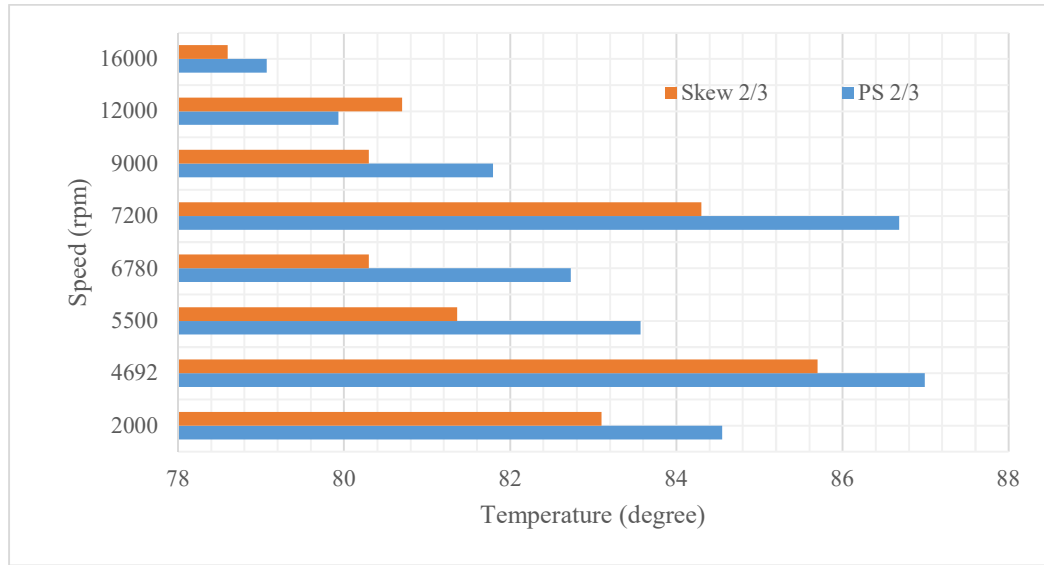


Fig. 35 Maximum stator temperature for WFSG design options with two different THD reduction techniques

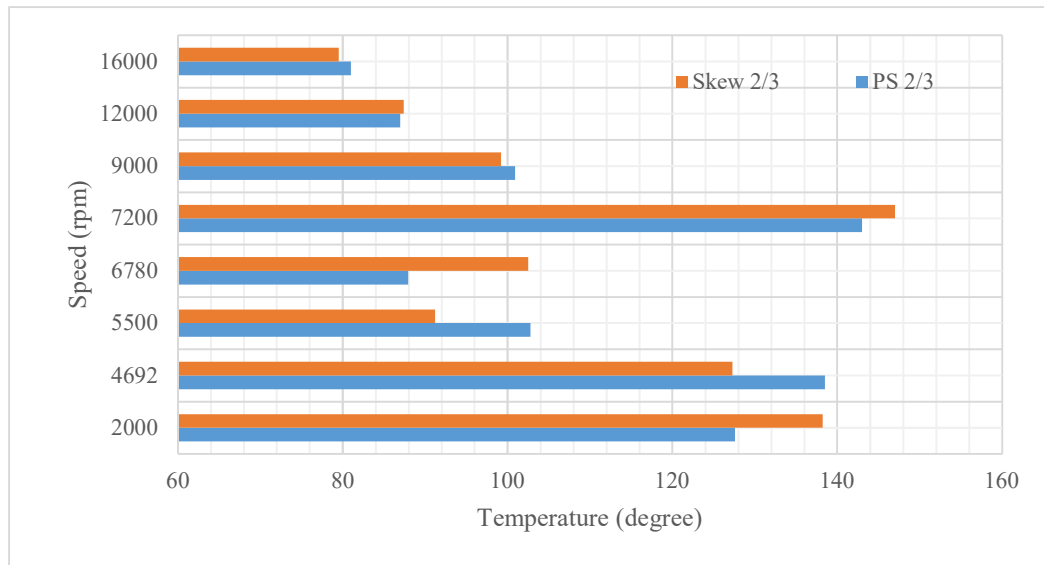


Fig. 36 Maximum rotor temperature for WFSG design options with two different THD reduction techniques

Fig. 38 depicts the THD level for full load operation with all the THD reduction techniques mentioned earlier been simulated. Although THD level at full load operating condition is not a required design objective, it gives an indication on how efficient a corresponding WFSG design option can be. Among all the design

considerations, a WFSG with $2/3$ short pitching and skewed stator core achieves the lowest THD level at full load condition. At the same time, the weight of WFSG design options 1) $2/3$ short pitching and skewed stator; 2) pole shaping and $2/3$ short pitching are 139.5 kg and 141.1 kg respectively. None of these options meets the target weight requirements.

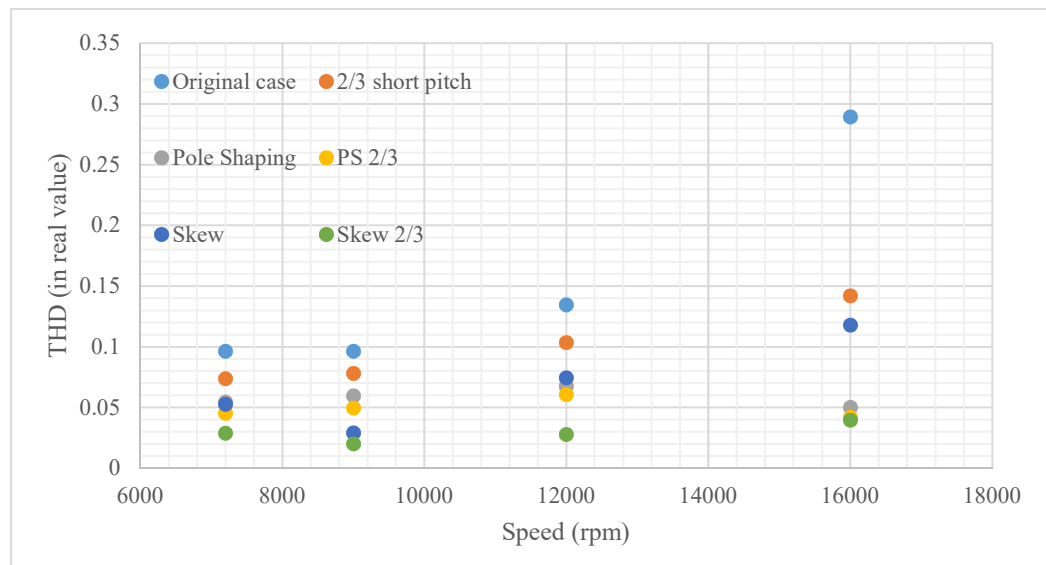


Fig. 37 Comparison of no-load THD level in real value for all the design cases been simulated

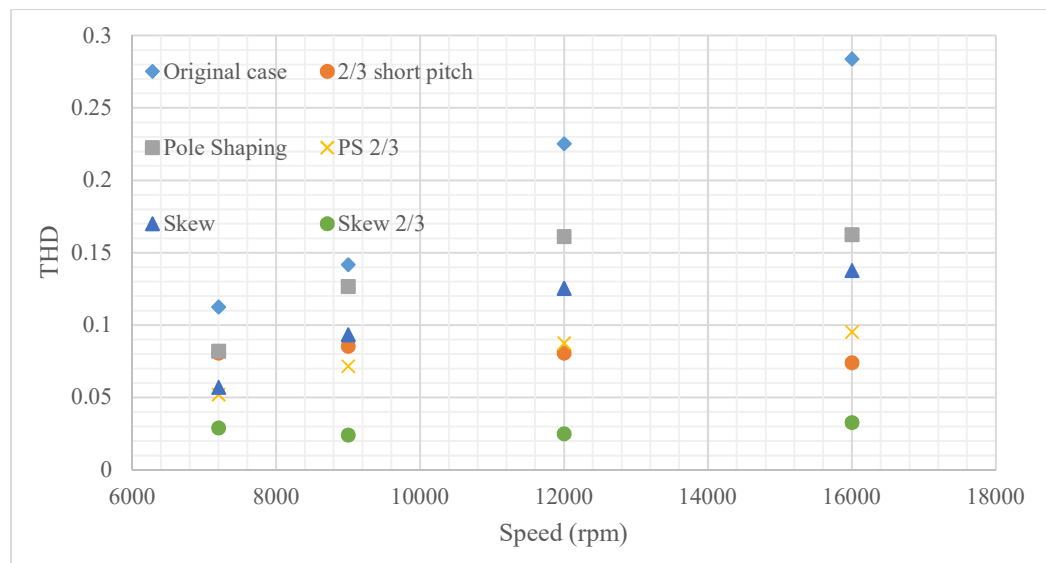


Fig. 38 Comparison of full load THD level in real value for all the design cases been simulated

4.1.3 Torque ripple consideration for WSFGs

Power quality is imperative for a WSFG as it has a direct impact on the efficiency of the power system and the functionality of the load appliances. A WSFG is often connected with a turbine or a diesel engine. Torque ripple for a WSFG needs to be minimized to suppress the vibration of the coupled system (a turbine and a generator). For a WSFG, the power quality for WSFGs is reflected on torque ripple in general. Therefore, torque ripple for WSFG design option modified with THD reduction techniques is investigated in this chapter.

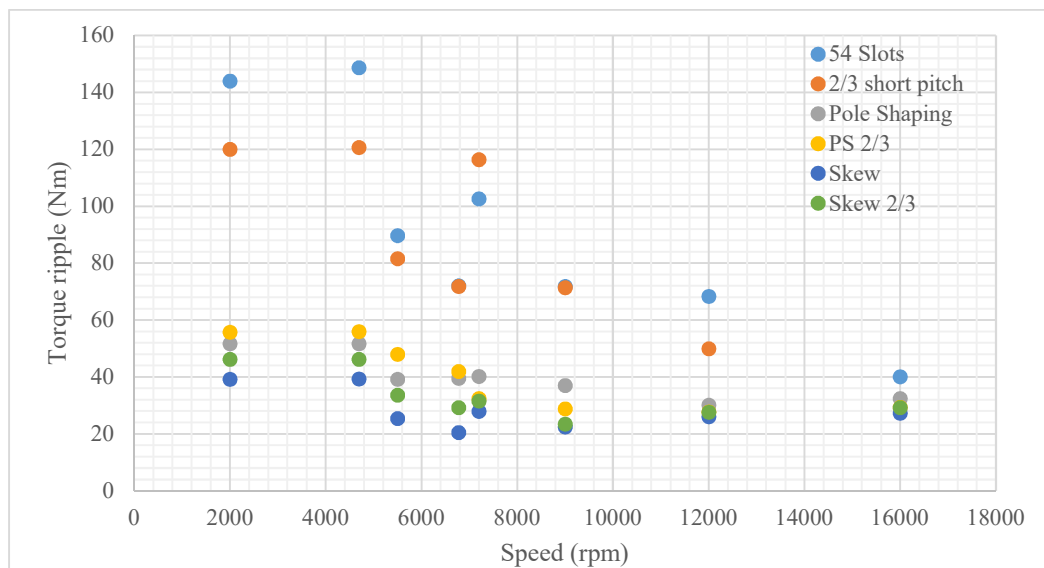


Fig. 39 Torque ripple for WSFGs design options with THD reductions techniques
 Fig. 39 presents torque ripple for WSFG design options with THD reduction techniques. Comparing Fig. 39 and Fig. 37, lower THD level for output terminal voltage generally results in lower torque ripple. A WSFG with skewed stator core achieves the lowest torque ripple value among all the design options. However, this

WFSG design option does not have its THD level below 5%. Therefore, a WFSG with 2/3 short pitching and skewed stator achieves second lowest torque ripple among all the design options and also reach THD level below 5% becomes an outstanding candidate among all the design options.

In summary, 6 pole 54 slot WFSG with 2/3 short pitching and skewed stator core achieves the minimum possible weight, the lowest torque ripple and targeted no-load THD level among all the design options. However, the active weight of the winning WFSG option is 139.5 kg that is 40% higher than the required weight. According to [40], the final weight of this generator is estimated to be 174 kg with not active parts completed such as a housing and a shaft. Under this circumstance, with a fixed cooling capability, increasing the temperature limit (change the insulation grade for copper wire) for highest coil operating point is one of the most cost-effective method to reduce machine size and weight. A WFSG is redesigned with a new temperature threshold value to reduce the weight to an accept level. Meanwhile, the outcomes for the wining THD reduction and torque ripple minimization methods can be kept for high temperature WFSGs.

4.2 Design methodologies for high speed wound field synchronous generators with high operating temperature

In chapter 4.1, the best performing WFSG candidate is a 6 pole 54 slot with 2/3 short pitching and skewed stator slots. This chapter goes directly to the best performing WFSG design option in chapter 4.1 with 220 class copper wire that is the top-grade insulated wire available in the lab. In this chapter, a new version of WFSG is designed with 220 class insulated copper wire. Therefore, the electric loadings been

selected for higher temperature wire are 30 kA/m and 50 kA/m as final coil temperatures are determined by using losses data from electromagnetic FE simulation. At initial sizing stage, those two electric loading are used to determine whether a WFSG is under or oversized.

4.2.1 Design process of a high-speed wound field synchronous generator at higher coil operating temperature

With new given electric loadings, two series of WFSGs are designed according to the process and initial design inputs as discussed in chapter 4.1.1. Meanwhile, chapter 4.1 finds out $2/3$ short pitching and one stator slot pitch skewing can results in the best performance in terms of power quality and torque ripple. Therefore, this chapter ignores the full WFSG design procedures in chapter 4.1 to find the best pole slot combinations, stator winding and stator slot configurations.

The first series of WFSGs designed with high temperature coils are generator with 30 kA/m . Critical temperature behaviour of high coil temperature WFSGs are designed using an OOD tool validated in chapter 3. Fig. 40 demonstrates the maximum stator coil temperature during starting operation. More stator slots help reduce the maximum stator coil temperature for a given design geometry that complies with the outcome in chapter 4.1. The maximum stator coil temperature is $167 \text{ }^\circ\text{C}$ under $4,692 \text{ rpm}$ (worst case operating scenario during starting) which is still way less than $220 \text{ }^\circ\text{C}$. Fig. 41 illustrates the maximum coil temperature during generating operation. A similar trend between maximum stator coil temperature and the number of slots can be found in Fig. 41. From stator coil temperature perspective,

the maximum coil temperature does not hit 220 °C and there is still room for generator performance improvements from stator side.

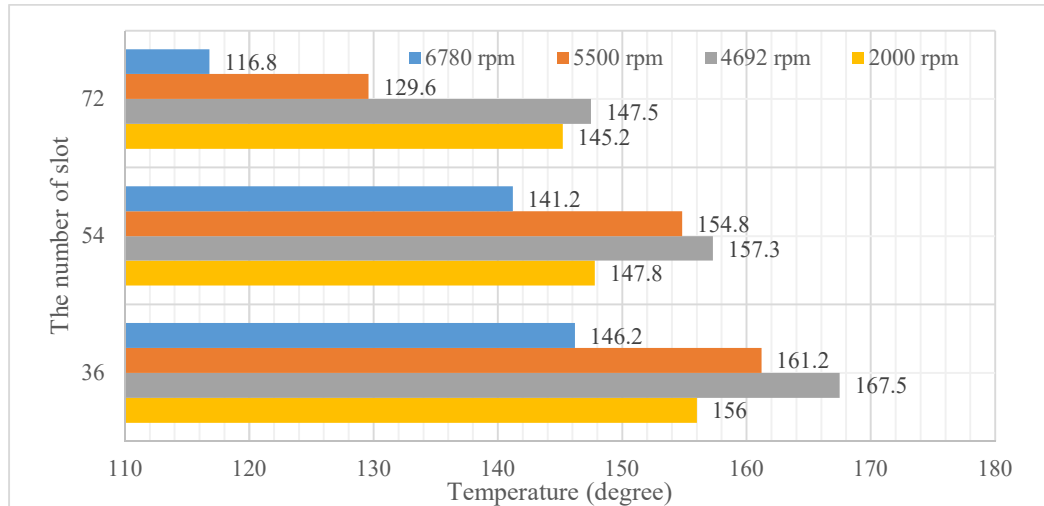


Fig. 40 Stator coil temperature of a WFSG with an electric loading of 30 kA/m during starting operation

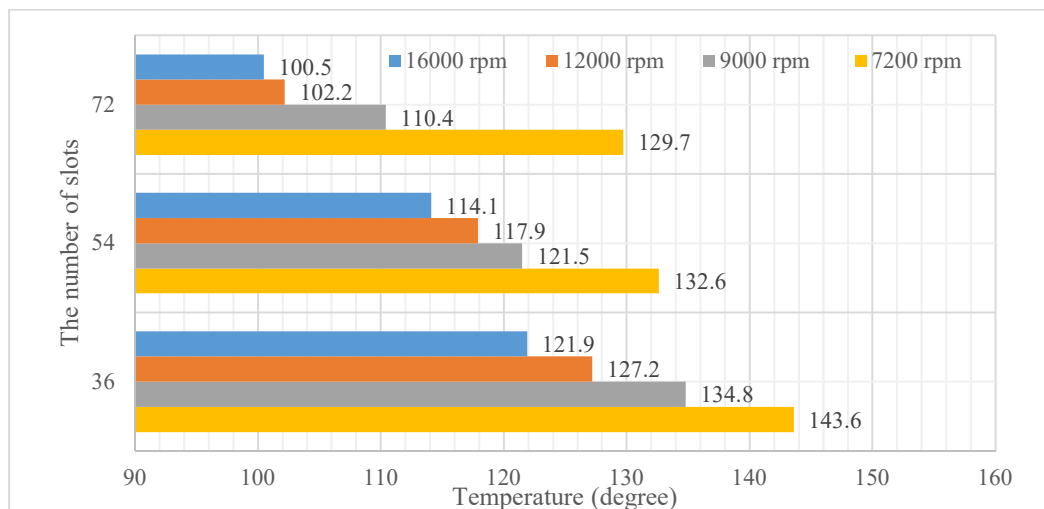


Fig. 41 Stator coil temperature of a WFSG with an electric loading of 30 kA/m during generation operation

Maximum rotor coil temperature is also analysed and the temperature results are shown in Fig. 42 and Fig. 43. The maximum rotor coil temperature during starting process hits almost 210 °C. The maximum rotor coil temperature during generation

is close to 170 °C. Regardless of the pole slot combination, the maximum rotor coils temperature does not hit the threshold value (220 °C) for the insulation materials. Therefore, by summarizing both rotor and stator temperature analysis, the weight and size of a WFSG can be further reduced by further increasing the electric loading for a WFSG. A series of WFSGs with 50 kA/m is presented in the next sector.

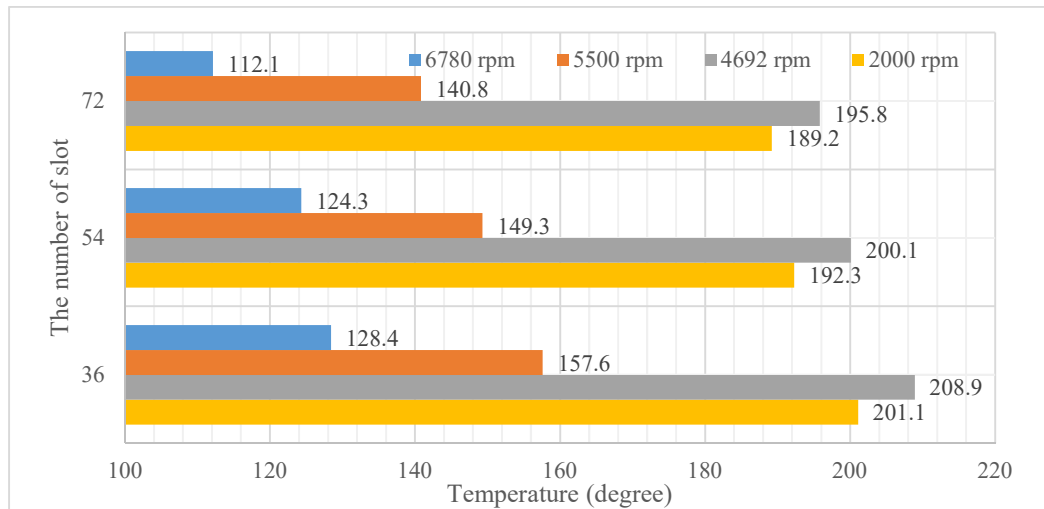


Fig. 42 Rotor coil temperature of a WFSG with an electric loading of 30 kA/m during starting operation

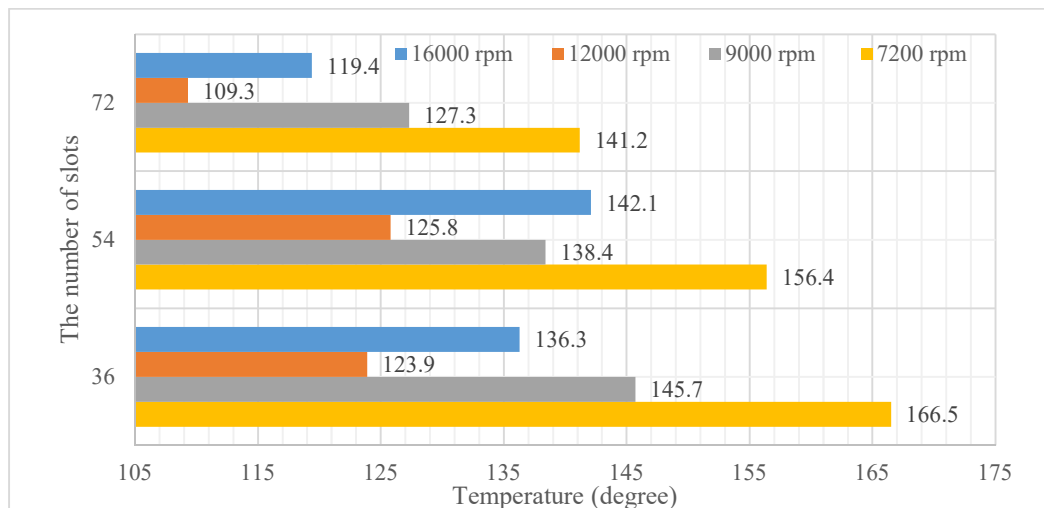


Fig. 43 Rotor coil temperature of a WFSG with an electric loading of 30 kA/m during generation operation

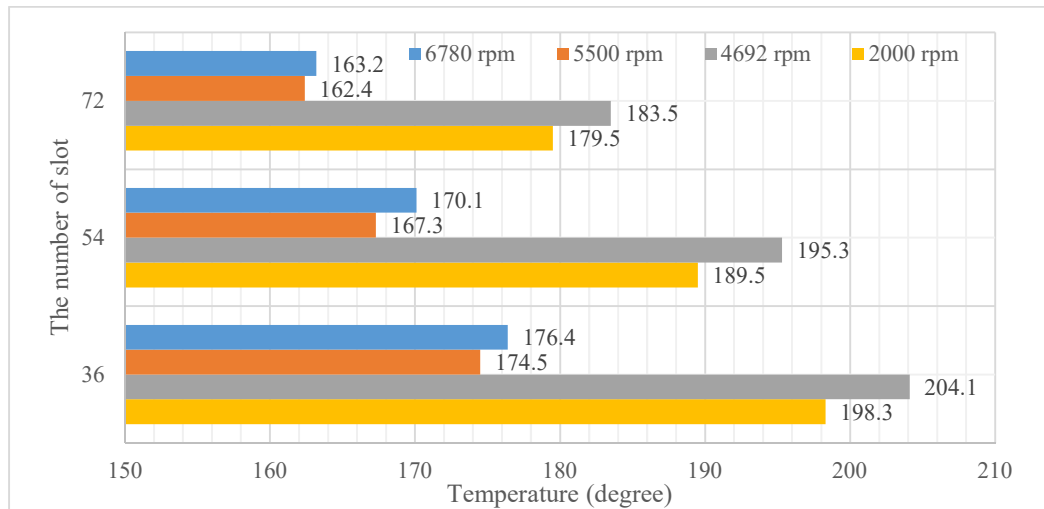


Fig. 44 Stator coil temperature of a WFSG with an electric loading of 50 kA/m during starting operation

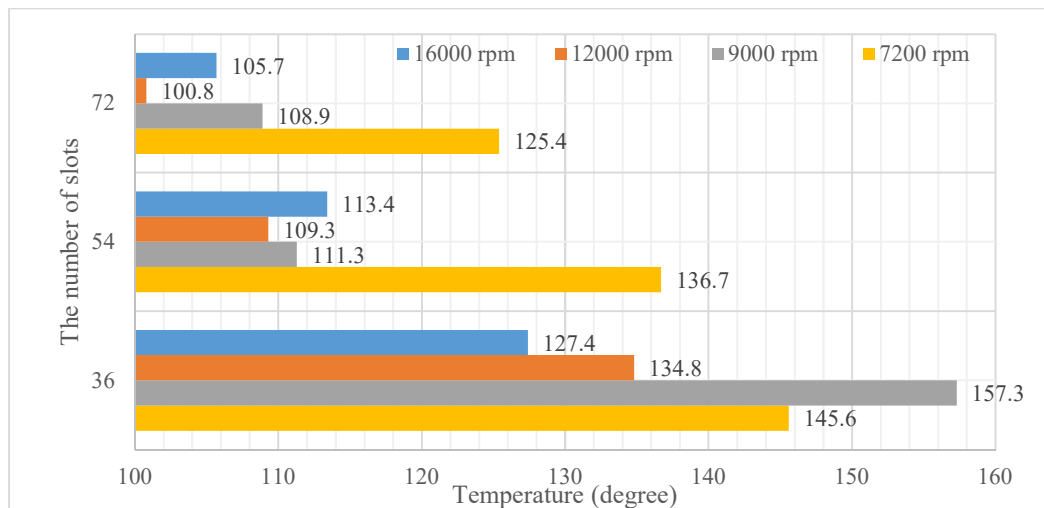


Fig. 45 Stator coil temperature of a WFSG with an electric loading of 50 kA/m during generation operation

This sector presents the temperature analysis of a series of WFSGs with 50 kA/m linear current density (electric loading). Fig. 44 and Fig. 45 presents the maximum stator coil temperature of during starting and generation conditions. With an increase of the number of stator slots, the coil temperature decreases in general. The maximum stator coil temperature ($204 \text{ }^\circ\text{C}$) during starting period almost hits the coil insulation threshold value ($220 \text{ }^\circ\text{C}$). Therefore, from the stator perspective, the room

for performance improvements is very limited since a safety margin should be left to ensure the safe operation of the first prototype.

Fig. 46 and Fig. 47 presents the maximum rotor coil temperature for generator working at starting and generation condition. The maximum rotor coil temperature during starting operation is the 223 °C. This temperature is over 220 °C threshold value but 3 °C is not a big concern for the lifetime for the insulation materials. The more number of slots still results in less maximum coil temperature in general based on information in Fig. 46 and Fig. 47. However, in Fig. 47, the maximum rotor coil temperature for 54 slots configuration is low than the other slot configuration for most operating speeds. This result is the same as the one found in chapter 4.1.1. Based on the outcomes in chapter 4.1.1, it is conclude that the 6 pole 54 slot configuration is still the best option to choose.

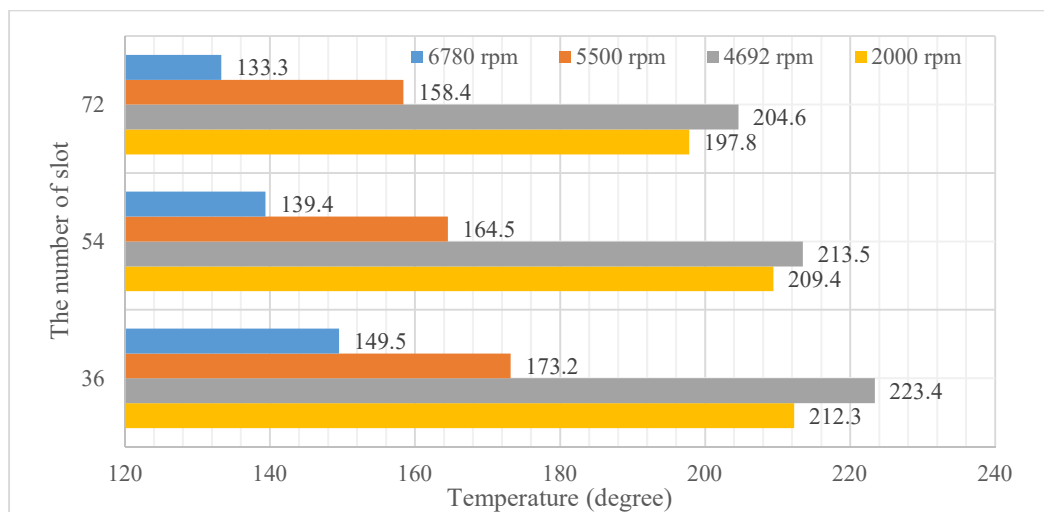


Fig. 46 Rotor coil temperature of a WFSG with an electric loading of 50 kA/m during starting operation

With pole slot combination settled, Fig. 48 depicts the torque production of WFSGs designed with high temperature coils and 54 stator slots. Compared with the required

torque speed profile, the high temperature 54 slots WFSG achieved the targeted torque production. Apart from the delivered average torque, torque ripple is also critical for a WFSG during starting operating scenario. During generation condition of a WFSG, minimizing torque ripple can help reducing unnecessary harmful vibration and noise.

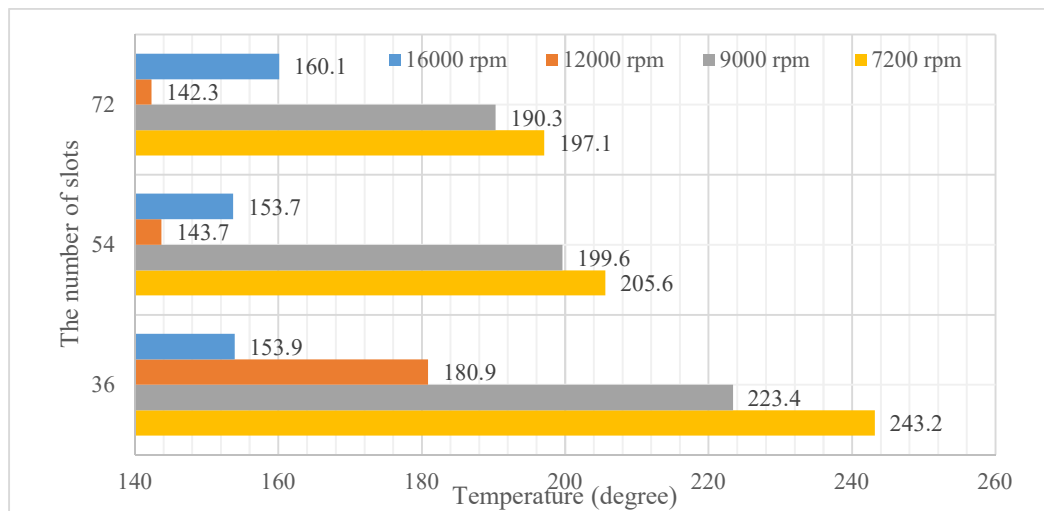


Fig. 47 Rotor coil temperature of a WFSG with an electric loading of 50 kA/m during generation operation

In chapter 4.1, it is concluded that a WFSG designed with skewed stator and short pitch winding achieve the best performance in terms of torque ripple production.

Fig. 49 presents the torque ripple for various operating speeds for a generator been designed. The resultant torque ripple and its percentage value is similar to Fig. 39. Although the percentage value for torque ripple at high speed region increase, this is due to the reduced fundamental average torque.

The active weight of different parts of a WFSG designed are listed in Table 11. The overall active weight is 80.2 kg . The overall weight requirement in chapter 1 is

around 100 kg. Thus, there is still a small margin left for non-active part for a generator.

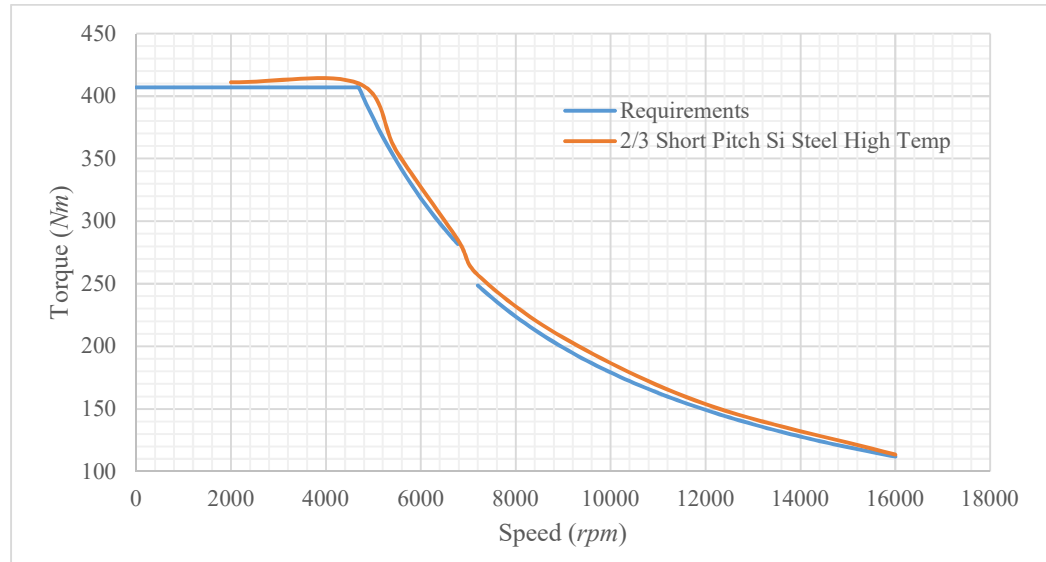


Fig. 48 Torque speed curve for WFSGs design with high temperature with 54 stator slots

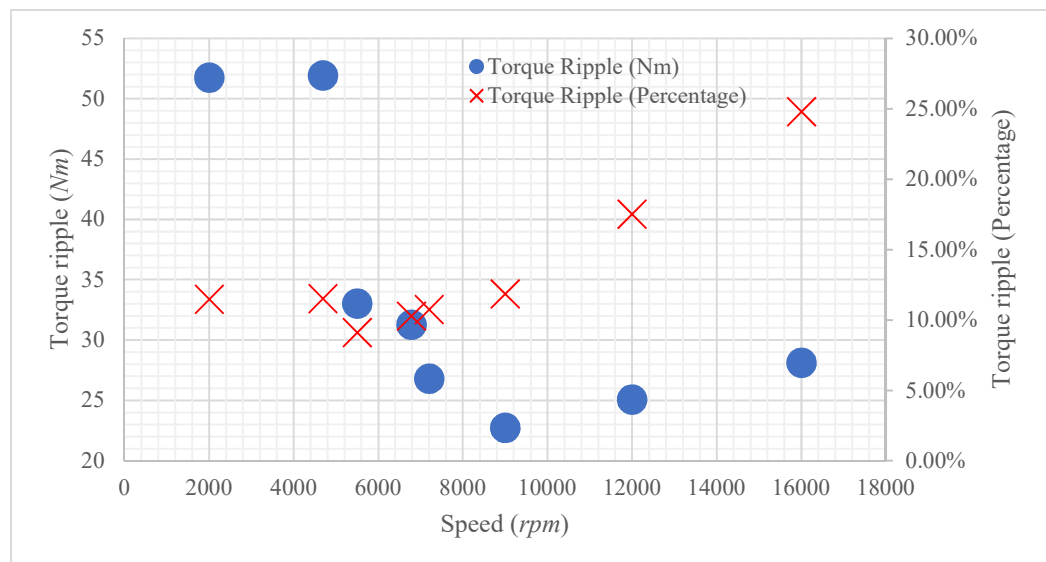


Fig. 49 Torque ripple for a high temperature 54 slot WFSG

Table 11 Active weight of the different parts of the WFSG designed

	Rotor pole	Rotor winding	Stator core	Stator winding	Overall
Unit (kg)	27.6	6.2	34.4	12	80.2

4.2.2 Losses consideration for a high speed wound filed synchronous generator

Chapter 4.2.1 has settled the 6 pole 54 slot WFSG with 2/3 short pitching and stator skew as the final design operation. For a variable high speed WFSG, the high frequency losses are an essential perspective. This chapter focuses on how high frequency losses are induced and how to tackle with high frequency losses.

The frequency of the output terminal voltage is 360 Hz to 800 Hz that is way higher than the 50 Hz conventional WFSG. Therefore, high frequency associated losses such as eddy current loss, hysteresis loss and ac copper loss rises significantly. Eddy current losses in the iron core are due to electric field induced by constantly varying magnetic field. According to equation (27) [106], eddy current loss is proportional to the volume of the lamination (V), the operating frequency (f^2), the thickness lamination (d^2) the peak flux density (\hat{B}_m^2). Thus, constants k_{eddy} is used to correct the loss calculation, which is determined by the empirical loss measurements under true machine operating scenarios.

$$P_{Fe} = \frac{k_{eddy} V \pi^2 f^2 d^2 \hat{B}_m^2}{6\rho} \quad (27)$$

Hysteresis loss are caused by the movements of magnetic domain due to the changing magnetic field. Equation (28) [106] characterize the analytical analysis of loss in an iron core. In equation (28), hysteresis loss is proportional to operating frequency (f), mass of the laminations (m_{Fe}) and summation of core flux density of all harmonics ($B_{tan,n}^2 + B_{norm,n}^2$). $B_{tan,n}$ and $B_{norm,n}$ are flux density values in the

tangential and normal direction respectively. However, this analytical equation deviates from experimental measurements. Therefore, a constant c_{Hy} is used to tune the loss calculation as close to the experimental measurements as possible.

$$P_{Fe} = c_{Hy} \frac{f}{100} m_{Fe} \sum_{n=1}^{\infty} n^2 (B_{tan,n}^2 + B_{norm,n}^2) \quad (28)$$

Eddy current and hysteresis loss are intricate electromagnetic phenomenon in iron cores during machine operations. These two types of losses categorized as iron loss are not easily spreadable during experimental measurements. Effective methods to reduce high frequency iron losses is reducing the thickness of the laminated materials or choose the low loss materials such as JNEX900. With core materials determined for this thesis, the iron losses for this WFSG been designed do not have room to be reduced.



Fig. 50 Shaped compacted litz wire

Copper loss is also increased dramatically due to high fundamental frequency and associated high frequency harmonics if the layout of windings is not properly twisted or selected [106]. Skin effects due to high frequency currents are the root reasons for the increase of copper losses. Litz wire can effectively reduce the skin effects as multiple strands are bundled together. Apart from the advantages of

reduced copper losses, litz wire also offers consistent equivalent thermal conductivities for preformed wires ranging from 0.99 W/m²K to 2.1 W/m²K [118]. Litz wire is pre-formed wire with a fixed shape as shown in Fig. 50. This requires the shape and dimensions of a stator slot been designed according to the size of litz wire. Connecting terminals of a litz wire is also a challenging job as insulation materials have to be removed from multiple thin wire strands forming a single wire. As a result, round single strand wires are considered for this high speed WFSG. Considering the role of skin effects, the diameter of round wires is chosen according to equation (29). In equation (29), δ_{depth} is the radius of a conductor; ρ is the resistivity of the material; f_0 is the frequency of signal passing through a conductor; μ_r is the relative permeability of a conductor; μ_0 is the permeability of free space.

$$\delta_{depth} = \sqrt{\frac{\rho}{\pi f_0 \mu_0 \mu_r}} \quad (29)$$

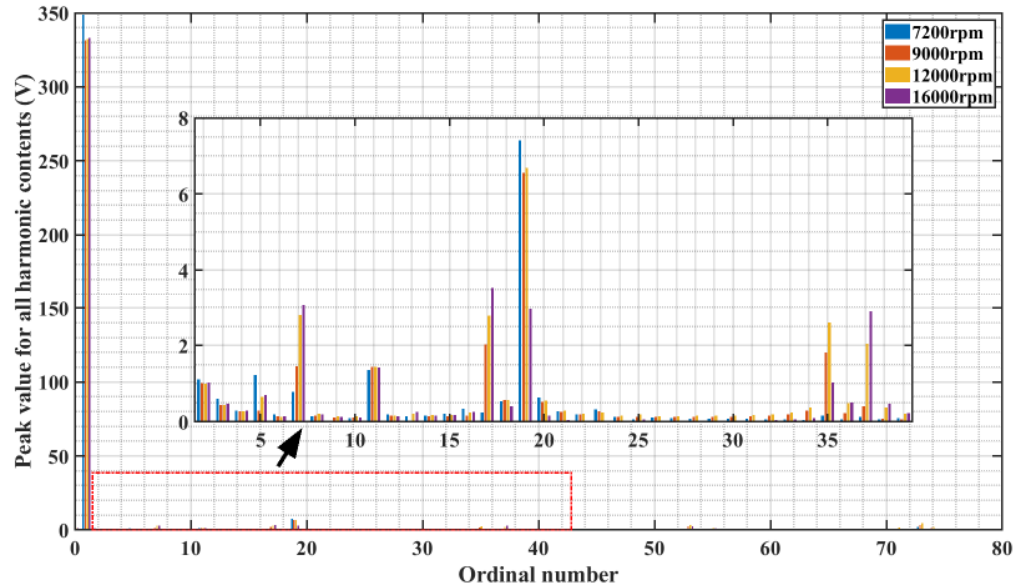


Fig. 51 No load harmonic content for a high temperature WFSG design option for 2/3 short pitch stator winding and a skew process of one slot pitch

Fig. 51 presents the harmonic contents of the no-load output terminal voltages at four different operating speed. Theoretically, $3n$ and $18n \pm 1$ (n is integer) high frequency harmonics are suppressed by $2/3$ short pitching and skew stator slot techniques. Nevertheless, the THD for a WFSG with performance shown in Fig. 51 is 2.6%. Harmonic contents for 7th, 11th, 17th, 19th, 35th and 37th harmonics are still observable compared with the fundamental content. Skewed one stator slot pitch is performed as the method introduced in [83]. Therefore, the penetration depth (skin depth) of round copper wires is calculated to accommodate seventh and eleventh harmonic contents without wasting copper area. Based on equation (29), the frequency of eleventh harmonic is 8.8 kHz. The skin depth is 0.88 mm resulting a theoretical wire diameter of 1.76 mm. Any wire diameter below 1.76 mm is a suitable candidate for stator wires. Considering the difficulty of wire assembly, wire gauge in stock from suppliers and the amount of budget, 0.9 mm, 220 °C copper wire supplied by Essex is chosen for this application. 0.9 mm of copper wire are able to address most of the harmonic contents, and thus, the AC losses in stator windings are suppressed dramatically.

In chapter 4.1.1, the stator winding losses results are simulated under conditions that stator coils are modelled as stranded wires. This means no skin effects are considered in the simulation. The selection of copper wires utilizing skin depth equation has minimized the AC loss drastically. Therefore, the stranded wire modelled in electromagnetic FE simulation reflects the practical situation.



Fig. 52 Cross sectional view of commercial WFSGs implemented on aircraft

Rotor coils dimensions are also critical for a WFSG. Both round wires and rectangular shaped wires are seen from industry partners shown in Fig. 52. Unlike solid metallic components designed for a WFSG assembly, the stiffness of wounded coils on the rotor is not easily determinable. This raise challenges for simulating the effects of coils on the rotor structures designed to constrain rotor coils. Two possible assumptions are possible to simplify the simulation; 1) assuming wounded coils are pointed mass been applied on a surface; 2) assuming wounded coils are solid copper piece. Rectangular shaped wires are considered to be more suitable for high speed applications as rectangular shaped wire are easy to be wounded in a uniformed rectangular manner. This potentially help the rotor coils to be tightened in a way that is mechanically more rigid. However, rectangular wire is hard to be bent and forming a right angle while winding a rotor pole can easily damage the insulation materials coated on bare copper wires.

During the assembly process of a WFSG, round wires are more versatile winding stator and rotor coils compared with rectangular wires. If rectangular wires are adopted, stator slots and rotor shape have to be designed complying with the shape of the rectangular wires. Therefore, commercially available rectangular wires have to be chosen during the electromagnetic sizing process. Customizing the dimensions of the wires are possible from Essex, but significant amount of investment is required as rectangular wires are made from customized mold. For a PhD prototype, this option is no longer considered. For majority medium sized commercial WFSGs, round wire are still commonly seen for rotor pole windings.

As round wires are determined to be the option for rotor coils, the number of turns and wire diameter are determined for the next stage. High frequency magnetic fields also exist near the air gap. Parasitic effects induced by those high frequency fields are neglected. Theoretically, only a small number of turns of rotor copper wires are influenced by those traveling magnetic fields. Only DC currents are passing through those wire, and thus, skin effects caused by DC currents are null. Apart from taking skin and parasitic effects into account, the influences from other components on the field winding design of a three stage WFSG should be investigated.

In electromagnetic FE simulation, field windings are fed by DC currents source which represents the ideal case. In Fig. 5, AC currents from an exciter are rectified by rotating diodes and then feeds the field coils. There are always be some DC ripples presented in the DC currents contents. The electromagnetic fields established by fluctuating field currents have negative effects on the power quality of the output

terminals voltages. Therefore, the DC currents feeding into the field coils has to be as smooth as possible.

Conventionally, DC side after the rectification has DC link capacitors to smooth the output voltage waveforms. However, soldering capacitors on a fast rotating body with limited space is a very difficult job to achieve. No industry WFSG found in this thesis installs DC link capacitors on a rotating shaft. Consequently, the smoothness of the DC currents feeding into field coils are determined by the inductance and resistance of the field coils itself. PLECS is used to simulate the ripple of the simple rotor rectifying circuits shown in Fig. 53.

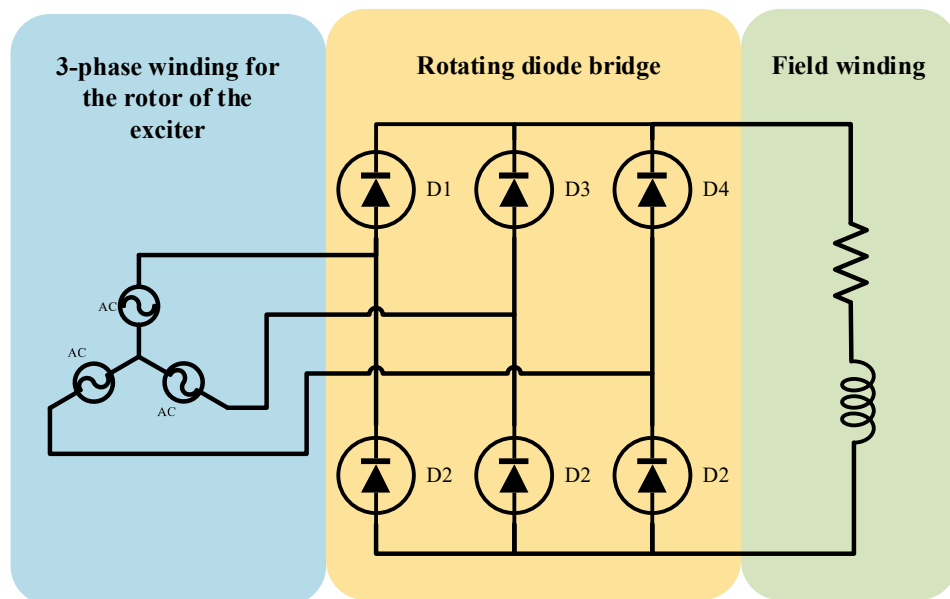


Fig. 53 Rectification circuit on the rotor

Fig. 53 demonstrates the rotor circuit setup modelling rotor phenomenon in PLECS.

Fig. 54 depicts the current ripple versus the inductance on the load side. The higher the load inductance is, the smoother the DC current in the load circuit is. The inductance of a coil is calculated by equation (30).

$$L = N^2 \lambda \quad (30)$$

In equation (30), the inductance of the coil is proportional to the number of turns (N^2) and the permeance (λ) of a complete magnetic circuit. The permeance of a complete magnetic circuit is determined by the size of a generator and the saturation level on each point of a complete magnetic circuit. There is not much to be changed once the geometry of a generator is finalized. Therefore, high number of turns for the field coils is a preferable choice for a WFSG to have high rotor coil inductance. Therefore, both rotor and stator coils are determined to be wounded by 0.9 mm round wire to simplify the manufacturing and procurement procedures.

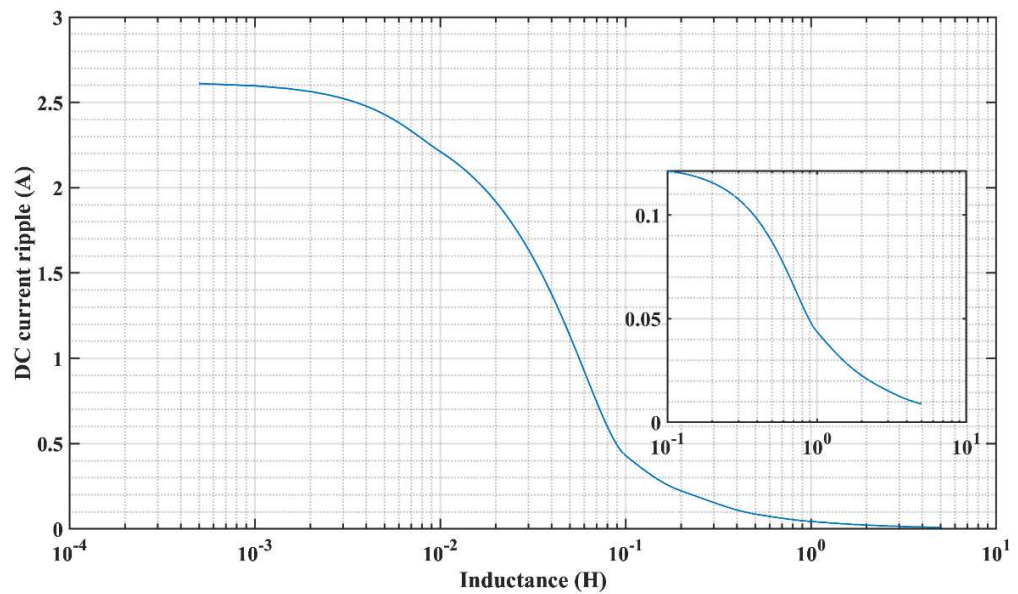


Fig. 54 DC current ripple after a six pulse rectifier with different load inductance

The WFSG geometry finalized at this stage has taken 180 m/s as the reference peripheral speed as a mechanical constraint at analytical WFSG sizing stage. This geometry of a WFSG achieved is passed to chapter 5 for mechanical analysis. However, how does the diameter to length ratio of a rotor core affect the weight, efficiency and other performance of a WFSG is unknown. One of the key aims for

this thesis is to reduce the weight of a WFSG as much as possible. Therefore, chapter 4.2.3 analyses the influence of the diameter to length ratio of a rotor core on the performance of the machine without the mechanical constraint.

4.2.3 Investigation of effects of length to radius ratio for wound field synchronous generators on maximum copper coil temperature

Chapter 4.2 concludes the methodologies for designing and analysing high speed WFSGs operated at high coil temperature condition. A finalized design has been passed to chapter 5 for mechanical analysis – 180 *m/s*. Although the core material for this thesis has been limited to M235-35A, this does not limit future WFSGs been designed with higher grade materials such as CoFe or 35HXT780T. The length to diameter (L2D) ratio of a rotor core that is a critical factor in design process in chapter 4.1.1 and 4.2.1. This chapter focuses on analysing the influence of a L2D ratio on the performance (mainly power density) of the machine without the mechanical constraint.

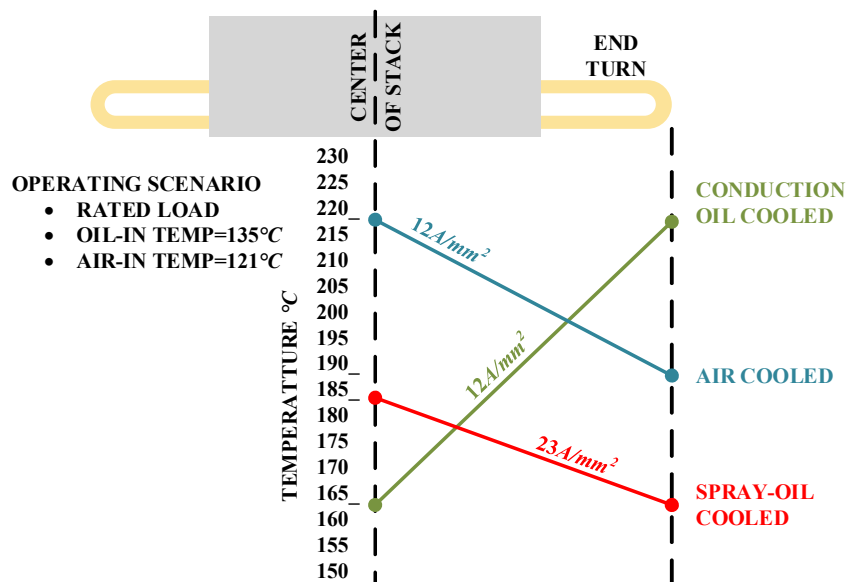


Fig. 55 Generator stator temperature (typical value)

Fig. 55 presents the temperature profile of a WFSG through the axial length based on literature [1] with an oil and air inlet temperature of 135 °C and 121 °C respectively. The temperature distributions inside stator coils are illustrated as blue, green and red solid lines for different cooling methodologies. The most effective cooling method is spray-oil cooling method. Regardless of the shape of the cooling channels, coolants for oil conduction and air cooling moves in an axial direction. Hot spots temperature follows a gradient line from the centre of a generator to the end windings. Therefore, the properties of coolants do affect the maximum stator temperature inside coils and the axial length does play a role in the gradient of the stator coil temperature profile. To understand the effect of axial length on the maximum temperature inside coils of a WFSG, the L2D ratio (a critical design parameter) is investigated. The analysis is performed while keeping all the WFSG design options with the same power rating and HTCs. The mechanical constraints of rotor core materials is not considered for WFSG designed in this chapter. A 6 pole 54 slots WFSG configuration is chosen to be the pole slot combination for the investigation of this chapter.

Since the main objective is to understand the maximum temperature profile of a given WFSG, temperature analysis while a generator operates at 7,200 *rpm* is adequate. Based on analysis in chapter 4.1.1 and 4.2.1, a WFSG operates at 7,200 *rpm* always results in the highest stator and rotor coil temperature during power generation mode. Starting process is a short time duty process that only counts for 120 seconds of the operating time. Therefore, the performance during power generation has a much bigger impacts on determination of generator size, weight and efficiency.

Fig. 56 presents the maximum temperature of stator and rotor coils of WFSGs with different L2D ratio on x-axes simulated under worst case operating scenarios. However, the connection between maximum coil temperature and the L2D ratio of a WFSG is not straight forward in Fig. 56. A descending trend of worst coil temperature with respect to an increase of L2D ratio can be observed in Fig. 56 for both stator and rotor. The hottest stator coil temperature for WFSGs with L2D ratios ranging from 0.7 to 1.3 are similar at 160 °C range. However, a sudden rotor maximum temperature jump occurs at the L2D ratio changing from 0.8 to 0.9. The maximum rotor coil temperature jumps from 232.4 °C to 199.1 °C.

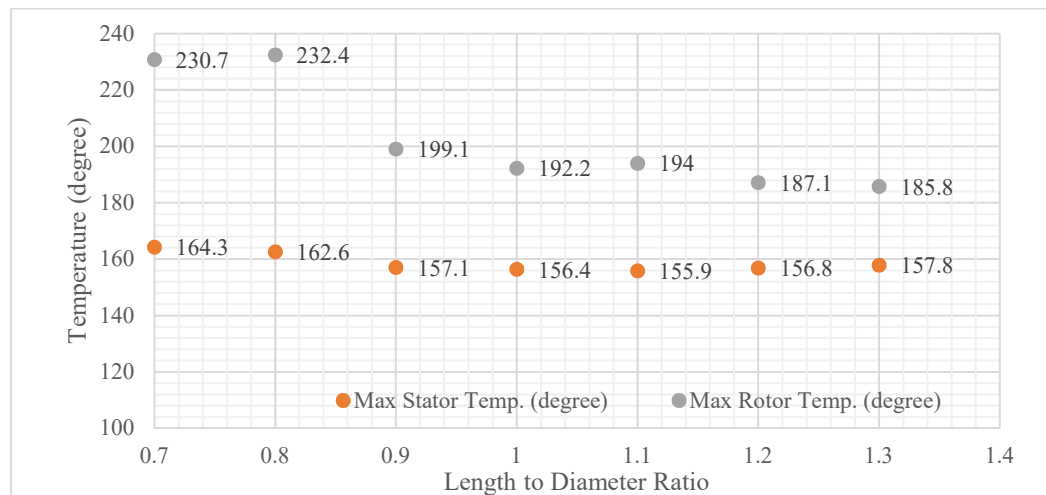


Fig. 56 Maximum stator and rotor temperature for WFSGs designed with different length to diameter ratio

Fig. 57 presents the weight of each individual component and overall active weight. With L2D ratios ranging from 1.2 to 0.9, the weight of the stator and rotor core material slightly increased by 2 kg. The weight for stator and rotor winding also increases with L2D ratios ranging from 1.3 to 0.9. The armature and field winding weight remains almost the same with the change of L2D ratio. The overall weight

of a WFSG is increased by 2.6 kg while the L2D ratio decrease from 1.3 to 0.9. An interesting aspect observed from Fig. 57 is that the overall weight of a WFSG decrease by 12% when the L2D ratio jumped from 0.9 to 0.8. In contrast, the overall weight for a WFSG increases from 68.8 kg to 70.9 kg while the L2D ratio drops from 0.8 to 0.7. Therefore, a general trend can be drawn at this stage is that the overall weight of a WFSG increases slightly with a decrease of L2D ratio. Once a magic L2D ratio is reached, the decrease of L2D ratio results in a sharp decrease of the overall weight of a WFSG.

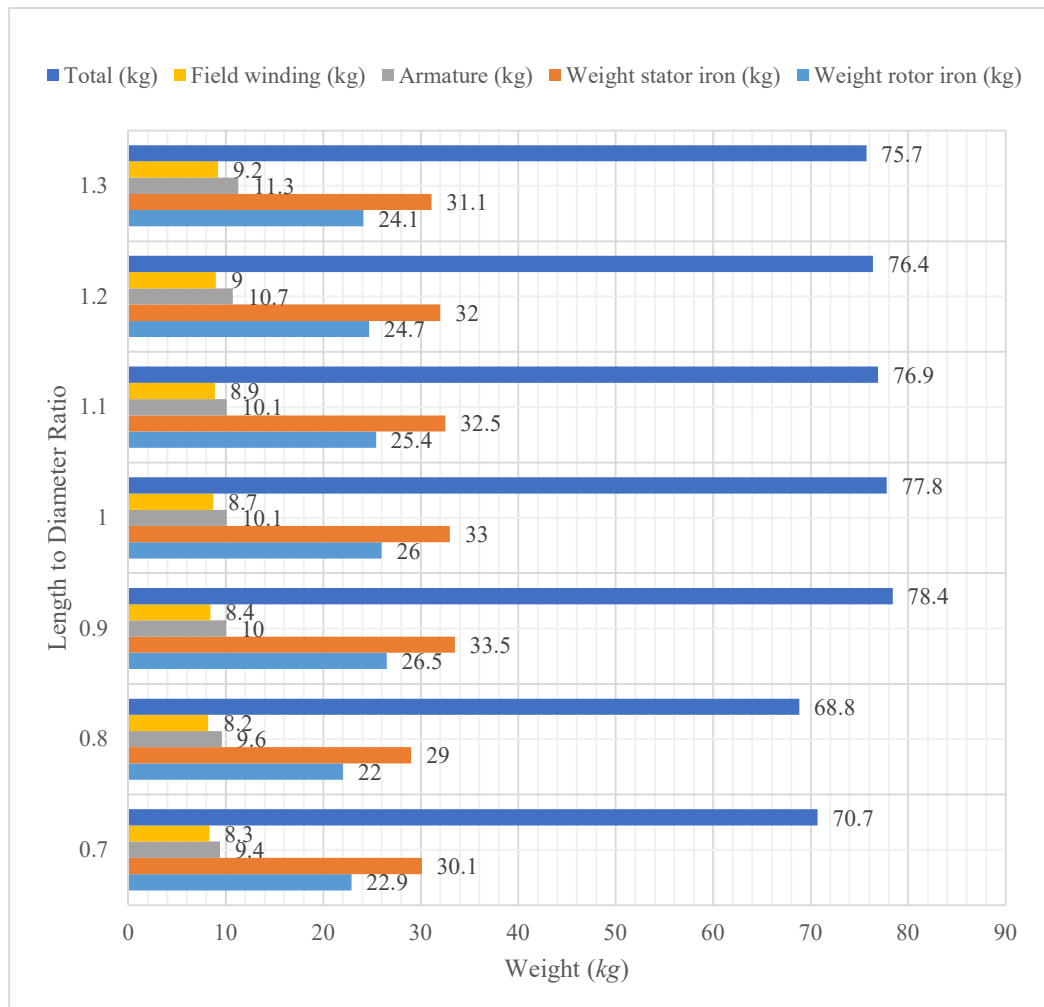


Fig. 57 Weight information for individual WFSGs designed with different L2D ratio

Although a general conclusion of the connection between L2D ratio and the weight of a WFSG can be found from information presented in Fig. 56 and Fig. 57, the fundamental change occurs inside a WFSG while the L2D ratio changes from 0.9 to 0.8 is still not clear. Further investigations are still needed. WFSGs designed and presented in Fig. 56 are kept with the same power rating and cooling capability. To achieve this, the flux linkage for stator coils proportional to rotor surface areas and the air gap flux density is kept at a point that guarantees the output terminal voltage is 235 *Vac*. Since the rotor surface areas are different for L2D ratio from 0.7 to 1.3, the peak flux density in the air gap is not the same as shown in Table 12 for different L2D ratios. Although the peak flux density in the air gap is different, the peak flux density is kept as close to 0.8 *T* as possible during design process also shown in Table 12. The reason for such design considerations is due to the fact that the peak air gap flux density affects the dimensions of stator and rotor cores. If not, the investigation of the effects of L2D ratio on the weight of a WFSG is affected by another variable apart from L2D ratio.

Table 12 Key parameters for WFSGs designed in Fig. 56

Length to Diameter Ratio	Efficiency	Peak Air Gap Flux Density (<i>T</i>)	N Phase	Axial Length (<i>mm</i>)	Rotor Outer Diameter (<i>mm</i>)
0.7	92%	0.82	6	153.4	219.2
0.8	92%	0.79	6	167.7	209.6
0.9	90%	0.85	5	185.6	206.2
1.0	91%	0.81	5	201.5	201.5
1.1	91%	0.79	5	214.7	195.2
1.2	92%	0.79	5	223.1	185.9
1.3	91%	0.80	5	231.8	178.3

In Table 12, reducing the L2D ratio from 1.3 to 0.9 does not have a significant impact on the overall weight of a WFSG as the number of turns of stator coils remains the same. The reasons for the slight increase of overall generator weight are as follows. 1) The current density of rotor and stator coils remains the same for all the WFSG design options in chapter 4.2.3. As a generator increases its diameter, the rotor winding slightly varies due to the slightly varied magnetic circuit. This results in similar armature and field winding weight presented in Fig. 57. 2) The high speed machine often results in a low number of turns in stator coils. The analytical script for designing a WFSG proposed in chapter 3 automatically regulates the number of turns of stator coils an integer value. If the change of rotor surface area at each L2D ratio (1.3 – 0.9) cannot lead to the different number of turns, the analytical sizing script regulates the rotor volume to similar values for different L2D ratios. As a result, the rotor and stator core weight remains similar.

In Table 12, the reason for the drastic change in terms of the weight of a WFSG is the abrupt alteration of the number of turns of stator coils from 5 to 6 when the L2D ratio varies from 0.9 to 0.8. While the L2D ratio is at a point where the new number of turns of stator coils is achieved, the rotor volume is substantially reduced in the analytical script to keep the power rating of a WFSG the same.

In conclusion, L2D ratio does affects the overall weight of a WFSG. This is valid while the change of L2D ratio can results in the different number of turns of stator coils. If a new L2D ratio results in the different number of stator turns compared with that of an old L2D ratio, smaller L2D ratio results in a lighter WFSG. In other words, a WFSG with larger diameter results in lower weight. However, this

conclusion is partially correct. The main reasons are as follows. The hottest temperature spots presented in Fig. 56 in the rotor coil when the L2D ratios are between 0.9 – 1.3 have a big margin to improve compared with hot rotor temperature spots while L2D ratios are 0.7 and 0.8. A significant temperature jump can be observed when L2D ratios varies from 0.9 to 0.8. To generalize the conclusion above, the hottest rotor and stator temperature should be kept the same or at least similar level at each L2D ratio presented in Table 12. In Fig. 56, maximum stator temperature is kept similar but not the maximum rotor temperature. The issue lies within the maximum rotor coil temperature. Re-designing the entire WFSG from scratch can potentially altering the stator temperature to a different one compared with the cases in Fig. 56. Therefore, increasing the current density of the field winding becomes a viable option to boost the rotor temperature without altering L2D ratio and the stator temperature in a significant way. Table 13 presents the axial length and rotor outer diameter which are not changed compared with Table 12. The magnetic loading are kept similar to those been presented in Table 12 to ensure field current density of a WFSG is the only parameter that is been changed.

Fig. 58 presents the maximum stator and rotor coil temperature of WFSGs with rotor coil field current density increased are marked with (▲) and field current density remain the old value as Fig. 56 are marked with (●). The temperature data labelled above the marker (▲) represents the results obtained for increased field current density cases. The temperature data labelled on the right hand side of the marker (●) represents the results obtained with field current density cases presented in Fig. 56. In Fig. 58, the maximum stator coil temperature remains similar compared with Fig.

56. The maximum rotor temperature in Fig. 58 are all around 230 °C. In this case, a relatively fair comparison can be performed to obtain the connection of L2D ratios and the overall active weight of a WFSG.

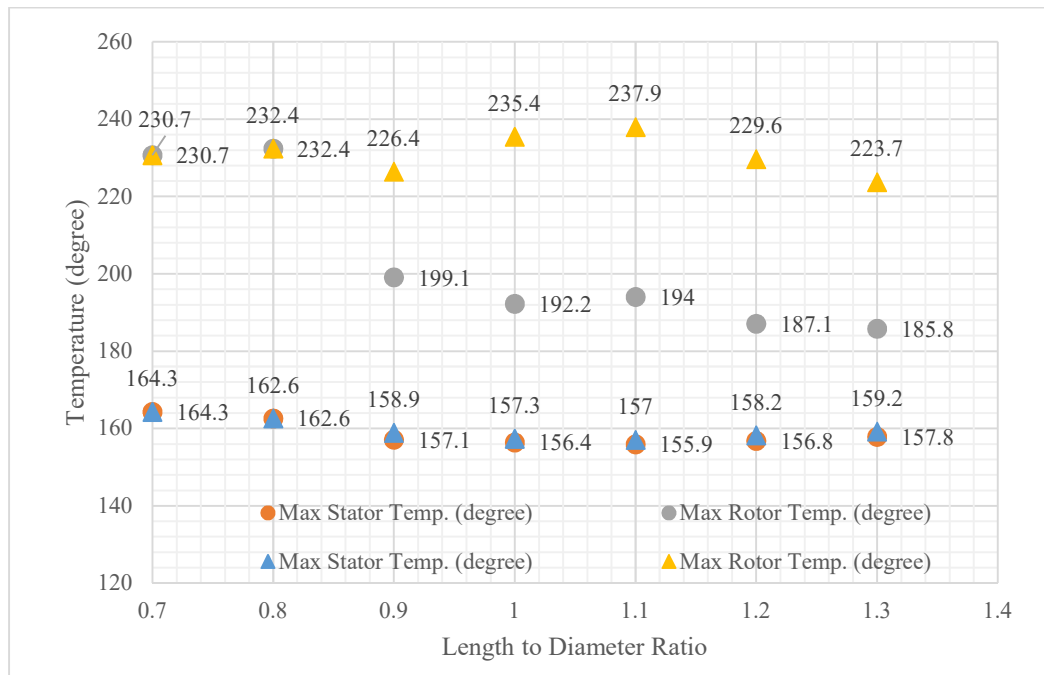


Fig. 58 Maximum rotor and stator coil temperature with increased field current density

Fig. 59 summarizes the active weight information for each individual generator components in Fig. 57 and the new weight information with increased field current density. The overall weight of a WFSG is labelled on the top of each bar. Comparing WFSGs with L2D ratio at 0.9 – 1.3, cases with increased field current density have their overall generator weight reduced by 2 to 3 kg relative to cases with original field current density. The explanations are as follows. The reduction of the overall generator weight is a result of reduced rotor core iron and field winding materials. Increasing the field current density results in lighter field coils and smaller areas required for field windings. Smaller field coil area means shorter magnetic circuits

can be implemented to maintain the air gap flux density during no-load and full-load. These two major reasons explain the overall generator weight reduction for WFSGs with L2D ratios from 0.9 – 1.3 in Fig. 59.

A trend for the weight of WFSGs with increased field current density can be observed while examining L2D ratios from 0.9 – 1.3 and 0.7 – 0.8 separately in Fig. 59 compared with those WFSGs on the left hand side of Fig. 59. Within the L2D ratio range of 0.9 – 1.3 and 0.7 -0.8, the overall weight of a generator decreases with the increase of L2D ratio.

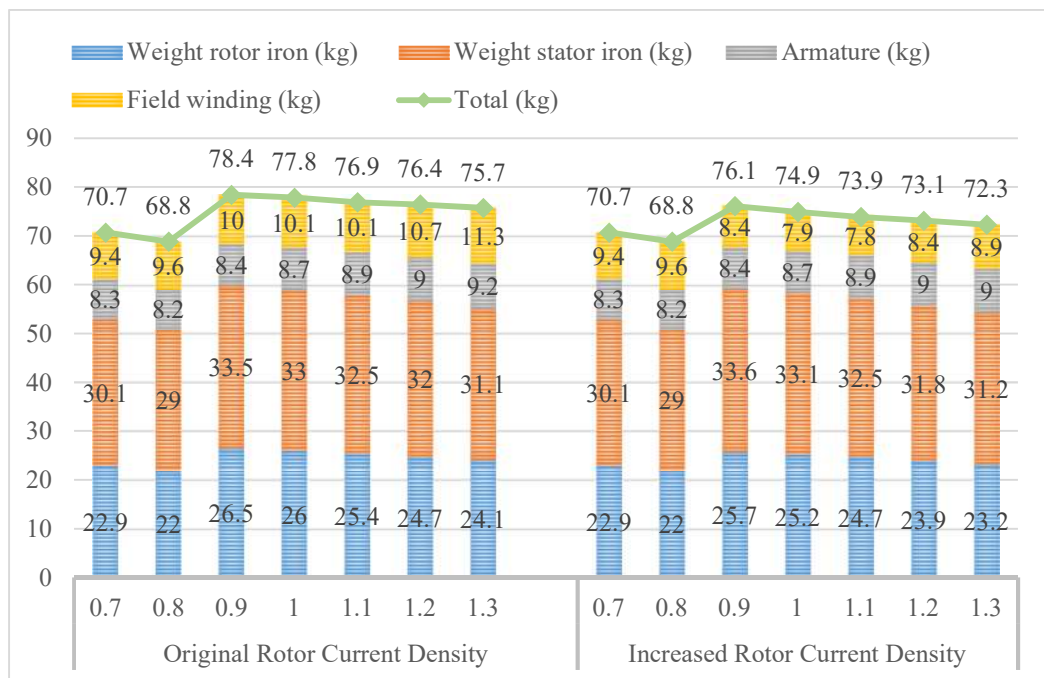


Fig. 59 Weight comparison when the rotor current density is increased

However, this trend cannot be individually concluded based on Fig. 59 only. Fig. 58, Fig. 59 and Table 12 should be analysed together to obtain a comprehensive results for the connection between L2D ratios and the weight of a WFSG.

Temperature simulation in Fig. 58 proved that there is no further improvements on the weight of a generator. The weight of a WFSG when L2D ratio is 0.8 is less than that of a WFSG when a L2D ratio is 1.3. Therefore, increasing the L2D ratio does help reducing the weight of a generator. This significant reduction of the weight of a generator is due to the fact that the number of turns of stator coils have jumped from 5 to 6. This leads to a significant reduction of the required flux from one pole pitch from rotor surface, and thus, the rotor surface area or rotor volume is substantially reduce while keeping the same terminal output voltage. When L2D ratios are between 0.9 – 1.3, the number turns for stator coils are not changed. This leads to flux required under one pole pitch remain a constant. In the analytical sizing script, the rotor volume is automatically regulated to a point where similar output terminal voltage can be achieved. Thus, the rotor volume is less likely to change in a dramatic way if the number of turns of stator coils remains a constant.

Table 13 Key parameters for WFSGs designed in Fig. 59 with increased field current density

Length to Diameter Ratio	Efficiency	Peak Air Gap Flux Density (T)	N Phase	L Axial (mm)	D rotor (mm)
0.7	92%	0.82	6	153.4	219.2
0.8	92%	0.79	6	167.7	209.6
0.9	89%	0.84	5	185.6	206.2
1	89%	0.82	5	201.5	201.5
1.1	90%	0.82	5	214.7	195.2
1.2	90%	0.8	5	223.1	185.9
1.3	91%	0.8	5	231.8	178.3

To summarize this chapter, L2D ratios do affect the weight of a generator when L2D ratio reaches a point where the number of turns of stator coils is altered. Under this condition, the smaller the L2D ratio is, the lighter WFSG is. When the L2D ratio

cannot change the number of turns of stator coils, the weight of a WFSG decreases with an increase of L2D ratio.

4.3 Conclusion

This chapter focused on implementing the OOD tool developed and validated in chapter 3 to design and analysis a WFSG (with 180 *m/s* mechanical constraints) adopting low and high temperature wires. As the result, a WFSG designed with high coil temperature achieves better performance in terms of weight. Meanwhile, the weight of the active materials of a WFSG achieved in chapter 4.2 is 80.2 *kg*. This achievements can potentially meets the weight requirements of the overall machine presented in chapter 1. 2/3 short pitching and one stator slot skew are implemented to reduce the power quality of the output terminal voltages to 5%. Meanwhile, the torque ripple of a WFSG for different THD reduction methods are also presented in chapter 4.1.3. It is concluded that a WFSG equipped with 2/3 short pitch winding and one stator slot skew achieves the lowest torque ripple. High frequency associated iron losses and AC copper losses are introduced and analysed. An optimum wire gauge is selected to minimize the AC copper losses.

At the end of this chapter, the impact of length to diameter ratio on weight of a WFSG is analysed without the mechanical constraints. L2D ratios do affect the weight of a generator when L2D ratio reaches a point where the number of turns of stator coils is altered. Under this condition, the smaller the L2D ratio is, the lighter WFSG is. When the L2D ratio cannot change the number of turns of stator coils, the weight of a WFSG decreases with an increase of L2D ratio. This investigation further help the study in chapter 7 when high yield strength material can be used as

rotor core material enabling a larger WFSG rotor radius. In this case, a comprehensive investigation has to be performed to determine the minimum weight of a WFSG within the limit of material strength.

Chapter 5 Mechanical design and FE analysis

Chapter 3 concludes three validated embedded OOD modules 1) an analytical sizing script for determining the size initial sizing for a WFSG; 2) an electromagnetic FE model for analysing the electromagnetic performance of a WFSG; 3) a 3D LPTN model for analysing the temperature behaviour of a WFSG. Chapter 4 designs a high speed high temperature WFSG using OOD tool setup in chapter 3. Mechanical analysis is performed on the design outcome in chapter 4.2.2. Von-Mises distribution is considered to understand whether the structure itself can withstand the operating speed required. The necessity for additional mechanical structures is discussed based on the outcome of Von-Mises distribution analysis. The development process of the mechanical analysis is embedded into the OOD design tool to enhance the capabilities of this multi-physics design tool.

5.1 Mechanical design and FE analysis

High speed machines in general are considered suffering from high stress level concentrated at rotor cores. However, the stress experienced by the rotor core not only related to rotational speed, but also the radius of the rotor cores. Therefore, the peripheral linear speed is a clearer definition for machines that can be categorized as a low speed or a high speed machine. Peripheral speed can be a valid quantity to evaluate whether the material has reached the limit for deformation. Based on some old literatures [116], the peripheral speed of a salient rotor core reaching 140m/s to 150m/s can be considered as high-speed machines. A rotor core under that speed range has reached a point where the actual stress experienced by the rotor material is very close to its yield strength or even tensile strength point. As a result, comprehensive investigations on stress level experienced by different area of the rotor cores are necessary to guarantee safe operation of a prototyped electric machine.

5.1.1 Challenges for WFSGs from mechanical perspective

WFSGs, compared with a PM, SR or induction machine, have an inherited downside – relatively complex rotor structure. In quite a lot of literatures [53] [119], WFSGs are concluded to have less chance to achieve high speed operation. In this case, materials selection becomes an important factor while designing WFSGs. CoFe developed by Vacuumschmelze can reach a yield strength up to 800 MPa . Special SiFe steel developed by Nippon steel can achieve a yield strength of 820 MPa . As discussed in chapter 1 and 2, this type of material is very expensive and the risks of failure using this material as rotor cores is unaffordable. In addition, yield strength

for CoFe at 800MPa is achieved by 0.35mm thick laminations. This grade of material can simplify the structure design of the rotor cores, but the iron losses provided by Vacuumschmelze is also higher than the rest of the soft magnetic materials. In chapter 3 and 4, a rotor core of a WFSG is difficult to be cooled based on the analysis of a 3D LPTN. Thus, reducing any unnecessary losses induced from soft magnetic core and copper materials is an effective method to reduce the weight of a WFSG.

An effective method to reduce the iron losses for iron core materials is reducing the thickness of soft magnetic materials. The minimum thickness of CoFe Vacuumschmelze can achieve is 0.05mm . Low loss thinner thickness CoFe laminations have their yield strength reduced. According to Vacuumschmelze, 0.1mm thick CoFe only achieves a typical yield strength of 600MPa that is close to the tensile strength of M235-35A. Standard SiFe steel such as M235-35A has a yield strength around 460MPa and tensile strength around 560MPa at room temperature. M235-35A is selected as the core materials mainly due to its lower costs compared with CoFe and 35HXT780T. If the geometry in chapter 4 can survive the high operating speed, further WFSG prototypes adopting high grade materials can achieve a way better performance than it currently is. Therefore, this chapter tries to employ mechanical structures that can allow a WFSG survive the high-speed operation as required in chapter 1.2 using M235-35A. In addition, this mechanical model can be used to analyse WFSGs adopting better grade CoFe or SiFe based materials with relatively lower electromagnetic losses.

5.1.2 Von-Mises distribution analysis of WFSG rotor cores

Chapter 4.2 has completed the electromagnetic and thermal analysis of a series of WFSGs. A 6 pole 54 slots option is considered to have better electromagnetic performance compared with the rest of the design options. A Von-Mises distribution analysis for 6 pole 54 slots option using geometry obtained from chapter 4.2 is presented in this section.

Ansys structural analysis is adopted as FE tool to analyse the Von-Mises distribution of a given design geometry. In Fig. 6, complex rotor geometry and mechanical structures increase the difficulty of correct analysis of the stress level at different parts of rotor cores. A completed 3D model is ideal for a comprehensive analysis. However, Fig. 6 demonstrates that a rotor assembly for a WFSG is intricate. This leads to careful identifications of the contact conditions, mesh densities and boundary conditions applied to each individual rotor component modelled in Ansys. This requires substantial amount of experiences and knowledge of manufacturing and processing of different materials. Without a prototype and hands on experimental tests, correct setups of a WFSG FE model is also challenging for an experienced engineer. Therefore, a few assumptions are made to simplify the mechanical FE model shown as below.

1. End windings wound on rotor cores are retained by rings preventing it from deforming towards the stator cores. It is assumed that drag force created by the rotor end windings is compensated by the end rings. Thus, rotor core is simulated based on a 2D geometry show in Fig. 10 a).

2. Extra mechanical structures preventing rotor coils from moving in a tangential direction are located in the inter pole region. Thus, it is assumed that rotor coils can only move alongside the pole axis direction.
3. Stress introduced by thermal expansion of the materials are not considered.

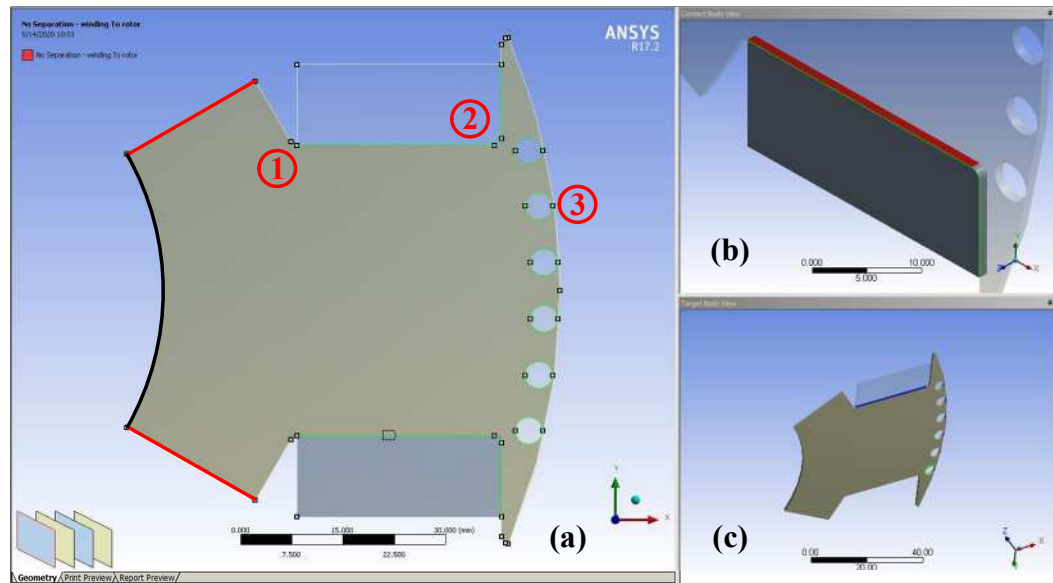


Fig. 60 Rotor pole structure including rotor body, field coils and damper cages

In Ansys, the assumptions made above simplify a 2D FE model consists of rotor core materials, copper windings and damper cages as shown in Fig. 60. The rotating speed of those four cases are all under 16,000 *rpm* which is the top required operating speed. Once the peak stress occurred on any of the rotor elements does not exceed the limitation of the material itself, a WFSG is able to survive the worst-case operating scenarios. This 6-pole rotor core has repeated features every 60 degrees and a one sixth rotor body can be simulated to simplify a 2D FE model. This requires correct boundary conditions and contact conditions been applied to a 2D FE model shown in Fig. 60. Faces for rotor core been divided into 6 pieces (highlighted in red solid line in Fig. 60 a)) are applied with frictionless support to

simulate the symmetry of 6 rotor poles. A single one sixth rotor core in Fig. 60 is simulated without a shaft. A common method to assemble rotor cores and shafts for electric machines is interference fit. Therefore, in Fig. 60 the rotor core faces that in contact with a shaft are applied with cylindrical support to constrain the displacements of the core materials.

In a FE tool, mesh densities always play a very essential role in terms of the accuracy of the final results. Locations on a rotor core that require more accurate stress analysis than other parts of the rotor core are marked from number 1 to 3 with a circle (corner 1, corner 2 and damper edge 3) in Fig. 60 a). Corner 1 is the transition between the rotor bore and rotor main body. Corner 2 is the transition between rotor main body and the pole tip. Damper edge 3 is edge that hold a damper bar. In Fig. 60, different mesh densities are applied to a 2D rotor core FE model shown in Fig. 60 c) which is a bare rotor core with no copper wire and damper cage in Ansys to understand the optimum mesh density balancing the accuracy and time consumptions. Table 14 demonstrates the outcomes of the sensitivity analysis of the mesh densities with respects to the stress level.

Table 14 Sensitivity analysis of mesh refinement size versus stress level

Mesh Size (<i>mm</i>)	0.1	0.2	0.3	0.4	0.5
Stress (<i>MPa</i>)	692	693	692	688	694
Mesh Size (<i>mm</i>)	0.6	0.7	0.8	0.9	
Stress (<i>MPa</i>)	684	684	680	669	

In Table 14, the stress level varies a lot while the mesh density is between 0.4 to 0.9 *mm* and the standard deviation for stress level at mesh size between 0.4 to 0.9 *mm* is 8.40. The stress level at mesh size between 0.1 to 0.3 *mm* steadies at around 692

MPa and the standard deviation for stress level at mesh size between 0.1 to 0.3 mm is 0.58. Therefore, mesh size at 0.1 to 0.3 mm can achieve stress level with relatively good accuracy compared with the rest mesh size in Table 14. Mesh size at 0.3 mm can obtain a relatively good accuracy while consuming least amount of simulation time. After the optimum mesh density is found (0.3 mm), the mutual mechanical effects between a rotor body, copper coils and damper cages are able to be simulated. To understand the stress level of a rotating rotor core itself and the effects of adding rotor coils and damper cages, the mechanical simulations are separated into four different cases; 1) a one sixth of an entire rotor core itself; 2) a one sixth of an entire rotor core and field windings; 3) a one sixth of an entire rotor core and damper cages; 4) a one sixth of an entire rotor core, damper cages and field coils all together.

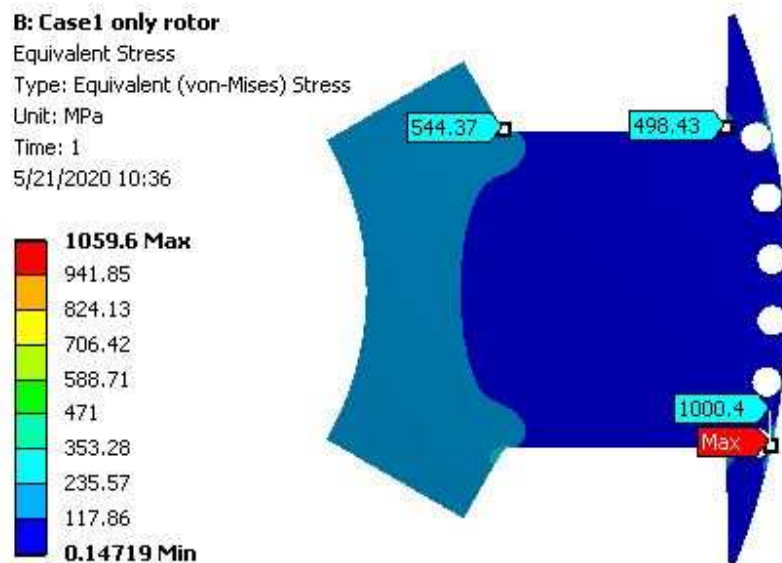


Fig. 61 Von-Mises distribution for case 1 (rotor core only)

Fig. 61 represents the stress level of case 1 where a rotor core is not equipped with field coils and damper cages. The boundary conditions applied to a one sixth of an

entire rotor core itself are the same as those been applied to FE model shown in Fig. 60. There are three places that suffer from high level stress. The first one is located at corner 1 (see Fig. 60) that experiences quite a significant drag from the entire rotor pole body. The stress level of 531 *MPa* is concentrated at this spot. The second spot is the corner 2 (see Fig. 60). This sharp right-angle corner sees a stress level at 476 *MPa*. The reason for this high level stress concentration is the 90-degree sharp transition which is not recommend from mechanical aspects in general. Third position that withstands more than 1,000 *MPa* is the damper edge 3 (see Fig. 60). During rotation of the rotor core, rotor pole tips deforms outwards. This leads to the thin edge holding the damper cages been pushed from neighbouring materials, which caused huge stress observed there.

The stress level seen by this single rotor core in Fig. 61 at damper edge 3 goes beyond the yield strength, even the tensile strength of M235-35A. With added structures such as rotor coils and damper cages, the stress experienced at corner 1, corner 2 and damper edge 3 are even worse. Therefore, extra mechanical structures are required to assist rotor core so as not to fall apart due to high centrifugal force. Extra retaining mechanical structures can be design after the full understanding of the effects of rotor coils and damper cages on rotor cores are established.

Fig. 62 demonstrates a FE model with one sixth of an entire rotor core and field windings representing the case 2 configuration. The assumptions made above simplified the FE mechanical model in Fig. 62. The copper coils are assumed to move in pole axis direction outwards. No separation is applied to contact surfaces between field coils and SiFe steel highlighted in red solid lines in Fig. 62 a). No

separation contact allows tiny displacements between field coils and a rotor core and constrains field coils at its original places without moving in direction orthogonal to red solid line. This complies the assumption made that extra mechanical structures are designed to retain field windings in place. Faces shown in Fig. 62 b) are applied with frictionless so that centrifugal forces caused by the mass of the field coils are applied to pole tips. The rest boundary setups are the same as those been configured in Fig. 61.

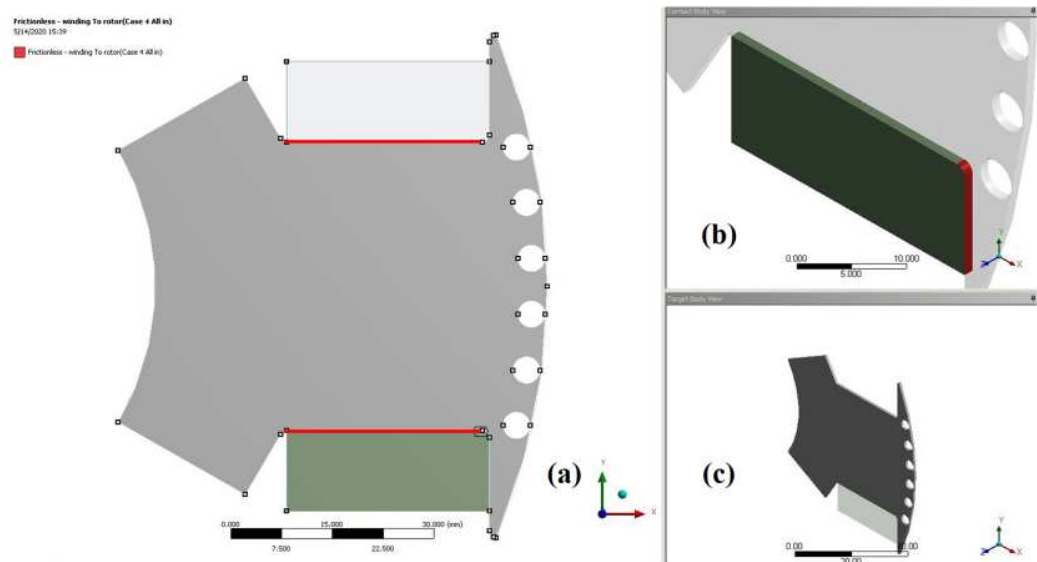


Fig. 62 Von-Mises distribution simulation setup for case 2 (rotor body and rotor copper coils)

Fig. 63 presents the Von-Mises distribution of a rotor core and the field coils. Corner 1 experience a stress level of 629 MPa . Compared with case 1, the stress level has a 13% increase. With added field coils, corner 2 suffers from a significant increase of stress to 1036 MPa . Compared with the case 1 where only a rotor core is simulated, the stress level increased by 102%. The damper edge 3 holds a damper bar experiences 1243 MPa . The stress level at damper edge 3 is increased by 27% compared with case 1. Extra weight introduced by field coils causes rotor bores to

withstand more centrifugal force during rotation. In case 2, rotor pole tips are used to hold field windings from moving outside. This leads to substantial increase of stress level concentrated at the sharp corner between a rotor body and rotor pole tips. In conclusion, the weight of field windings causing three most critical spots on the rotor pole to increase. Corner 1 and 2 are affected dramatically.

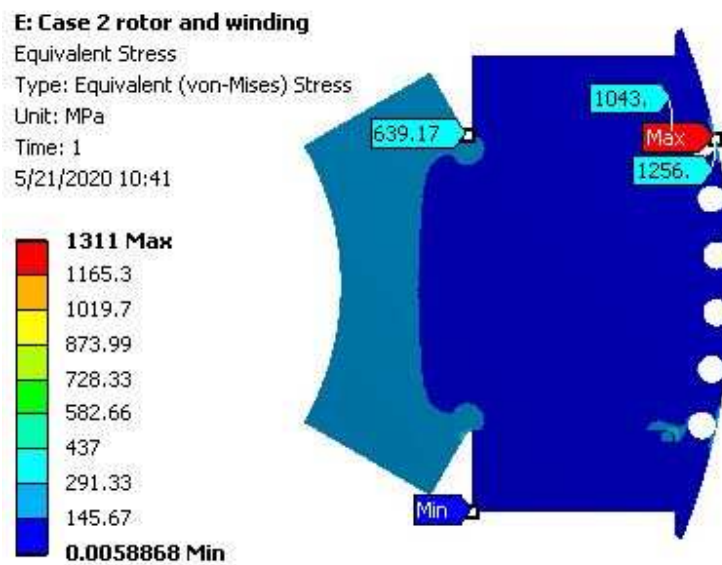


Fig. 63 Von-Mises distribution for case 2 (rotor core and field coils)

Fig. 64 depicts the FE model established for case 3 which consists of a rotor core and damper cages. 6 damper bars shown in Fig. 64 are shorted, but not connected with neighbouring poles as conventional WFSG shown in Fig. 6. Therefore, the thin edges surrounding the damper bars (damper edge 3) are the only structures that holds the damper cages in place. For aerospace WFSGs, those damper cages are often slid into the position and shorted by the end plates on both sides. Under this circumstance, the contact conditions between damper bars and the surrounding rotor cores as shown in Fig. 64 b) and c) is defined as frictional contacts. The friction coefficient

between two faces are defined as 0.1 to simulate the tiny movements of damper bars inside the hollow structures during rotation.

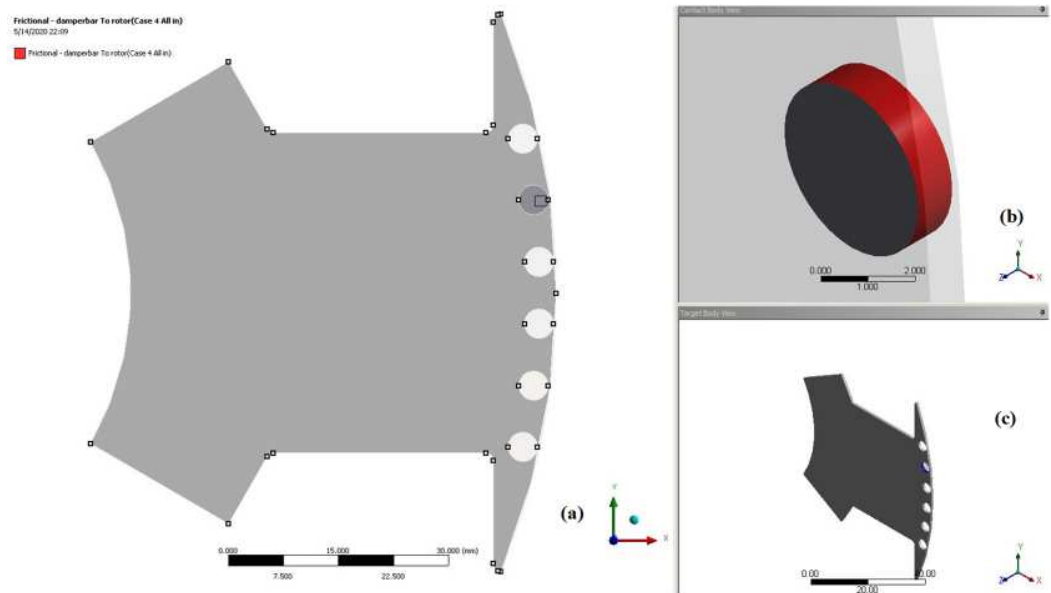


Fig. 64 Von-Mises distribution simulation setup for case 3 (rotor body and damper cages)

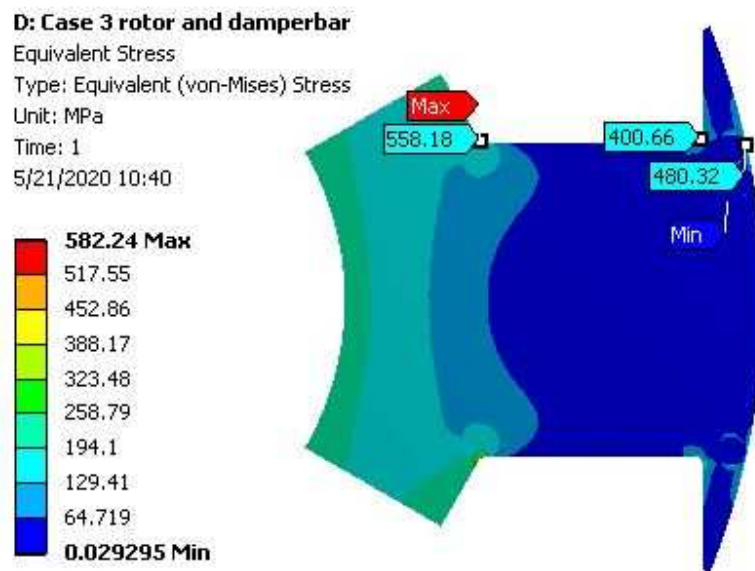


Fig. 65 Von-Mises distribution for case 3 (rotor core and damper cages)

Fig. 65 represents the stress distribution of a rotor core and its damper cages. A 4% increase of stress located at corner 1 (557 MPa for case 3) compared with case 1. A 16% decrease at the corner 2 (557 MPa for case 3) is also observed. The stress experienced by the thin edge holding damper cages damper edge 3) are seen with a significant decrease about 527 MPa (almost 61%). An increase of stress for corner 1 is within expectation as more weights are introduced by the damper cages. Although damper cages are allowed to slide inside the hollow slots designed for damper cages, solid materials filling those hollow structures give rotor pole tips more strength. Therefore, corner 2 and damper edge 2 are less severely deformed outwards. A decrease of local stress concentration at these two points are within expectation under this circumstance.

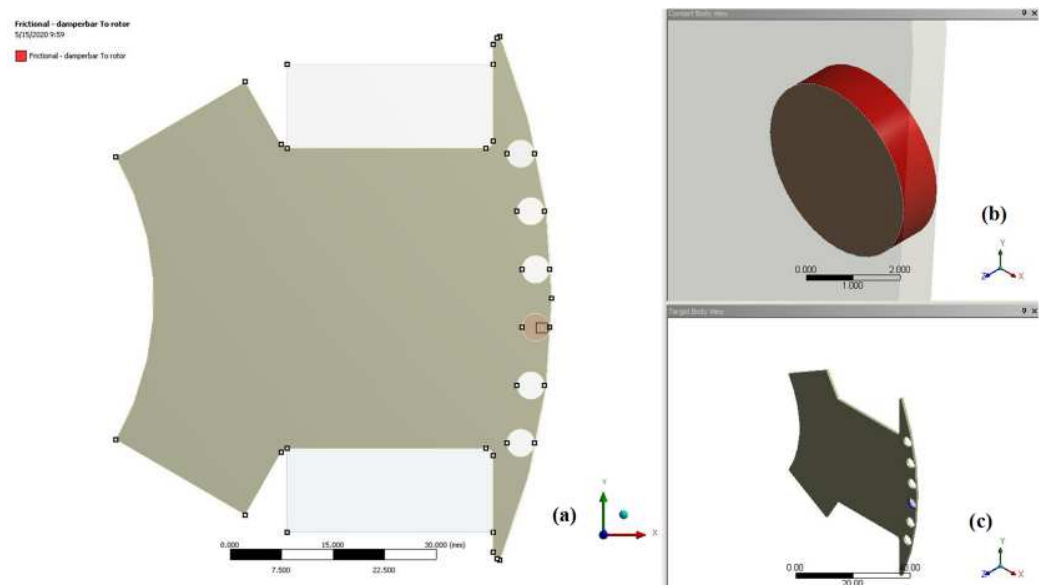


Fig. 66 Von-Mises distribution simulation setup for case 4 (rotor body, field coils and damper cages)

Fig. 66 demonstrates a FE model in Ansys of a rotor core, field coils and damper cages representing case 4. This model simulates the stress distribution behaviour of

a complete mechanical model. The boundary conditions applied to case 1, 2 and 3 are all been transferred to the FE model for case 4.

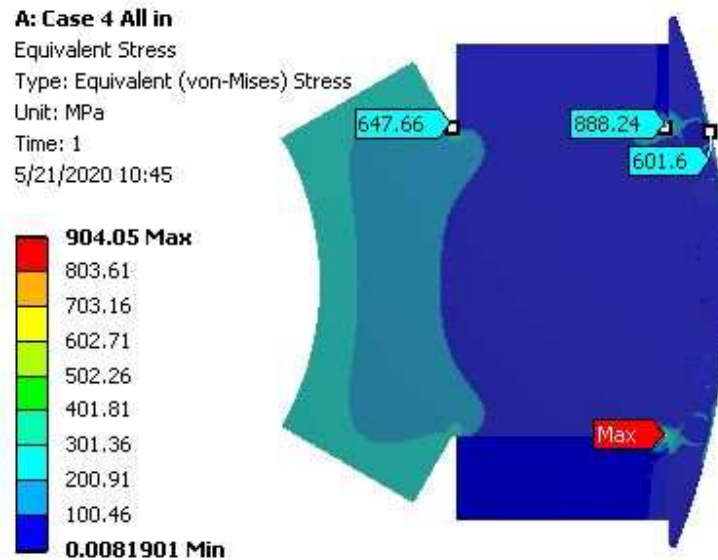


Fig. 67 Von-Mises distribution for case 4 (rotor core, field coils and damper cages)

Fig. 67 depicts the Von-Mises distribution of a case 4 model. The stress concentrated at the transition place between rotor bores and a rotor body and the sharp corner between a rotor body and rotor pole tips increases. The local stress levels at corner 1 and corner 2 mentioned are 647 MPa and 885 MPa respectively. The damper edge 3 sees a stress at 577 MPa .

The above analysis of four different cases has studied the Von-Mises distribution of 1) a rotor core itself under high speed; 2) the effects of the rotor coils on rotor cores; 3) the effects of damper cages on rotor cores; 4) the effects of both rotor coils and damper bars on rotor cores. The extra mass introduced by rotor coils and damper cages push the rotor core outwards causing stress level concentration at two corner 1 and 2. The thin edges on the rotor core holding damper cages (damper edge 3)

experience significant stress during rotation. The root reason for causing this problem is the deformation of rotor pole tips. Rotor pole tips bending outwards pushing those thin edges (0.4 mm) together leading to very high stress concentration.

In Fig. 67, the stress concentration at those three critical spots exceeds the yield strength (460 MPa) even the tensile strength (580 MPa). In addition, thermal stress caused by thermal expansions are not included in the simulation to simplify a mechanical FE model. Therefore, stress level at the thin edge exceeds 577 MPa . As a result, SiFe steel M235-35A cannot sustain in one piece under the top speed operation. Adequate measures should be taken to allow SiFe steel core to survive the high speed operation.

The analysis above has clearly identified the spots on rotor cores that suffer from high stress concentration. Meanwhile, possible reasons for causing high stress concentration are discussed. Possible solutions addressing above mentioned issues are investigated later. In Fig. 61, Fig. 63, Fig. 65 and Fig. 67, corner 1 and 2 relatively sharp. According to [120], sharp transition without fillets results in high level of stress concentration. In general, large fillets potentially has less stress concentration compared with small fillets. This method can also be applied to a right angle corner between a rotor body and rotor pole tips. However, rotor copper wires are wounded uniformly for easier manufacturing and assembly purpose. Ideally, copper wires are wounded in a rectangular region. Thus, increasing the fillets at those two corners helps reducing the stress concentration but also reduces the area that allows copper wires to be wounded uniformly. Hence, more heat is generated during machine operation resulting in higher temperature than simulated values in

chapter 4.2. An iteration starts from analytical sizing stage considering the dimensions for the fillets on the rotor core is required allowing high speed operations. Meanwhile, temperature simulation for a new WFSG during the iteration process is also critical to keep maximum coil temperature below the threshold values.

Adding fillets is one of the effective methods to reduce the stress concentration at a cost of reducing active area for the copper wires. In this case, extra mechanical retaining rings and caps are introduced as Fig. 6. These structures help confine copper wires at its original places without requiring a rotor core to withstand all the centrifugal forces introduced by the copper wires. Therefore, there is a balance between increasing the dimensions of fillets and the size of the mechanical structures.

Apart from corner 1 and 2 mentioned above, the thin edges surrounding the damper cages suffer from high risks of exceeding the yield strength of M235-35A. An easy way to address this issue is to increase the thickness of these thin edges. In contrast, increasing the thickness of the thin edges means move damper cages closer to the centre (origin) of a rotor core. This design change has a negative impact on the THD level for the terminal voltages [84]. Therefore, a compromise between the thickness of that thin edges and the THD level of the terminal voltage must be considered. As discussed in early chapter 4.3.2. High level of stress concentration located at thin edges are due to outwards deformation of pole tips. Thus, thin edges are pushed together causing high stress there. Thus, removal of those thin edges for each damper bar (open slot configuration) potentially removed the risks of high stress concentration. However, analysis is also necessary to understand whether open slot

configuration reduces the average flux density in the air gap, hence, terminal voltages. Secondly, whether open slots configurations (holding damper bars) result in more severe stress concentration still require detailed analysis.

Another focus to address high stress concentration from mechanical perspective is complete removal of damper cages. However, damper cages are critical elements for WFSGs as discussed in chapter 2.5.1. Damper cages embedded inside the rotor poles see a traveling magnetic field as shown in Fig. 68 to compensate the negative impact of unbalanced three phase load [43]. In Fig. 68, during load operation, the right hands side pole tip is highly saturated and a significant amount of magnetic flux are travelling outside the soft-magnetic material. Flux channelled outside the iron core are highlighted in red enclosed region in Fig. 68. In this case, altering a location for damper cages for a WFSG while keeping the functionality become a possible solution to high stress concentration. In Fig. 6, end rings and caps are implemented to prevent rotor coils from flying outside. If the materials for those end rings and caps are with high electric conductivity, these caps and end rings can be alternative damper bars and plates shorting damper bars in Fig. 6 respectively. End rings and winding caps together can function as a damper cage as well as mechanical structures holding field windings in its place. However, those caps designed for retaining copper wires as mentioned in this chapter must fill in space where travelling flux passes through as shown in Fig. 68 to perform as damper cages. At the same time, the performance of the proposed integrated damper cages is investigated to understand if a WFSG still perform in desired transient envelope.

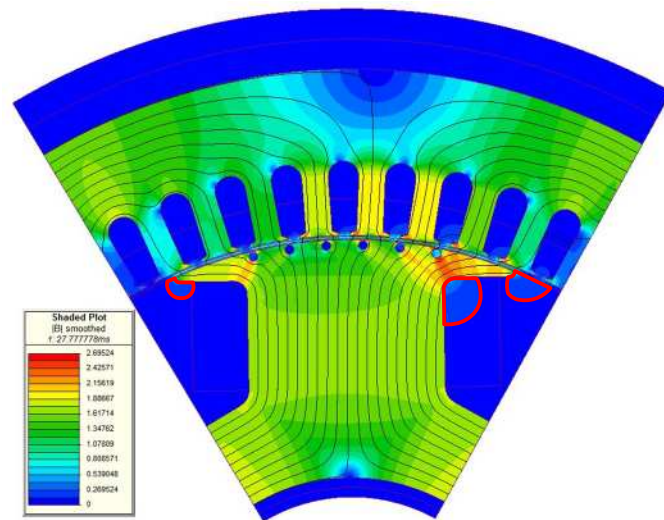


Fig. 68 Field distribution for a WFSG finalized in chapter 4.2 full load condition
In conclusion, the possible solution that can potentially resolve the high stress concentration is summarized below.

1. Appropriate implementation of fillets.
2. Increasing the thickness of the thin edges.
3. Open slots configurations for damper cages.
4. Integrated damper cages designed for retaining copper wires and damping asynchronous oscillations.

5.2 Von-Mises distribution analysis of proposed stress reduction methods

Chapter 5.1 concludes 4 possible solutions for solving the stress concentration at corner 1, corner 2 and damper edge 3. This chapter analyses 4 possible solutions proposed in chapter 5.1.

5.2.1 Fillets sizing for corner 1 and 2

In Fig. 69, a 3 mm and a 5 mm fillets are applied to corner 1 and 2 to release the stress located at those two spots. 471 MPa is observed at corner 1 in Fig. 69 and a 27% reduction is achieved compared with case 4 in Fig. 67. 359 MPa is observable

at corner 2 in Fig. 69 and a 59.4% reduction is achievable. Damper edge 3 in Fig. 69 sees a 13.5% compared with case 4 in Fig. 67. A conclusion can be drawn that fillets do help decrease the local stress concentration at corner 1 and 2. The stress at damper edge 3 is also decreased due to a 5 mm fillet enhances the pole tip. This enhanced pole tip prevents itself bending outside which releases some stress at damper edge 3.

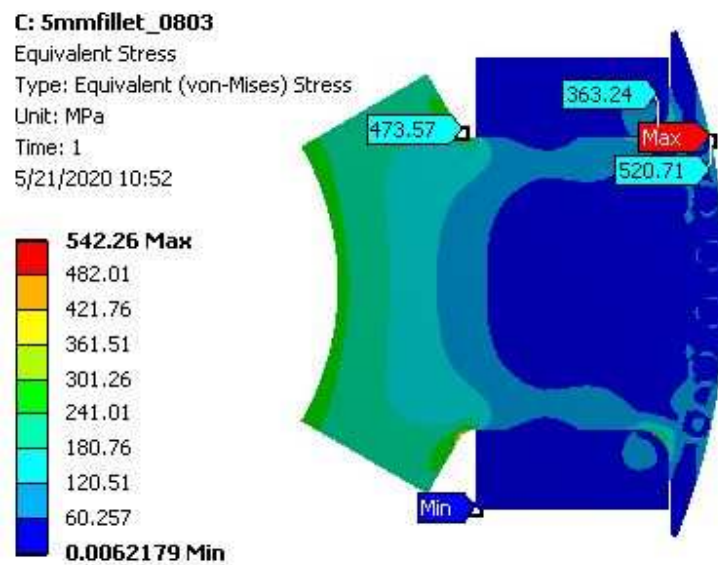


Fig. 69 Von-Mises distribution for case 4 (rotor core, field coils and damper cages) with 3 mm and 5 mm fillets at corner 1 and 2 respectively

From the results in Fig. 69, increasing the size of fillets do help reduce the local stress concentration. However, even with the help of increased fillets, stress at corner 1 still reaches a dangerous point where the typical yield strength for M235-35A is exceeded. In Fig. 69, the simulation is still performed assuming that the coil can be wound uniformly at corner 2 even the surface is not flat. This is very difficult to achieve in practical. In Fig. 70, a Cummins Generator also wound its rotor core uniformly but not in region with curvature surface. The downside for increasing

fillets at corner 1 and 2 is reduced area to uniformly wind the rotor coil. The effective flat area to wind rotor coil for the case presented in Fig. 69 is reduced by roughly 27% compared with case presented in Fig. 67. This leads to an increase of rotor coil temperature by roughly 17%.



Fig. 70 A complete rotor core (Courtesy Cummins Generator Technologies)

Based on the Von-Mises analysis in Fig. 70, increasing the size of the fillets can help reducing the stress concentration at a cost of increasing the overall size of the machine. Therefore, a balance has to be found between survivability of rotor core at high speed and the overall size of a generator. The Von-Mises distribution results in Fig. 69 shows that with help of fillets only there is no chance that this rotor core can survive the high speed rotation with M235-35A. As a result, the end cap holding the field winding should be extended to pole tip region as shown in Fig. 6 to prevent the field windings to move in the radial directions. In this case, it is assumed that the external structures hold the field winding in place which did not have a significant negative impact on pole tip at corner 2.

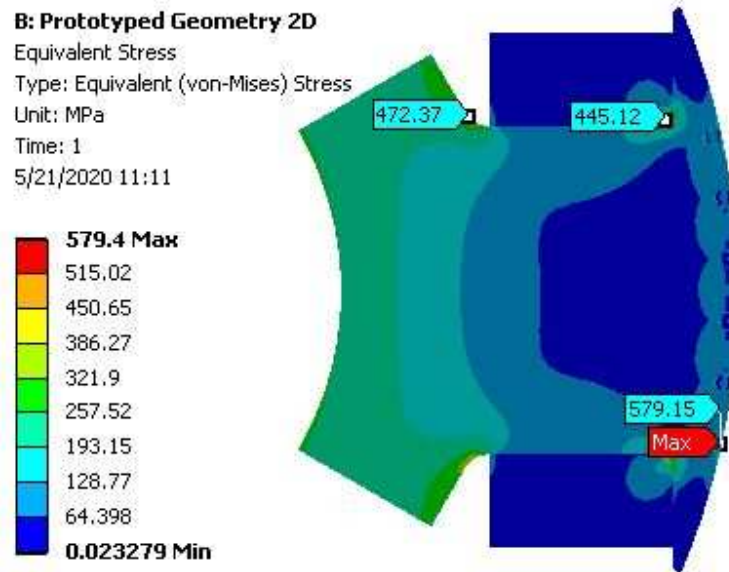


Fig. 71 Von-Mises distribution for case 4 (rotor core, field coils and damper cages) with 4 mm and 3 mm fillets at corner 1 and 2 respectively

Fig. 71 presents a more practical fillets option while balancing rotor core survivability and overall weight constraint (temperature constraint). However, the results in Fig. 71 still hits closely to the tensile strength of M235-35A. Therefore, under the circumstance that the material cannot be changed to high grade CoFe or 35HXT780T, extending endcap under the pole tip to prevent field winding moving in axial direction is necessary.

5.2.2 Increasing the thickness of the thin edges holding damper cages (damper edge 3)

Based on the analysis and knowledge learnt in [84], damper edge 3 must be kept under 0.5 mm to obtain required THD level below 5% under 2/3 short pitching and one skewed one slot pitch. Any thickness above 0.5 mm requires a comprehensive FE analysis of the effects of damper cages on THD level. The WFSG geometry used in this chapter is the one used for simulation in Fig. 71. In Fig. 72, the thickness of

the damper edge 3 is 0.5 mm . Thicker damper edge 3 reduces the stress at that point from 572 MPa to 282 MPa . Therefore, increasing the edge of the damper edges 3 helps decrease the local stress concentration.

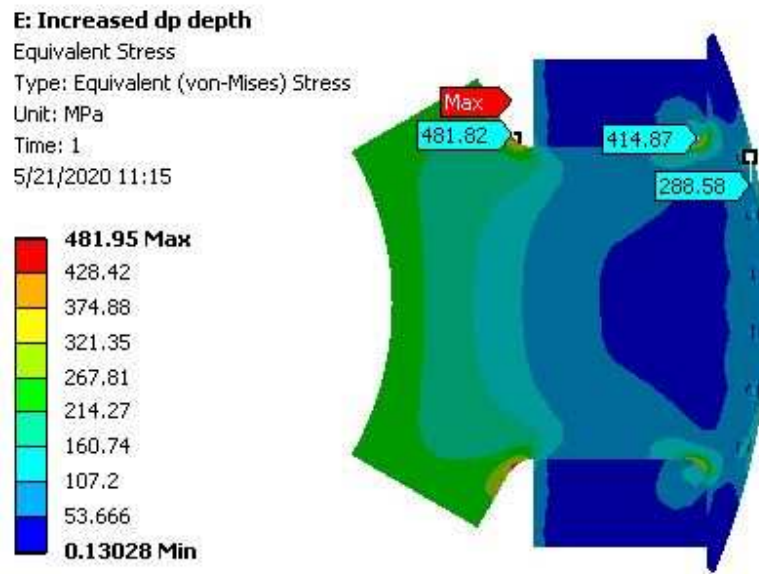


Fig. 72 Von-Mises distribution for case 4 (rotor core, field coils and damper cages) with 4 mm and 3 mm fillets at corner 1 and 2 respectively the depth of damper edge 0.5 mm

Fig. 73 presents the harmonic contents for increased damper edge 3 WFSG simulated with geometry in Fig. 72. The THD levels at $7,200\text{ rpm}$, $9,000\text{ rpm}$, $12,000\text{ rpm}$, $16,000\text{ rpm}$ are 2.65% , 2.57% , 3.04% , 2.69% respectively. As expected, the THD level for the no-load output terminal voltage does not go beyond 5% . Comparing the Fig. 73 and Fig. 51, major harmonic contents are still similar, but the magnitude for same order harmonic at the same speed are changed significantly. As long as the depth of damper edge 3 does not enhance the 5th and 7th harmonic contents which affects the stability of generator connected grid system [117],

increasing depth of damper edge 3 can be an effective method to solve local stress concentration problem.

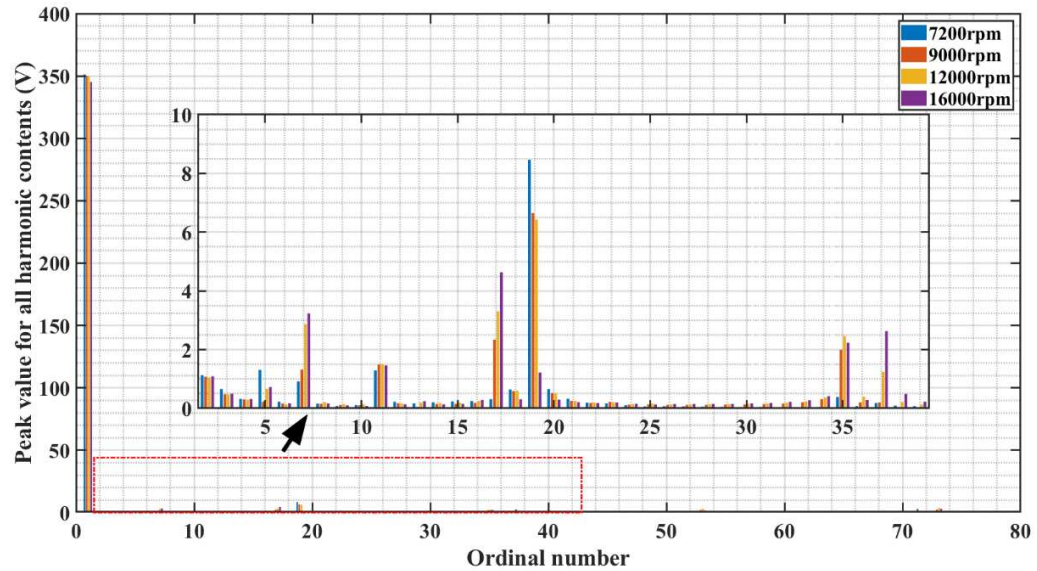


Fig. 73 Harmonic contents for increased damper bar depth configuration at no-load (see Fig. 72) at 7,200 rpm, 9,000 rpm, 12,000 rpm and 16,000 rpm

5.2.3 Open slot configuration for damper cages

Increasing the depth of damper edge has been proved to an effective methods to reduce the stress concentration at damper edge 3. Another method named open slot configuration for a damper bar is investigated to find out the effects on the stress concentration at damper edge 3. The WFSG geometry used in this chapter is the one used for simulation in Fig. 71. The slot opening for damper edge 3 is set to be 1 mm.

In Fig. 74, stress level at corner 1 and 2 does not vary much compared with case 4 simulated in Fig. 71. High local stress concentration at damper edge 3 disappears. The high stress spots are moved from damper edge 3 to regions that surrounds a damper bar.

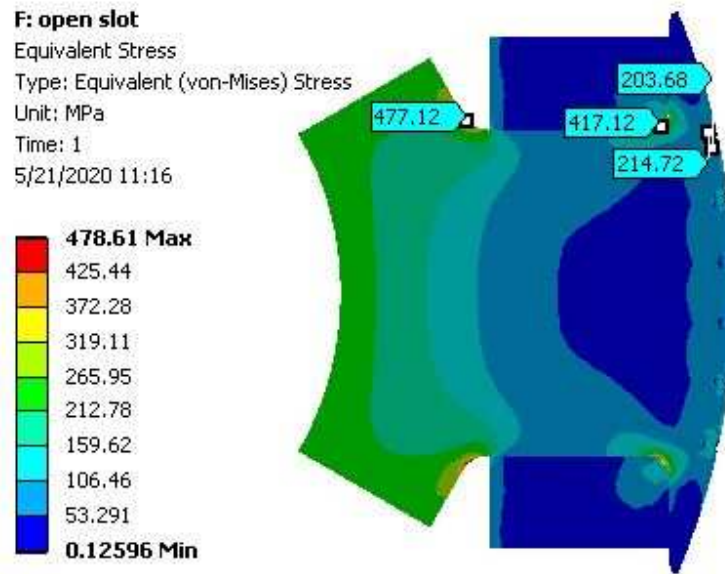


Fig. 74 Von-Mises distribution for case 4 (rotor core, field coils and damper cages) with 4 mm and 3 mm fillets at corner 1 and 2 respectively damper bar slot opening is set as 1 mm

Fig. 75 demonstrates the stress level at damper edge 3 for a WFSG without modification on damper edge 3 (case 4 simulated in Fig. 69) and a WFSG with open slot configuration on damper edge 3 (case 4 simulated in Fig. 74). In Fig. 75 a), damper edge 3 are pushed together creating huge stress close to the tensile strength of M235-35A that is very dangerous during high speed operation. In Fig. 75 b), the thin edge (damper edge 3) is removed and the high stress concentration is resolved. Highest stress spots are shifted to spots around a damper bar as shown in Fig. 75 b).

Open slot configuration for damper bars theoretical reduces the mean value and increases the harmonic contents of the air gap flux density. But, these effects has to be checked with electromagnetic FE analysis tool. Fig. 76 presents the harmonic contents for no-load terminal voltage for damper bar open slot configuration.

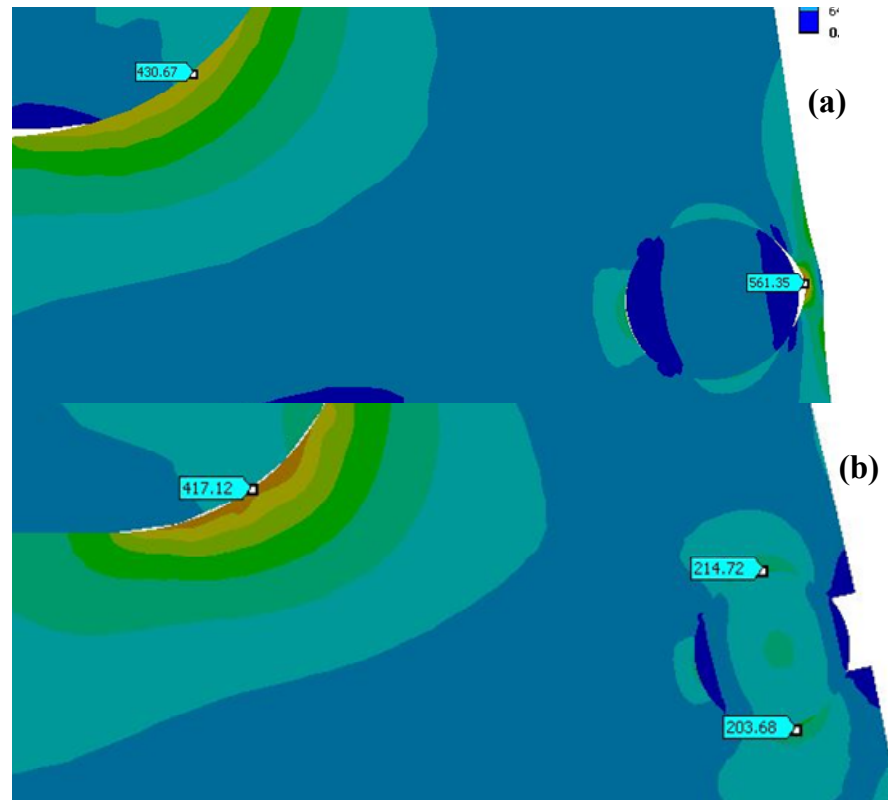


Fig. 75 Zoomed in damper edge 3 a) case 4 simulated in Fig. 69 b) case 4 simulated in Fig. 74

Compared with Fig. 51, the magnitude and the number of harmonic contents remain similar. The total THD for Fig. 76 is 2.5% on average. Only a 0.2% difference can be found compared with the case in Fig. 51. In conclusion, 1 mm slot opening at damper edge does not affect the THD and output terminal voltage dramatically, which can be considered as an effective methods to solve local stress concentration at damper edge 3.

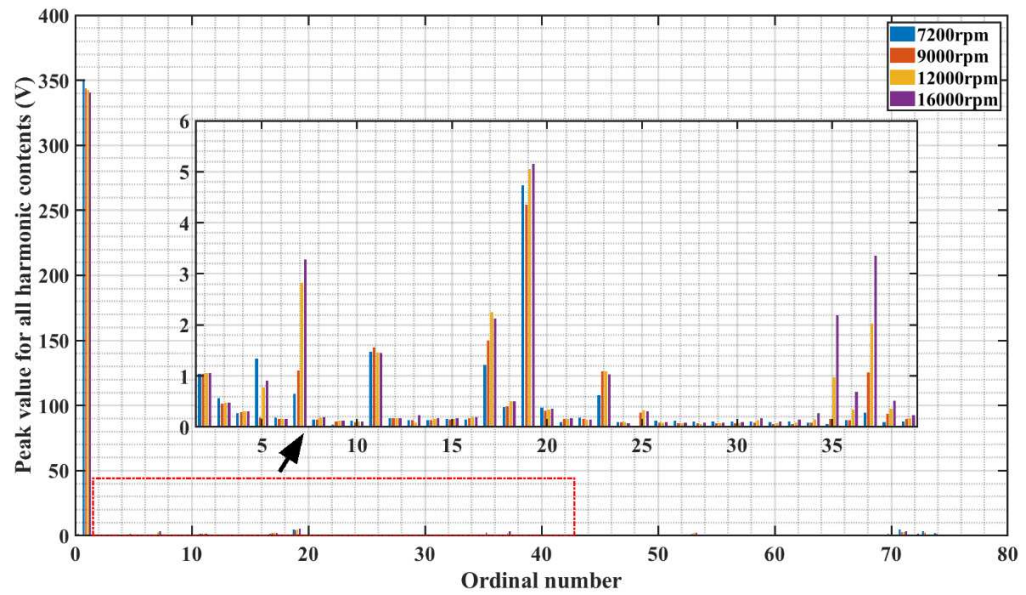


Fig. 76 Harmonic contents for damper bars open slot configuration at no-load (case 4 in Fig. 74) at 7,200 rpm, 9,000 rpm, 12,000 rpm and 16,000 rpm

5.2.4 Integrated damper cages designed for retaining copper wires and THD reduction

In chapter 5.2.2 and chapter 5.2.3, it is proved that increasing thickness and removal of damper edge 3 can ease the local stress concentration at damper edge 3. The resultant stress level at damper edge 3 is kept at point way below yield strength of the material. Promisingly, these two methods does not affect the stress concentration at corner 1 and 2 in a negative orientation. However, methods presented in chapter 5.2.1, 5.2.2 and 5.2.3 still cannot allow M235-35A to operate below the yield strength at corner 2. In [70], the tensile strength of the material is considered as the threshold point for failure comparison and a minimum safety 1.24 at maximum speed is introduced by UoN with respect to its material tensile strength. The above analysis in Fig. 72 and Fig. 74 only achieve a safety factor of 1.16 which is not recommended for the first prototype to guarantee the safe operation. Therefore, extra retaining structures enclosure field windings in its place are necessary. Therefore,

an integrated damper cage functions both as a cap and a damper cage is proposed in this chapter.

An integrated damper cage adopting metal or alloy is designed and structured as blue hatched regions in Fig. 77 to allow rotor pole tip travelling flux highlighted in Fig. 68 passing blue hatched regions. Therefore, travelling flux at corner 2 induces currents in the blue hatched regions in Fig. 77 functioning as a damper cage. Under this circumstance, there is no need for embedding conventional damper bars inside each rotor pole which is not easy to be cooled. Welding rotor bars under each rotor pole with a small plate is also challenging while excessive heat potentially damages the thin insulation between each rotor lamination. No significant effort is spent to fit integrated damper cages in between rotor poles. Meanwhile, an integrated damper cage is also easy to be cooled as it has more surface area than conventional damper bars that is available to cooling media.

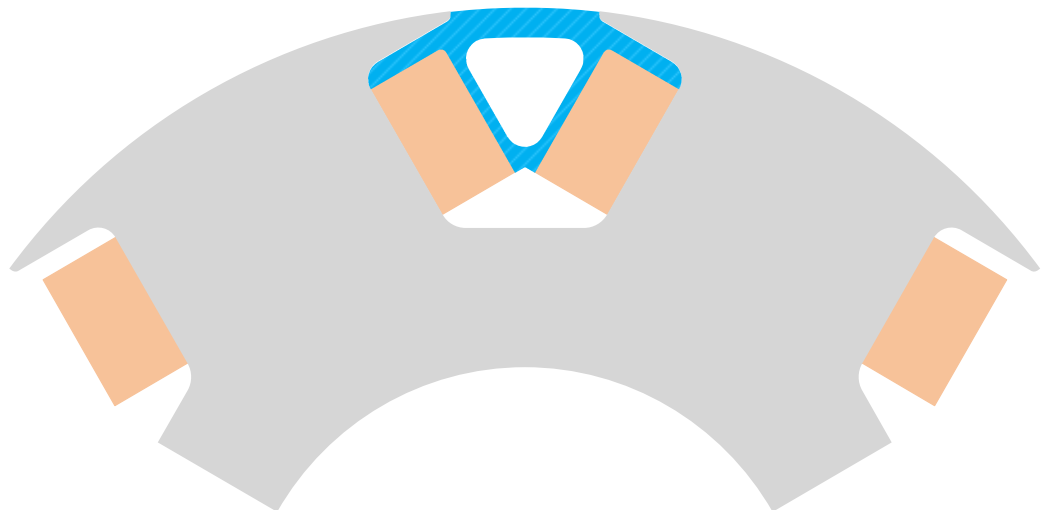


Fig. 77 End caps for retaining field windings (hatched region)

Since retaining structures requires high yield strength, high strength stainless steel or copper alloy is a very good candidate for the first prototype. Copper alloy such as CuCrZr can achieve a yield strength of 450 *MPa*. Stainless steel with proper heat treatment can achieve 1,300 *MPa*. Since rotor stress level with coils is not an easy task to determine, high yield strength stainless would be a good candidate for the first prototype to give an extra mechanical safety. However, martensitic stainless steel without relatively low yield strength (400 *MPa*) is not magnetically conductive and high yield strength (more than 600 *MPa*) austenitic stainless steel is magnetically conductive.

This requires a detailed electromagnetic performance analysis to understand whether an integrated damper cage adopting different materials will have a negative impact on generator performance. In [106], it is concluded that regardless of how rotor poles and rotor windings are designed, a 15% - 20 % pole leakage flux is inevitable for salient pole synchronous machines as shown in Fig. 78 a). If copper or martensitic stainless steel is used as the materials for integrated damper cage, the magnetic circuit is not changed much compared with the conventional damper cage (see Fig. 78 b)). In contrast, if austenitic stainless steel is used as the integrated damper cage, it creates a small reluctance path for originally existing leakage flux and potentially more leakage flux to channel through (see Fig. 78 c)). However, the extra magnetically conductive path might have a positive effect on enabling a more sinusoidal air gap flux density.

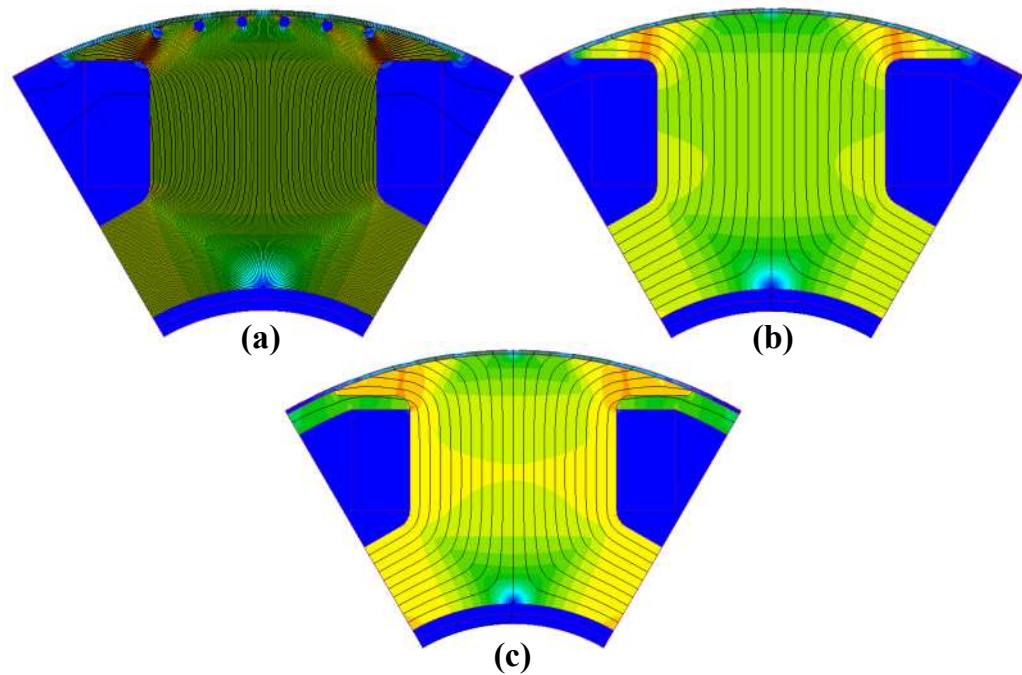


Fig. 78 A WFSG equipped with different damper cage options a) conventional damper cage b) integrated damper cage made of copper c) integrated damper cage made of stainless steel

Copper alloy C18150 and stainless steel 17-4PH with H900 heat treatment are chosen for establishing the FE model shown as Fig. 78 b) and Fig. 78 c) respectively. The no-load terminal voltage behaviour are analysed as a starting point. Fig. 79 plots the air gap flux density of WFSGs equipped with copper C18150 and stainless steel 17-4PH integrated damper cages coloured in red and black line respectively. The air gap flux density of a WFSG with conventional damper cages are also plotted in Fig. 79 (blue dashed lines) for a reference. It is clear that the no-load air gap flux density for a WFSG with conventional damper cages and copper C18150 made integrated damper cages are similar both in terms of waveform and mean flux density ($0.66 T$ and $0.69 T$ respectively). The no-load air gap flux density for 17-4PH made integrated damper cages are the most sinusoidal one among all three options.

However, the downside is that the average flux density is the 0.63 T about 4.5% less than that of conventional damper cages since magnetically conductive stainless steel 17-4PH introduced more leakage flux to the overall magnetic circuit.

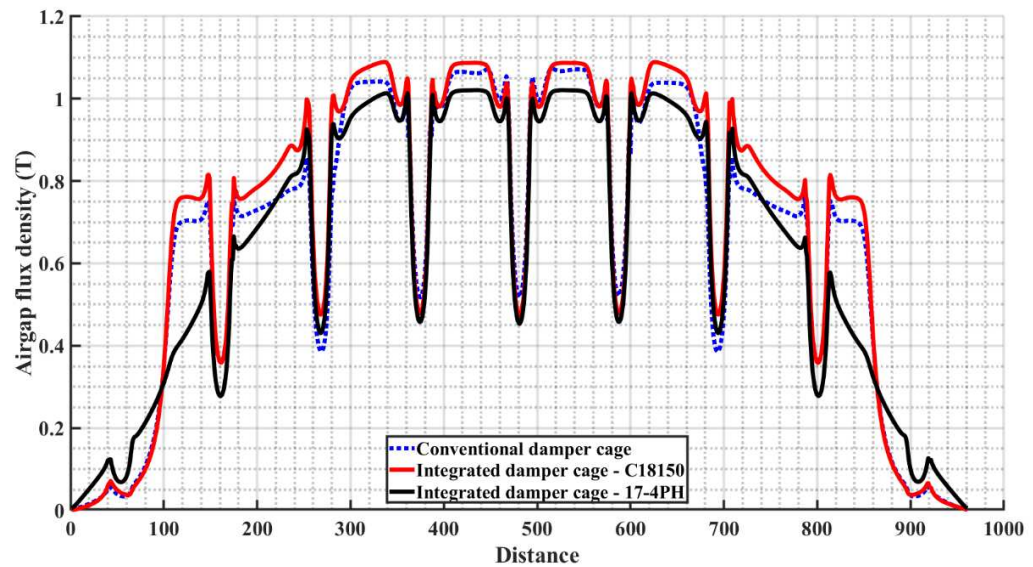


Fig. 79 No-load air gap flux density for three different damper cage options

Based on the analysis above, it is clear that stainless steel 17-4PH made integrated damper cage are able to cancel harmonics presented in the no-load air gap flux density. THD reduction techniques summarized in [77] focuses on single operation speed optimization. The THD level been optimized with techniques introduced in chapter 4.1.2 has an optimum point at 9,000 rpm. For the rest operating speed region, an observable increase of THD level from 2% to 4.5% is shown in Fig. 37. The WFSG designed in this thesis has to focus on the THD reduction through the entire operating speed region. Therefore, the harmonic cancelling capability of integrated damper cages made of magnetically conductive materials are studied regarding to which type of harmonics are cancelled and whether THD reduction can be kept consistent through all the variable speed conditions. The no-load harmonic contents

of a WFSG without any THD reduction techniques at 7,200 *rpm*, 9,000 *rpm*, 12,000 *rpm* and 16,000 *rpm* are plotted in Fig. 80 as a reference. 3rd, 7th, 9th, 11th, 13th, 15th, 17th, 19th, 33rd, 35th and 37th high frequency harmonics are all presenting in Fig. 80. The 17-4PH made integrated damper cages are firstly installed on a WFSG with no THD reduction techniques, such as short pitching, pole shaping or skewing. The no-load harmonic contents for this harmonic rich WFSG (17-4PH integrated damper cages) at four different speeds are presented in Fig. 80.

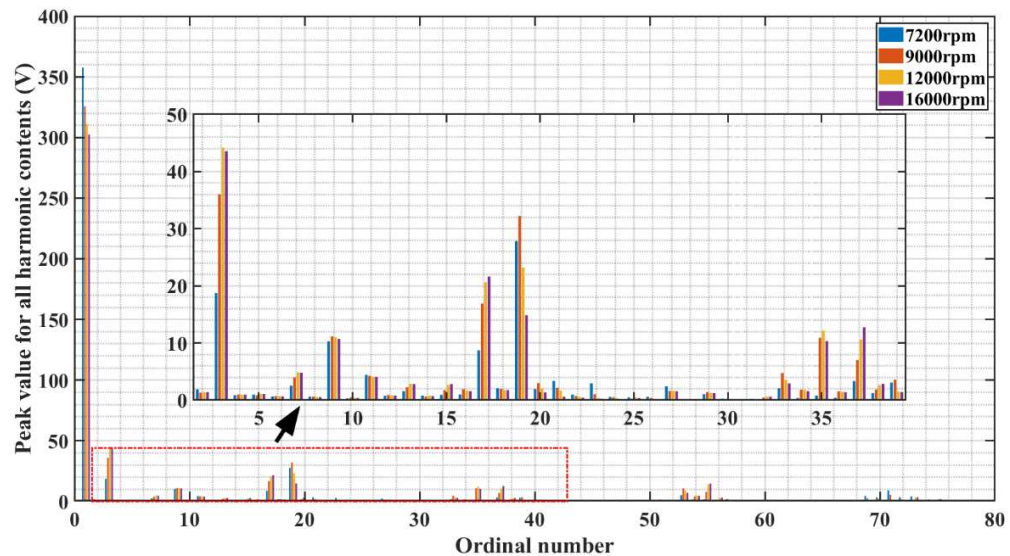


Fig. 80 Harmonic contents for a WFSG without any THD reduction technique at 7,200 *rpm*, 9,000 *rpm*, 12,000 *rpm* and 16,000 *rpm*

By comparing Fig. 80 and Fig. 81, 17-4PH made damper cages cancels almost all the harmonics apart from the 3rd harmonic. Observable higher order harmonics (greater than 3) left in Fig. 81 is 17th and 35th harmonics. Meanwhile, the magnitude of each higher order harmonic (greater than 3) contents presented in Fig. 81 at 7,200 *rpm*, 9,000 *rpm*, 12,000 *rpm* and 16,000 *rpm* are quite similar. The higher order harmonic (greater than 3) contents at 7,200 *rpm*, 9,000 *rpm*, 12,000 *rpm* and 16,000

rpm are 1.58%, 1.41%, 1.90% and 1.93% respectively. Therefore, by getting rid of 3rd harmonics, 17-4PH made integrated damper cages are able to suppress higher order harmonics significantly while keeping the THD level consistent among all the operating speed. Hence, 2/3 short pitching and 17-4PH made integrated damper cages are implemented together to reduce the 3rd harmonics. Fig. 82 plots the harmonic contents a WFSG with 2/3 short pitching and 17-4PH made integrated damper cage at 7,200 *rpm*, 9,000 *rpm*, 12,000 *rpm* and 16,000 *rpm*.

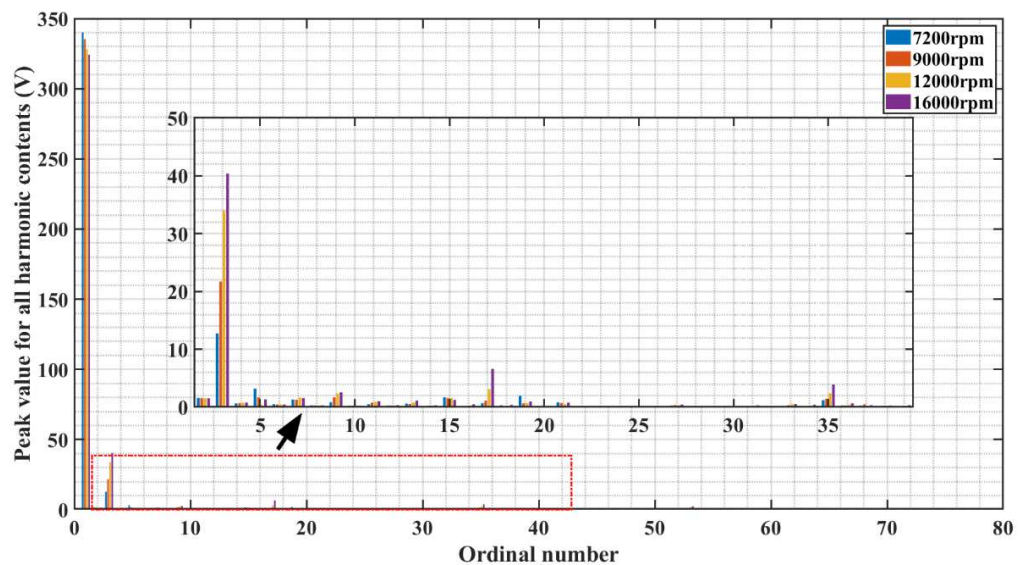


Fig. 81 Harmonic contents for a WFSG with 17-4PH made integrated damper cages with no 2/3 short pitching and no skewing at 7,200 *rpm*, 9,000 *rpm*, 12,000 *rpm* and 16,000 *rpm*

With two THD reduction techniques introduced in Fig. 82, nearly all the harmonic contents are eliminated from the three phase thermals. The 2nd to 40th order harmonic contents are zoomed in in Fig. 82 at each speed are almost the same as the harmonic contents presented in Fig. 81. Therefore, combined 2/3 short pitching and 17-4PH H900 made integrated damper cage has little combined effects on higher order harmonics. The THD level for the WFSG configuration in Fig. 82 at 7,200 *rpm*,

9,000 *rpm*, 12,000 *rpm* and 16,000 *rpm* are 1.62%, 1.40%, 1.28% and 1.76%. This amount of THD level are already lower than the WFSG proposed at the end of chapter 4 that is designed with 2/3 short pitching and a skewed stator with one slot pitch. In this case, another FE analysis is performed to see if 2/3 short pitching, one stator slot pitch and a 17-4PH made integrated damper cage reduces the THD even further.

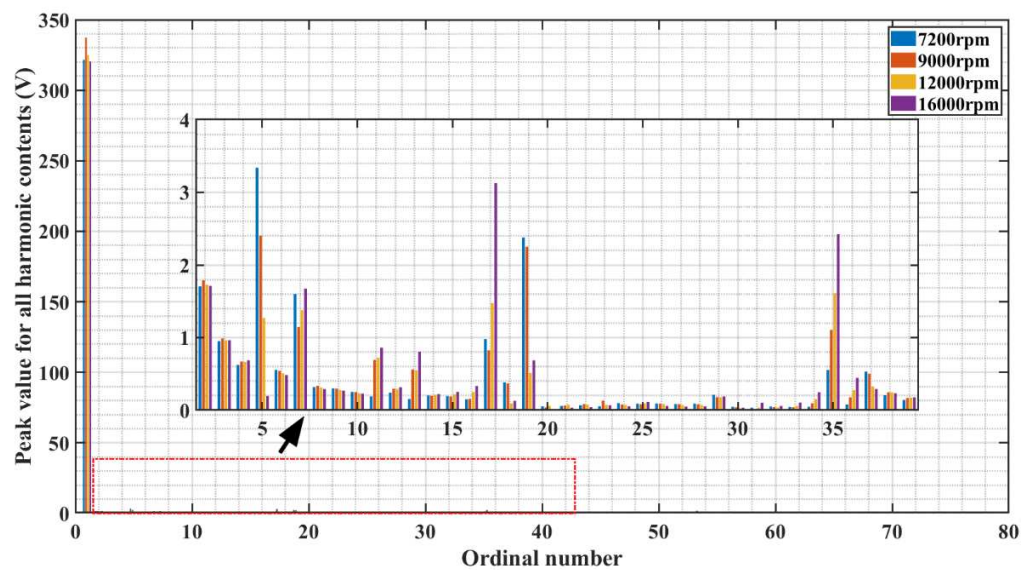


Fig. 82 Harmonic contents for a WFSG with 17-4PH H900 made integrated damper cages and 2/3 short pitching at 7,200 *rpm*, 9,000 *rpm*, 12,000 *rpm* and 16,000 *rpm*

Fig. 83 presents the harmonic contents for a WFSG with 17-4PH made integrated damper cages, 2/3 short pitching and one stator slot pitch skew at 7,200 *rpm*, 9,000 *rpm*, 12,000 *rpm* and 16,000 *rpm*. By comparing the zoomed in window in Fig. 82 and Fig. 83, one stator slot skew helped suppressing the 7th, 11th, 13th, 17th, 19th, 35th and 37th harmonics which is within expectations. The THD level for the WFSG configuration in Fig. 82 at 7,200 *rpm*, 9,000 *rpm*, 12,000 *rpm* and 16,000 *rpm* are 1.11%, 0.83%, 0.58% and 0.69%. A 17-4PH H900 based integrated achieves a much

lower THD compared with those value achieved in chapter 4. There is still copper C18150 based integrated damper cage option been proposed in this thesis. A FE analysis is performed next to understand the impacts of magnetically non-conductive materials on the THD level.

Based on the no-load air gap flux density waveform in Fig. 79, the no-load flux density for copper C18150 made integrated damper cage contains almost the same amount of harmonics compared with no-load flux density for a WFSG with conventional damper cages. Therefore, copper C18150 made integrated damper cages are not able to cancel the 3rd harmonic. A WFSG equipped with 2/3 short winding and C18150 made integrated damper cages are investigated to understand the harmonic cancelling capabilities. Fig. 84 plots the harmonic contents for a WFSG equipped with C18150 made damper cage with 2/3 short pitching. By comparing Fig. 84 and Fig. 80, it is clear that the 3rd and 9th harmonic are eliminated by 2/3 short pitching. Meanwhile, with the presence of C18150 made integrated damper cage, the 9th and 19th harmonics are suppressed but the 17th harmonic is enhanced. Therefore, it can be concluded that the harmonic cancelling capability for non-magnetic conductive integrated damper cage is not effective.

The harmonic cancelling capabilities for 17-4PH and C18150 made integrated damper cage has been elaborated. The THD level for WFSG equipped with different integrated damper cage are presented in Fig. 85. A 2/3 short pitching WFSG with 17-4PH H900 made integrated damper cage achieve better THD performance compared with the best performing WFSG option designed in chapter 4 (2/3 short pitching and stator skewing). In Fig. 85, 2/3 short pitching WFSG with 17-4PH

H900 made integrated damper cage maintains its THD level at 1.2% to 1.6% at speed region from 7,200 *rpm* to 16,000 *rpm*. In contrast, a WFSG with 2/3 short pitching and stator skew technique can only obtain a THD from 2.4% to 4.4% from 7,200 *rpm* to 16,000 *rpm*. By combining 2/3 short pitching, stator skewing and 17-4PH H900 integrated damper cages, the THD level can be reduced to an astonishing level which is close to 1% as shown in Fig. 85. Meanwhile, the THD level are at higher speed for a WFSG with 2/3 short pitching, stator skewing and 17-4PH H900 made damper cage is between 0.6 to 0.8% . An integrated damper cage made of C18150 did not have a powerfully harmonic cancelling technique. Therefore, the THD level for a WFSG equipped with C18150 made integrated damper cage is still governed by the conventional THD reduction technique.

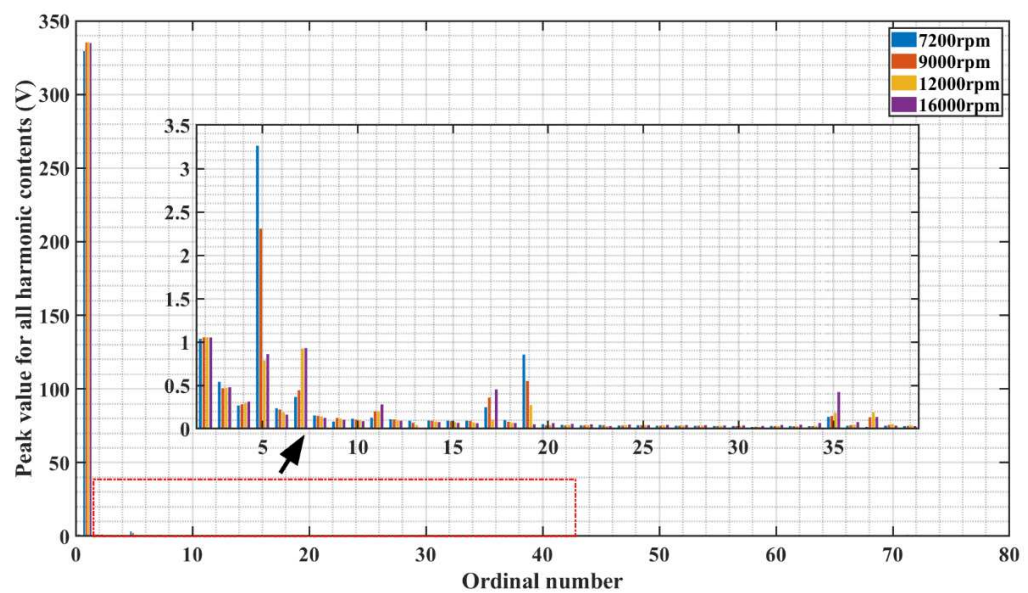


Fig. 83 Harmonic contents for a WFSG with 17-4PH made integrated damper cages, 2/3 short pitching and one stator slot pitch skew at 7,200 *rpm*, 9,000 *rpm*, 12,000 *rpm* and 16,000 *rpm*

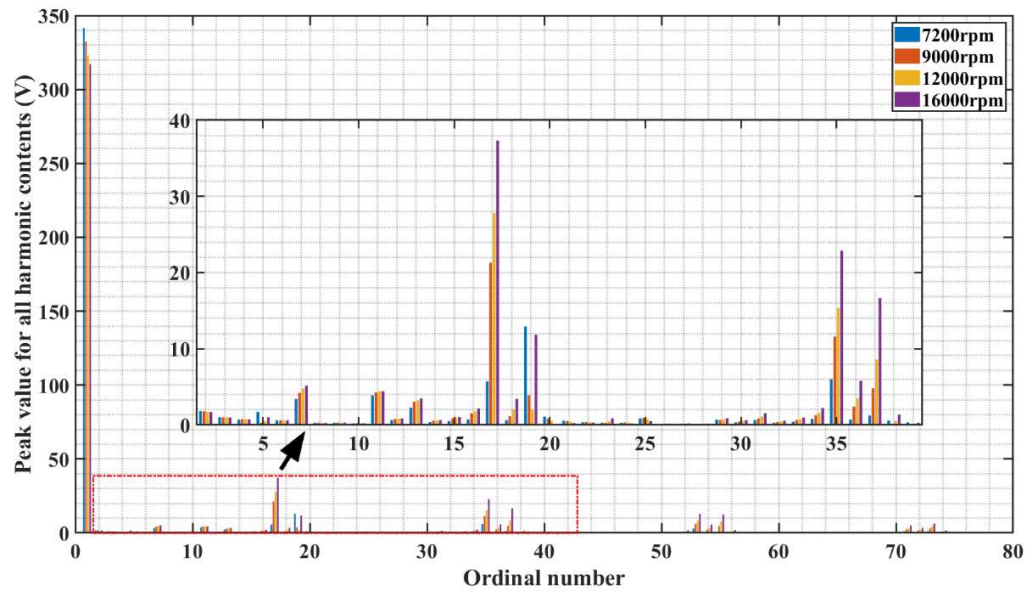


Fig. 84 Harmonic contents for a WFSG with C18150 made integrated damper cages, 2/3 short pitching at 7,200 rpm, 9,000 rpm, 12,000 rpm and 16,000 rpm

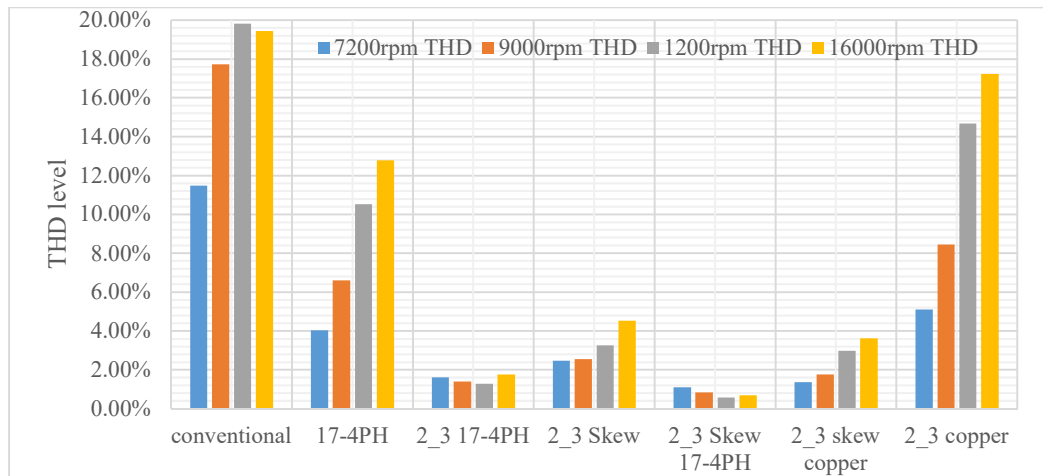


Fig. 85 THD level for WFSG equipped with integrated damper cage made of 17-4PH and C18150

In conclusion, a WFSG equipped with 17-4PH made damper cages help a WFSG to maintain the THD at similar value across the entire speed region compared with the WFSG designed in chapter 4. This feature is a great benefit to variable speed drives it has to operate under large speed range continuously. Consistent THD level at all

speed region ensures the power quality at any condition is at its lowest possible state. Since the expanded applications field also requires a WFSG to operate as a motor. Torque ripple becomes an essential factor that determines the performance of a machine. The torque ripple for a WFSG equipped with 17-4PH H900 integrated damper cages achieves a torque ripple at 2000 *rpm*, 4692 *rpm* 5500 *rpm* and 6780 *rpm* are 15 *Nm*, 15 *Nm*, 8.4 *Nm* 7.6 *Nm*. Comparing these value with Fig. 39, a 50% reduction in term of torque ripple is achieved. Hence the vibration and noise level for WFSG designed with 17-4PH integrated damper cages are significantly reduce. Meanwhile, a damper cage must have the capability to recover the generator from disturbance. Fig. 86 presents three phase terminal short circuit transient behaviour from no-load operation. It shows that an integrated damper cage does function like a conventional damper cages. At around 400 *ms*, the short circuit current reaches the steady state.

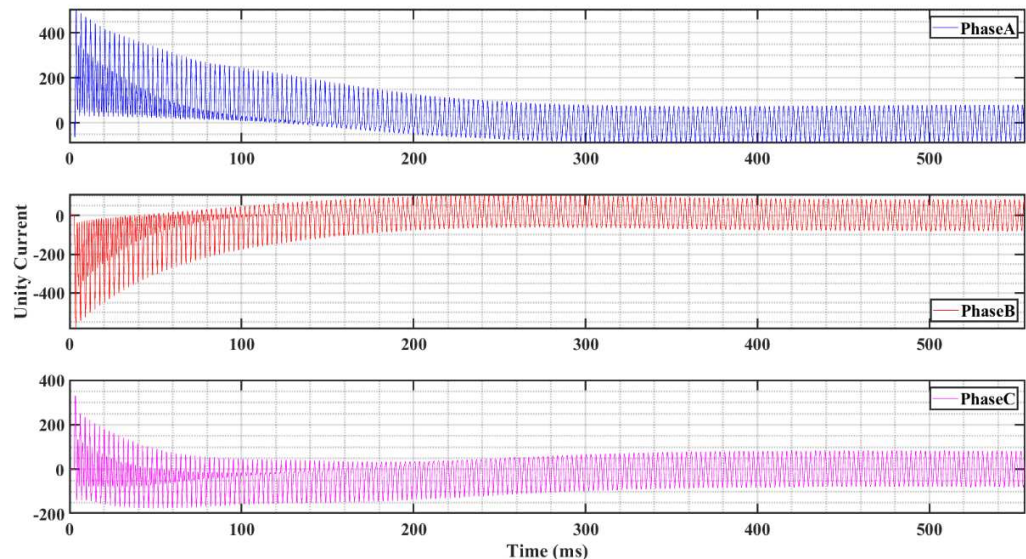


Fig. 86 Short circuit transient behaviour for a WFSG equipped with 17-4PH H900 made integrated damper cages

At this stage, 17-4PH H900 made integrated damper cage has showed its advantageous features for THD minimization under full range operating speed and torque ripple during generator starting period. However, 17-4PH H900 is not the only magnetic conductive materials. Next part investigates how magnetic properties can affect the performance of an integrated damper cage. A3 steel and 17-4PH H1150 are chosen for electromagnetic FE analysis.

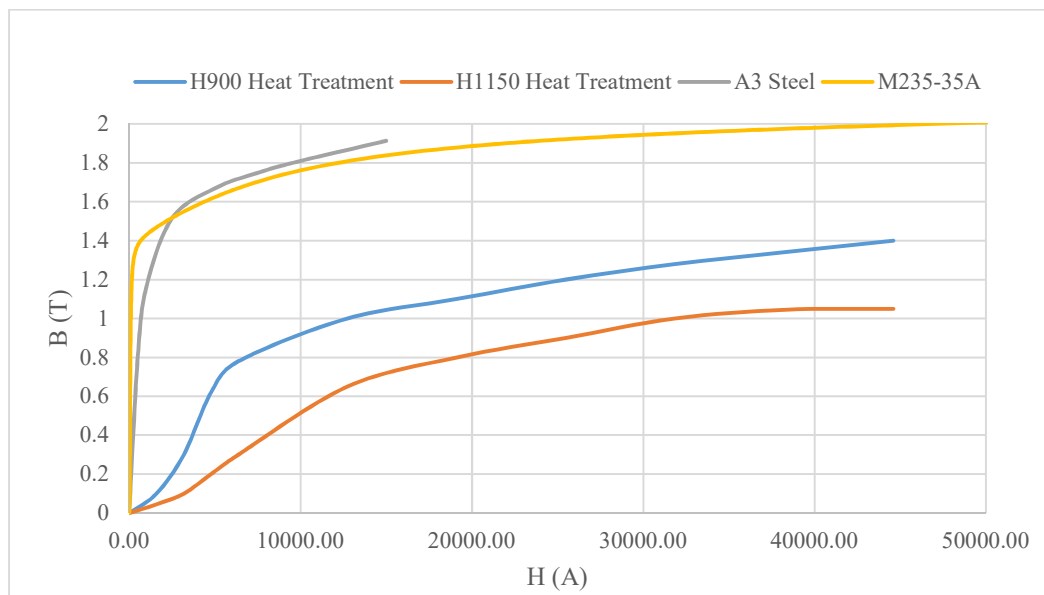


Fig. 87 B-H properties for A3 steel, 17-4PH with H900 heat treatments, 17-4PH with H1150 heat treatments and M235-35A

Fig. 87 presents the BH properties for A3 steel, 17-4PH with H900 heat treatments and 17-4PH with H1150 heat treatments. A3 steel almost have identical BH properties compared with M235-35A. 17-4PH with H1150 heat treatments has a much lower saturation point compared with M235-35A. 17-4PH with H900 heat treatments has a moderate saturation point compared with M235-35A. All of these three steel are implemented as integrated damper cages for a WFSG THD performance analysis.

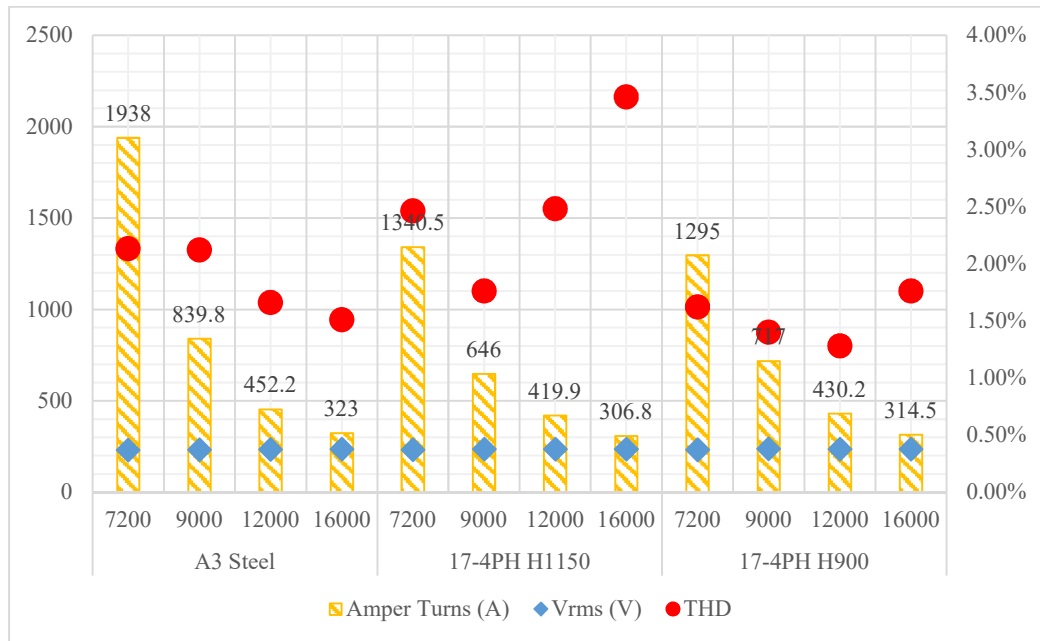


Fig. 88 Phase RMS voltage, no-load amper-turns and no-load THD for WFSGs equipped with integrated damper cages with different materials

Fig. 88 shows the no-load analysis for WFSGs with integrated damper cages with different BH properties. To obtain the 235 volts RMS at terminals, a WFSG equipped with A3 steel costs the highest amper-turns since A3 steel is a very good magnetic conductor which produces significant amount of leakage flux during operation. The THD level for A3 steel marked in orange circle in Fig. 88 is about 23% higher than that of 17-4PH with H900 heat treatments. From both rotor amper-turns and THD perspective, high magnetic conductive A3 steel is not a good option for WFSG integrated damper cage design. 17-4PH H1150 has 4% higher rotor amper-turns compared with 17-4PH H900 at no-load condition. However, the THD level for 17-4PH H1150 is 51% to 108% higher than 17-4PH H900. Therefore, 17-4PH H900 has better performance in terms of rotor amper-turns and THD level. Due to the advantages offered by 17-4PH integrated damper cage, the final prototype is

decided to be equipped with integrated damper cage rather than the conventional damper cage.

As discussed in chapter 5.2.1 endcaps (cross sectional view) for retaining field winding is necessary as shown in Fig. 77. Another function for endcaps are holding field windings at their original places. Two end rings lock endcaps moving towards both axial and radial directions as indicated in Fig. 6. Weight contributed by field windings weakens the pole tip (corner 2) by comparing Fig. 65 and Fig. 67. Endcaps are there to reduce centrifugal force from being applied on the pole tip. Therefore, a small gap is left between pole tip and endcaps to accommodate the deformation of endcaps. The distance is determined by the maximum deformation of rotor pole tips with the equivalent mass been applied on the endcaps under worst operating speed. An assumption is made here that the centrifugal force is not entirely transferred to rotor body and pole tip. Therefore, the stress simulation with added endcaps is close to the scenario of case 3 presented in Fig. 65. The practical stress level in reality for the rotor core is between the stress simulation presented in Fig. 89 and Fig. 74.

Fig. 89 presents the Von-Mises distribution of case 3 analysis with 4 mm and 3 mm fillets at corner 1 and 2 respectively considering the negatives impact of copper coils on SiFe steel is tackled by endcaps. In Fig. 89, the stress at corner 1 and 2 are reduced substantially by applying endcaps compared with case 4 in Fig. 71. Stress at damper edge 3 are not considered as methods presented in chapter 5.2.2 and 5.2.3 can successfully reduce the stress level at damper edge 3.

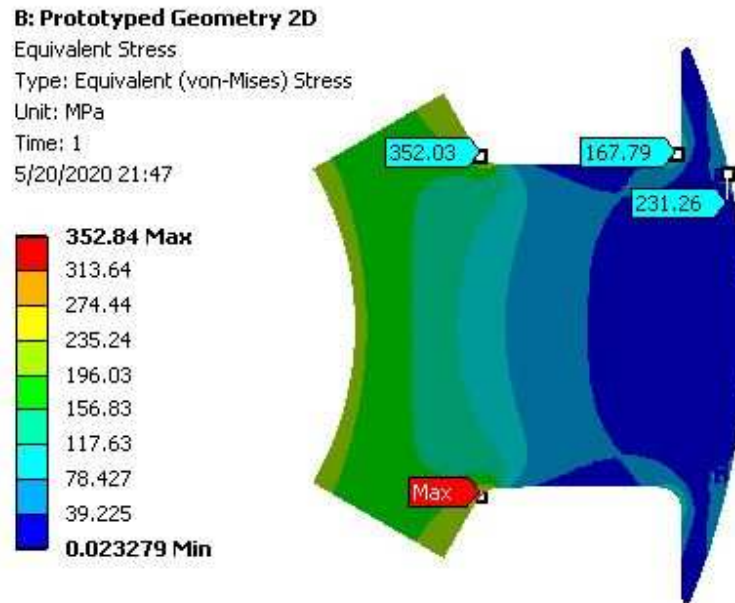


Fig. 89 Von-Mises distribution for case 3 (rotor core and damper cages) with 4 mm and 3 mm fillets at corner 1 and 2 respectively

In summary, considering a real rotor core presented in Fig. 6 and Von-Mises distribution analysis in chapter 5.2, the presence of endcaps is inevitable. Therefore, this chapter takes one step further considering merging a damper cage with endcaps while keeping all the functionalities of damper cage possible. Since the end caps are solid material filling region under pole tips, traveling flux are presented under the pole tip as shown in Fig. 68 under loaded conditions. As a result, end caps under the pole tips have eddy current induced and circulating inside. This solid piece of metallic structure is acting like a solid damper cage. A damper cage starts its operation during scenario listed in chapter 2.5.1.

5.2.5 Deformation of rotor structure for WFSGs

The Von-Mises distribution analysis for the WFSG geometry proposed in chapter 4 has been finished. Solutions to address high stress concentration on rotor pole are

proposed in chapter 5.2 and Von-Mises distribution analysis on those solutions are also given. In addition to this, another important factor contributing to the sizing of a WFSG dimensions is the total deformation of a rotor geometry. Materials deforms during high speed rotation and this increases the chance of a collision between a rotor and stator core. In this case, the diameter of the rotor core is not only determined by whether a rotor core can sustain in one piece during high speed operation, but also governed by the magnitude of the geometrical deformation at high speed. Therefore, an understanding of rotor core deformations must be taken into consideration so that any rotor core part does not touch the stator core during maximum speed operation.

Fig. 90 presents the total deformation of a rotor core with damper bars and field windings at maximum speed. The maximum total deformation is located at pole tip region which is about 0.13 mm . This amount of deformation counts for 13% of the overall air gap length. The minimum deformation alongside the rotor periphery is at the centre of the rotor pole. The deformation at the centre is 0.06 mm as shown in Fig. 90. The understanding of the deformation of rotor core is essential both from a mechanical and electromagnetic perspective. The air gap length is 7.7 times the maximum deformation. Therefore, rotor structures did not touch the stator core. From an electromagnetic perspective, the maximum deformation of the rotor core has reduced the air gap length by 13%. Meanwhile, the centre of rotor core in Fig. 90 is increased by 0.06 mm . The deformation of rotor core from the centre to a pole tip is not a constant as shown in Fig. 90. This forms an in-consistent air gap which is similar to pole shaping but with a different style compared with the method mentioned in chapter 4.1.2.

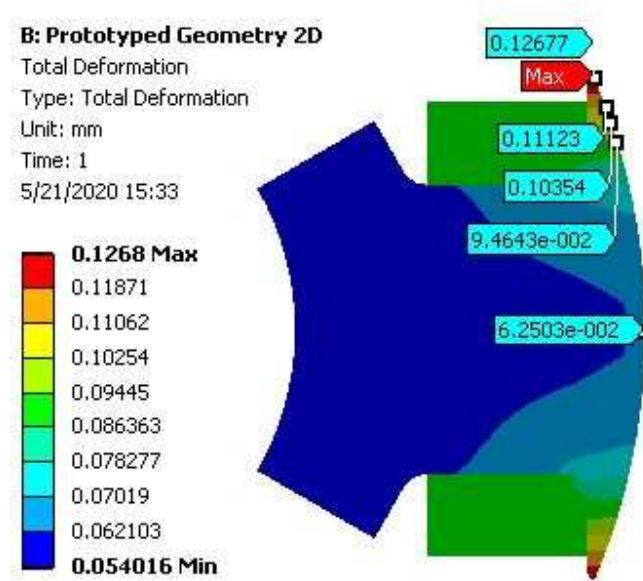


Fig. 90 Total deformation for a rotor core geometry for case 4 (rotor core, damper bars and field windings)

5.3 Further considerations for improving the performance of a WFSG

All the above analysis in chapter 4 and 5 concludes the performance of a WFSG in electromagnetic, thermal and mechanical aspects. Purple dots in Fig. 2 presents the development path for WFSGs. The performance of a WFSG has been essentially increased from 150 to late 1980s [1]. However, after the late 1980s till 2003 the WFSG has not been really improved for WFSGs installed on board. The state of the art WFSG with starting functions introduced by the Boeing 787 in 2003 achieved a power density of 2.7 kW/kg which is similar to WFSG without starting function installed on the Boeing E-4B Command Post. WFSGs have not seen any break through or improvement for almost 15 years. On the other hand, aerospace industry and academic fields are seeking for other options such as PM and SR generators to gain enhancements in weight.

Promising results in terms of weight saving can be seen in Fig. 2 from PM and SR generator families. Although WFSGs are still a preferable option due to reliability and safety concerns, PM and SR generators are quickly catching up with more resources spent on developing these two generator families. However, in 2013 Honeywell introduced their astonishing 1 MW WFSG with a power density of 7.9 kW/kg . This is a true breakthrough in industry that the power density of a WFSG is increased up to an unprecedented point. This chapter focuses on how to improve the performance of a WFSG from a design perspective.

5.3.1 Effects of air gap length on the overall WFSG performance

WFSGs introduced by Honeywell can adapt both AC and DC grid (230 VAC , 300 VDC and 600 VDC). Table 15 compares the Honeywell 200 kVA, 1 MW and the Boeing 250 kVA generators in terms of some key performance value. At system level, Honeywell system still achieves a power density at 7.6 kW/kg and 6.3 kW/kg for AC and DC grid respectively. These values are still competitive against quiet a lot of PM and SR generators alone presented in Fig. 2. Since a PM or SR generator requires an over-rated converter, the power density of PM or SR generators at system level is lower than values indicated on Fig. 2. Therefore, overall performance of Honeywell's WFSG is pretty outstanding even compared with PM and SR systems.

Comparing 200 kVA, 1 MW Honeywell prototypes and the Boeing 787 WFSG, the efficiency are 90%, 97% and 85% respectively. As a result, the efficiency of Honeywell mega-watt class WFSG is very competitive among its family and other generator topologies (see Table 1). Theoretically, when the power density of a

machine increases, the efficiency drops due to increased losses caused by increased current density. However, the efficiency of an even higher power density machine has increased in the comparison. Thus, how to reduce losses during the operation of a WFSG become a challenging aspects.

Table 15 Key performance comparison of the state of art WFSG introduce lately

	Honeywell	Honeywell	Boeing 787
Dimensions (mm)	203×203×241	355×355×609	350×368×459
Rated Power (kVA)	200	1000	250
Weight of Generator (kg)	25	127	92
System weight for AC Grid (kg)	28	131	
System weight for DC Grid (kg)	45	158	
Efficiency (Rated)	90%	98% (AC) 97%(DC)	85%

The power density of the active part of a WFSG designed with geometry in Fig. 71 is 3.1 kW/kg . The resultant overall efficiency for a WFSG is 88.5% at rated load based on electromagnetic FE analysis. The real power density for the WFSG designed with geometry in Fig. 71 is lower than 3.1 kW/kg since none active weight reduces the overall power density. However, the WFSG designed with geometry in Fig. 71 hits the limitation for soft-magnetic materials (B-H curve), temperature (220 °C insulation grade for copper wire), yield strength of M235-35A based on analysis in chapter 4 and 5.

Therefore, aggressive approaches for generator design choice are necessary to be considered to push the performance of a WFSG to an unprecedented value. Air gap length is a critical parameter during the design process of a WFSG since air gap

length has a chain effect on WFSG performance such as required field currents, rotor temperature mechanical feasibility and efficiency.

Table 16 MMF consumed by different part of a WFSG for case 4 geometry (see Fig. 71) with specific flux density

	MMF (A)	Flux density (T)
Air gap	802	0.9
Stator teeth (straight)	273	1.8
Stator teeth (round)	25	1.7
Stator yoke	153	1.6
Rotor body	107	1.6
Rotor yoke	91	1.7

Table 16 compares the MMF consumed by different part a WFSG for case 4 geometry (Fig. 71) at specific flux density. The MMF consumed by 1 mm of air gap is 802 *A-turns* to establish magnetic field in the air gap with peak flux density of 0.9 T. This amount of MMF for establishing air gap flux density counts for 55% of the overall MMF created by the field windings.

For a PM machine, pushing flux density in the air gap, stator teeth and rotor body etc. is one way to reduce the amount of core material used for a machine for weight critical application. However, for a WFSG this is not entirely true. Pushing flux density in the rotor core means more MMF is required, which results in the high number for turns wounded on the rotor core. Practically, the area reserved for a given rotor geometry is not infinite to accommodate largely increased number of coils. In addition, increased MMF created by the field winding means higher rotor core losses which results in spiked rotor temperature and reduce efficiency.

Therefore, a feasible way to improve the performance of a WFSG is the decrease the MMF required from rotor coils. Reducing the flux density on the core of a

generator at the knee point balances the utility of the soft-magnetic material and the MMF required from field winding. Another more effective method is to reduce the air gap length since magnetizing the air gap requires a significant amount of MMF as shown in Table 16. However, the air gap length is also a critical parameter that is determined by mechanical constraints such as rotor core deformation and assembly misalignment of rotor shaft. Based on the analysis of chapter 5.2.5, the maximum deformation of the rotor core is 0.13 mm at a pole tip. Theoretically, the air gap length can be reduce to 0.5 mm while still retain the safe operation at the maximum speed.

Shorter air gap length means less copper wire required from field windings. This results in less A-turns on the rotor pole which increase the performance in four aspects: 1) reduced rotor losses 2) reduced rotor temperature 3) reduce rotor copper weight 4) potentially reduce centrifugal force applied on pole tips.

5.3.2 Methodologies for stress reduction at critical spots

Based on the information in Table 15, the radial envelope for three WFSGs presented in the table remains unchanged. Since no information is available in terms of the reasons behind it, this chapter tries to answer it with several guesses. One possible reason is that the empty envelope to accommodate a WFSG inside an aero-engine is limited to 350 mm. Therefore, it is not possible to further increase the radial size of a WFSG regardless of the constraint limited by the yield strength of the material. Under this circumstance, there is nothing that a machine designer can do to help increase the performance of a machine.

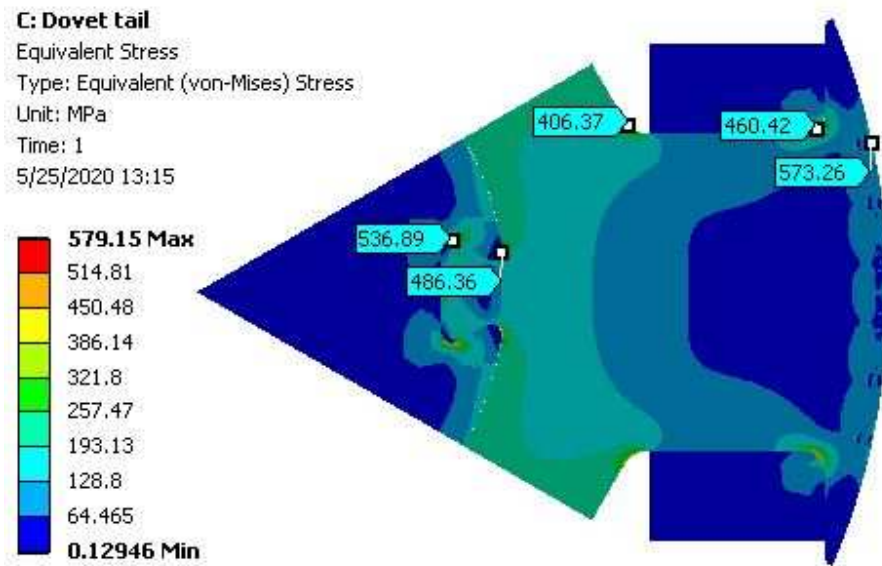


Fig. 91 Von-Mises distribution for case 4 (rotor core, field coils and damper cages) with 4 mm and 3 mm fillets at corner 1 and 2 respectively; a dovetail is added at the bottom of the rotor core

Another highly possible reason is that is radius of the rotor core of a WFSG is limited the yield strength or the tensile strength of the material. Based on the analysis in chapter 5.2, the safety margin is not enough without adopting high grade materials. This chapter gives some design considerations to reduce the stress concentration at three critical spots. In [121], advanced fitting techniques from aerospace turbine blade roots are implemented to fit magnetic cores in place. However, this type of fittings is potentially difficult and requires substantial amount of knowledge of manufacturing and processing. Therefore, a less difficult dovetail fittings adopted by aerospace industry to fit fan blades onto a fan disk is considered as an option to reduce the stress level at three critical spots appeared in chapter 5.1.2. The geometry used for adding a dovetail is the geometry presented in Fig. 71. The stress

concentration at corner 2 and damper edge 3 are not discussed here as those issues have been tackled by the methods presented in chapter 5.2.

The fittings between the rotor core including dovetail and the shaft is designed to have a clearance to ensure the smooth assembly of the complex rotor structure and the shaft. In Fig. 91, the stress at corner 1 is reduced from 472 *MPa* to 406 *MPa* achieving a 14% reduction. However, the stress at the dovetail sees a stress at 486 *MPa* which is dangerous for core material to sustain by itself. On the other side, the shaft experiences a stress level up to 536 *MPa*. The material for the shaft implemented in Fig. 91 is 17-4PH H900 which has a yield strength of 1300 *MPa* with H900 heat treatment process. Therefore, this shaft is able to handle the maximum stress at the worst case operating speed with more than 2 times the safety factor.

Since the stress level concentrated at the corner of the dovetail is of great concern, a modified version of a WFSG with bigger radius at the root corner is presented in Fig. 92. This method has shown a reduction of stress level at the bottom corner from 486 *MPa* (Fig. 91) to 344 *MPa* (Fig. 92) achieving a 30% reduction. Meanwhile, the stress a corner 1 only varies by 1.7% which is negligible. With an extra introduced dovetail, the stress a corner 1 reached a safe point where the safety factor is 1.4. This value is higher than the UoN recommended value 1.24. The stress level experienced by the inverse dovetail is 485 *MPa* that is substantially less than the yield strength of shaft material (17-4PH, 1300 *MPa*).

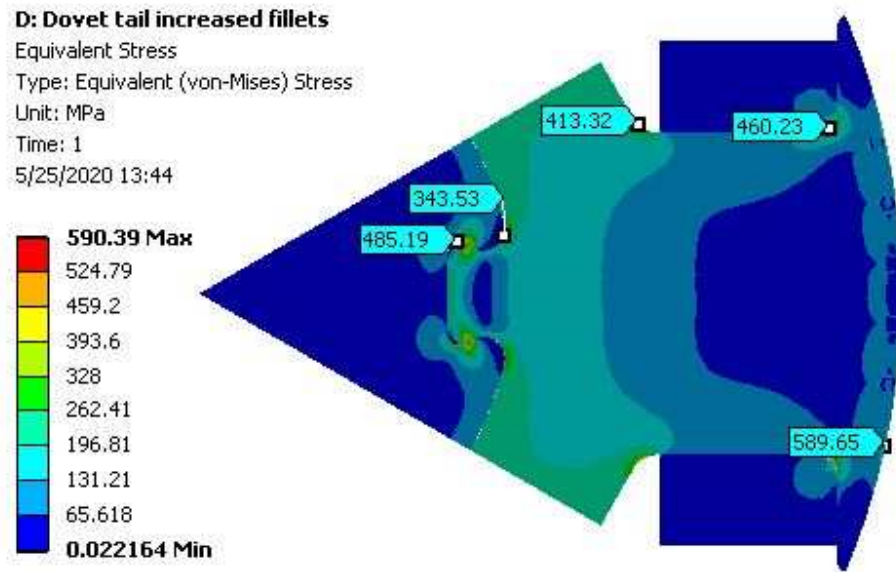


Fig. 92 Von-Mises distribution for case 4 (rotor core, field coils and damper cages) with 4 mm and 3 mm fillets at corner 1 and 2 respectively; a dovetail is added at the bottom of the rotor core with increased fillets

Due to limited available time, the shape of the dovetail root is not optimized using the Ansys built optimizer. Therefore, the optimized shape for a dovetail root and the dovetail accommodation on the shaft have not been found in this thesis, which is carried out as further work for this thesis. But, with the assistance of the dovetail root, it is possible to increase the radius of a WFSG without selecting better grade material such as CoFe and 35HXT780T. Increasing the radius of a generator potentially helps reducing the overall weight of a generator.

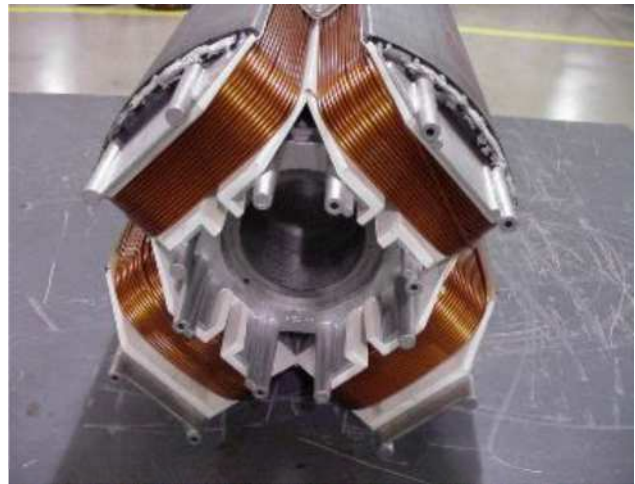
To summarize, the air gap length reduction and dovetail methods presented in chapter 5.3.1 and 5.3.2 together are able to assist geometry in Fig. 92 function more safety and potentially reduce the weight of the generator by increasing the radius of the rotor core with changing high grade materials.

5.3.3 Practical limitations for assembling a WFSG in house

In chapter 5.2 and 5.3, a Von-Mises distribution for a complete 6 pole rotor core is analysed. Mature industry enterprises such as Cummins Generator Technologies Inc. and Alliance Winding Equipment Inc. are able to wind the rotor coils on each rotor pole using specialized equipment, tool and jigs with a single wire as presented in Fig. 93 a) and b). However, by having a discussion with these industry representatives, the lead time and cost for winding these types of coils is unaffordable. Due to the lack of specialized equipment, tools and jigs, technicians in house suggested separating a rotor core into 6 pieces and wind the rotor coils on each rotor pole individually. Under this circumstance, geometry presented in Fig. 71 is not available for connecting each individual pole onto the shaft. Therefore, having a dovetail on each pole becomes a solution to the issue raised by the winding process.



(a)



(b)

Fig. 93 a) Cummins generator winding process b) Rotor core wound by Alliance winding

Given the circumstance, the final geometry decided for manufacturing is 17-4PH H900 integrated damper cage option with dovetail dimensions presented in Fig. 91 considering both the manufacturing availability, lead time, assembly capability in house and cost. Another Von-Mises distribution analysis for a separated rotor core case is necessary to understand the maximum achievable speed of the WFSG for the geometry described.

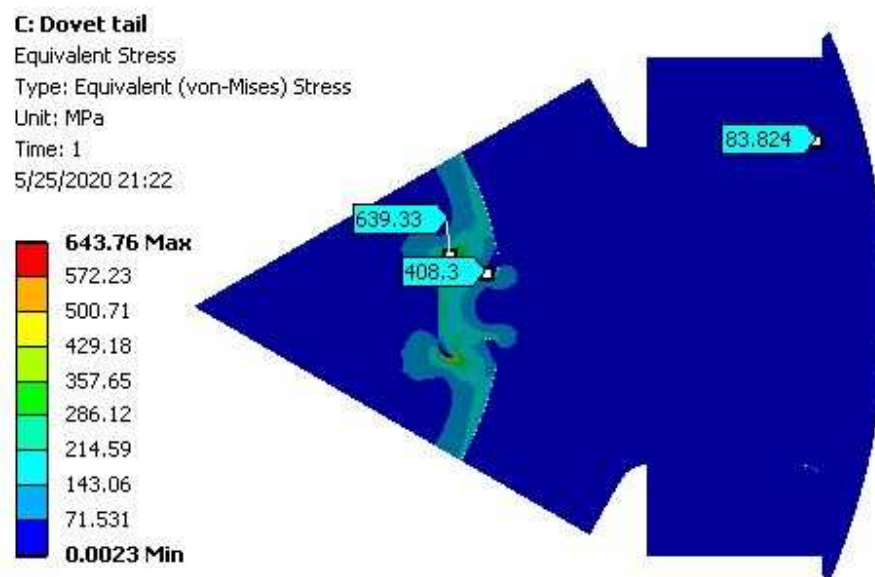


Fig. 94 Von-Mises distribution of a separate rotor core at 6,800 *rpm*

Fig. 94 and Fig. 95 presents the Von-Mises distribution of a rotor core been separated into 6 pieces under 6,800 *rpm* and 7,200 *rpm*. A dovetail carries all the weight on the rotor core including core material itself. At 6,800 *rpm*, the maximum stress (408 *MPa*) occur at the bottom of the dovetail corner in Fig. 94. A safety factor of 1.37 is achievable at 6,800 *rpm*. At 7,200 *rpm*, the stress level at the bottom corner of the dovetail has reached the yield strength of M235-35A achieving a safety factor of only 1.2.

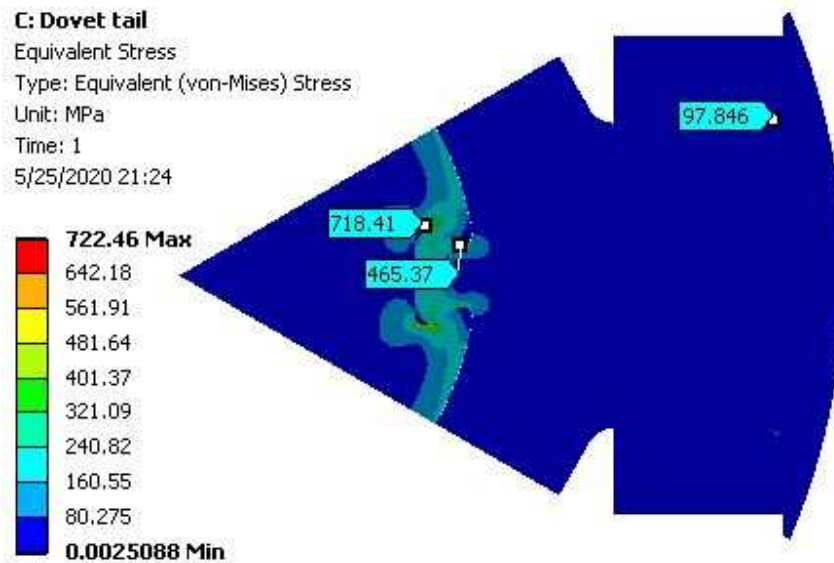


Fig. 95 Von-Mises distribution of a separate rotor core at 7,200 *rpm*

Although the new rotor configuration presented in Fig. 94 and Fig. 95 cannot operate at full speed that is required in chapter 1, the knowledge learnt by manufacturing the geometry in Fig. 94 is still valid. The main reasons are as follows. First, the conventional fittings between rotor core and the shaft adopting geometry in Fig. 71 using either interference fit or keyways with some clearance are pretty mature techniques. The mechanical understanding of the geometry shown in Fig. 71 is also quite mature [70]. Second, the unknown of adopting dovetail structures is well understood by aerospace industry [122]. The only difference between aerospace and electric machine industry is that aerospace industry uses solid titanium alloy while electric machine industry uses laminated steel. Therefore, if a generator with separate rotor core structures can survive 6,800 *rpm*, this proves the boundary conditions applied to an Ansys model simulating a dovetail structure for separate rotor cores are correct. As a result, a complete rotor core geometry presented in Fig.

92 is able to survive the maximum operating speed (16,000 *rpm*) adopting M235-35A.

5.3.4 Solidworks 3D explosive view

In chapter 5.3.4, it is concluded that the theoretical maximum operating speed is 6,800 *rpm* for separated rotor cores geometry. The final geometry determined for final prototype is the geometry in Fig. 95. Selected bearing for this application is SKF 6211-2Z that can guarantee 7,000 *rpm* with the cheapest cost. In order to test a WFSG individually, a slip ring made by MOFLON capable of running at 8,000 *rpm* is implemented to transfer the rotor signals such as the amount of field currents and rotor temperature from rotating body and stationary measurement devices.

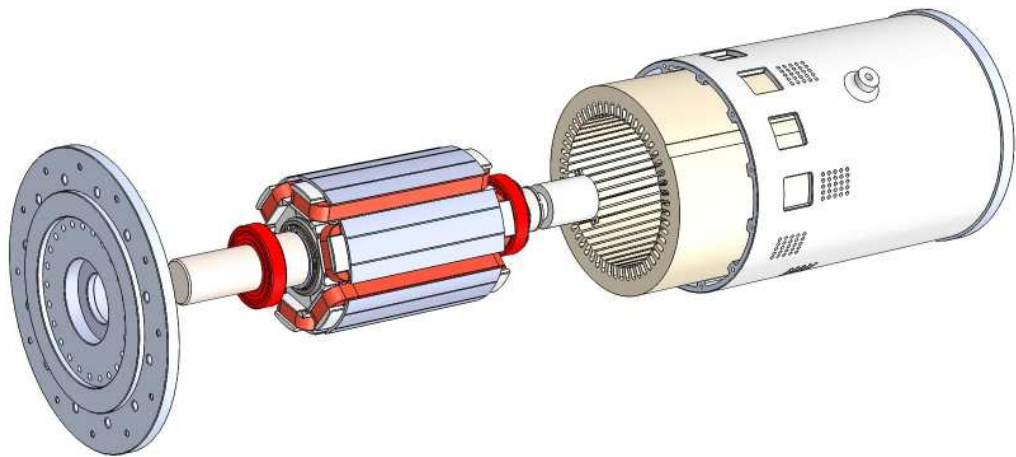


Fig. 96 3D explosive view of a WFSG designed based on geometry in Fig. 95

Fig. 96 is an explosive view of a final design for a WFSG prototyped based on geometry in Fig. 95. Due to the limited time constraint, the aluminium housing and end plates are designed using 7075-T6 grade aluminium. The dimensions of aluminium housing and end plates are determined adopting similar existing machine

dimensions. A shaft is designed using stainless steel 17-4PH H900 with H900 heat treatments for best mechanical performance. The cross sectional view of a WFSG is shown in Fig. 97 illustrating the essential components that are designed for a WFSG.

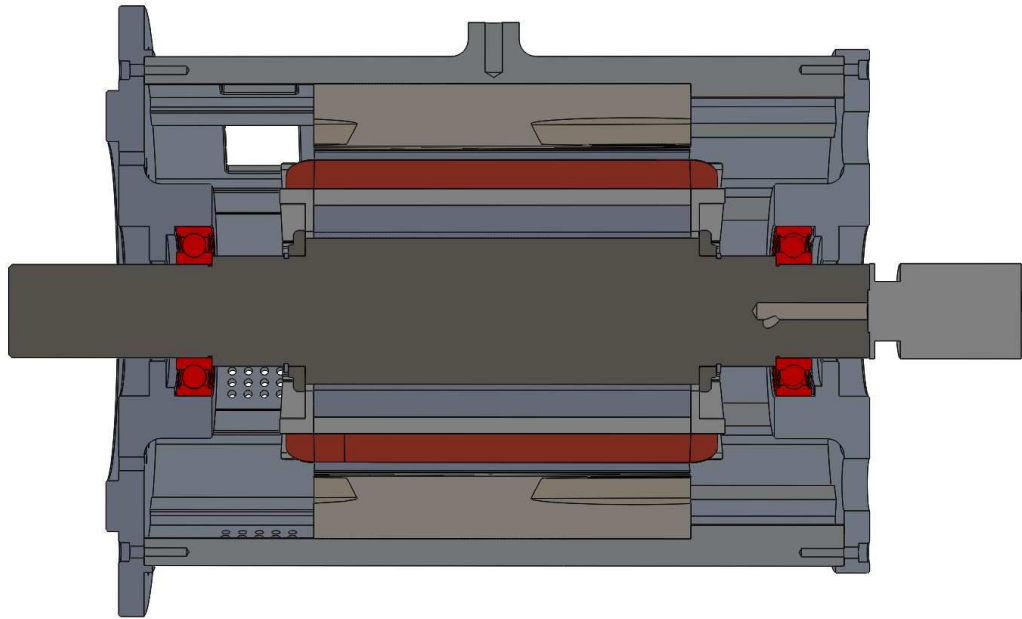


Fig. 97 Cross sectional view of a WFSG designed based on geometry in Fig. 95

5.4 Conclusion

In this chapter, the Von-Mises distribution analysis is performed based on the geometry of a WFSG designed with high temperature wire. Chapter 5.1 investigated the stress level of the rotor body at 16,000 *rpm* and the mutual effects of core components (copper wire and damper cages) on the rotor body. The stress level concentrated at corner 1, corner 2 and the damper edge 3 reaches a margin that is not recommended while the core material is M235-35A. In this chapter, fillets on the sharp corners, increased thickness of damper edge 3 and open slots configurations for damper bar slots presented in chapter 5.2 have eased the stress

concentration at corner 1 and 2 and solved stress concentration at damper edge 3. The last option in chapter 5.2.4 proposed a novel integrated damper cages structure to erase the damper edge 3 stress concentration and retain the field winding at its original place.

At this stage, the estimated power density for a WFSG designed in this chapter is slightly over than 2 kW/kg. This value is not compatible against Honeywell generator (7.9 kW/kg) presented in Fig. 2. Therefore, novel methods has to be invented to push the performance (temperature and local stress level reduction) of rotor core analysed in chapter 5.2 even further with M235-35A.

In chapter 5.3.1, air gap length reduction method based on knowledge learnt from rotor deformation analysis can help reduce the weight of the copper used on rotor core, losses in the copper winding and the rotor core temperature. Increased efficiency is also another benefit offered by air gap reduction method. Meanwhile, reduced copper wire weight on the rotor pole experiences less centrifugal force. This causes stress level at corner 1 and corner 2 been reduced.

In chapter 5.3.2, a dovetail structure similar to aerospace fan blades fitted into a fan disk is adopted to reduce the stress level at corner. This is proved to be very effective as the stress level at corner 1 is reduced from 472 MPa to 407 MPa achieving a 15.9% reduction. The safety factor at corner 1 is at 1.34 which is above recommended value 1.24.

Both methods (air gap length reduction and introducing dovetail at the bottom) presented in chapter 5.3.1 and 5.3.2 together theoretically can reduce the stress level

presented in Fig. 92 (lowest found in the thesis) to an even lower state when M235-35A is considered as the only available core materials.

An essential fact has to be pointed out that the solutions presented in chapter 5 to address high stress concentration cannot solve issues for corner 1, 2 and damper edges 3 at the same time. A combination of methods presented above would be idea to resolve the stress concentration at different places. For example, air gap length reduction frees more space on the rotor geometry. Therefore, stress at corner 2 can be solved by a 5 mm fillets (363 MPa) which is original not feasible. An extra dovetail suppress the stress at corner to 407 MPa. Open slot configurations tackles the stress concentration at damper edges 3. As a result, a combination of air gap length reduction, increased fillets and an extra dovetail can potentially solve the mechanical challenges for a WFSG adopting M235-35A.

However, an important aspect has to be pointed out that the error between a 2D simulation and the real case. Practically, end rings are used to retain the end windings. The bending trend for the copper wires and integrated damper cages in the axial directions is a U shape. However, a 2D simulation cannot reflect the U shape bending of these mentioned structures. Therefore, this results in the difference between the model used for simulation and the actual machine that is implemented.

Another fact that contributes to the error is the contact conditions that are applied to each contact surface. Contact conditions result in highly non-linear calculation of stress distribution and total deformation. However, the determination of contact conditions highly depends on the practical experience. In addition to this, the coefficients related to different contact conditions are also a challenging aspects to determine. Therefore, the error is also expected between a simulation and a

practical machine implemented. Therefore, a safety factor is introduced to compensate the effects of inaccurate simulation results.

Chapter 6

Manufacturing and experimental validation of high speed wound field synchronous generators

Chapter 3, 4 and 5 concludes the design methodologies for high speed WFSGs. The analytical and FE setups for an OOD tool is settled. Solutions for challenges raised due to high speed rotation regarding to electromagnetic, thermal and mechanical aspects are given. Novel design considerations are given in chapter 5.3 that potentially enable the high speed operation of a WFSG using M235-35A at the maximum speed required in chapter 1. This chapter focuses on explaining the manufacturing and assembly process of a WFSG designed in chapter 4 and 5. The proposed OOD tool dedicated to be able to design and analyse a WFSG is validated against the experimental measurements. With the experimental validation of the OOD tool finalized in this chapter, this OOD tool can be used for future WFSG prototype designs and performance improvements iterations.

At the beginning of this chapter different generator components are presented. Basic generator characteristics such as weight of each individual components and envelop of the dimensions are listed. The second part of this chapter focuses on explaining the experimental setups for collecting testing results. Those experimental data is compared against the simulation results obtained from the OOD tool developed in chapter 3, 4 and 5.

6.1 Manufacturing of a main alternator

Chapter 6.1 focuses on introducing the details of individual components been manufactured. Meanwhile, the assemble process of the WFSG is discussed in this chapter. Basic characteristics such as weight, size of each individual component and the overall envelop of a WFSG are listed.

6.1.1 Basic characteristics

Table 17 summarizes the weight of each metallic components. The overall weight in total is 120.6 kg. Envelop of this WFSG is 360 mm × 360 mm × 450 mm. The radial envelop for the generator designed in chapter 5.3.4 is similar to Honeywell's mega-watts class generator and the Boeing 787 starter generator. The axial length of the WFSG designed in chapter 5 is similar to the Boeing 787 starter generator.

Table 17 Weight of different components and the overall weight

	Single Unit (kg)	Net weight (kg)
End Plate Front	5.6	5.6
End Plate Rear	4	4
Housing	10.2	10.2
Stator core	34.4	34.4
Rotor pole	4.6	27.6
Shaft	14.2	14.2
Bearing	0.64	1.28
Stator wire	0.55	9.9
Rotor wire	NA	6
Axial cap	0.25	0.5
Accessories	NA	6.92
Total		120.6

The stator phase resistance measured from the WFSG prototype is 5.115 mΩ, 5.118 mΩ and 5.105 mΩ respectively for U V W phase.

6.1.2 Presentation of the individual components

An aluminium housing and two end plates are shown in Fig. 98 a) made of 7075-T6. All the components are inspected under coordinate measurement machine (CMM) according to the dimensions annotated in the engineering drawings. Fig. 98 b) shows the aluminium front end plate measured under CMM. Rotor cores made of M235-35 lamination is presented in Fig. 99 a), which is back-lacked together. In Fig. 99 b), the rotor core material is also made of M235-35A but are welded together with laser. Stator core laminations are shown in Fig. 99 c) made of M235-35A welded together with laser on the outer surface. A slip ring and a SKF bearing 6211-2Z is depicted in Fig. 100. A customized rotor shaft designed in chapter 5.3.2 is also shown in Fig. 101 made of 17-4PH with H900 heat treatment achieving a yield point of 1,300 MPa. The copper wire used for the final WFSG prototype is ESSEX Amide-Imide 220 °C class. At this stage, all the key necessary components have arrived. The next process is to assemble all the components together. A detailed description of the assembly process is completed in chapter 6.2.

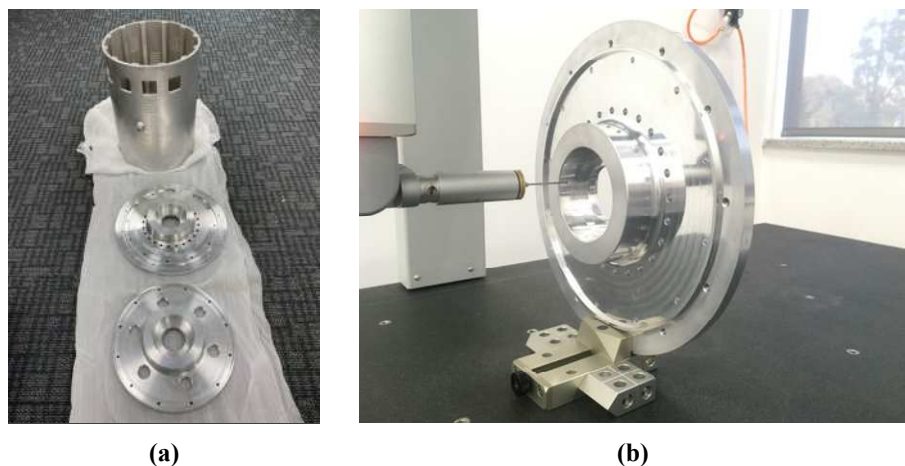


Fig. 98 a) A housing and end plates for the WFSG b) Front end plate quality check under coordinate measurements machine CMM

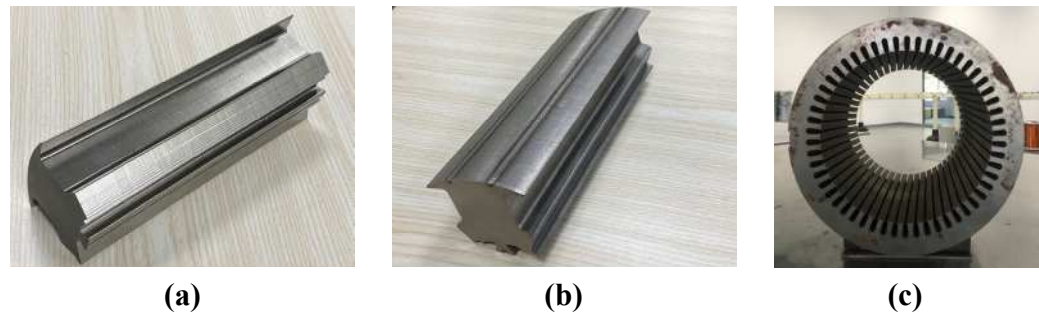


Fig. 99 a) A rotor core made by A b) A rotor core made by B c) A stator core made by C



Fig. 100 a) A slip ring b) SKF bearing 6211-2Z k



Fig. 101 A customized shaft for a WFSG designed in chapter 5.3.3

6.2 Assembly process of the WFSG

All the individual component presented in chapter 6.1.2 are performed with quality check under CMM shown in Fig. 98 b). This chapter mainly focuses on the assembly process of the final WFSG prototype depicted in Fig. 96.

6.2.1 Stator assembly and thermal couples setup

To measure the temperature profile of a stator core, thermal couples are placed under the layer insulation as shown in Fig. 102 b) to capture a hottest temperature spot among the radial slot area. The reference point for the thermal couples in axial direction is the drive end (DE). Five individual thermal couples are placed at a point indicated by Fig. 102 a) with respect to the reference point in Fig. 102 a). The overall distance between the DE and non-drive end (NDE) is 222 *mm*. A complete stator assembly is shown in Fig. 103 a) with five thermal couples embedded in the active part of the stator core (Fig. 103 b)) according to the explanation in Fig. 102 a). An extra thermal couple is placed inside the end windings at DE to measure temperature of the end winding. Once all the thermal couples are in their position, the completed stator core are merged into a chamber for VPI process. Fig. 103 b) is the stator core with VPI process been finished twice for better thermal performance. Nevertheless, the resin filled inside the end winding are not as much as those been filled in the active part. This is mainly due to the viscosity of resin is high and it flow away while the stator core was move from VPI chamber to an oven. An obvious consequence is that the temperature behaviour of the end winding is poorer than that inside the active parts.

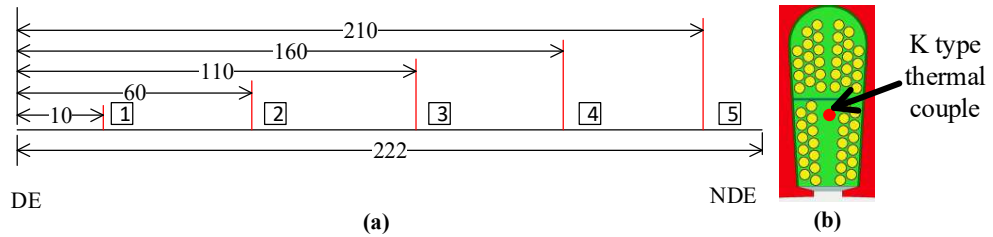


Fig. 102 a) axial position for 5 thermal couples b) radial location for thermal couples

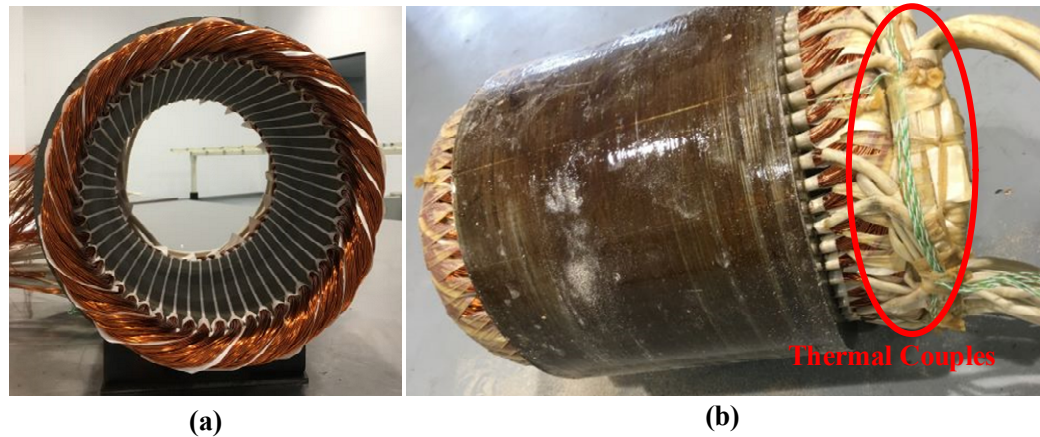


Fig. 103 a) full stator assembly setup b) thermal couples assemblies inside stator coil

6.2.2 Rotor core assembly process

The rotor core assembly is the most difficult part of this entire assembly project. The first difficulty is to wind the rotor coil uniformly as shown in Fig. 93 a) and b). The second difficulty comes from the mechanical design considerations from chapter 5.3.2, which are precision manufacturing raised by six extra dovetails on the rotor cores.



Fig. 104 a) first rotor core assembly b) modified winding process c) outcome of final rotor core outlook

Fig. 104 presents the improved rotor core from an unqualified rotor pole winding to a uniform rotor pole winding. Since the rotor winding is fed with DC voltage and each pole share only $1/6$ of the total voltage, the rotor core is tried to wind its coils without insulation paper. Although the rotor core passed the insulation testing while the number of turns on the rotor coils is still low, but shape edges on the rotor metallic components damages the insulation of the copper wire. Therefore, 0.13 mm insulation paper is used to prevent solid contact between enamel wires and solid metal materials. In Fig. 104 a), wires located at upper layers are misplaced even tensions are applied to the wire. In this case, plastic jigs Fig. 104 b) are applied to

the winding process to prevent wires from misplacement. Fig. 104 b) presents the last few layers of rotor windings to be finished and the arrangements of each layer of wires are much better compared with the case in Fig. 104 a). Fig. 104 c) shows a final completed rotor core. The rotor wire are uniformly wounded on the pole body which complies with the industry standard shown in Fig. 93. Meanwhile, rotor signals such as field currents and rotor temperature are passed from rotor coil to external power supply and measurement devices via a slip ring shown in Fig. 100 a). At this point, the first challenging task is addressed.

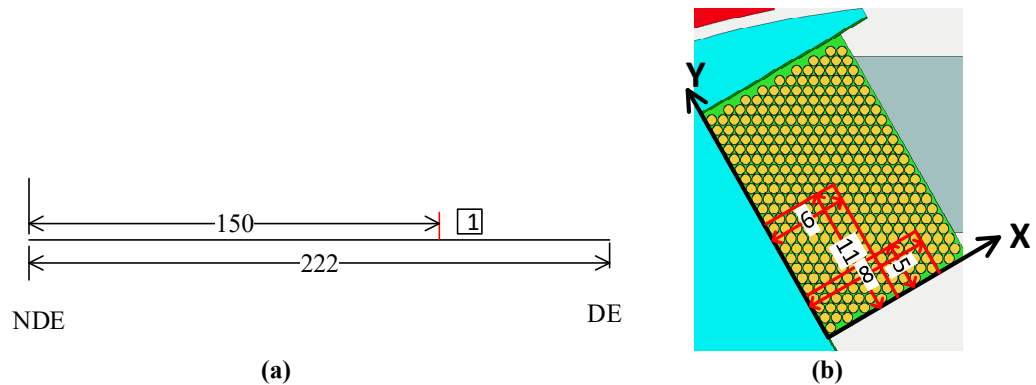


Fig. 105 a) Position of two k type thermal couples on rotor axial direction b) position of two k type thermal couples on rotor radial direction

Due to the available space on the rotor core and the slip rings available, only two k type thermal couples are attached to the rotor coils. Fig. 105 a) presents the positions for two k type thermal couples inside the rotor coils axially. Both k type thermal couples are places 150 mm apart from the non-drive end. Fig. 105 b) present the positions of two k type thermal couples on the rotor coils radially. The bottom of rotor bore is considered as the origin. The first thermal couple is placed 6 mm and 11 mm away from the origin in x-axes and y-axes respectively. The second thermal

couple is placed 8 *mm* and 5 *mm* away from the origin in x-axes and y-axes respectively.

The second challenging task is to assemble six rotor cores on the shaft adopting fitting with clearance of six dovetails. A dovetail at the bottom of each rotor pole can reduce the stress level at core 1 defined in chapter 5 by around 10%. However, fitting a rotor with 6 dovetails into the shaft requires high precision for rotor cores and shaft manufacturing. The lack of understanding of how tolerance affects the assembly process can floor the entire project. At the same time, due to the practically limitation explained in chapter 5.3.3, six individual cores has to be individually slotted into the channels on the shaft shown in Fig. 101. A six individual rotor core configuration creates more issues while defining the tolerance as six rotor poles generates a possibility of a closed dimensional chain which is not allowed in mechanical field. Under this circumstance, a necessary gap between each individual rotor pole is required from mechanical engineering perspective otherwise a successful assembly of six rotor poles cannot be guaranteed. However, the dimension for the gap can be a factor that deteriorates the performance of a generator (consuming MMF produced by the MMF). A dilemma between a successful assembly and the electromagnetic performance of a WFSG is raised here. A gap too small mean the assembly might fail. A gap too large results in compromised generator performance. A completed rotor assembly is complex shown in Fig. 96. This potentially causes the radius of the rotor core to be increased a little compared with the rotor outer radius specified in the engineering drawing.

The only method which can be think of to address rotor assembly issue is precise calculation of tolerances been applied to a rotor pole and the channels on a shaft that accommodates those dovetails. A precision of 8 micrometers on reverse dovetails on a shaft (Fig. 101) that accommodates rotor poles is guaranteed. A precision of 20 micrometers on the rotor pole laminations (Fig. 99 a) and b)) are achieved.

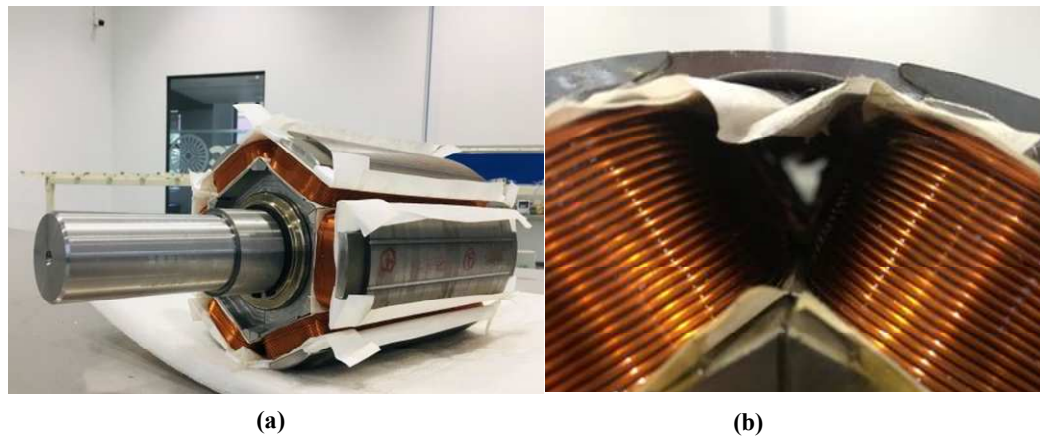


Fig. 106 a) A rotor core assemble with rotor coils ready b) 17-4PH integrated damper cage in place

Fig. 106 demonstrates the assembly of the entire rotor core with rotor pole and field coils ready. No repair of rotor pole is needed during the process of sliding a rotor pole into reverse dovetails on a shaft. A single successful attempt of fitting six rotor poles on the shaft is completed which is shown in Fig. 106. This is due to the precise manufacturing of rotor core laminations (Fig. 104 c)) and a rotor shaft (Fig. 101). Once the rotor assemble is finished, integrated damper cages are assembled in the place shown as Fig. 77. Another five 17-4PH made integrated damper cage are installed at the same places. These are the crucial elements for obtaining lowest possible THD for a variable speed WFSG in this thesis.

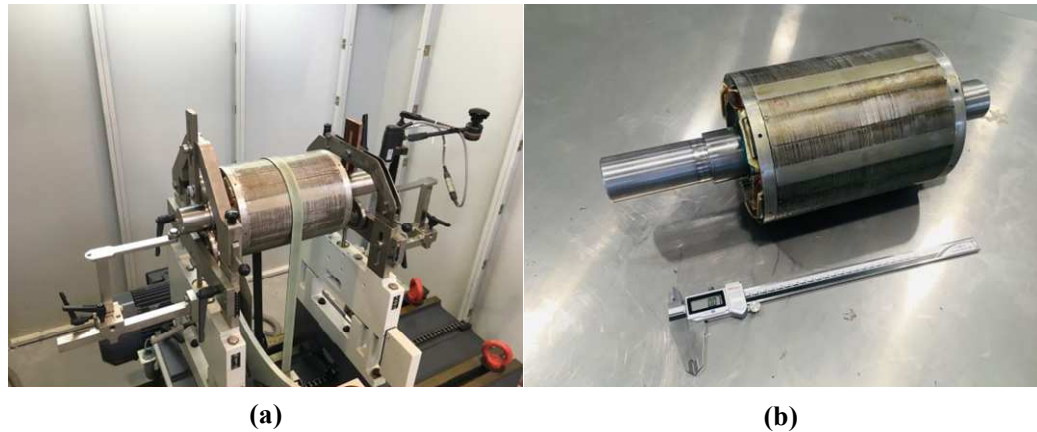


Fig. 107 a) rotor balancing with SCHENCK balancing machine b) the entire rotor core after rotor balancing

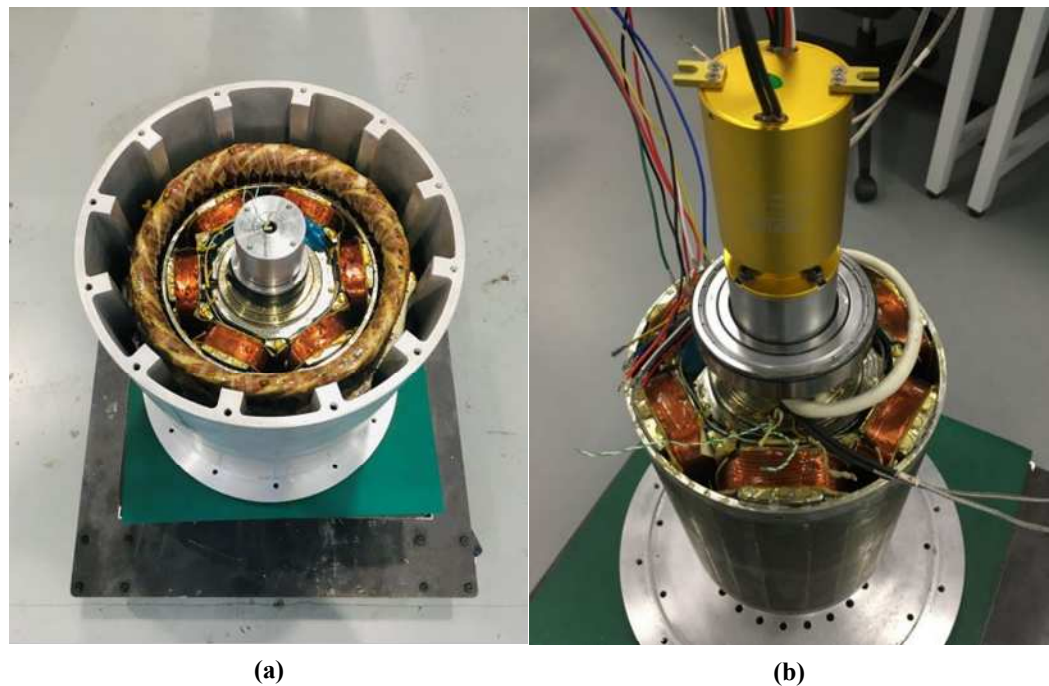


Fig. 108 a) a rotor core been installed inside the stator housing b) a slip ring installation process

A slip ring is required to pass signals between a rotor and stationary external power supply. Before installing a slip ring, a completed rotor core in Fig. 107 b) without a slip ring is assembled in the stator housing to check if a stator and a rotor core has touched each other. A collision between a rotor and a stator is not discovered. After

this, a slip ring is installed at the end of the shaft shown in Fig. 108 b). This slip ring is able to pass the rotor field currents and two rotor k type thermal couples on to the shaft to magnetize a generator and measure the rotor coil temperature.

6.2.3 Final complete assembly process



Fig. 109 The final assembly for a WFSG prototype

In chapter 6.2, the major parts for a WFSG have all been prepared and ready for the final assembly. Fig. 109 presents a fully assembled WFSG installed on a Kistler testing rig. Three phase four wire layout is coded in red, green, yellow and blue for phase U, V, W and a neutral point respectively. Six k type thermal couples monitoring stator coil temperature and two monitoring rotor coil temperature extended from a golden slip ring are depicted in Fig. 109.

6.3 Experimental testing of the WFSG prototype

The experimental rig been setup is shown in Fig. 110. Three vibration sensors are placed in x-y-z direction respectively to monitor the 3D vibration level of a WFSG in real time. The vibration level is monitored by the velocity (*mm/s*). Power cables extended from a slip ring is connected to DC power source of a Kistler rig to magnetize rotor coils of a WFSG. According to the aftermath in the simulation in chapter 4, the inductance of rotor coil for the WFSG designed is 5 *H*. A sudden loss of DC supply to a rotor field with 5 *H* is catastrophic to both the WFSG and power supply. Therefore, in parallel to the DC power supply, a CREE C4D10120 diode is arranged in an acrylic box to create a path for reverse current flow from the big inductor protecting all the equipment as shown in Fig. 110. Twelve k type thermal couples are plugged into a bay for accommodating k type thermal couples in the bottom left corner of Fig. 110 provided by Kistler for temperature measurements. 6 thermal couples are implemented to measure stator coil temperature; another 2 thermal couples are utilized to determine rotor coil temperature. One thermal couple is stuck on the surface of the aluminium housing using Kapton tape to measure the housing temperature. Another three thermal couples are implemented to measure the inlet and outlet air temperature, and ambient air temperature respectively. Real time temperature behaviour of stator, rotor coils, housing surface, inlet, outlet and ambient air is monitor by a host PC. Six air inlets are connected to an external black fan indicated in the middle of Fig. 111 which can provide an air flow of 0.22 cubic meter per second.

Chapter 6 Manufacturing and experimental validation of high speed wound field synchronous generators

The U V W terminals from a WFSG are connected to Kistler chamber for voltage and current measurements. The measuring device is Yokogawa 1800E integrated in Kistler. Meanwhile, the phase voltage are also measured by three differential probes connecting to Keysight oscilloscope for confirming the results from Kistler. The neutral point current is measured by current clamp connecting to Keysight oscilloscope shown in Fig. 111. Another cable from the measurements chamber is connected to a resistive load bank.

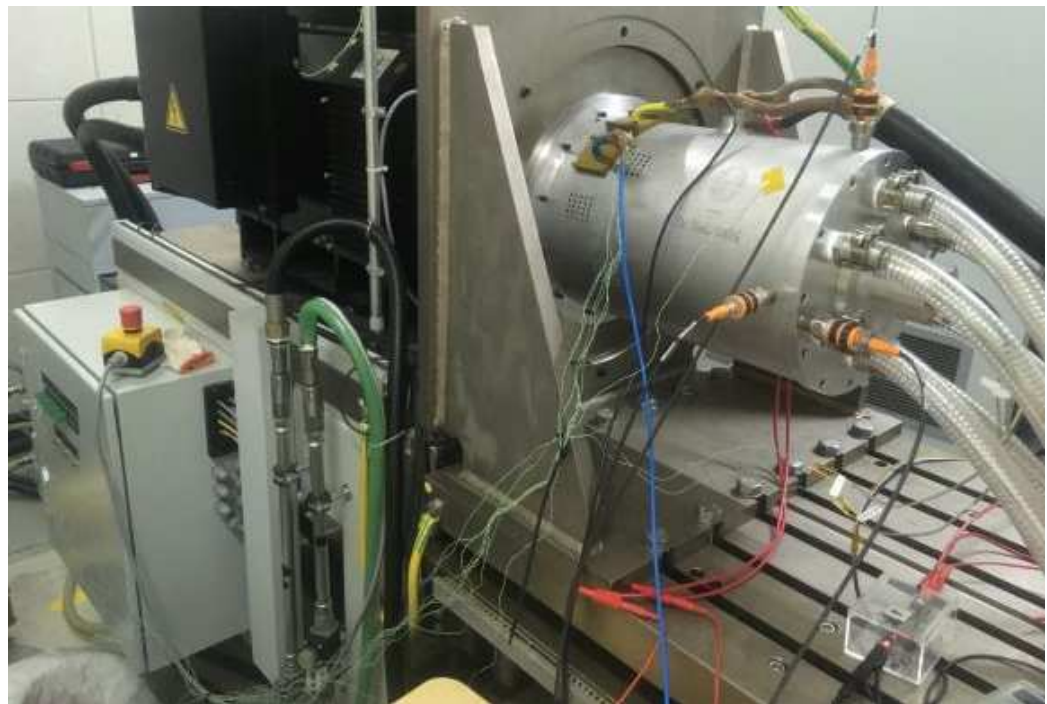


Fig. 110 An experimental rig setup for a WFSG testing

The WFSG thermal module within the OOD tool determines the temperature of a WFSG based on an air flow rate of around 2 *m/s*. The air flow rate from the air outlet is measured by an OMEGA anemometer and the flow rate of air from the outlet of the WFSG Fig. 112 is 1.97 *m/s* with an external fan.

Chapter 6 Manufacturing and experimental validation of high speed wound field synchronous generators

With the air flow rate confirmed by the anemometer at stand still condition, the test rig is ready for further experimental tests with minimum adjustments such as open and short circuit test, load test, etc.



Fig. 111 Overall rig setup for a WFSG testing



Fig. 112 The flow rate of air from the outlet port of a generator

6.3.1 Open circuit and short circuit characteristics

Open circuit test for this WFSG is performed with U V W connected to Kistler measurement chamber and neutral point left open outside the chamber. Yokogawa

1800 series is able to measure the phase voltage by the three phase four wire layout connection within Yokogawa setups. The DC field current is controlled by Kistler DC side voltage. Kistler measures the RMS phase voltage of this WFSG with a corresponding DC field current. Meanwhile, three differential probes are also arranged to measure the phase voltage U-neutral, V-neutral and W-neutral to compare with Yokogawa measurements for power quality analysis.

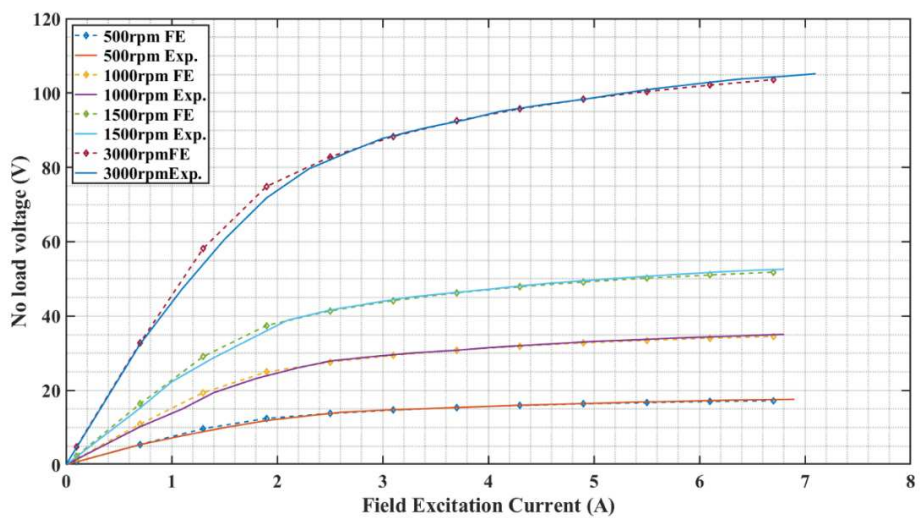


Fig. 113 Open circuit test for a WFSG prototype experiment (exp.) results vs FE simulation

Fig. 113 plots the open circuit characteristic between experimental measurements of a WFSG prototype versus its FE simulation. Open circuit voltage is measured with field current increased from 0.7 A to 6.9 A with a 0.4 A step. Experimental measurements are plotted as solid lines with different colours in Fig. 113. The FE results are plotted as dashed lines with diamonds. Since this WFSG is designed as a variable speed machine, multiple open circuit tests at 500 rpm, 1000 rpm, 1500 rpm and 3,000 rpm are performed. A close match between experimental measurements and FE simulation with minor difference can be observed in Fig. 113. Therefore,

from open circuit tests perspective the final prototype meets the design requirements. In addition, the built in FE model in OOD tool is valid to predict the performance of a WFSG at various speed points.

Another crucial test for a WFSG prototype is the short circuit tests under an increase of rotor field current. The short circuit test of this WFSG prototype has its U V W terminals shorted by cables able to handle more than 400 A RMS in the Kistler measurement chambers. In the measurement chamber, built in Hall Effect current sensors are able to sense current up to 1000 A.

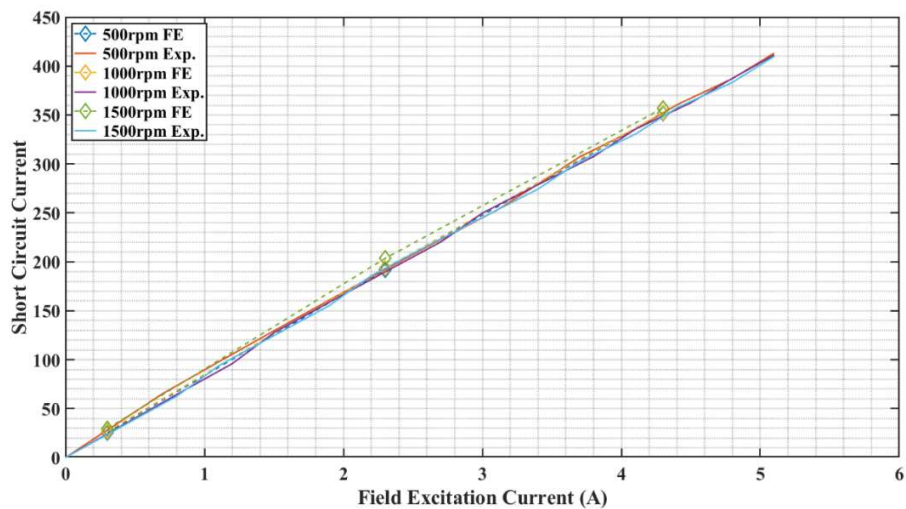


Fig. 114 Short circuit test for a WFSG prototype experiment (exp.) results vs FE simulation

The FE short circuit characteristic is performed under 500 rpm, 1,000 rpm and 1,500 rpm with an increase of rotor field current from 0.7 A to 6.9 A with a 0.4 A step. The FE results are plotted as dashed line with diamonds on it in Fig. 114. In Fig. 114, experimental measurements are plotted as solid colour lines. Experimental measurement for short circuit current at 500 rpm, 1,000 rpm and 1,500 rpm matches

the simulation results with minor deviation. Thus, the performance of the WFSG prototype meets the design requirements. Both open and short circuit test for a WFSG prototype has demonstrated a well matched machine performance and the FE simulation prediction at various speed conditions. Therefore, the OOD tool is able to predict the machine performance at even higher speeds.

6.3.2 Power quality results

Another imperative issue for a WFSG is its power quality during continuous power generation period. This chapter focuses on validating the FE power quality results for a WFSG equipped with integrated damper cages in chapter 5.2.4 against experimental outcomes. Fig. 115 a), b), c) and d) plot the FE no-load voltage waveform of a WFSG at 500 rpm, 1,000 rpm, 1,500 rpm and 3,000 rpm from an OOD tool respectively.

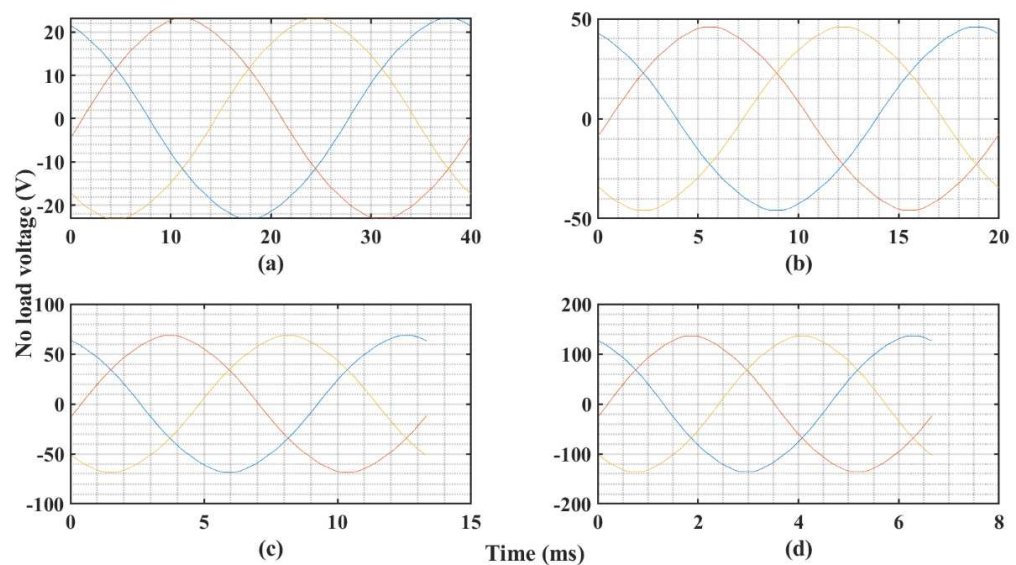


Fig. 115 FE no-load voltage waveform at different speeds a) 500 rpm b) 1,000 rpm c) 1,500 rpm d) 3,000 rpm

The THD levels for no-load terminal voltage in Fig. 115 at 500 rpm, 1,000 rpm, 1,500 rpm and 3,000 rpm are very low, which complies with the analysis in chapter 5.2.4. Fig. 116 depicts the harmonic contents for the FE no-load voltage waveform plotted in Fig. 115. Observable harmonic contents are third, fifth and nineteenth harmonics. These harmonics (THD) only counts for 1.10%, 1.09%, 1.08% and 1.08% in total against fundamental value respectively.

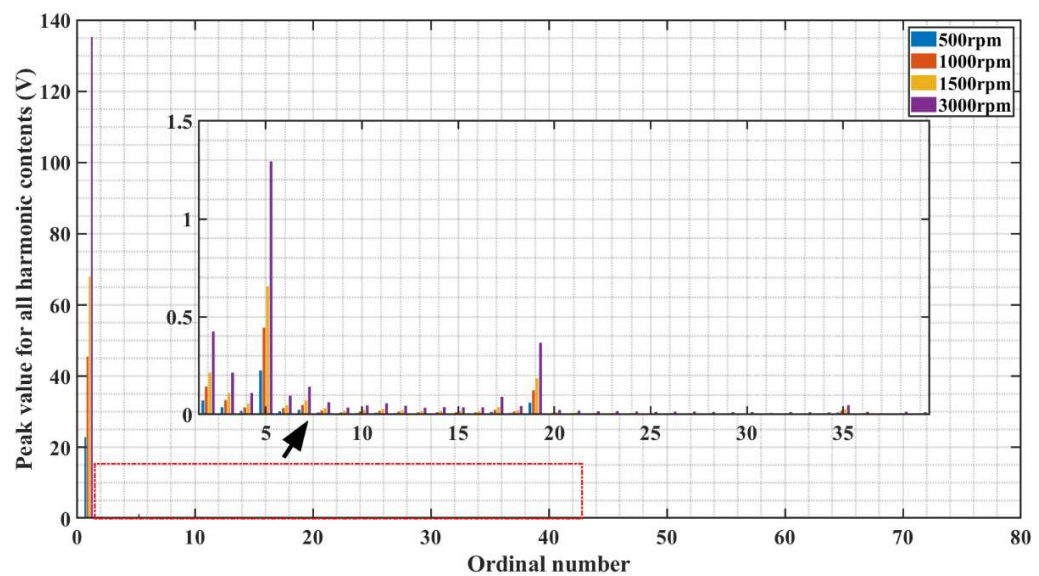


Fig. 116 Harmonic contents for FE no-load terminal voltage waveform at 500 rpm, 1,000 rpm, 1,500 rpm and 3,000 rpm

Fig. 117 plots the experimental measurements of U V W phase voltage of a WFSG prototype through an oscilloscope via differential probes. Phase voltage in Fig. 117 a) is obtained at 500 rpm for a WFSG with terminal U V W neutral open. Fig. 117 b) is the no-load phase voltage at 1,000 rpm, 1,500 rpm and 3,000 rpm. Observable distortion can be found from the waveform in time domain. Fig. 118 presents the Fourier analysis of the experimental no-load voltage waveform at 500 rpm, 1,000 rpm, 1,500 rpm and 3,000 rpm. Even though, the third, fifth and nineteenth

harmonics are still observable in the experiment, but the magnitudes are 0.25 volts, 0.41 volts for the 5th and 19th harmonics which are five times smaller than FE simulation. The magnitude of the harmonic contents over the fundamentals are nearly negligible. In addition, other order harmonics such as second, eighth and seventeenth harmonics presents in the harmonic contents and are comparable against 3rd, 5th and 19th harmonics. However, the harmonic contents are nearly negligible compared with the fundamental components. The THD level for the experimental measured no-load terminal voltage are 1.42%, 1.68%, 1.15% and 1.17% for 500 rpm, 1,000 rpm, 1,500 rpm and 3,000 rpm respectively.

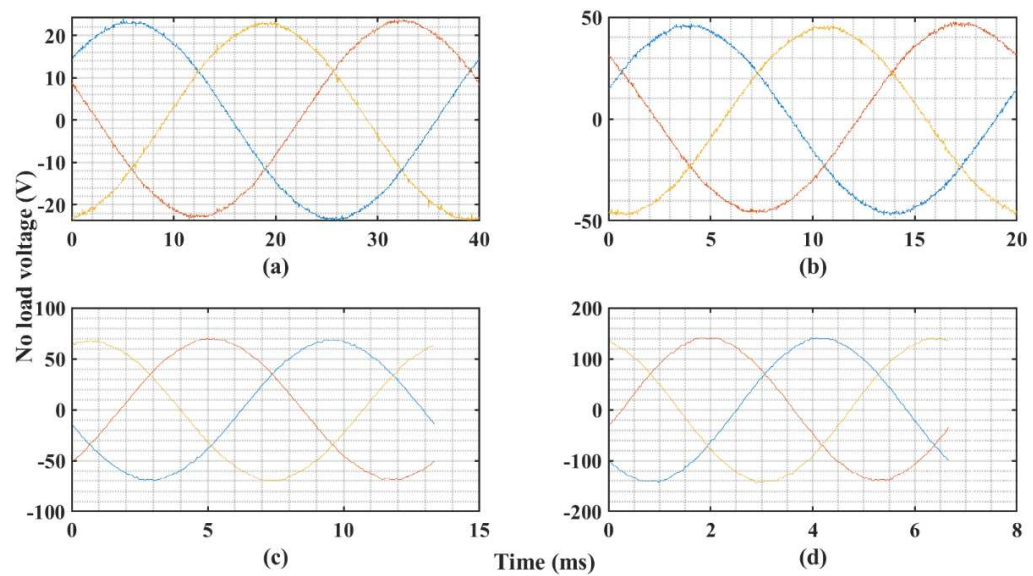


Fig. 117 Experimental no-load voltage waveform at different speeds a) 500 rpm b) 1,000 rpm c) 1,500 rpm d) 3,000 rpm

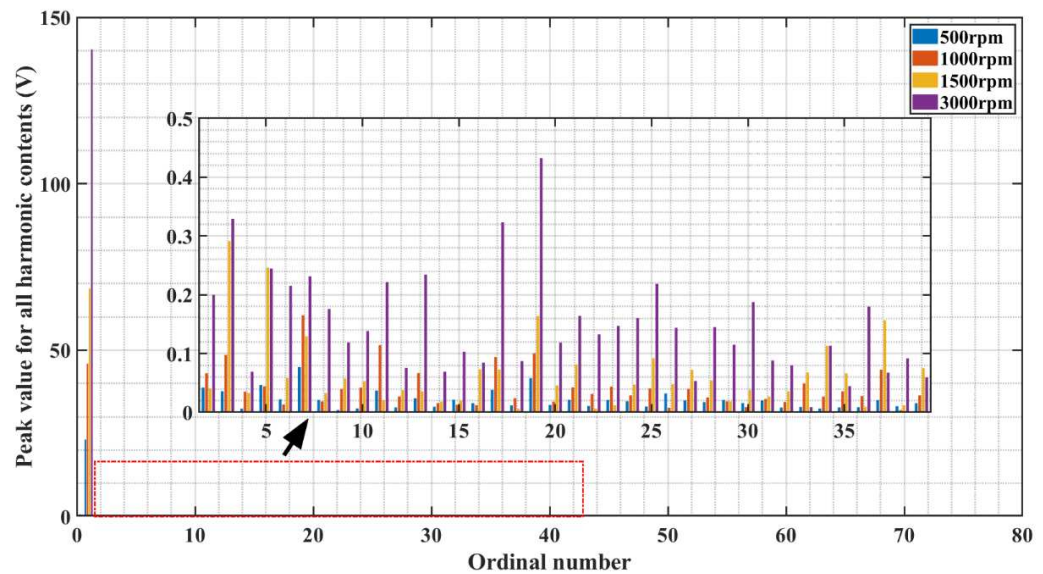


Fig. 118 Harmonic contents for experimental no-load terminal voltage waveform at 500 rpm, 1,000 rpm, 1,500 rpm and 3,000 rpm

Fig. 119 summarizes the FE and experimental THD level for no-load terminal voltage at 500 rpm, 1,000 rpm, 1,500 rpm and 3,000 rpm. The difference between simulated THD and the experimental measurements are 29%, 54%, 6% and 8% respectively. Although the difference is not very consistent while generator speed changes, the absolute THD values obtained from experimental measurements are quite close to the FE results. Meanwhile, based on Fig. 118, there are even harmonics presented in the experimental measurements and these might be caused by the noise from a Kistler rig captured by the probes. Since the THD level is already close to 1% which is quite a low value, the experimental measurements can be easily distorted. The THD readings from Yokogawa device is about 0.42% for all four different speed conditions with the line filter on. The cut-off frequency has been set as 2.5 kHz to 200 kHz and the THD level remains unchanged.

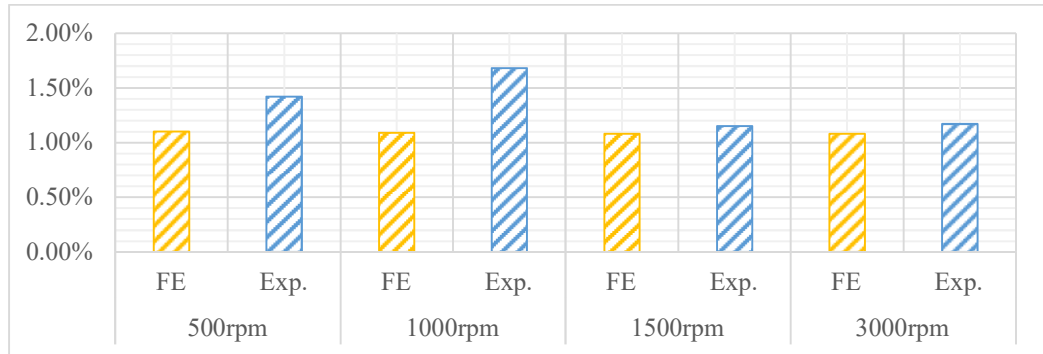


Fig. 119 FE and experimental THD level for no-load terminal voltage at 500 rpm, 1,000 rpm, 1,500 rpm and 3,000 rpm

In conclusion, the experimental THD level remains at about 1% from 500 rpm to 3,000 rpm. The THD level predicted by the electromagnetic FE modules in the OOD tool at those speed range meets the experimental measurements. Therefore, the THD prediction capability for an OOD tool embedded FE modules is validated in this chapter. Consequently, THD behaviour for this WFSG at higher speeds can be analysed by the embedded FE module. Low and consistent THD value for the output terminal voltages has been shown in chapter 5.2.4 at speed above 7,200 rpm. Therefore, integrated damper cages is able to help improve the power qualities for a variable speed generator at various speeds. Meanwhile, the power quality can be kept close or under 1% which is way better than the required THD level by MIL-STD-704F standards.

6.3.4 Thermal performance of a WFSG prototype

Thermal performance of an electric machine is also imperative for machine performance analysis. The maximum coil temperature of an air cooled generator is greatly affected by the inlet air temperature. Therefore, the experimental temperature rise (the difference between measured temperature and the inlet

temperature) inside stator and rotor coils are compared with that of a 3D LPTN simulation. The initial room temperature inside the testing chamber is 28 °C. The ambient temperature plugged in a 3D LPTN simulation is 30 °C

Due to the limited available equipment, there is no 250 kW inductive load available that can be connected to a WFSG. To test the generator at its full load capability, the generator are tested under short circuit condition with the full load stator current circulating inside the stator coils.

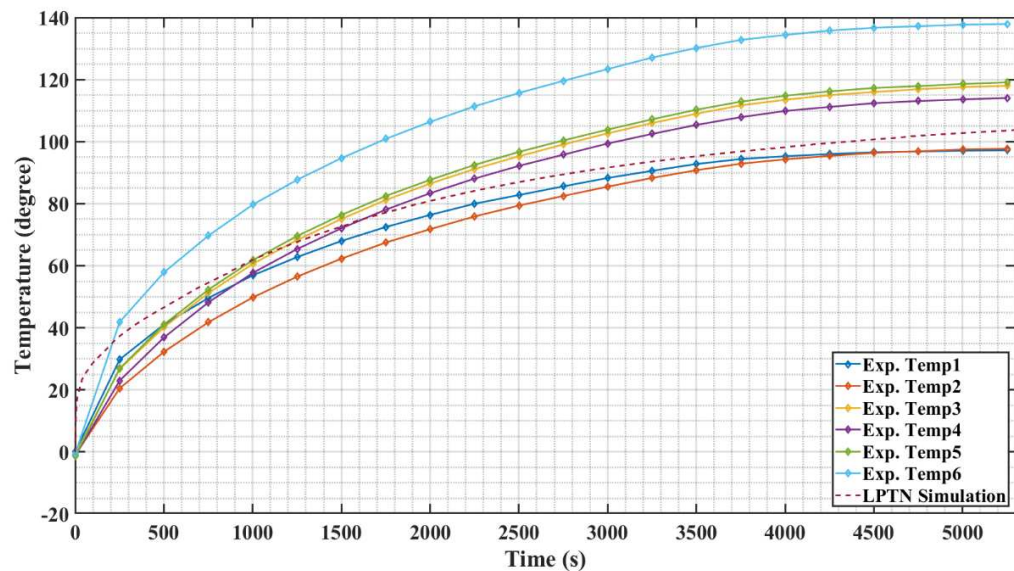


Fig. 120 Stator temperature rise at full load stator currents - experimental measurements versus a 3D LPTN simulation

In Fig. 120, thermal couple 1 to 5 (Exp. Temp1 to Exp. Temp5) measures the stator coil temperature inside stator slots (active part). Thermal couple 6 measures the coil temperature of an end winding locating at non-drive end which stays on the opposite side of the cooling inlets shown in Fig. 109. In Fig. 120, experimental temperature measurements are plotted as solid diamonds with different colours. The maximum stator coil temperature obtained from a 3D LPTN simulation (Fig. 45 7,200 rpm) is

plotted as purple dashed lines. The stator coil temperature reaches thermal equilibrium in about 5,000 seconds. Thermal couple 6 (Exp. Temp6) measured an end winding temperature 20 °C higher than the thermal couple 3, 4 and 5. This does not comply with the coil temperature results in [1] presented as Fig. 55. One possible explanation is that a significant amount of resin flowed away after the VPI process before the stator was put in an oven. Even with VPI process done twice, air voids still presents inside the end windings resulting in poor end winding equivalent thermal conductivities. Another explanation is that cooling air at non-driven end side flows less turbulent than the drive end. Therefore, the heat transfer coefficient is lower than that at drive end side.

In Fig. 120, the simulated maximum stator coil temperature rise (dashed purple line) falls within an envelope of measured stator coil temperature rise. The maximum steady state temperature rise error is around 15 °C which count for 10% error. The maximum coil temperature is smaller than some of the experimental measurements which causes the error might due to the wind-age losses not been counted in a 3D LPTN model. The transient thermal behaviour for a 3D LPTN model is also reflected in Fig. 120. A relatively good match between a 3D LPTN simulation and experimental measurements can be observed. In conclusion, the both steady state and transient stator coil thermal behaviour of the WFSG prototype can be analysed by the 3D LPTN model. An accurate modelling is proved by the comparison in Fig. 120.

During the short circuit test, the stator coil current can be maintained at maximum designed stator currents (354 A RMS). However, the rotor field current cannot be

maintained at the maximum required value during the short circuit test. Therefore, rotor temperature test are performed under open circuit condition with rotor field current maintained at the maximum designed field currents. Fig. 121 presents the rotor temperature rise during an open circuit test at the maximum rotor field currents that a WFSG can reach during its continuous operation. The red dashed line represents the maximum rotor coil temperature obtained by a 3D LPTN simulation. The blue solid line is the experimental rotor temperature measurements from thermal couple number 8.

In Fig. 121, the simulated maximum temperature rise obtained by a 3D LPTN results is 18 °C counting for 18% higher than the measured temperature via thermal couple number 8. The rotor temperature rise in a 3D LPTN model is higher than that for experimental measurements. One possible explanation is that the available thermal couple that can be located on the rotor coils are limited by the available channels provided by a slip ring. Therefore, the maximum rotor coil temperature might not be able to be captured by the one thermal couple only, although a thermal couple has been arranged at a place close to the hottest temperature spot according to the 3D LPTN simulation. According to the stator experimental measurements in Fig. 120, the maximum temperature difference counting axial and radial locations is about 30 °C. With a 30 °C super-positioned on the top of the experimental measurements, an expected hottest spot is only 8% higher than a 3D LPTN simulation. Meanwhile, the transient rising time for rotor temperature reaching steady state for both a 3D LPTN simulation and experimental measurements also

comply with each other in a good manner. Thus, the 3D LPTN model predicts the hot temperature spot in an accurate manner in both transient and steady state.

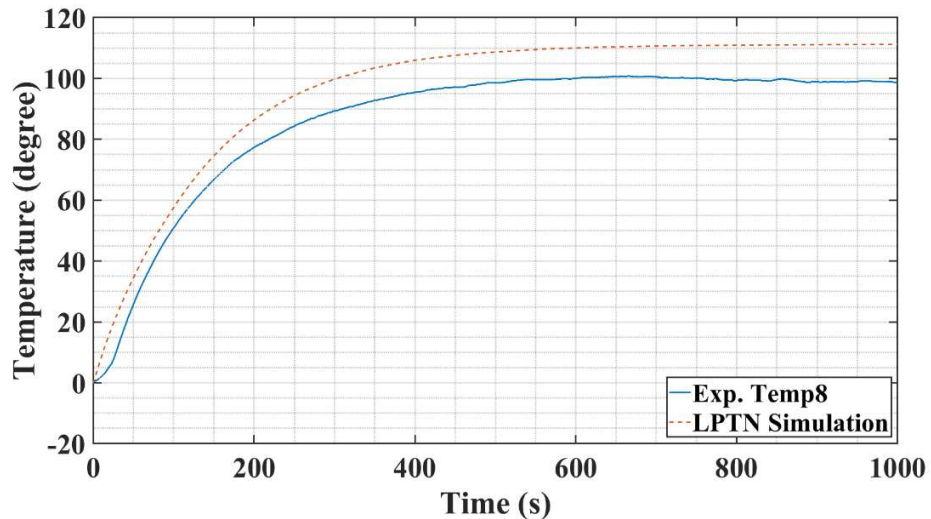


Fig. 121 Rotor coil temperature rise maximum rotor currents - experimental measurements versus a 3D LPTN simulation

Another possible reason for the difference between an experimental rotor temperature rise and a 3D LPTN simulation expectation in chapter 4.2.1 is the difference between the rotor resins filling process for an industry WFSG calibrating the 3D LPTN model in chapter 3.4. An existing generator in the lab adopts rotor dipping process. The WFSG manufactured in this thesis is done through VPI process. The VPI process is much better than the rotor dipping in term of eliminating air voids inside rotor coils especially rotor coils are wound layer by layer resulting in tight air space. Therefore, the VPI process results in higher equivalent thermal conductivity than dipping process.

The third possible reason might be the mutual effects between stator and rotor coils as both sides affect the air temperature inside the air gap that affects the final

temperature rise of rotor and stator coils. Therefore, a full load test under 1,500 rpm with a resistive load bank is performed to check if a 3D LPTN network is able to predict the temperature rise behaviour for both rotor and stator coils. Fig. 122 depicts the stator coil temperature rise in about 6,000 seconds. Similar transient responses for a LPTN simulation and experimental measurements can be observed in Fig. 122. 90% rising time for both conditions are around 5,000 seconds. The experimental stator temperature rise for stator coils are 20 to 25 °C. The temperature rise for stator coils obtained from a 3D LPTN simulation is 15 °C. The 10 °C difference between experimental and LPTN results are also close to the outcomes shown in Fig. 120.

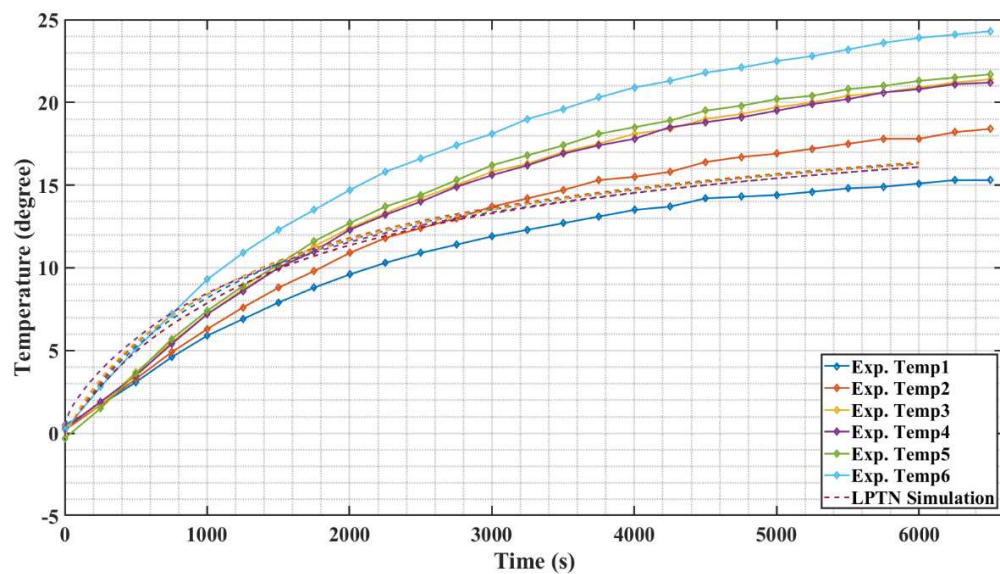


Fig. 122 Stator temperature rise at 1,500 rpm full load stator temperature measurements versus a LPTN simulation

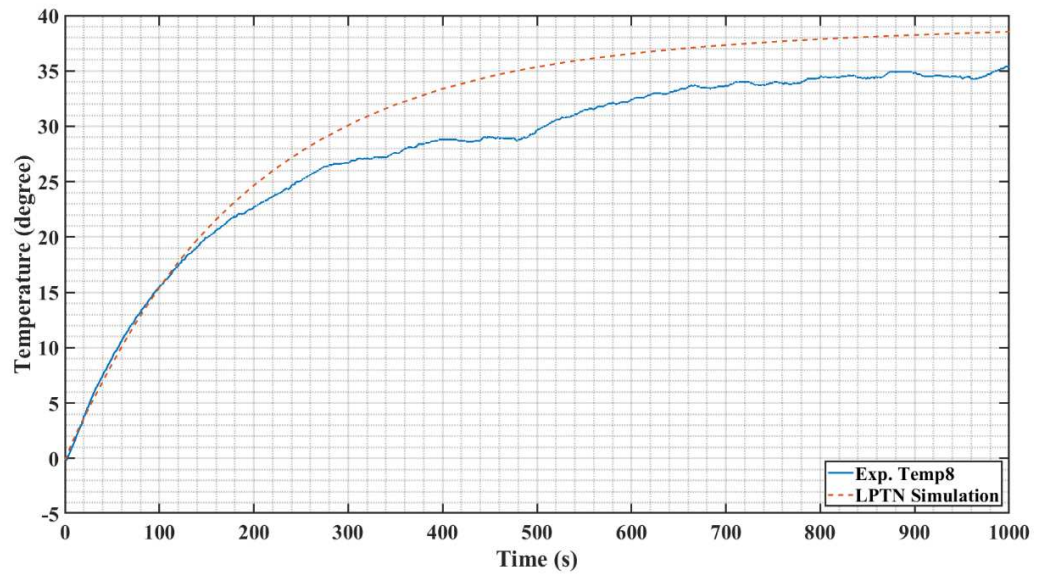


Fig. 123 Rotor coil temperature rise at 1,500 rpm full load rotor temperature measurements versus a LPTN simulation

Fig. 123 present the rotor temperature rise for experimental measurements and LPTN simulations. The 90% rising time for transient response for both condition are close to 500 seconds. The rotor coil temperature rise obtained from a LPTN simulation is 39 °C. The experimental outcomes for rotor coil temperature rise is 35 °C. The LPTN simulation matches the experimental measurements in a good manner. Therefore, the LPTN model developed in this chapter is accurate enough to predict both transient and steady state behaviour of a WFSG.

6.4 Conclusion

In conclusion, the WFSG prototype satisfies the FE electromagnetic design objectives from an open circuit and a short circuit test. The power quality results of the WFSG prototype also confirm that an integrated damper cages are able to help the entire system to achieve the targeted no-load THD results (1% or less than 1%). Meanwhile, conventional single speed WFSGs are optimized for single speed

performance. The power qualities for a WFSG gradually becomes worse when variable speed operation is required. The no-load THD measurements at various speed conditions for the WFSG prototype designed in this thesis also prove that integrated damper cages are able to guarantee a consistent the power quality at various speed conditions. This is one of the important objectives for variable speed generators and this can be a unique feature offered by integrated damper cages. The 3D LPTN model is also validated by the WFSG prototype. Both transient and steady coil temperature can be analysed by the proposed 3D LPTN model. Therefore, this validated 3D LPTN model is able to analyse the generator performance under continuous variable load conditions. At the same time, transient overload conditions or a load duty cycle for a WFSG are also able to be analysed to determine the maximum temperature with a given load condition for example a WFSG starting process. At the end, the analytical sizing, FE electromagnetic analysis and 3D LPTN modules packaged inside the OOD tool are all been validated and this OOD tool can be further implemented as a WFSG design tool. In addition, other WFSG design modules such as an exciter module, rotor dynamic module, bearing life time module and insulation life time module are able to be integrated into this existing OOD tool due to the unique objected oriented architecture.

Chapter 7

Updated design for wound field synchronous generators

An OOD tool dedicated for WFSGs is proposed in chapter 1; designed and validated from chapter 3 to 6. An understanding of WFSGs in terms of electromagnetic, thermal and mechanical aspects are established. Apart from safety requirements from any transportation application field, tight weight and budget requirements are essential for aerospace and automotive industry. Effective weight reduction methods for a WFSG are choosing better materials and increasing the cooling capacity. Increasing the cooling capability of an existing WFSG dramatically demands great efforts been spent on investigating advanced cooling methods such as spray or effective internal cooling channels. Both of these two orientations for increasing cooling capacities require detailed and comprehensive CFD analysis. In this thesis, this particular part related to CFD analysis is not covered. Thus, designing an advanced cooling methods is beyond the scope of this thesis. Under this circumstance, selecting high grade material for designing WFSGs with less weight adopting the OOD tools validated becomes the major focus of this chapter. Meanwhile, application field such as automotive industry are very sensitive to the cost of a machine. Known automotive industry such Renault and BWM iX3 has implemented WFSGs as their drivetrains on Renault ZOE and BMW iX3. Therefore, SiFe based machine is still worthy for consideration during the design process. The

objective of this chapter is investigating the weight of a resultant WFSG with different combination of stator and rotor core materials. These high grade materials includes Vacodur 49, Vacodur S Plus, 35HXT series SiFe materials and JNEX900. The best performing WFSG option accounting different weight ratio of cost against weight are presented at the end of this chapter.

7.1 Descriptions of high grade materials

Advanced materials such as CoFe (Vacodur S Plus, Vacodur 49), SiFe based steel (10JNEX900, 35HXT780T) are the lately introduced materials that process appealing features for high speed high power density generators for example high yield strength, high magnetic saturation points or low iron losses for high speed machines. An investigation of high speed WFSGs adopting different advanced materials is performed in this chapter to understand how materials can affect the weight of a WFSG. Fig. 124 summarizes some common materials with their yield strength versus losses data at 400 Hz with a magnetization polarity of 1.0 T.

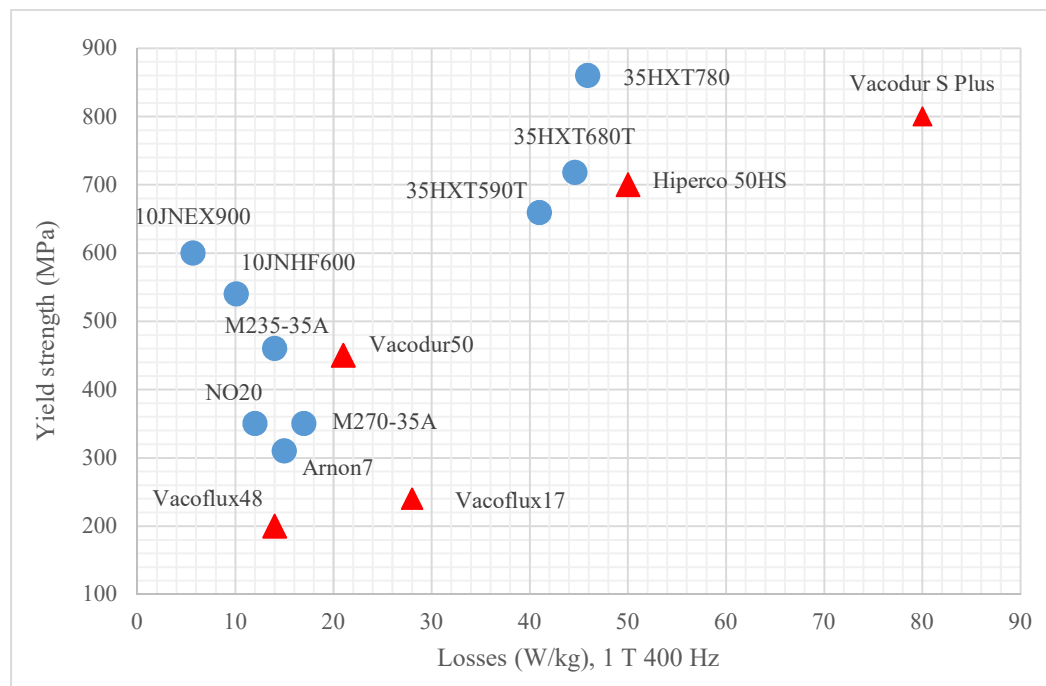


Fig. 124 Comparison of core losses and yield strength for different high performance electrical steels

In Fig. 124, materials marked with blue circles (●) are SiFe based electrical steels and those marked with red triangles (▲) are CoFe. In general, CoFe based materials have high saturation point compared with SiFe based materials. Therefore, CoFe

can potentially result in high power density in general. For a high speed WFSG application, stator core material selection is more flexible since stator core does not suffer from high stress resulting from high centrifugal forces. Therefore, materials with high saturation point and low losses at high frequency presented in Fig. 124 are potential choices for a stator core. Stator core materials are chosen from Vacoflux 48, 10JNEX900 and 35HXT590T.

A rotor core for a salient-pole synchronous generator suffers from natural born high stress concentration as presented in chapter 5. The yield strength for salient-pole synchronous generator rotor core must be higher than 560 MPa for a WFSG with rotor outer radius designed in chapter 4. Only material with such strength can it survive the high speed rotation for a WFSG required in chapter 1. However, 10JNEX900 is not recommend for embedded rotor core application due to its high silicon content resulting in poor ductility. Therefore, 10JNEX900 might not be a good candidate for rotor core materials for a WFSG as pole tips of a WFSG might fail due to vibration during high speed operations. Materials located at the top right corner can potentially be the core material for the rotor of a WFSG with careful losses management.

Although there are several high grade materials from various suppliers, the material contents are similar. With different annealing process, the electrical and mechanical properties of CoFe and SiFe based materials can be adjusted. For example, Vacodur S Plus in Fig. 124 can be annealed to material property similar to Hiperco 50HS. Therefore, this chapter picks several representative materials for rotor and stator cores respectively. Rotor core material can be chosen as Vacodur S Plus,

35HXT590T, 35HXT680T and 35HXT780T. The B-H property of 35HXT series materials are nearly the same based on the datasheet from Nippon steel. The difference in terms of yield strength of 35HXT series materials changes the radius of the rotor core. This potentially affects the weight of the overall generator. Meanwhile, 1 *mm* of air gap can handle the total deformation of rotor geometry designed in chapter 4.2 and based on the feedbacks in chapter 5.2.5, smaller air gap length can help improve the performance of a generator. This information can be adopted in this chapter to further enhance the performance of a WFSG by reducing the air gap length to a relatively safe margin such as 0.8 *mm*.

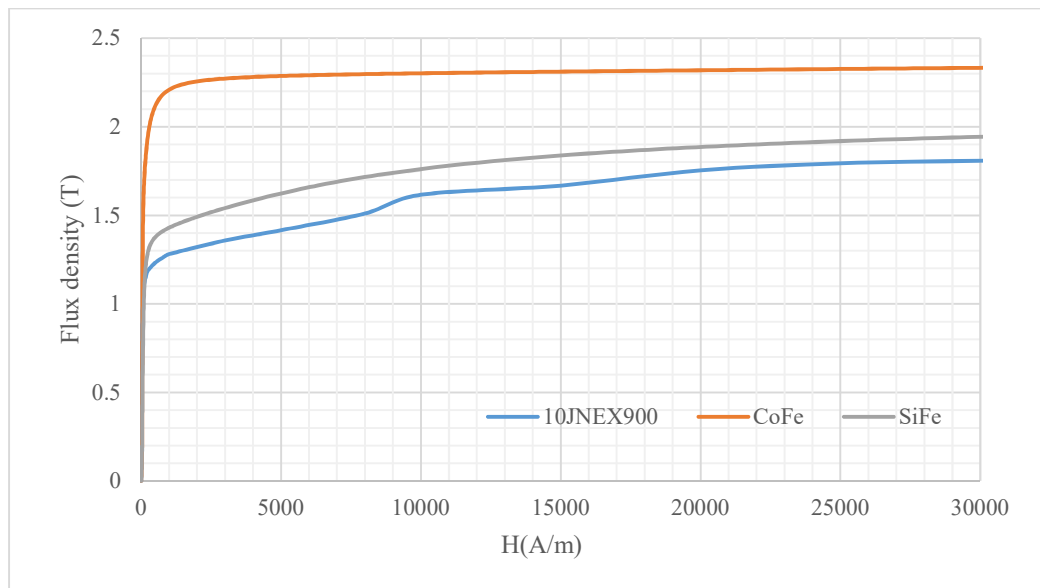


Fig. 125 BH curve for representative materials such as 10JNEX900, CoFe and SiFe. Since the materials contents are similar for SiFe and CoFe based materials, Fig. 125 presents the BH properties for several representative SiFe and CoFe materials. In this chapter, apart from SiFe materials from JFE (10JNEX900, 10JNHF600), all SiFe and CoFe materials are using BH properties in Fig. 125.

In chapter 4, based on the temperature behaviours of WFSGs been analysed, for a 54 slots 6 pole WFSG, the highest temperature occurs at 7,200 *rpm*. The main focus of this chapter is to find out if better grade material can help reduce the overall weight of a generator. Thus, as long as a WFSG survives the worst temperature condition at 7,200 *rpm*, this guarantees that a WFSG can survive high speed operation from temperature perspective and deliver designed power to required loads. Von-Mises distribution analysis of a rotor core geometry designed with different core materials is performed under 16,000 *rpm* to ensure the mechanical integrity.

7.2 CoFe based rotor core material – Vacodur S Plus

This chapter focuses on WFSG with rotor core material designed with Vacodur S Plus, 0.35 *mm* thick strip with 800 *MPa* yield strength saturating at 2.1 *T* is selected. Although thinner strip Vacodur S Plus material has lower losses compared with 0.35 *mm* strip material, but its yield strength is reduced to 600 *MPa*. The stator core material is chosen from Vacoflux 48, 10JNEX900 and 35HXT590T. Mechanical safety factor – 1.24 introduced in chapter 5 is adopted in this chapter to ensure safe operation of each rotor core designed in this chapter. The maximum allowable stress occurred in the simulation for Vacodur S Plus is 645 *MPa*. In addition, the rotor radius for WFSGs designed in chapter 7.2 is kept the same to understand how stress levels and total deformations are affected by the different rotor geometries.

7.2.1 Stator core made of Vacoflux 48

The stator core material is chosen as CoFe based material – Vacoflux 48. The advantages for CoFe based material is its high magnetic saturation point compared

with SiFe based materials. The downside for CoFe based materials are the high core losses compared with SiFe based material if the thickness for the strip is the same for different materials.

The maximum fundamental frequency from the design requirements is 800 *Hz*. Therefore, the iron losses induced from alternating magnetic field is still manageable based on the losses data shown in Fig. 124 if 0.1 *mm* strip Vacoflux 48 is implemented as stator core material. However, the overall temperature is still necessary to be analysed based on the losses simulation.

The magnetic saturation points for Vacoflux 48 and Vacodur S Plus are 2.4 *T* and 2.1 *T* respectively. Therefore, the analytical design points are as follows 1) the peak flux density in the air gap is 1.1 *T*; 2) the peak flux density on the stator teeth is 2.4 *T*; 3) the peak flux density on the stator yoke is 2.2 *T*; 4) the peak flux density on the rotor body and rotor yoke are 2.0 *T*.

An automated WFSG design process using validated OOD tool gives the flux density plotted in Fig. 126 a) at rotor pole body and rotor bore are 1.9 *T* and 1.91 *T* respectively. The flux density at stator teeth and stator back iron are 2.3 *T* and 2.1 *T* respectively. Fig. 126 b) presents the Von-Mises distribution of a rotor core made of Vacodur S Plus designed according to the electromagnetic performance of Vacoflux 48. The maximum stress level occurs at corner one and two are 503 *MPa* and 466 *MPa* respectively. The stress level experience by the rotor core is less than the recommended threshold value (645 *MPa*) stated at the beginning of this chapter. In Fig. 126 c), the maximum deformation occurs at the rotor pole tips at the

maximum operating speed (16,000 *rpm*). The total deformation of the rotor core depicted in Fig. 126 c) is 0.1 *mm* which counts for 12.5% of the overall air gap length. Thus, a collision between a rotor and stator core is not possible from total deformation perspective with the rotor geometry designed in this chapter.

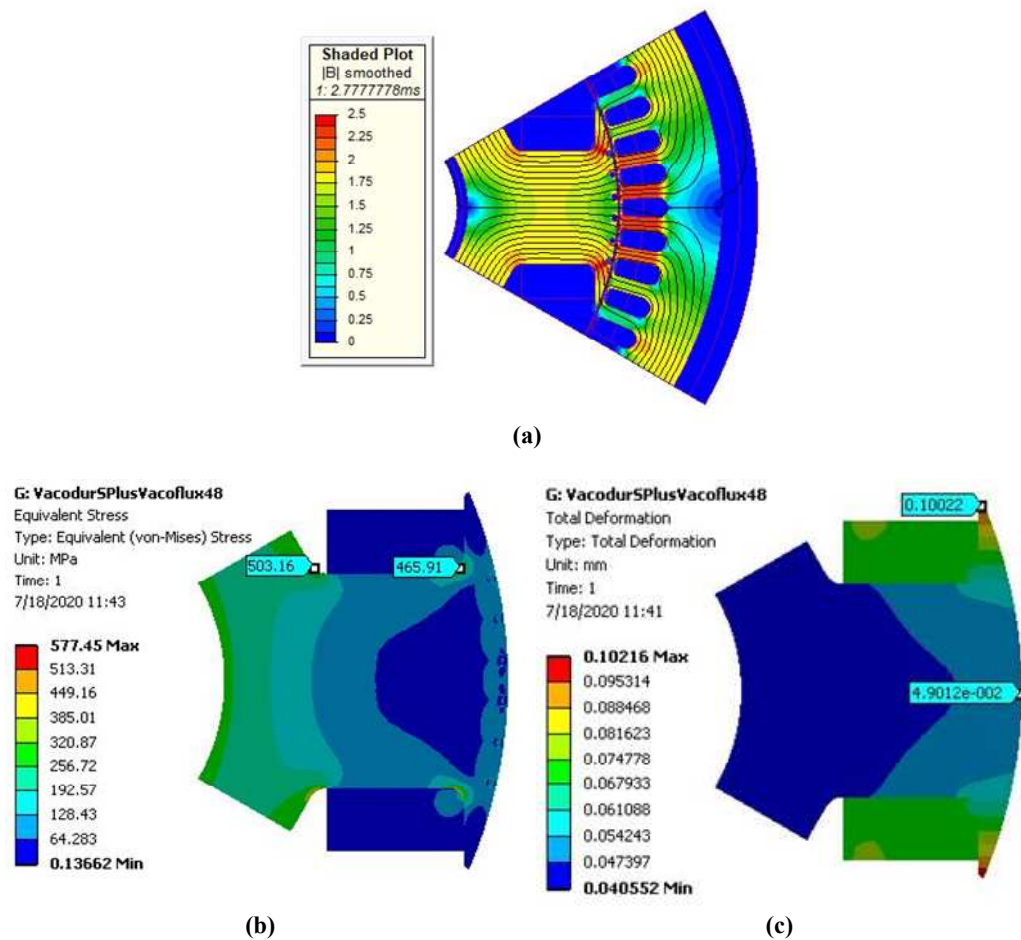


Fig. 126 a) No-load field plot for WFSGs with rotor core made of Vacodur S Plus and stator core made of Vacoflux 48 at 7,200 *rpm* b) Von-Mises distribution of rotor geometry made of Vacodur S Plus with stator core made of Vacoflux 48 at 16,000 *rpm* c) Total deformation of rotor geometry made of Vacodur S Plus with stator core made of Vacoflux 48 at 16,000 *rpm*

Table 18 full load performance of a WFSG designed with Vacodur S Plus and Vacoflux at 7,200 rpm

Stator Max. Temp. (degree)	Rotor Max. Temp. (degree)	Total Mass (kg)	Rotor Iron (kg)
146.1	234.9	59.4	19.3
Field Winding (kg)	Stator Iron (kg)	Armature Winding (kg)	Magnetic loading (T)
6.6	26.3	7.2	0.76

Table 18 demonstrates the full load temperature performance of a WFSG designed with Vacodur S Plus and Vacoflux 48. The maximum stator coil temperature is way below the temperature threshold value of Essex 220 class wire. On the other hand, the maximum rotor coil temperature is around 235 °C. Although this temperature is 5 °C above the threshold, but this small amount of over temperature condition does not affect the life time of the generator significantly. Meanwhile, in Fig. 126 a), the area of the rotor coil has reached the maximum allowable space within the inter-pole region. Therefore, further reduction of maximum rotor coil temperature is not possible by increasing the rotor coil area. The active weight achieved by adopting CoFe based materials for both stator and rotor cores is 59.4 kg. The active weight for a WFSG designed in this chapter is 23.7% less than the WFSG option finalized in chapter 4.2.

7.2.2 Stator core made of 10JNEX900

The major reason for choosing 0.1 mm strip 10JNEX900 material is due to its low losses characteristic at high operating frequency region. JFE steel cooperation suggests the maximum operating frequency for 10JNEX900 is from 1 kHz to 5 kHz. However, the downside for 10JNEX900 is its low saturation point (1.2 T) compared with other SiFe for CoFe based materials.

The maximum operating fundamental frequency for the required WFSG is 800 Hz. This operating frequency is way below the recommended value for 10JNEX900. Meanwhile, the magnetic saturation point for 10JNEX900 is the lowest among materials presented in Fig. 124. These two factors may result in a heavier WFSG compared with high magnetic saturation materials since core losses may not be a dominant factor affecting the weight of a WFSG.

Vacodur S Plus and 10JNEX900 saturate at 2.2 T and 1.2 T respectively. A big gap exists between the saturation points of two different materials. Based on empirical experience, the ratio between the width of a stator teeth and the slot width is close to one. Since the same amount of flux has to travel from the air gap to a stator core and back to the air gap, the width of a stator teeth has to handle all the flux passed from the air gap without too much saturation. If the peak flux density in the air gap is chosen to be half of the saturation point of Vacdur S Plus (1.1 T), this results in large stator teeth width with a peak flux density of 1.2 T (10JNEX900). The resultant slot width is very tiny to allocate enough copper in the stator slots. This rule is applied to WFSG designed with rotor saturation point higher than stator saturation point. Under this circumstance, peak flux density in the air gap is chosen to be around half of the saturation point of 10JNEX900 (0.7 T). Under this circumstance, the analytical machine design choices are as follows 1) the peak flux density on the rotor body and rotor bore are 2.1 T; 2) the peak flux density on the stator teeth is chosen to be 1.1 T; 3) the peak flux density on the stator back iron is 1.0 T.

Fig. 127 a) presents the no-load field map for a WFSG designed with Vacodur S Plus and 10JNEX900. The peak flux density on the rotor body and rotor bore are

1.83 T and 1.73 T. These two values deviate from the expected value by about 12.8% which is higher than analytical value and tolerance expected within the analytical script. The flux density on the stator teeth and stator back iron in Fig. 127 a) is about 1.21 T and 1.13 T, which is around 10% different from the expected analytical value. The major reasons for causing this is that the saturation point for Vacodur S Plus and 10JNEX900 are almost doubled. The magnetic loading for the combination of Vacodur S Plus and 10JNEX900 is less than the case in chapter 4.2. Therefore, the width of the magnetic path required from rotor core made of Vacodur S Plus for passing same amount of flux from stator core is smaller than the case in chapter 4.2. The thinner pole width is reflected clearly in the magnetic field plot in Fig. 127 compared with that in chapter 4.2. Meanwhile, in Fig. 127, the rotor pole tips saturates quite heavily which consumes significant amount of MMF created by rotor field winding. Under this circumstance, the magnetic field density on the magnetic circuit is smaller than the expected analytical values.

Fig. 127 a) plots the Von-Mises distribution analysis of rotor core made of Vacodur S Plus designed according to the electromagnetic performance of 10JNEX900. The alteration of rotor pole structure has negative impacts on the stress level of the rotor poles at corner 1 and 2. A 21% increase of stress at corner 2 is observable compared with the rotor core designed in chapter 7.2.1. The maximum stress level shown in Fig. 127 b) is smaller than threshold value (645 MPa) mentioned at the beginning of this chapter. Thus, from static structure perspective this rotor is able to operate under 16,000 rpm.

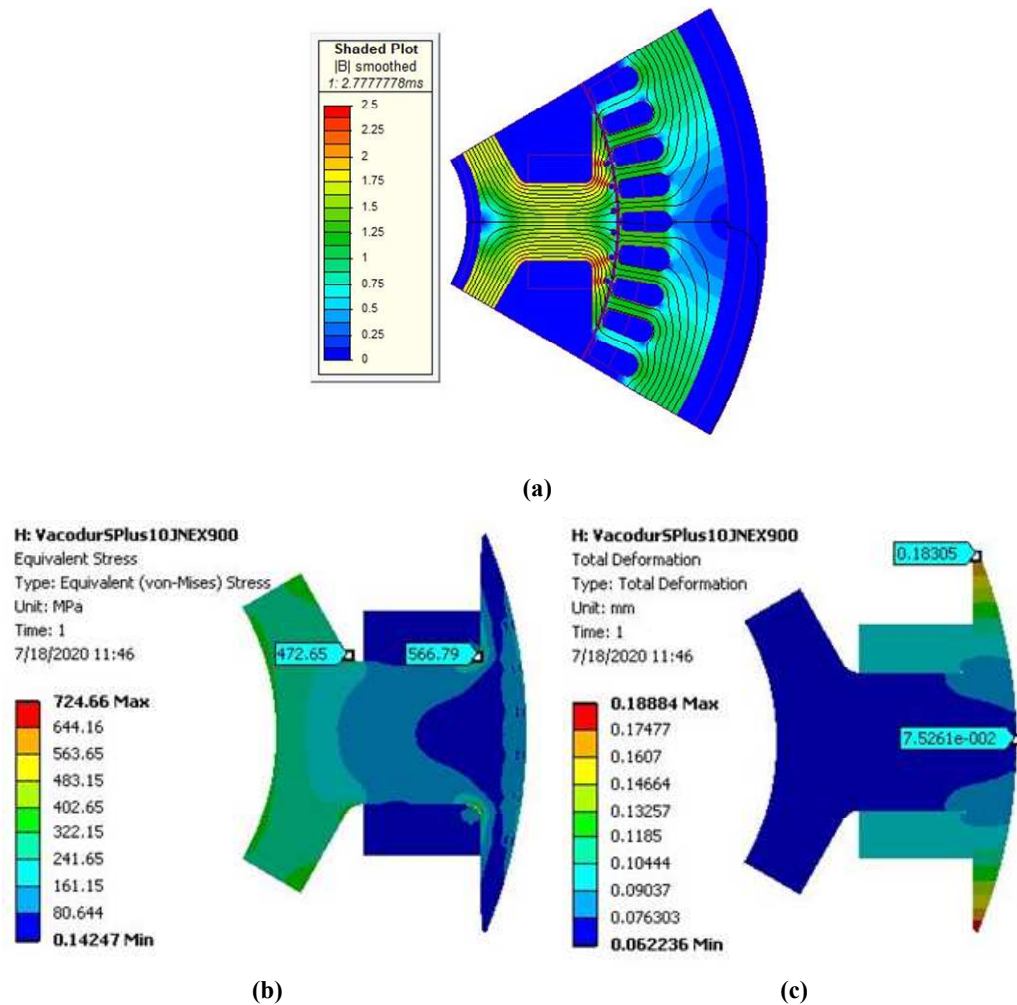


Fig. 127 a) No-load field plot for WFSGs with rotor core made of Vacodur S Plus and stator core made of 10JNEX900 at 7,200 rpm b) Von-Mises distribution of rotor geometry made of Vacodur S Plus with stator core made of 10JNEX900 at 16,000 rpm c) Total deformation of rotor geometry made of Vacodur S Plus with stator core made of 10JNEX900 at 16,000 rpm

The maximum total deformation of the rotor core presented in Fig. 127 c) is 0.18 mm which counts for 22.5% of the overall air gap length. This amount of deformation is 50% larger than that of chapter 7.2.1. Theoretically, from total deformation perspective this rotor core can operate at 16,000 rpm without causing a collision between a rotor and stator core. However, even this rotor core is able to survive the high speed rotation, a significant increase of stress level and particular

total deformation is a still dangerous for practical implementation. Therefore, this design option is considered as a backup plan compared with the design option in chapter 7.2.1.

Table 19 full load performance of a WFSG designed with Vacodur S Plus and 10JNEX900 at 7,200 rpm

Stator Max. Temp. (degree)	Rotor Max. Temp. (degree)	Total Mass (kg)	Rotor Iron (kg)
155.1	216.6	84.8	23.3
Field Winding (kg)	Stator Iron (kg)	Armature Winding (kg)	Magnetic loading (T)
5.9	44.3	11.1	0.47

Table 19 presents the full load temperature analysis of this WFSG at 7,200 rpm. The maximum temperature on the rotor coil only hits 216 °C leaving a safe margin for rotor coil to have enough life time. The total active weight of the generator is 84.8 kg which is even higher than the active weight of the generator designed in chapter 4.2. Based on the analysis in this chapter, the property of stator core materials has a much higher impact on the weight performance of a WFSG even with the presence of CoFe based rotor core materials. This observation has to be elaborated according to WFSGs designed with JNEX900 stator core in the next few chapter.

7.2.3 Stator core made of 35HXT590T

Stator cores made of 35HXT590T material have similar magnetic properties compared with the common M235-35A but higher core losses. The combination of Vacodur S Plus and 35HXT590T for rotor and stator core materials respectively is similar to material combination in chapter 7.2.2. Therefore, the analytical design points are listed as follows; 1) the air gap flux density is chosen to be 0.8 T; 2) the

peak flux density on the rotor body and rotor bore are $2.1 T$; 3) the peak flux density on the stator teeth and stator back iron are $1.7 T$ and $1.5 T$ respectively.

Fig. 128 a) plots the no-load field map of a WFSG designed in this chapter. The magnetic flux density on the rotor body and bore are $1.7 T$ and $1.83 T$ respectively. The flux density at the stator teeth and stator back iron are $1.83 T$ and $1.45 T$. A well matched FE simulation and the analytical is observable.

Fig. 128 b) depicts the Von-Mises distribution analysis of a rotor core made of Vacodur S Plus at $16,000 rpm$. The stress level at corner one and two are $574 MPa$ and $615 MPa$ respectively which is less than the maximum allowable stress for Vacodur S Plus.

Fig. 128 c) presents the total deformation of a rotor geometry designed with Vacodur S Plus at $16,000 rpm$. The maximum total deformation this rotor geometry presented in Fig. 128 c) is $0.15 mm$. This amount of deformation counts for around 19% of the overall air gap length. Under this circumstance, from total deformation perspective, a collision between a stator and rotor core is not possible. From a mechanical perspective, it is concluded that a WFSG rotor core designed in this chapter performs not as good as a rotor core designed in chapter 7.2.1, but better than the rotor core in chapter 7.2.2.

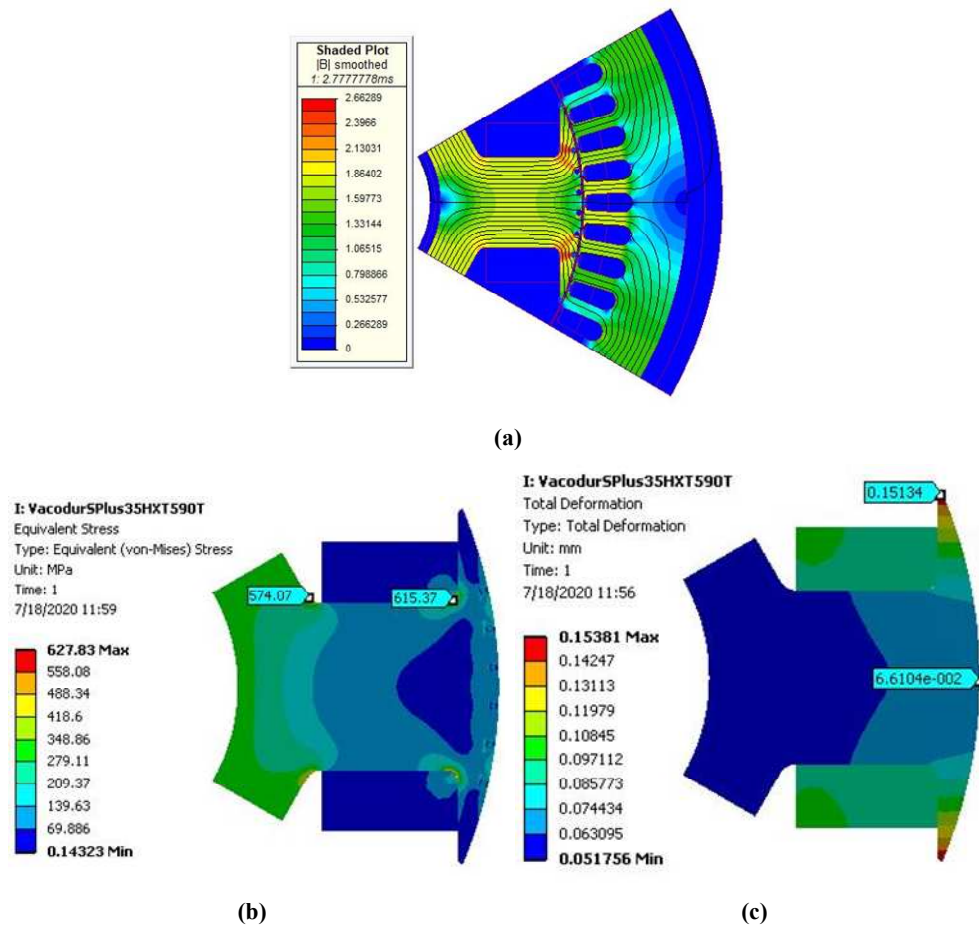


Fig. 128 a) No-load field plot for WFSGs with rotor core made of Vacodur S Plus and stator core made of 35HXT590T at 7,200 rpm b) Von-Mises distribution of rotor geometry made of Vacodur S Plus with stator core made of 35HXT590T at 16,000 rpm c) Total deformation of rotor geometry made of Vacodur S Plus with stator core made of 35HXT590T at 16,000 rpm

Table 20 full load performance of a WFSG designed with Vacodur S Plus and 10JNEX900 at 7,200 rpm

Stator Max. Temp. (degree)	Rotor Max. Temp. (degree)	Total Mass (kg)	Rotor Iron (kg)
161.8	207.6	65.7	18.5
Field Winding (kg)	Stator Iron (kg)	Armature Winding (kg)	Magnetic loading (T)
7.9	30.5	8.8	0.62

Table 20 lists the full-load temperature analysis of a WFSG designed in this chapter.

The maximum temperature inside the rotor coils are 207.6 °C. An adequate

temperature margin is left for guarantee enough life time for the generator. The active weight of this generator is 65.7 kg which is 15.6% less than the generator designed in chapter 4.2. Considering both the weight and mechanical aspects, the WFSG designed in this chapter is the second best option among chapter 7.2.

7.3 SiFe based rotor core material – 35HXT590T

Different industry field such as aerospace, automotive and marine applications have criteria balancing aspects such as budget, power density and efficiency. As mentioned in chapter 1, CoFe based material are quite expensive. Thus, an investigation of using cheaper SiFe based material is necessary to understand how the performance of a WFSG can be affected. Meanwhile, several SiFe based materials can also achieve high yield strength that is a suitable choice for high speed WFSG applications. Therefore, analysing the weight performance of WFSGs with cheaper SiFe based materials is still meaningful. Chapter 7.3, 7.4 and 7.5 analyses the weight performance of WFSGs with SiFe based rotor materials. 35HXT590T has better mechanical performance compared with M235-35A achieving a yield strength up to 659 MPa. The maximum limit for 35HXT590T by introducing a 1.24 safety factor is 531 MPa. Therefore, the rotor radius can be increased to reduce the overall active weight of a WFSG. In addition, the rotor radius for WFSGs designed in chapter 7.3 are kept the same to understand how stress levels and total deformations are affected by the different rotor geometries.

7.3.1 Stator core made of Vacoflux 48

The rotor core material 35HXT590T has a lower saturation point compared with Vacoflux 48. This is the WFSG design case introduced in chapter 7.2.2. Hence,

following rules in chapter 7.2.2, analytical design points for the peak air gap flux density is chosen at $1.1 T$. The peak flux density at the rotor body and rotor bore are $1.4 T$ and $1.5 T$ respectively. The flux density in the stator teeth and stator back iron are $2.1 T$ and $2.0 T$ respectively.

Fig. 129 a) plots the no-load magnetic field map of a WFSG designed in this chapter. The flux density at rotor bore and rotor body based on FE analysis in Fig. 129 a) are $1.41 T$ and $1.52 T$ respectively. The flux density at stator teeth and stator back iron are $2.28 T$ and $2.10 T$. The difference between FE analysis and analytical expectations at all four different spots are less than 10%. Thus, the electromagnetic design requirements for this WFSG are met. The peak air gap flux density in the air gap is chosen to be about half of the saturation point ($1.1 T$) of Vacoflux 48. Since the same amount of flux must passing through the rotor and stator core, the width of the rotor core is wider than the one designed in chapter 4.2 as shown in Fig. 129 a) due to increased magnetic loading.

Fig. 129 b) presents the Von-Mises distribution of a rotor core made of 35HXT590T showing the maximum stress occurs at corner 1 indicating roughly $348 MPa$. The stress level at corner 2 is $234 MPa$. Both of stress level at these two corners are below $531 MPa$.

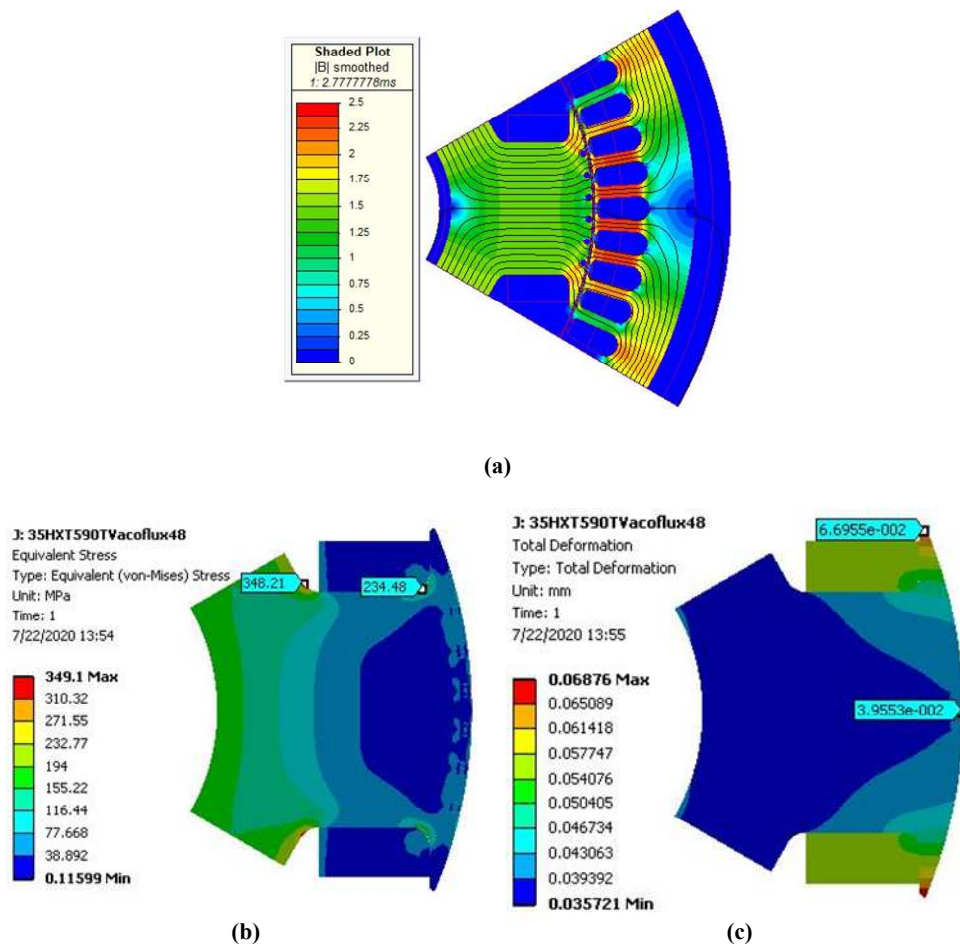


Fig. 129 a) No-load field plot for WFSGs with rotor core made of 35HXT590T and stator core made of Vacoflux 48 at 7,200 *rpm* b) Von-Mises distribution of rotor geometry made of 35HXT590T with stator core made of Vacoflux 48 at 16,000 *rpm* c) Total deformation of rotor geometry made of 35HXT590T with stator core made of Vacoflux 48 at 16,000 *rpm*

Fig. 129 c) demonstrates the total deformation of a rotor core made of 35HXT590T designed according to the electromagnetic performance of Vacoflux 48. The maximum total deformation occurs at the rotor pole tips bending outwards by 0.065 *mm*. This amount of deformation counts for 8% of the overall air gap length. From both total deformation and static structure analysis perspective, this rotor core is able to survive the top speed operation at 16,000 *rpm*.

Table 21 full load performance of a WFSG designed with 35HXT590T and Vacoflux 48 at 7,200 rpm

Stator Max. Temp. (degree)	Rotor Max. Temp. (degree)	Total Mass (kg)	Rotor Iron (kg)
160.9	304	60.5	22
Field Winding (kg)	Stator Iron (kg)	Armature Winding (kg)	Magnetic loading (T)
4.4	25.8	8.2	0.72

Table 21 gathers the full-load temperature analysis of a WFSG designed with 35HXT590T and Vacoflux 48. The maximum stator temperature stays at a safe region. However, the maximum rotor coil temperature touched 304 °C. This temperature is way higher than the recommended maximum temperature threshold value (230 °C) provided by Essex magnet wire group. Based on the general accepted rule that a 10 °C increase of coil temperature halves the life time of insulation coated on the wire. Thus, a WFSG under this condition does not guarantee adequate life time. Meanwhile, while Fig. 129 a) shows that there is no room for accommodating more rotor coils to reduce rotor temperature. Therefore, this WFSG design options is removed from the option list.

7.3.2 Stator core made of 10JNEX900

The rotor (35HXT590T) core materials have a higher magnetic saturation point compared with stator core (10JNEX900) materials. This combination is similar to that of chapter 7.2.2. Therefore, analytical design points are 0.7 T for the peak flux density in the air gap; 1.5 T for the peak flux density on the rotor body and 1.5 T for the rotor bore; 1.1 T and 1.0 T for the peak flux density on the stator teeth and stator back iron respectively. The design requirements of the flux density locates at rotor

body, rotor bore, stator teeth and stator back iron complies with the no-load FE field map in Fig. 130.

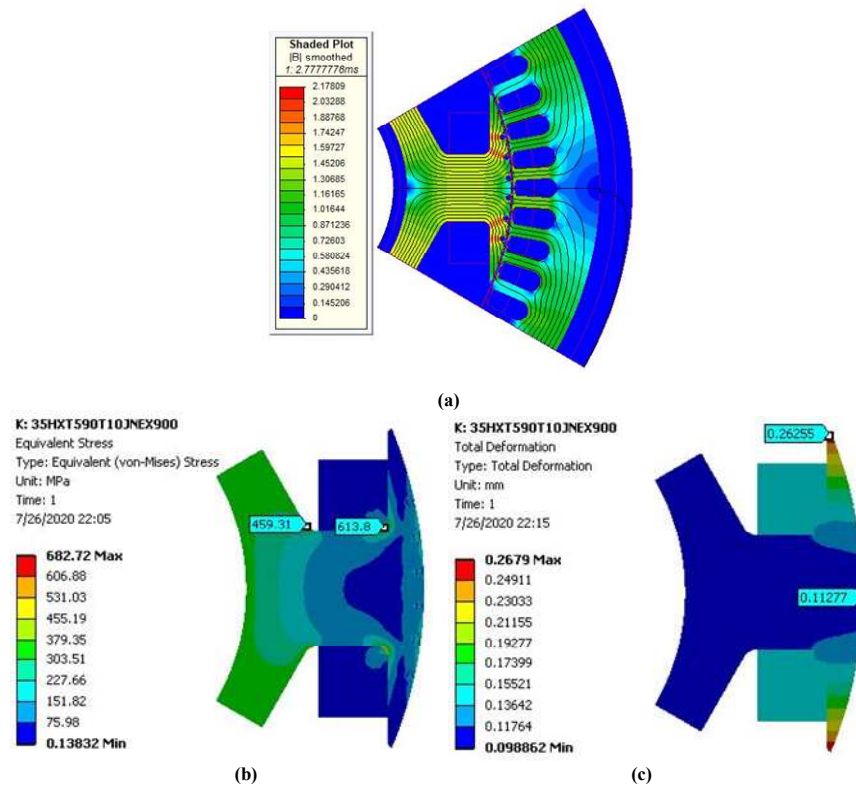


Fig. 130 a) No-load field plot for WFSGs with rotor core made of 35HXT590T and stator core made of 35HXT590T at 7,200 *rpm* b) Von-Mises distribution of rotor geometry made of 35HXT590T with stator core made of 35HXT590T at 16,000 *rpm* c) Total deformation of rotor geometry made of 35HXT590T with stator core made of 35HXT590T at 16,000 *rpm*

Fig. 130 b) presents the Von-Mises distribution of a rotor core made of 35HXT590T with a stress level at corner 2 up to 614 *MPa* that is 8% higher than the case in chapter 7.3.2. Fig. 130 c) depicts the total deformation of a rotor core designed in this chapter. In accordance to the expectation, the maximum total deformation shown in Fig. 130 c) is 0.26 *mm* that is almost 4 times larger than that in Fig. 129 c). Although this amount of deformation counts for 32% of the overall air gap length,

theoretically it is still safe to avoid a collision between a rotor and stator core. However, practical implementation of this rotor core can be very dangerous. Therefore, this design option is also not considered as an option on the list.

Table 22 full load performance of a WFSG designed with 35HXT680T and 10JNEX900 48 at 7,200 rpm

Stator Max. Temp. (degree)	Rotor Max. Temp. (degree)	Total Mass (kg)	Rotor Iron (kg)
156.9	227.3	93.1	26.2
Field Winding (kg)	Stator Iron (kg)	Armature Winding (kg)	Magnetic loading (T)
9.1	26.2	12	0.38

Table 22 collects the full-load temperature analysis of a WFSG designed in this chapter. The maximum stator coil temperature is kept in a very safe margin. Meanwhile, the maximum rotor coil temperature is also kept below the threshold temperature (230 °C). Therefore, the WFSG designed in this chapter has enough life time. Nevertheless, the active weight of a WFSG designed in this chapter with 10JNEX900 is about 19.5% heavier than the WFSG designed in chapter 4.2 and 53.9% heavier than the active weight of a WFSG designed in chapter 7.3.1. This information indicates that a WFSG designed with a 35HXT590T rotor and a 10JNEX900 stator core is less competitive regarding to the power to weight ratio compared with the combination of 35HXT590T and Vacoflux 48 in chapter 7.3.1.

7.3.3 Stator core made of 35HXT590T

The rotor core materials are the same as stator materials. Since the magnetic property for 35HXT590T is similar to M235-35A, the electromagnetic design choices for a WFSG design option with 35HXT590T are the same as those presented

chapter 4.1.1 such as the flux density design at places such as rotor body, stator teeth and stator back iron.

Fig. 131 a) plots the field map for a WFSG design with 35HXT590T. In Fig. 131 a), the flux density at rotor body and rotor bore at around 1.42 T; the flux density at stator teeth and stator back iron are 1.8 T and 1.5 T. The peak air gap flux density is 0.85 T. Therefore, the resultant no-load magnetic field is under expectation.

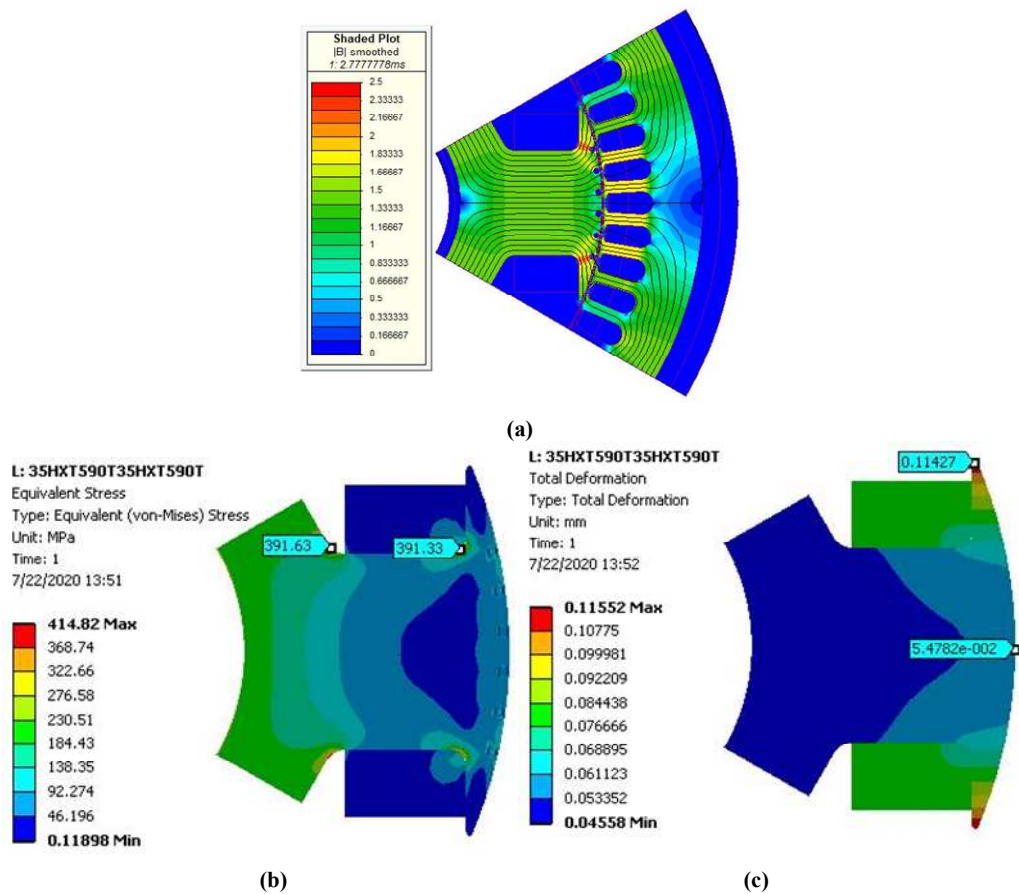


Fig. 131 a) No-load field plot for WFSGs with rotor core made of 35HXT590T and stator core made of 35HXT590T at 7,200 rpm b) Von-Mises distribution of rotor geometry made of 35HXT590T with stator core made of 35HXT590T at 16,000 rpm c) Total deformation of rotor geometry made of 35HXT590T with stator core made of 35HXT590T at 16,000 rpm

Fig. 131 b) presents the Von-Mises distribution analysis of a rotor geometry made of 35HXT590T with similar stress level for corner 1 and 2 - 391 *MPa*. This value is way smaller than the recommended stress limit (531 *MPa*) for 35HXT590T. Therefore, from static structure analysis perspective, the rotor geometry is able to survive the high speed rotation at 16,000 *rpm*.

Fig. 131 c) presents the total deformation of a rotor geometry made of 35HXT590T. The maximum total deformation of this rotor core locates at rotor pole tips bending outwards by 0.11 *mm*. This amount of deformation counts for 13.7% of the overall air gap length. Theoretically, the rotor geometry designed in this chapter is able to survive the high speed rotation at 16,000 *rpm* without a collision between its rotor and stator core.

Table 23 full load performance of a WFSG designed with 35HXT590T and 35HXT590T at 7,200 *rpm*

Stator Max. Temp. (degree)	Rotor Max. Temp. (degree)	Total Mass (<i>kg</i>)	Rotor Iron (<i>kg</i>)
158.4	223.5	73	24.1
Field Winding (<i>kg</i>)	Stator Iron (<i>kg</i>)	Armature Winding (<i>kg</i>)	Magnetic loading (<i>T</i>)
8.7	32.5	7.5	0.56

Table 23 collects the full-load temperature analysis of a WFSG designed in this chapter. The maximum stator coil temperature stays in the safe margin. Meanwhile, the maximum rotor coil temperature also stays below the threshold value (230 °C). Therefore, the WFSG designed in this chapter have enough life based on Essex wire life time charts. The active weight of this generator is about 6% less than the WFSG designed in chapter 4.2.

In summary, by using the same SiFe rotor core materials, a WFSG with Vacoflux 48 shows the highest competitiveness among Vacoflux, 10JNEX900 and 35HXT590T. The second competitive WFSG is the one with 35HXT590T on both rotor and stator core. A WFSG designed with 10JNEX900 shows the least competitiveness among all three design options.

7.4 SiFe based rotor core material – 35HXT680T

Chapter 7.2 investigates the performance of a WFSG designed with SiFe based materials – 35HXT590T with larger rotor radius. The stress level of all the design options in chapter 7.3 still has a big margin towards the maximum threshold value for 35HXT590T. Meanwhile, the total deformation also plays a vital role in limiting the maximum rotor radius since a collision due to rotor deformation must be avoided as well. The competitiveness of WFSGs with different materials are listed at the end of chapter 7.3. However, how increasing rotor radius affects the active weight of a WFSG practically is still unknown. Therefore, all three design options with 35HXT680T are analysed based on similar processes in chapter 7.3.

35HXT680T can achieve a yield strength of 718 MPa which allows machine designer to design a WFSG with larger rotor radius which can potentially help reduce the weight of a WFSG according to the conclusion in chapter 4.2.3. By introducing a 1.24 safety factor, the maximum allowable stress level occurred in a rotor core designed in this chapter cannot exceed 579 MPa . However, the increase of rotor radius also results an increased total deformation of rotor pole tips. Therefore, careful attention must be paid to three factors: 1) rotor geometry 2) rotor total deformation 3) stress concentration at critical rotor locations. In addition, the

rotor radius for WFSGs designed in chapter 7.4 are kept the same to understand how stress levels and total deformations are affected by the different rotor geometries.

7.4.1 Stator core made of Vacoflux 48

The electromagnetic design considerations for this chapter are similar to a case presented in chapter 7.2.1 since the electromagnetic properties for 35HXT680T are similar to 35HXT590T. The electromagnetic design choices for the materials combinations in this chapter are the same as those in chapter 7.3.1. In contrast, 35HXT680T can allow a machine designer to size a WFSG with larger rotor radius.

Fig. 132 a) presents the no-load magnetic field plot for a WFSG designed in this chapter. The magnetic flux density at the rotor body and rotor bore are 1.43 T and 1.5 T respectively. The flux density at the stator teeth and stator back iron are 2.28 T and 2.13 T.

Fig. 132 b) indicates the Von-Mises distribution analysis of a rotor core made of 35HXT680T designed according to the electromagnetic performance of Vacoflux 48. The maximum stress occurs at corner 1 hitting 443 MPa. The stress level at corner 2 hits 303 MPa. Stress level of these two region are way below 579 MPa. Therefore, from the static structural perspective, the rotor core can survive the high speed rotation at 16,000 rpm.

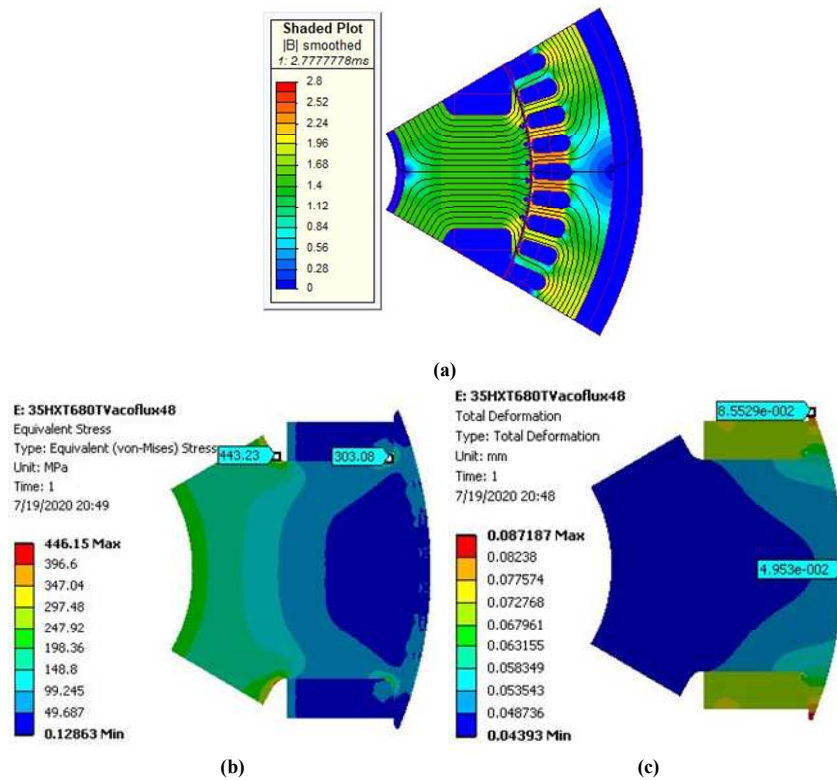


Fig. 132 a) No-load field plot for WFSGs with rotor core made of 35HXT680T and stator core made of Vacoflux 48 at 7,200 *rpm* b) Von-Mises distribution of rotor geometry made of 35HXT680T with stator core made of Vacoflux 48 at 16,000 *rpm* c) Total deformation of rotor geometry made of 35HXT680T with stator core made of Vacoflux 48 at 16,000 *rpm*

Fig. 132 c) shows the total deformation of a rotor core made of 35HXT680T designed according to the electromagnetic performance of Vacoflux 48. The maximum total deformation of the rotor core geometry at 16,000 *rpm* on the pole tips is 0.086 *mm*. This amount of total deformation only counts for roughly 11% of the overall air gap length. Thus, a collision between the rotor and stator core is avoided and a smooth rotation is guaranteed. Although, the rotor radius for the geometry designed in this chapter is 1.1 times of that in chapter 7.3, the total deformation is the smallest compared with cases presented in chapter 7.3.

Table 24 full load performance of a WFSG designed with 35HXT680T and Vacoflux 48 at 7,200 rpm

Stator Max. Temp. (degree)	Rotor Max. Temp. (degree)	Total Mass (kg)	Rotor Iron (kg)
147.6	234.7	63.3	23.6
Field Winding (kg)	Stator Iron (kg)	Armature Winding (kg)	Magnetic loading (T)
4.9	27.2	7.6	0.74

Table 24 presents the full-load temperature analysis of a WFSG designed in this chapter. The maximum stator core temperature is in the safe region. However, the maximum rotor coil temperature hits almost 235 °C. Although the coil temperature is higher than the rated value, slight rotor over temperature does not decrease the life time of the rotor coil significantly. In addition, the amount of rotor coil is also limited by the actual space available for the rotor coils. In Fig. 132 a), the area for the rotor coil is not enough for adding more coil into the inter-pole space. Therefore, given the rotor geometry, it is not possible decrease the rotor temperature without increasing the cooling capacity. The weight of the active material is 63.3 kg that is 18.7% less than the active weight of the machine designed in chapter 4.2. The active weight is only 1.7 % heavier than a WFSG in chapter 7.2.1 designed with CoFe on both stator and rotor core. Therefore, this option is also very competitive against CoFe based WFSGs from weight performance and budget perspective.

7.4.2 Stator core made of 10JNEX900

The electromagnetic design choices for materials combinations in this chapter are the same as those in chapter 7.3.2. Fig. 133 a) presents the no-load field plot of a WFSG designed with 35HXT680T and 10JNEX900. The flux density at rotor body and rotor bore are 1.38 T and 1.48 T respectively. The flux density at the stator teeth

and stator back iron are 1.3 T and 1.1 T respectively. The FE simulation results for rotor flux density are close to the design specifications. In contrast, the flux density on the stator core has a roughly 10% difference.

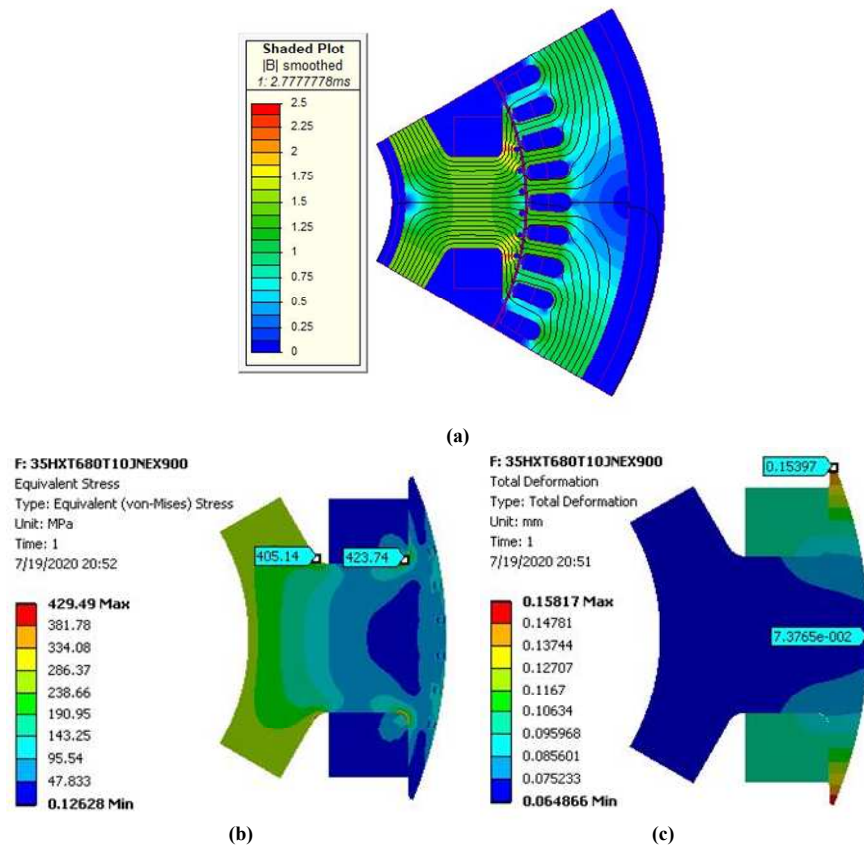


Fig. 133 a) No-load field plot for WFSGs with rotor core made of 35HXT680T and stator core made of 10JNEX900 at 7,200 rpm b) Von-Mises distribution of rotor geometry made of 35HXT680T with stator core made of 10JNEX900 at 16,000 rpm c) Total deformation of rotor geometry made of 35HXT680T with stator core made of 10JNEX900 at 16,000 rpm

Fig. 133 b) summarize the Von-Mises distribution of a WFSG rotor core made of 35HXT680T designed according to the electromagnetic performance of 10JNEX900. The maximum stress level occurs at corner 2 achieving about 424 MPa. The stress at corner 1 is 405 MPa. Both stress level at corner one and two are below

threshold value 579 MPa . Therefore, the rotor geometry designed in this chapter can survive the high speed rotation at $16,000 \text{ rpm}$ from the static structure analysis perspective.

Fig. 133 c) demonstrates the total deformation of the rotor geometry made of 35HXT680T designed according to the 10JNEX900. The maximum total deformation locates at the rotor pole tips that is 0.15 mm . This amount of total deformation counts for roughly 19% of the entire air gap length. Theoretically, this rotor core is able to survive the high speed rotation at $16,000 \text{ rpm}$.

Table 25 full load performance of a WFSG designed with 35HXT680T and 10JNEX900 48 at $7,200 \text{ rpm}$

Stator Max. Temp. (degree)	Rotor Max. Temp. (degree)	Total Mass (kg)	Rotor Iron (kg)
169.5	222.8	97.3	26.6
Field Winding (kg)	Stator Iron (kg)	Armature Winding (kg)	Magnetic loading (T)
7.9	47.3	8.2	0.5

Table 25 summarizes the full-load temperature analysis of a WFSG designed with 35HXT680T and 10JNEX900. The maximum stator coil temperature and rotor temperature in Table 25 are lower than $230 \text{ }^\circ\text{C}$. Thus, adequate life time can be guaranteed by 220 class Essex wire. Although the temperature behaviour of a WFSG designed in this chapter gives a generator enough life time, but the active weight of a generator behaves in the opposite way compared with temperature of a generator. In Table 25, the active weight of a generator is 97.3 kg that is almost 25% heavier than a WFSG designed in chapter 4.2. In summary, a WFSG designed with 10JNEX900 stator core is not competitive against a WFSG designed in chapter 4.2 with CoFe based materials and 7.4.1 with SiFe based materials in terms of weight.

7.4.3 Stator core made of 35HXT590T

In this chapter, the rotor and stator core materials are 35HXT680T and 35HXT590T respectively. Thus, the same electromagnetic design considerations proposed in chapter 7.3.3 are adopted in this chapter.

Fig. 134 a) plots the magnetic field map for a WFSG designed in this chapter at no-load. The flux density at the rotor body and rotor bore are $1.42\ T$ and $1.43\ T$ respectively. The flux density at the stator teeth and stator back iron are $1.85\ T$ and $1.54\ T$ respectively. The difference between the FE results and analytical expectations are less than 10%.

Fig. 134 b) presents the Von-Mises distribution analysis of a rotor geometry made of 35HXT680T designed according to the electromagnetic performance of 35HXT590T. The maximum stress level locates at corner 1 achieves $591\ MPa$ and the stress level at corner 2 is $589\ MPa$. Both of these maximum stress are around 1.7% to 2% larger than threshold value ($579\ MPa$). However, the yield strength for 35HXT680T is $718\ MPa$. The minimum safety factor that can be achieved by the rotor geometry in Fig. 134 b) is 1.21. From the static structure perspective, the rotor geometry designed in this chapter is able to survive the high speed rotation ($16,000\ rpm$). However, the risk still presents since the safety factor is 2% less than the minimum requirements. Therefore, the rotor geometry presented in Fig. 134 b) can be considered as a backup plan.

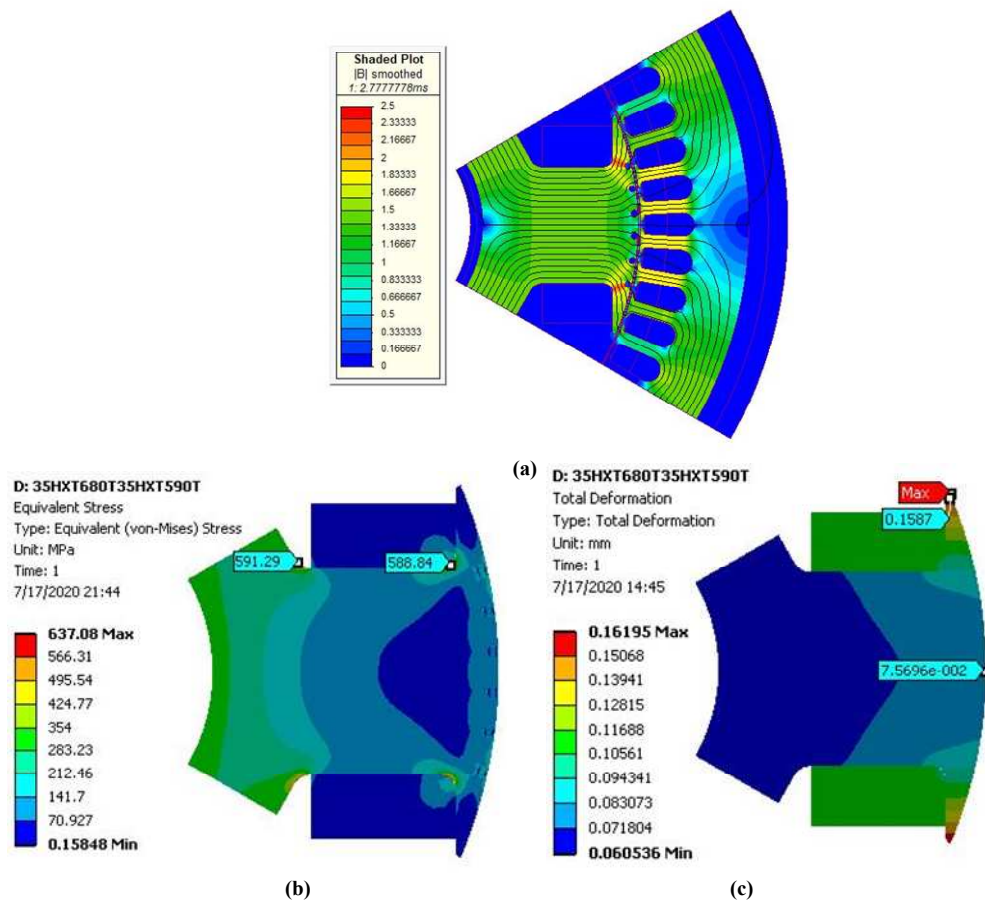


Fig. 134 a) No-load field plot for WFSGs with rotor core made of 35HXT680T and stator core made of 35HXT590T at $7,200\text{ rpm}$ b) Von-Mises distribution of rotor geometry made of 35HXT680T with stator core made of 35HXT590T at $16,000\text{ rpm}$ c) Total deformation of rotor geometry made of 35HXT680T with stator core made of 35HXT590T at $16,000\text{ rpm}$

Fig. 134 c) presents the total deformation of the rotor geometry made of 35HXT680T designed according to the electromagnetic performance of 35HXT590T. The maximum total deformation locates at rotor pole tips bending outwards by 0.16 mm at $16,000\text{ rpm}$. This amount of total deformation counts for about 20% of the overall air gap length. Therefore, from total deformation perspective, the rotor geometry in Fig. 134 c) is able to survive the top speed operation at $16,000\text{ rpm}$ without causing a collision between its stator and rotor core.

However, this design option is still considered as a backup option unless there is not better option available designed in chapter 7.

Table 26 full load performance of a WFSG designed with 35HXT680T and 35HXT590T at 7,200 rpm

Stator Max. Temp. (degree)	Rotor Max. Temp. (degree)	Total Mass (kg)	Rotor Iron (kg)
159.4	229.8	73.9	24.8
Field Winding (kg)	Stator Iron (kg)	Armature Winding (kg)	Magnetic loading (T)
7.2	33.4	8.4	0.66

Table 26 gathers the full-load temperature analysis of WFSG designed in this chapter. The maximum rotor coil temperature hits 229.8 °C and the stator coil temperature hits 159.4 °C. With 220 class Essex wire, adequate life time can be guaranteed. The active weight of a new WFSG designed in this chapter achieved a 5% reduction hitting 73.9 kg compared with WFSG design option chapter 4.2.

7.5 SiFe based rotor core material – 35HXT780T

This chapter considers SiFe based core material 35HXT780T as the rotor core material for new WFSGs with larger radius to see if weight saving is possible or not. 35HXT780T provided by Nippon steel can handle yield strength up to 822 MPa which can help to increase the rotor radius. Since there is no empirical value for peripheral speed from literatures, the criteria for considering safe operation stress level is 1.24 times smaller than the maximum yield strength of 35HXT780T, which is 663 MPa. In addition, the rotor radius for WFSGs designed in chapter 7.3 is kept the same to understand how stress levels and total deformations are affected by the different rotor geometries.

7.5.1 Stator core made of Vacoflux 48

The electromagnetic design consideration for a rotor core made of 35HXT780T and a stator core made of Vacoflux 48 is similar to design options in chapter 7.3.1. Fig. 135 a) plots the magnetic field map for a rotor core designed according to the electromagnetic performance of Vacoflux 48. The FE results are quite close to the analytical design considerations.

Fig. 135 b) presents the Von-Mises distribution of rotor core made of 35HXT780T designed according to the electromagnetic performance of Vacoflux 48. The geometry is slightly wider compared with rotor geometry designed in chapter 4.2. The maximum stress level occurs at corner one which is 519 MPa . Corner two only experiences a stress level at 434 MPa . The safety factor obtained with the geometry presented in Fig. 135 c) is above 1.24 achieving a safety factor of 1.58.

Apart from the Von-Mises distribution, the total deformation of the rotor core is another important factor that ensures the successful implementation of a rotor core. Fig. 135 c) shows the maximum total deformation is 0.13 mm , which is located at rotor pole tips. This amount of maximum deformation counts for 16% of the overall air gap length. Therefore, the rotor geometry designed in this chapter is able to operate safely without causing a collision between its stator and rotor core under maximum operating speed ($16,000 \text{ rpm}$).

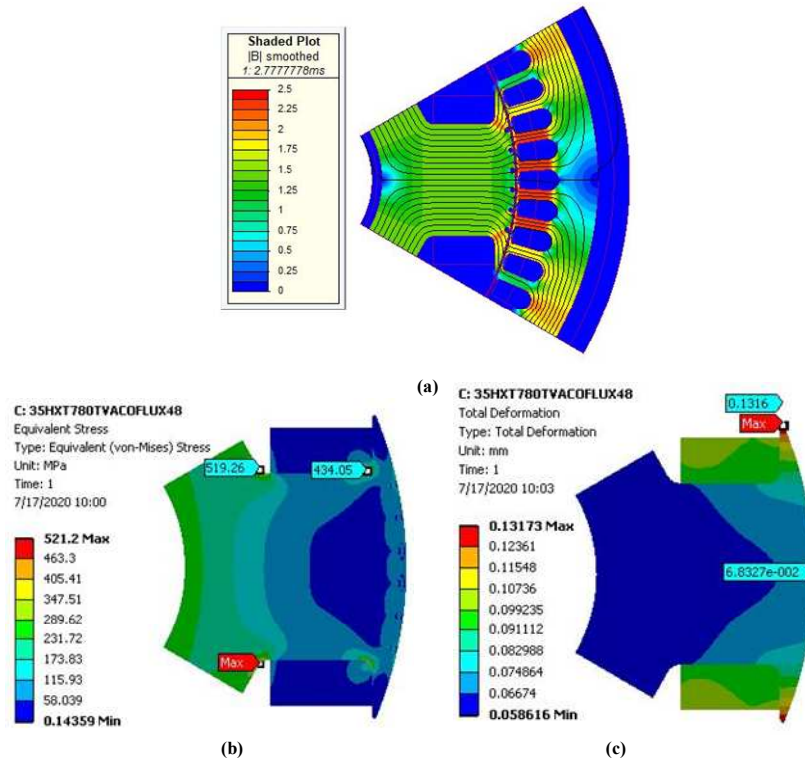


Fig. 135 a) No-load field plot for WFSGs with rotor core made of 35HXT780T and stator core made of Vacoflux 48 at 7,200 rpm b) Von-Mises distribution of rotor geometry made of 35HXT780T with stator core made of Vacoflux 48 at 16,000 rpm c) Total deformation of rotor geometry made of 35HXT780T with stator core made of Vacoflux 48 at 16,000 rpm

Table 27 full load performance of a WFSG designed with 35HXT780T and Vacoflux 48 at 7,200 rpm

Stator Max. Temp. (degree)	Rotor Max. Temp. (degree)	Total Mass (kg)	Rotor Iron (kg)
157.4	231.6	60.1	21.8
Field Winding (kg)	Stator Iron (kg)	Armature Winding (kg)	Magnetic loading (T)
6.3	23.3	8.6	0.7

Table 27 presents the maximum temperature analysis inside rotor and stator coil.

The maximum rotor coil temperature hits 231 °C which is the almost the maximum temperature that Essex 220 class wire can provide standard life time. The active weight of the generator designed in this chapter is 60.1 kg.

7.5.2 Stator core made of 10JNEX900

The electromagnetic design consideration for a rotor core made of 35HXT780T and a stator core made of 10JNEX900 is the same as the design options in chapter 7.3.2. Based on the field plot in Fig. 136 a), the flux density on rotor bore, rotor body, stator teeth and stator back iron are 1.55 T , 1.58 T , 1.13 T and 1.02 T respectively, which are similar to the design requirements.

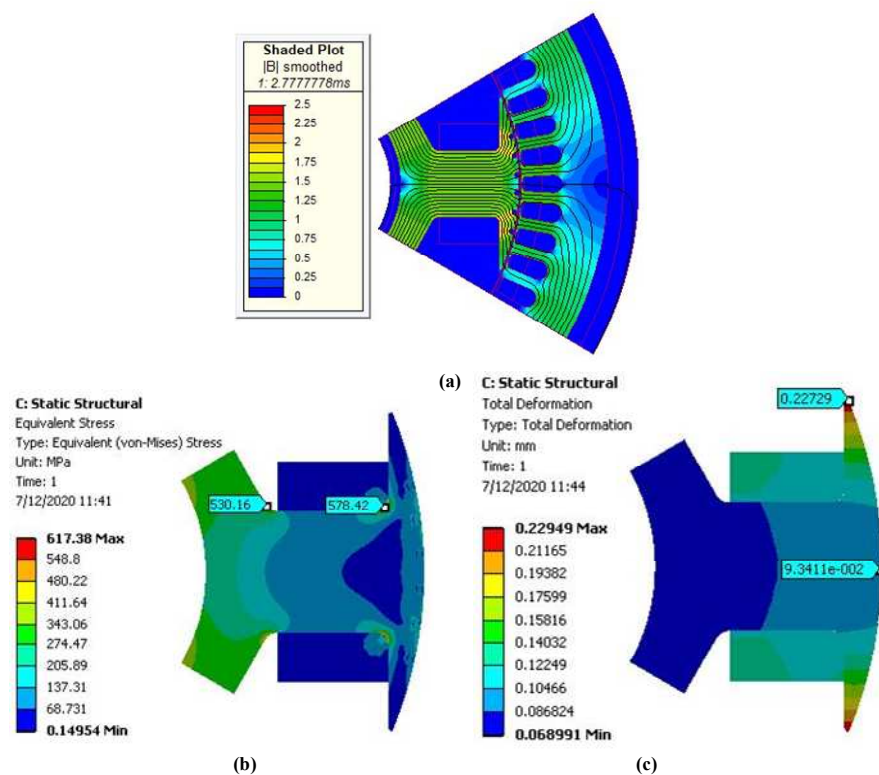


Fig. 136 a) No-load field plot for WFSGs with rotor core made of 35HXT780T and stator core made of 10JNEX900 at $7,200\text{ rpm}$ b) Von-Mises distribution of rotor geometry made of 35HXT780T with stator core made of 10JNEX900 at $16,000\text{ rpm}$ c) Total deformation of rotor geometry made of 35HXT780T with stator core made of 10JNEX900 at $16,000\text{ rpm}$

The next step is to analysis the mechanical stress level of a new rotor core designed according to the electromagnetic performance of 10JNEX900. The stress level at

corner 1 and corner 2 are 530 *MPa* and 578 *MPa*. The stress level is way less than the required safe stress level (663 *MPa*) indicated at the beginning of chapter 7.5. Although the rotor radius can be further increased to reduce the overall active weight of a generator, but the total deformation of rotor pole tips also limits the rotor radius. Excessive deformation of rotor pole tips can cause a collision, which is a fatal mistake for a WFSG.

Fig. 136 c) demonstrates the total deformation of a rotor core designed according to the electromagnetic performance of 10JNEX900. The maximum total deformation locates at the pole tip that is 0.227 *mm*. This amount of total deformation counts for nearly 28% of the overall. Therefore, further increase of rotor radius is not an ideal option even it can reduce the active weight of a generator. Under this circumstance further, larger rotor radius results in high rotor pole tip deformation.

Table 28 full load performance of a WFSG designed with 35HXT780T and 10JNEX900 at 7,200 *rpm*

Stator Max. Temp. (degree)	Rotor Max. Temp. (degree)	Total Mass (<i>kg</i>)	Rotor Iron (<i>kg</i>)
157.3	225.6	89	25.3
Field Winding (<i>kg</i>)	Stator Iron (<i>kg</i>)	Armature Winding (<i>kg</i>)	Magnetic loading (<i>T</i>)
8.5	44	11.1	0.43

Fig. 136 a) shows similar design outcomes compared with that in chapter 7.3.2 and 7.4.2. The magnetic loading for stator made of 10JNEX900 is the lowest among three stator material options, which is shown in Table 28. Therefore, the rotor body width is thinner than that for stator core made of Vacoflux 48, which is shown in Fig. 136 a). The downside is that the overall active weight for this generator is 89

kg that is even heavier than an overall active generator weight designed with M235-35A. Therefore, 10JNEX900 shows no competitiveness for WFSGs at 16,000 *rpm*.

7.5.3 Stator core made of 35HXT590T

Since the material properties for 35HXT780T and 35HXT590T are similar to M235-35A, the flux density design at places such as rotor body, stator teeth and stator back iron are the same for the design criteria in chapter 4.2. Fig. 137 plots the field map for a WFSG design with 35HXT780T and 35HXT590T. In Fig. 137, the flux density at rotor body and rotor bore at around 1.42 *T*; the flux density at stator teeth and stator back iron are 1.8 *T* and 1.5 *T*. Therefore, the resultant no-load magnetic field is under expectation.

The full load performance of the WFSG presented in Fig. 137 a) is analysed using the OOD tool developed in chapter 5. The outcomes are presented in Table 29. The maximum temperature for this design option still hits 230 °C which can be handled by Essex wire in house under 7,200 *rpm*.

Stator Max. Temp. (degree)	Rotor Max. Temp. (degree)	Total Mass (<i>kg</i>)	Rotor Iron (<i>kg</i>)
163.7	218.9	70.4	22.9
Field Winding (<i>kg</i>)	Stator Iron (<i>kg</i>)	Armature Winding (<i>kg</i>)	Magnetic loading (<i>T</i>)
7.9	30.1	9.5	0.57

Table 29 full load performance of a WFSG designed with 35HXT780T and 35HXT590T at 7,200 *rpm*

The last step is to analyse the Von-Mises distribution of this WFSG using the mechanical modules to ensure that the rotor core is able to survive the high speed rotation. Fig. 137 b) depicts the Von-Mises distribution of a rotor geometry designed with 35HXT780T according to a stator core made of 35HXT590T at 16,000 *rpm*.

The maximum stress level at corner one and corner 2 are 583 MPa and 601 MPa respectively. Since a 1.24 safety factor has to be introduced into the mechanical design, maximum stress level shown in the Fig. 137 b) should not exceed 663 MPa as introduced at the beginning of chapter 7.5. Therefore, according to the mechanical simulation in Fig. 137 b), the rotor geometry designed in this thesis is able to sustain the maximum rotational speed without structural failures.

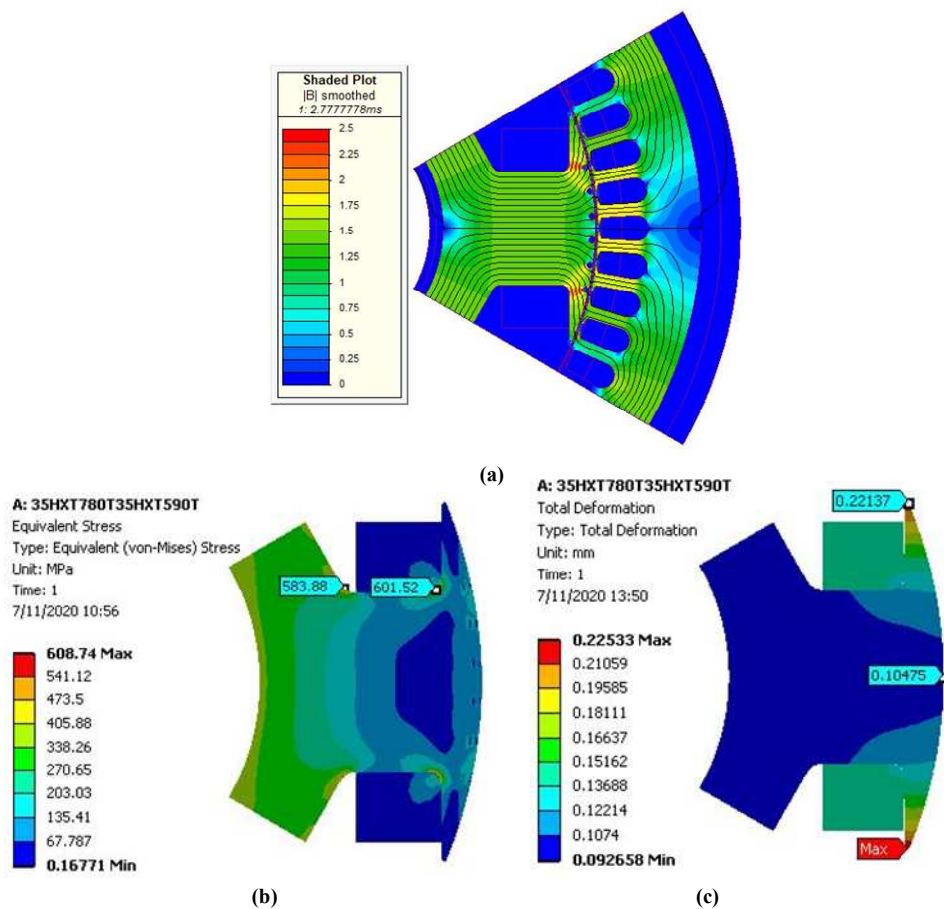


Fig. 137 a) No-load field plot for WFSGs with rotor core made of 35HXT780T and stator core made of 35HXT590T at 7200 rpm b) Von-Mises distribution of rotor geometry made of 35HXT780T with stator core made of 35HXT590T at 16,000 rpm c) Total deformation of rotor geometry made of 35HXT780T with stator core made of 35HXT590T at 16,000 rpm

But apart from the structural failures due to the strength of the material, collisions between a rotor and stator core is also important during the operation of a salient pole synchronous generator. Thus, the total deformation of any rotor pole tip must stay in a safe region where a collision is not possible. In Fig. 137 c), the maximum deformation of the rotor geometry designed in this chapter is 0.22 mm. The air gap length chosen for this WFSG is 0.8 mm. Therefore, 0.22 mm total deformation counts for around 27% of the overall air gap length. Theoretically, this is not a fatal risk for a WFSG with high rotor radius. This WFSG can still operate safely without a collision.

7.6 Summary of the design considerations adopting high graded materials

Chapter 7.6 summarizes the outcomes of investigating WFSG design options with high grade materials. Suitable material candidates for WFSGs at speed range defined in chapter 1 are also given and reasons for materials selections are also given.

Chapter 7 completes the design options for WFSGs with SiFe and CoFe based materials at several rotor radius options. Although from Fig. 126 to Fig. 137, the rotor geometries for 12 cases are substantially different, there are still some general conclusions can be made for WFSGs rotor geometry designed in chapter 7.2, 7.3, 7.4 and 7.5.

Fig. 138 gathers the maximum total deformation of rotor pole tips for a generator designed in chapter 7 and compiles the safety achieved by each rotor geometry. Material name written horizontally forms a rotor core and vertical name represents the stator core materials. For each rotor material, the rotor radius is kept as the same since not only the maximum stress level but also the maximum total deformation

has to be kept within the safe margin. The maximum total deformation is essential for the design process of a WFSG as a shorter air gap length results in less required rotor currents (less rotor heat and temperature) for establishing the field but higher risk of a collision between rotor and stator core. However, the maximum total deformation of rotor pole tips also restricts the length of an air gap. This dilemma between the rotor temperature performance and the mechanical feasibility makes the design process of a WFSG a difficult multi-physics problem.

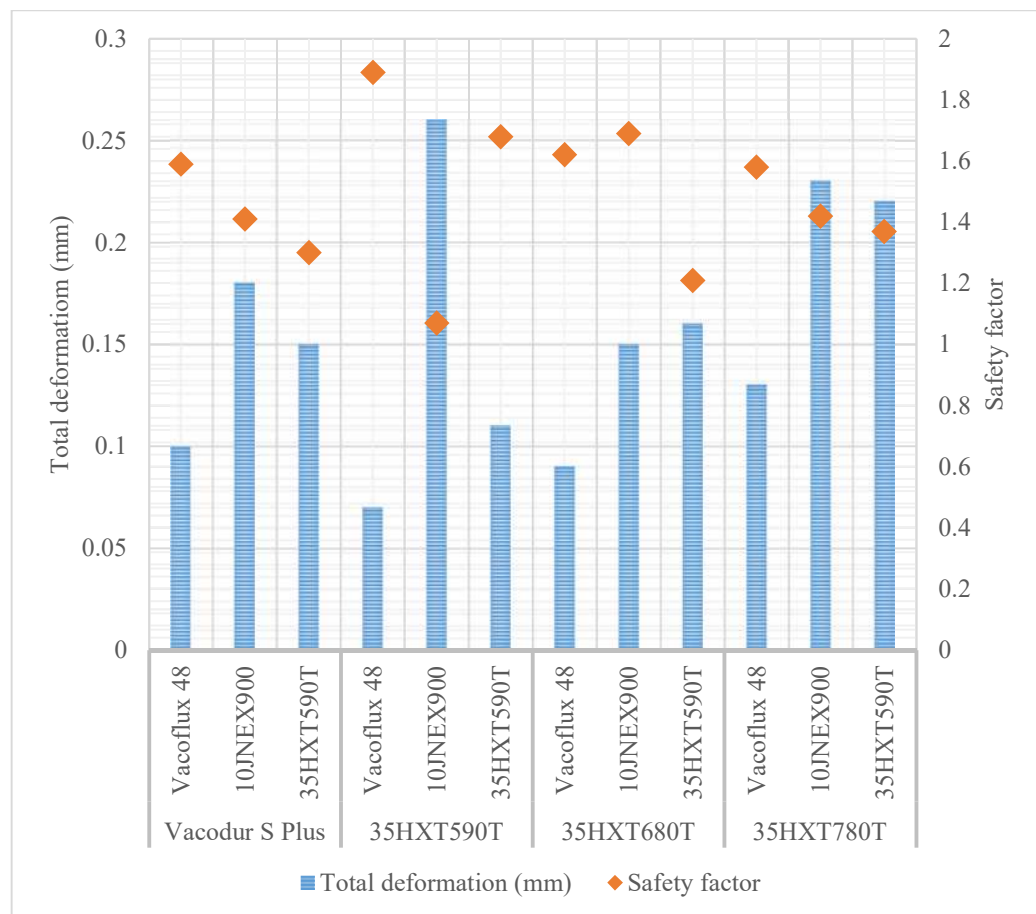


Fig. 138 Total deformation and actual safety factor for WFSG with each combination of materials

In general, WFSGs designed with 10JNEX900 stator core has low magnetic loading compared with Vacoflux 48 and 35HXT590T. Thus, as shown in Fig. 127, Fig. 130, Fig. 133 and Fig. 136, the rotor width is way smaller than the rotor pole span compared with stator cores made of Vacoflux 48 and 35HXT590T. This results in some detrimental effects (high stress concentration and large total deformation locates on the pole tips) on the mechanical performance of a WFSG. The maximum total deformation for WFSGs designed with 10JNEX900 cores are close to or above (except 35HXT680T 10JNEX900) 0.2 mm that is almost 25% of the overall air gap length. In contrast, WFSGs with stator materials other than 10JNEX900 (except 35HXT780T 35HXT590T) has a maximum total deformation less than or close to 0.15 mm that only counts for almost 19% of the overall air gap length. Several special cases such as Vacdur S Plus-Vacoflux 48, 35HXT590T-Vacoflux48, 35HXT590T-35HXT590T, 35HXT680T-Vacoflux48 and 35HXT780T-Vacoflux 48 shows a maximum total deformation less than or close to 0.1 mm that is only 12% of the overall air gap length. Therefore, WFSG design options equipped with 10JNEX900 stator cores do not have a competitive mechanical performance in terms of rotor core tip deformation. Hence, the WFSG designed with 10JNEX900 is not on the top of the list to be selected as the material options best suited for WFSGs at the speed required in this thesis.

Although stress level for each rotor core are a bit conservative, the total deformation of rotor cores for some WFSG design options have reached a dangerous region for practical implementation. Therefore, apart from WFSGs designed with 10JNEX900,

other WFSG designed with 35HXT series materials and CoFe based materials are still demonstrates the feasibility of achieving high speed rotation at 16,000 rpm.

Fig. 139 presents the maximum stator (blue triangle ▲) and rotor coil (red diamond ◆) temperature. The maximum stator coil temperature are all below 230 °C which can guarantee enough life time for the coils. However, except 35HXT590T-Vacoflux 48, the maximum rotor coils temperature are all below or close to a circle enclosed by 230 °C. Based on the information in Fig. 139, stator core materials equipped with Vacoflux 48 generally experiences higher maximum rotor coil temperature than SiFe based materials. Higher magnetic loading induced by CoFe based materials than SiFe based materials is the major reason. For a WFSG, increasing the magnetic loading means increased rotor field currents. Higher maximum coil temperature for WFSGs designed with CoFe based materials is a typical result shown in Fig. 139. A WFSG design option 35HXT590T-Vacoflux 48 in Fig. 139 achieves a maximum coil temperature up to 304 °C. This temperature significantly harms the life time of the rotor winding and this design options is eliminated from the WFSG design considerations. Therefore, 35HXT590T – Vacoflux 48 is not eliminated from the design options from a thermal perspective.

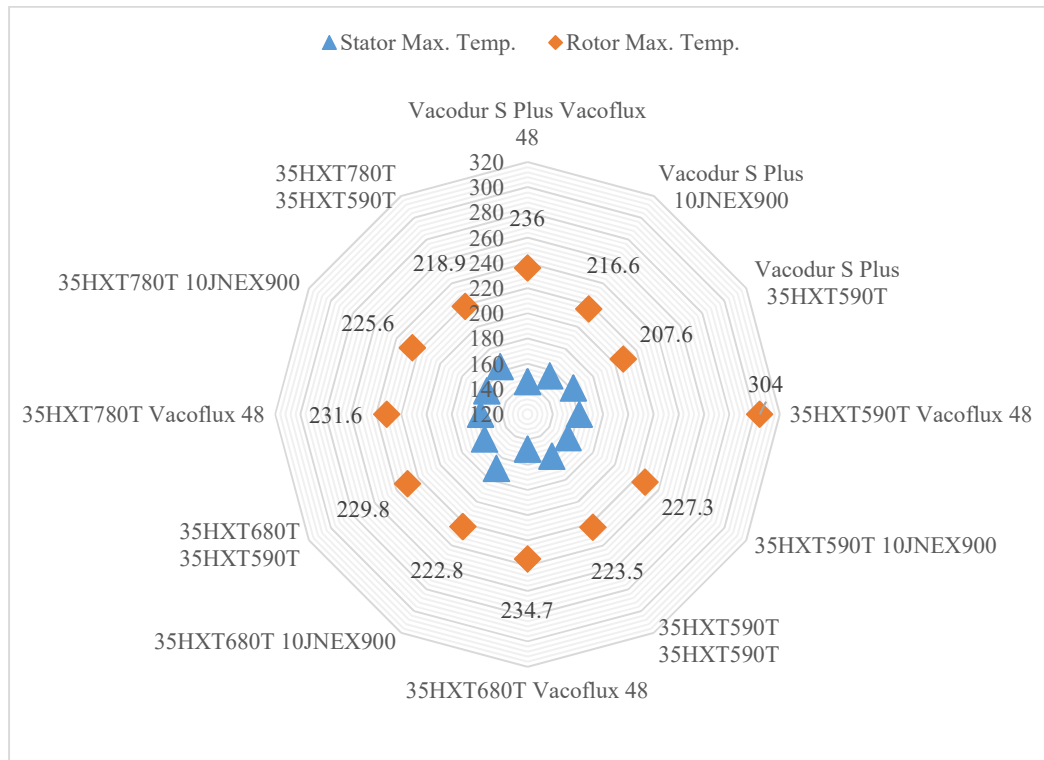


Fig. 139 Maximum stator and rotor coil temperature for 12 different materials combinations

Fig. 140 presents the weight of overall WFSG and individual part of a WFSG for all 12 cases designed in chapter 7 referring its value to the y-axes on the left hand side. The magnetic loading of each design option is presented as a red cross (×) referring to the y-axes on the right hand side. WFSGs designed with 10JNEX900 core perform worst among each WFSG group with the same rotor core materials in terms of weight. For each rotor material, stator cores designed with 10JNEX900 obtain the lowest magnetic loading among three stator core material options. As a result, the mass of stator cores designed with 10JNEX900 hits a range from 44 to 48 kg. Large 10JNEX900 stator cores (large volume) are designed to compensate downside of low magnetic loading. Therefore, it can be concluded that 10JNEX900

is not a suitable stator core materials for a WFSG operates at 360 Hz – 800Hz both from weight and mechanical perspective.

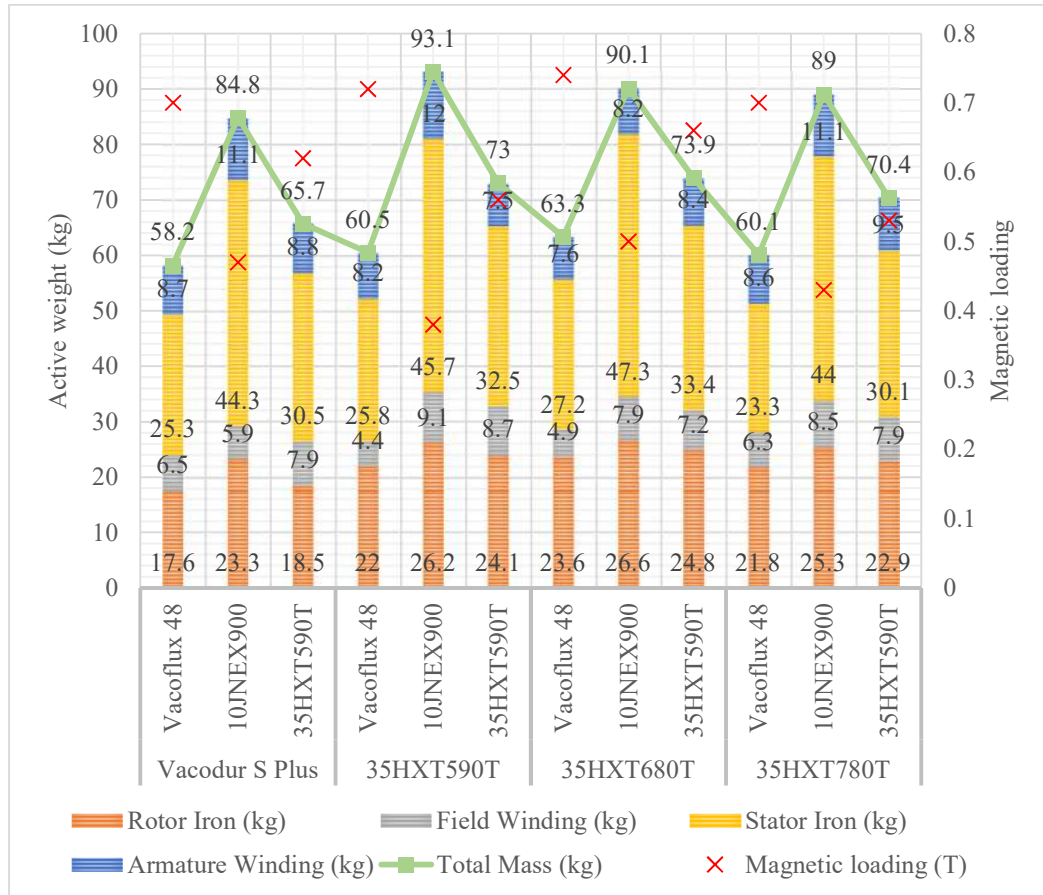


Fig. 140 Weight information for generator designed with these 58.2 kg is the minimum active weight achieved by a WFSG designed with Vacodur S Plus and Vacoflux 48 achieved by air cooled capability. However, CoFe based materials are way more expensive compared with SiFe based materials. By replacing Vacodur S Plus with 35HXT series materials, the 35HXT680T – Vacoflux 48 and 35HXT780T - Vacoflux 48 can demonstrates a very good competitive weight outcomes. An increase of weight for two case mentioned just now is about 3.2% to 8.7% compared with Vacodur S Plus – Vacoflux 48.

While a WFSG is designed with SiFe based materials only, 35HXT590T - 35HXT590T, 35HXT680T - 35HXT590T demonstrates a relatively more competitiveness compared with M235-35A. 6.3% to 9.6% weight saving is achieved by adopting high grade SiFe based materials. 35HXT780T - 35HXT590T is potentially not a good candidate due to high rotor pole tip deformation. Although the weight saving is not much by adopting SiFe based materials, the cost savings in general are favourable by budget critical industry.

In conclusion, CoFe based materials such as Vacodur S Plus and Vacoflux 48 are good candidates for high power dense WFSGs at base frequency lower than 1 *kHz*. If the rotor and stator core materials are chosen to be different from cost perspective, the saturation point of a rotor core has to be less than that of a stator core materials to achieve good weight performance. Since the fundamental frequency for a WFSG does not exceed 1 *kHz*, the advantages for low saturation extreme low losses material – 10JNEX900 is not a suitable candidates. A suitable rotor geometry dimensions are the one shown in Fig. 127. WFSG designed with the combination of 35HXT based rotor materials and the Vacoflux 48 based stator materials (35HXT680T - Vacoflux 48, 35HXT780T - Vacoflux 48) perform second best in terms of weight, but the maximum total deformation of rotor pole tips are smaller than or close to all CoFe based generators. The key difference of rotor geometry in Fig. 127 and rotor geometry in Fig. 135 and Fig. 132 is the proportion of rotor pole tips over the entire pole span. In Fig. 127, each pole tips count for 20.5% of the overall pole span. In Fig. 132 and Fig. 135, each rotor pole tip only counts for 12.8%

of the overall pole span. Thus, short pole tips help a WFSG survive the high speed operation.

Based on the analysis of this chapter, for less budget concern aerospace industry, a forced air cooled WFSG can potentially hit 2.5 kW/kg with CoFe materials which is very competitive towards quite a lot of current market available aerospace machines. As for low cost required automotive industry, a WFSG can still hit 2.1 kW/kg continuous which in automotive industry is also very competitive.

Chapter 8

Conclusion

Recent advancements in PE has driven PM, SR and induction machines forward for wider application fields such as automotive industry, marine and renewable energy generation. The expended market for variable speed drives appeals more investments on research activities spent on new machine topologies. In contrast, classical WFSGs are widely adopted as power generation methods. Further enhancements for this classical machine are rarely seen. However, even with numberless enhancements on new machine topologies, aviation industry still favours WFSGs as the main bus power generation methods. Meanwhile, automotive industry such as Renault ZOE and BMW iX3 started to look at wound field machine as the powertrain methods. Most importantly, an article named ‘Diesel Generator Set Future Developments and Alternative Technologies 2019-2020’ estimates the global market for diesel generator will reach 4.8 billion US dollars. Therefore, the era for WFSG is not over yet, much more research efforts can be spent to find out affordable and reliable powertrains or power generation methods. Under this circumstance, developing an multi-physics design tool with given power, speed, voltage, air gap flux density electrical loading parameters dedicated for WFSG design and analysing process is the key focus of this thesis.

8.1 Object oriented analytical, electromagnetic FE, thermal and mechanical design tool for a WFSG

An analytical sizing script for determining dimensions of a WFSG is proposed and validated against an existing WFSG in the lab. The dimensional information is passed to a MATLAB for automatically creating a FE model in MagNet. The FE electromagnetic performance for example terminal voltage, THD, output power of a WFSG is also compared with the experimental measurements of an existing WFSG. A 3D LPTN model for a WFSG is also proposed in this thesis. The losses data is obtained from FE electromagnetic simulation. The dimension of a WFSG is given from the outcome of an analytical sizing script of a WFSG. The proposed LPTN model processes the dimensional and losses data and presents the temperature behaviour of a WFSG in Simulink. The temperature profile simulated by a 3D LPTN is validated against the experimental measurements.

Although an analytical sizing script, scripting controlled electromagnetic simulation tool and 3D LPTN can be automated individually, complex data communication and post processing between different simulation tools require intricate data re-arrangements. Therefore, to achieve easy data communication between different modules and maintain the capability of individual module upgrades, an objected oriented design architecture is proposed in this thesis to combine three tools been developed. Uniform machine dimensional data are securely packaged as structure arrays with read only feature. Therefore, individual machine analysing modules can only access an array of machine dimensional data to setup FE electromagnetic and 3D LPTN model. This enables tidy upgrades of an individual module and adding

further modules to analyse a machine such as Von-Mises distribution analysis, rotor dynamic analysis, bearing life analysis and optimization modules, etc.

Since the rotor geometry has been decided by the iteration process of electromagnetic and thermal sizing process, a Von-Mises distribution analysis is necessary to determine whether the rotor core can survive the worst speed operation scenario. Based on the Von-Mises analysis, a rotor core made of M235-35A cannot survive the top speed as required using the conventional rotor geometries. Under this circumstance, novel rotor structures are added to assist the rotor core survive the top speed. Increasing the size of fillets at high stress concentration corners eases the stress. Reducing the air gap length helps minimizing the mass of rotor coils that is need to establish the magnetic field. This helps reduce the mass that pole tips have to carry during high speed operation. An extra dovetail under each rotor pole significantly reduces the stress level at the bottom corner of a rotor body to hold everything together. These extra dovetails eventually create a chance for a rotor core designed with M235-35A operating at top speeds with a safety factor adopted.

Thin edges holding damper cages cannot withstand the high centrifugal force been exerted on them. Open slots configurations are the most effective methods resolving high stress concentration mechanically while maintaining electromagnetic performance of a WFSG. An innovative integrated damper cage is also proposed in this thesis to reduce the assembly complexity and separate damper cages that is required. The mechanical analysing process is packaged as a single unit and integrated into the objective oriented design tool dedicated for WFSGs.

8.2 Integrated damper cages for THD improvements

THD level is always an imperative factor in determination of the quality of a generator. Conventional THD reduction techniques are able to cancel required harmonics. However, those THD reduction techniques are not able to tackle THD issues under the entire speed range for a variable speed drive. Therefore, this thesis has proposed an integrated damper cage to solve THD issues while maintaining the functionality of conventional damper cages to reduce the THD level through the entire speed region. With the H900 heat treated integrated damper cages, the THD performance can be significantly improved. The integrated damper cage has proved its capability to reduce THD level to a point lower than a one stator slot pitch can achieve. This thesis has combined 2/3 short pitching, one stator slot skew and integrated damper cage to obtain the THD level below 1%.

8.3 Major contributions to research

The major contributions to technical research for high speed wound field synchronous generators proposed during this research activity are listed as follows.

- 1) Accurate electromagnetic analytical and FE models for a WFSG are proposed. The accuracy of those models are demonstrated by comparing analytical calculation, FE simulation and experimental measurements
- 2) An accurate 3D LPTN model analysing the maximum coil temperature for WFSGs is presented. This 3D LPTN can also be modified with cooling methods with a reasonable known HTCs.
- 3) A commercially unavailable object oriented design tool dedicated to design and analyse the performance of WFSGs combining tools developed in 1), 2)

and a mechanical analysing tool is proposed in this thesis. This OOD tool allows a full automation of a WFSG design process from analytical sizing, FE electromagnetic analysis and thermal analysis to mechanical analysis. The objected oriented feature for this tool also allows individual upgrades of each tool box and other tool box such bearing life, rotor dynamic analysis.

- 4) An extra dovetail under each rotor pole allows an initial rotor core made of M235-35A unable to survive the top speed able to spin at the top speed. This substantially reduces the cost of a high speed WFSG compared with those made of CoFe. Therefore, low cost high speed WFSG can have its application fields been extended to several budget critical area other than aerospace industry such as automotive industry, marine and wind power generation.
- 5) An integrated damper cage replaces the conventional damper cages on the surface of a rotor core. This new damper cages configuration maintains the functionality of original damper bars. Meanwhile, the manufacturing and assembly difficulties of damper cages are suppressed.

8.4 Future work

The current OOD tool completes the design and analysing process of a WFSG. There are several other areas that can be identified as interesting aims for future development of a complete three stage starter generator.

- 1) Gathering the design and manufacturing experiences developed from the work in this thesis to design and develop a WFSG able to achieve the top speed operation with the conventional SiFe steel.

- 2) Separate objected oriented design modules that cover an analytical sizing script, a LPTN and mechanical analysing aspects of an exciter are developed. These OOD modules should be capable of designing an exciter for a group of given design inputs separately and be integrated with existing OOD tool developed in this thesis for combined analysis.
- 3) Separate objected oriented design modules that cover an analytical sizing script, a LPTN and mechanical analysing aspects of a PMG are developed. These OOD modules should be capable of designing a PMG for a group of given design inputs separately and be integrated with existing OOD tool developed in this thesis for combined analysis.
- 4) Further reduction of the air gap length for the WFSG designed in this thesis. This helps to reduce the field copper that is needed. Under this circumstance, more rooms are given to the rotor core geometry so that optimization towards less stress concentration on the rotor core can be achieved. Thus, materials with lower yield strength such as M235-35A can be adopted for high speed low cost WFSGs. This potentially increases the competitiveness of a high speed WFSGs. Meanwhile, this study also benefits thinner sheets of CoFe laminations that has lower iron losses but also a yield strength around 600 *MPa*.
- 5) A complete three stage starter generator can be developed with the completion of previous four tasks. Meanwhile, this three stage starter generator can be equipped with oil cooling to investigate whether oil cooling can achieve a more compacted a three stage starter generator compared with an air cooled WFSG.

Appendix A

Modelling: Heat Transfer Coefficients Calculation

Forced air cooling is often adopted as cooling method for WFSGs. Thus, the HTC's in the air gap at high speed can be estimated using (31)-(35) [123].

$$Nu = 0.0214(Re^{0.8} - 100)Pr^{0.4} \left[1 + \frac{d_h}{L_\delta} \right] \quad (31)$$

$$Nu = \frac{hd_h}{k} \quad (32)$$

$$Re = \frac{\rho v_{red} d_h}{\mu} \quad (33)$$

$$d_h = \delta \sqrt{\frac{8}{3}} \quad (34)$$

$$v_{red} = \sqrt{\left(\frac{\omega r_1}{2}\right)^2 + v_m^2} \quad (35)$$

Where Nu is the Nusselt number, Re is the Reynolds number, Pr is the Prandtl number, and

h heat transfer coefficient [W/m²K]

k thermal conductivity [W/mK]

d_h hydraulic diameter [m]

L_δ	axial length of the air gap [m]
δ	air gap length [m]
ρ	density of the cooling media [kg/m ³]
v_{red}	the velocity been reduced in the helical direction in the air gap [m/s]
ω	angular velocity of the rotor [rad/s]
r_l	rotor diameter [m]
v_m	mean axial cooling media velocity [m/s]

The HTC's in the air gap at low speed operation can be calculated as in (6)-(8) [124].

The Nusselt number can be calculated using the modified Taylor number Ta_m that can be obtained by Taylor numbers Ta with (9).

$$Nu = 2 \quad (Ta_m < 1700) \quad (6)$$

$$Nu = 0.128Ta_m^{0.367} \quad (1700 < Ta_m < 10^4) \quad (7)$$

$$Nu = 0.409Ta_m^{0.241} \quad (10^4 < Ta_m < 10^7) \quad (8)$$

$$Ta_m = \frac{Ta}{F_g} \quad (9)$$

In (9), F_g is represented as (10) and the Taylor number is written as (11),

$$F_g = \frac{\pi^4 \left[\frac{2r_m - 2.304\delta}{2r_m - \delta} \right]}{1697 \left[0.0056 + 0.0571 \left(\frac{2r_m - 2.304\delta}{2r_m - \delta} \right)^2 \right] \left[1 - \frac{\delta}{2r_m} \right]} \quad (10)$$

$$Ta = \frac{\rho^2 \omega^2 r_m \delta^3}{\mu^2} \quad (11)$$

where

r_m average stator and rotor diameter [m]

μ dynamic viscosity of the cooling media [kg/s.m]

The HTCs channeled through air ducts located outside the stator back iron can be roughly estimated using (12) to (14) [110], f is the friction factor, A is the cross-sectional area of the flow, P is the wetted perimeter, Pr is the Prandtl number.

$$Nu = \frac{\left(\frac{f}{8} \right) Re Pr}{1.07 + 12.7 \left(\frac{f}{8} \right)^{0.5} (Pr^{\frac{2}{3}} - 1)} \quad \begin{matrix} (0.5 < Pr < 200) \\ (10^4 < Re < 5 \times 10^5) \end{matrix} \quad (12)$$

$$f = \frac{1}{(1.82 \log_{10} Re - 1.64)^2} \quad (13)$$

$$d_h = \frac{4A}{P} \quad (14)$$

When Re is less than 2300 and forced air is laminar flow, the Nusselt number is determined to be 4.364 [125]. When Re is within the range of 2300 to 10000, the Nusselt number can be determined by a modified equation of (12) presented as (15) [125].

$$Nu = \frac{\left(\frac{f}{8}\right)(Re - 1000)Pr}{1.07 + 12.7\left(\frac{f}{8}\right)^{0.5} (Pr^{\frac{2}{3}} - 1)} \quad (2300 < Re < 10^4) \quad (15)$$

As explained in the revised version of the paper, the determination of air flow located at inter-pole region is always a challenging task to tackle. In [126], empirical equations have been developed to estimate the HTC for air travelling through the inter-pole region for a 8 MW salient-pole generator. These equations can be roughly used to give an evaluation of HTCs implemented for this 3D LPTN network. h_{End} is the HTC located at the end portion of field winding in the axial direction, h_{Front} is the HTC at active region of field windings in the front side of the rotation, h_{Back} is the HTC at active region of field windings in the back side of the rotation.

$$h_{End} = \frac{0.0171Re^{0.78}k}{Y} \quad (36)$$

$$h_{Front} = \frac{0.0148Re^{0.65}k}{Y} \quad (37)$$

$$h_{Back} = \frac{0.0649Re^{0.54}k}{Y} \quad (38)$$

The thermal resistances are calculated using the basic equations presented in [109]. Regarding the rotor and stator coils, being the slots hosting them filled with several materials (such as copper, enamels, resin, etc.), (5) is used in this paper for determining their equivalent thermal conductivities [127]. In (5), R_e is the equivalent thermal conductivity of the overall compound material, k_c is the thermal conductivity of copper; PF is the fill factor of pure copper; k_{fill} , whose expression can be found in (6), is the equivalent thermal conductivity of the insulation material

(enamel and impregnation materials) between each strand of copper wire; k_{ii} is the thermal conductivity of impregnation materials; k_{ci} is the thermal conductivity of copper insulation (enamel insulation); v_{ii} is the impregnation volume; v_{ci} is the copper insulation volume. This approach has been utilized and validated in multiple works [128], [129].

$$R_e = k_{fill} \frac{(1 + PF)k_c + (1 - PF)k_{fill}}{(1 - PF)k_c + (1 + PF)k_{fill}} \quad (39)$$

$$k_{fill} = k_{ii} \frac{v_{ii}}{v_{ii} + v_{ci}} + k_{ci} \frac{v_{ci}}{v_{ii} + v_{ci}} \quad (40)$$

REFERENCES

- [1] J. V. Burns, "Constant Speed Generating Systems," SAE Technical Paper, 1977-02-01, 1977.
- [2] C. Anghel, "Modeling and Simulation of a Power Generation System With a High Power Generator," 2013-09-17, 2013.
- [3] J. Hale, "Boeing 787 from the Ground Up," *Boeing Aero Mag.*, vol. 4, no. 24, pp. 17-23, 2006.
- [4] M. Lukic, P. Giangrande, A. Hebala, S. Nuzzo, and M. Galea, "Review, Challenges, and Future Developments of Electric Taxiing Systems," *IEEE Transactions on Transportation Electrification*, vol. 5, no. 4, pp. 1441-1457, 2019, doi: 10.1109/TTE.2019.2956862.
- [5] P. Giangrande, A. Galassini, S. Papadopoulos, A. Al-Timimy, G. Lo Calzo, M. Degano, M. Galea, and C. Gerada, "Considerations on the Development of an Electric Drive for a Secondary Flight Control Electromechanical Actuator," (in English), *Ieee Transactions on Industry Applications*, vol. 55, no. 4, pp. 3544-3554, Jul-Aug 2019, doi: 10.1109/Tia.2019.2907231.
- [6] I. Moir, *Aircraft systems : mechanical, electrical, and avionics subsystems integration / Ian Moir, Allan Seabridge*, 3rd ed. ed. Chichester: Chichester : John Wiley & Sons, 2008.
- [7] W. Pearson, "The more electric/all electric aircraft-a military fast jet perspective," in *IEE Colloquium on All Electric Aircraft (Digest No. 1998/260)*, 17 Jun 1998 1998, pp. 5/1-5/7, doi: 10.1049/ic:19980343.
- [8] L. Andrade and C. Tenning, "Design of the Boeing 777 electric system," in *Proceedings of the IEEE 1992 National Aerospace and Electronics Conference@m_NAECON 1992*, 18-22 May 1992 1992, pp. 1281-1290 vol.3, doi: 10.1109/NAECON.1992.220573.
- [9] B. Sarlioglu and C. T. Morris, "More Electric Aircraft: Review, Challenges, and Opportunities for Commercial Transport Aircraft," *IEEE Transactions on Transportation Electrification*, vol. 1, no. 1, pp. 54-64, 2015, doi: 10.1109/TTE.2015.2426499.
- [10] V. Madonna, P. Giangrande, and M. Galea, "Electrical Power Generation in Aircraft: review, challenges and opportunities," *IEEE Transactions on Transportation Electrification*, pp. 1-1, 2018, doi: 10.1109/TTE.2018.2834142.
- [11] M. Pastura, S. Nuzzo, M. Kohler, and D. Barater, "Dv/Dt Filtering Techniques for Electric Drives: Review and Challenges," in *IECON 2019 - 45th Annual Conference of the IEEE Industrial Electronics Society*, 14-17 Oct. 2019 2019, vol. 1, pp. 7088-7093, doi: 10.1109/IECON.2019.8926663.
- [12] M. Johnson, P. R. Wilson, L. Empringham, and L. D. Lillo, "IEEE ITRW Working Group Position Paper-Packaging and Integration: Unlocking the Full Potential of Wide-Bandgap Devices," *IEEE Power Electronics Magazine*, vol. 5, no. 2, pp. 26-33, 2018, doi: 10.1109/MPEL.2018.2822246.
- [13] Z. Huang, T. Yang, P. Giangrande, S. Chowdhury, M. Galea, and P. Wheeler, "An Active Modulation Scheme to Boost Voltage Utilization of the Dual Converter With a Floating Bridge," *IEEE Transactions on Industrial Electronics*, vol. 66, no. 7, pp. 5623-5633, 2019, doi: 10.1109/TIE.2018.2873539.
- [14] S. R. MacMinn and W. D. Jones, "A very high speed switched-reluctance starter-generator for aircraft engine applications," in *Aerospace and Electronics Conference, 1989. NAECON 1989., Proceedings of the IEEE 1989 National*, 22-26 May 1989 1989, pp. 1758-1764 vol.4, doi: 10.1109/NAECON.1989.40453.
- [15] M. Tosetti, P. Maggiore, A. Cavagnino, and S. Vaschetto, "Conjugate Heat Transfer Analysis of Integrated Brushless Generators for More Electric Engines," *IEEE Transactions on Industry Applications*, vol. 50, no. 4, pp. 2467-2475, 2014, doi: 10.1109/TIA.2013.2296657.
- [16] M. J. Provost, "The More Electric Aero-engine: a general overview from an engine manufacturer," in *2002 International Conference on Power Electronics, Machines and Drives (Conf. Publ. No. 487)*, 4-7 June 2002 2002, pp. 246-251, doi: 10.1049/cp:20020122.
- [17] R. Newman, "The More Electric Engine Concept," SAE Technical Paper, 2004-11-02, 2004.
- [18] E. Richter, R. E. Anderson, and C. Severt, "The Integral Starter/Generator Development Progress," SAE Technical Paper, 1992-04-01, 1992.

References

- [19] M. Koerner, E. Ganev, and J. Freudenberger, "A Turbine-Driven Electric Power Generation System for Launch Vehicles & Other High-Power Aerospace Applications," SAE Technical Paper, 2004-11-02, 2004.
- [20] R. van Millingen and J. van Millingen, "Phase shift torquemeters for gas turbine development and monitoring," in *ASME 1991 International Gas Turbine and Aeroengine Congress and Exposition*, 1991: American Society of Mechanical Engineers, pp. V005T15A003-V005T15A003.
- [21] "VICKERS VC10 Part Five-Systems, Equipment and Testing," *Aircraft Engineering and Aerospace Technology*, vol. 34, no. 6, pp. 182-184, 1962, doi: 10.1108/eb033570.
- [22] J. Burns and C. Tenning, "Electric Power Generating System for the Boeing 777 Airplane," SAE Technical Paper, 1991-09-01, 1991.
- [23] S. F. Clark, "787 Propulsion System," *Boeing Aero Mag.*, vol. 3, no. 47, pp. 7-16, 2012.
- [24] C. A. Ferreira and E. Richter, "Detailed Design of a 250-kW Switched Reluctance Starter/Generator for an Aircraft Engine," SAE Technical Paper, 1993-04-01, 1993.
- [25] A. Radun, J. Rulison, and P. Sanza, "Switched Reluctance Starter/Generator," SAE Technical Paper, 1992-10-01, 1992.
- [26] R. M. F. Klaass and C. DellaCorte, "The Quest for Oil-Free Gas Turbine Engines," SAE Technical Paper, 2006-11-07, 2006.
- [27] G. Smith, D. Halsey, and E. P. Hoffman, "Integrated Power Unit-Advanced Development," SAE Technical Paper, 1998-04-21, 1998.
- [28] D. N. V. Taneja, OH, US), Huang, Hao (Troy, OH, US), Padgett, Gary A. (Kettering, OH, US), Zywoot, Jan (Centerville, OH, US), Wirsch Jr., Paul J. (Springboro, OH, US), Abbas, Mohamed A. (Huber Heights, OH, US), "Dual-structured aircraft engine starter/generator," United States Patent Appl. 7687928, 2010.
- [29] M. Koerner and E. Ganev, "An Electric Power Generation System for Launch Vehicles," SAE Technical Paper, 2006-11-07, 2006.
- [30] P. Arumugam, C. Gerada, S. Bozhko, H. Zhang, W. Fernando, A. La Rocca, and S. Pickering, "Permanent Magnet Starter-Generator for Aircraft Application," SAE Technical Paper, 2014-09-16, 2014.
- [31] J. Vaidya and E. Gregory, "High Speed Induction Generator for Applications in Aircraft Power Systems," SAE Technical Paper, 2004-11-02, 2004.
- [32] J. Borg Bartolo and C. Gerada, "Design and Modeling of a 45kW, Switched Reluctance Starter-Generator for a Regional Jet Application," SAE Technical Paper, 2014-09-16, 2014.
- [33] L. Sorkin and E. Liebermann, "28VDC Brushless Starter Generator Technology," SAE Technical Paper, 2004-11-02, 2004.
- [34] A. J. Mitcham and J. J. A. Cullen, "Permanent magnet generator options for the More Electric Aircraft," in *Power Electronics, Machines and Drives, 2002. International Conference on (Conf. Publ. No. 487)*, 4-7 June 2002 2002, pp. 241-245, doi: 10.1049/cp:20020121.
- [35] M. Olaiya and N. Buchan, "High power variable frequency generator for large civil aircraft," in *Electrical Machines and Systems for the More Electric Aircraft (Ref. No. 1999/180), IEE Colloquium on*, 1999 1999, pp. 3/1-3/4, doi: 10.1049/ic:19990832.
- [36] Safran. "Electrical Systems." <http://www.safran-electrical-power.com/electrical-systems/our-electrical-generation-systems> (accessed).
- [37] T. Jornier, "More open electric technologies -final report," *Eu FP6 Project Report*, Brussels, Belgium: European Union December 2009, doi: Brussels, Belgium: European Union.
- [38] M. Siemens AG, Germany. "World record electric motor for aircraft." www.siemens.com/press/electric-aircraft (accessed).
- [39] E. Ganev, "High-Reactance Permanent Magnet Machine for High-Performance Power Generation Systems," SAE Technical Paper, 2006-11-07, 2006.
- [40] D. Golovanov, L. Papini, D. Gerada, Z. Xu, and C. Gerada, "Multidomain Optimization of High-Power-Density PM Electrical Machines for System Architecture Selection," *IEEE Transactions on Industrial Electronics*, vol. 65, no. 7, pp. 5302-5312, 2018, doi: 10.1109/TIE.2017.2772188.
- [41] D. D. Pollard and G. E. Krajci, "Packaging the VSCF System for an Aircraft Engine Environment," SAE Technical Paper, 1981-10-01, 1981.

References

- [42] P. Giangrande, V. Madonna, S. Nuzzo, and M. Galea, "Moving Toward a Reliability-Oriented Design Approach of Low-Voltage Electrical Machines by Including Insulation Thermal Aging Considerations," *IEEE Transactions on Transportation Electrification*, vol. 6, no. 1, pp. 16-27, 2020, doi: 10.1109/TTE.2020.2971191.
- [43] B. A. Raad, "Unbalanced and Nonlinear Loads in Aircraft Electric Systems," SAE Technical Paper, 1988-10-01, 1988.
- [44] W. G. Finn, "Variable Speed Constant Frequency Power Source," SAE Technical Paper, 1968-02-01, 1968.
- [45] E. B. Canfield and J. W. Summerford, "Variable Speed Constant Frequency (VSCF) Aircraft Electrical Power," SAE Technical Paper, 1977-02-01, 1977.
- [46] D. E. Baker, "DC Link VSCF Starter/Generator Systems," SAE Technical Paper, 1987-10-01, 1987.
- [47] H. W. Gayek, "Trends in Aircraft Direct-Current Electrical Systems," SAE Technical Paper, 1967-02-01, 1967.
- [48] A. Emadi and M. Ehsani, "Electrical System Architectures for Future Aircraft," SAE Technical Paper, 1999-08-02, 1999.
- [49] F. Gao, S. Bozhko, A. Costabeber, C. Patel, P. Wheeler, C. I. Hill, and G. Asher, "Comparative Stability Analysis of Droop Control Approaches in Voltage-Source-Converter-Based DC Microgrids," *IEEE Transactions on Power Electronics*, vol. 32, no. 3, pp. 2395-2415, 2017, doi: 10.1109/TPEL.2016.2567780.
- [50] T. A. Stoneham, "F-22 Aircraft Battery-Charger-Controller System," SAE Technical Paper, 1999-04-06, 1999.
- [51] M. Sinnett, "787 No-Bleed Systems: Saving Fuel and Enhancing Operational Efficiencies," *Boeing Aero Mag.*, vol. 4, no. 28, pp. 06-11, 2007.
- [52] T. A. Inc. Electrical Systems Powerful thinking. Available: www.thalesgroup.com
- [53] E. Ganey, "Advanced Electric Drives for Aerospace More Electric Architectures," *SAE International Journal of Aerospace*, vol. 1, no. 1, pp. 852-860, 2008, doi: <https://doi.org/10.4271/2008-01-2861>.
- [54] E. D. Beauchamp, "Opportunities and Challenges for Electric-Drive Systems on Aircraft," SAE Technical Paper, 1984-10-01, 1984.
- [55] B. D. Harmon, "Considerations for V-22 Electrical Power System Improvements," SAE Technical Paper, 2008-11-11, 2008.
- [56] E. Richter, J. P. Lyons, C. Ferreira, A. V. Radun, and E. Ruckstadter, "Initial Testing of a 250 KW Starter/Generator for Aircraft Applications," SAE Technical Paper, 1994-04-01, 1994.
- [57] G. Buticchi, L. Costa, and M. Liserre, "Improving System Efficiency for the More Electric Aircraft: A Look at dc/dc Converters for the Avionic Onboard dc Microgrid," *IEEE Industrial Electronics Magazine*, vol. 11, no. 3, pp. 26-36, 2017, doi: 10.1109/MIE.2017.2723911.
- [58] S. Kaboli, *Reliability in power electronics and electrical machines : industrial applications and performance models / Shahriyar Kaboli, Hashem Oraee*. Hershey, PA: Hershey, PA : Engineering Science Reference, 2016.
- [59] J. Falck, C. Felgемacher, A. Rojko, M. Liserre, and P. Zacharias, "Reliability of Power Electronic Systems: An Industry Perspective," *IEEE Industrial Electronics Magazine*, vol. 12, no. 2, pp. 24-35, 2018, doi: 10.1109/MIE.2018.2825481.
- [60] H. Wang, M. Liserre, and F. Blaabjerg, "Toward Reliable Power Electronics: Challenges, Design Tools, and Opportunities," *IEEE Industrial Electronics Magazine*, vol. 7, no. 2, pp. 17-26, 2013, doi: 10.1109/MIE.2013.2252958.
- [61] E. D. Ganey, "Advanced Electric Generators for Aerospace More Electric Architectures," SAE Technical Paper, 2010-11-02, 2010.
- [62] L. Papini, T. Raminosa, D. Gerada, and C. Gerada, "A High-Speed Permanent-Magnet Machine for Fault-Tolerant Drivetrains," *IEEE Transactions on Industrial Electronics*, vol. 61, no. 6, pp. 3071-3080, 2014, doi: 10.1109/TIE.2013.2282604.
- [63] A. Al-Timimy, P. Giangrande, M. Degano, Z. Xu, M. Galea, C. Gerada, G. L. Calzo, H. Zhang, and L. Xia, "Design and Losses Analysis of a High Power Density Machine for

- Flooded Pump Applications," *IEEE Transactions on Industry Applications*, vol. 54, no. 4, pp. 3260-3270, 2018, doi: 10.1109/TIA.2018.2821623.
- [64] S. Nuzzo, M. Galea, C. Gerada, and N. Brown, "Analysis, Modeling, and Design Considerations for the Excitation Systems of Synchronous Generators," *IEEE Transactions on Industrial Electronics*, vol. 65, no. 4, pp. 2996-3007, 2018, doi: 10.1109/TIE.2017.2756592.
- [65] V. Madonna, A. Walker, P. Giangrande, G. Serra, C. Gerada, and M. Galea, "Improved Thermal Management and Analysis for Stator End-Windings of Electrical Machines," *IEEE Transactions on Industrial Electronics*, vol. 66, no. 7, pp. 5057-5069, 2019, doi: 10.1109/TIE.2018.2868288.
- [66] K. Bersch, S. Nuzzo, P. H. Connor, C. N. Eastwick, M. Galea, R. Rolston, and G. Vakil, "Combined Thermofluid and Electromagnetic Optimisation of Stator Vent Cooling," in *2018 XIII International Conference on Electrical Machines (ICEM)*, 3-6 Sept. 2018 2018, pp. 1116-1122, doi: 10.1109/ICELMACH.2018.8507231.
- [67] D. Gerada, A. Mebarki, N. L. Brown, C. Gerada, A. Cavagnino, and A. Boglietti, "High-Speed Electrical Machines: Technologies, Trends, and Developments," *IEEE Transactions on Industrial Electronics*, vol. 61, no. 6, pp. 2946-2959, 2014, doi: 10.1109/TIE.2013.2286777.
- [68] A. L. Rocca, Z. Xu, P. Arumugam, S. J. Pickering, C. N. Eastwick, C. Gerada, and S. Bozhko, "Thermal management of a high speed permanent magnet machine for an aeroengine," in *2016 XXII International Conference on Electrical Machines (ICEM)*, 4-7 Sept. 2016 2016, pp. 2732-2737, doi: 10.1109/ICELMACH.2016.7732908.
- [69] Z. Xu, A. Al-Timimy, M. Degano, P. Giangrande, G. L. Calzo, H. Zhang, M. Galea, C. Gerada, S. Pickering, and L. Xia, "Thermal management of a permanent magnet motor for an directly coupled pump," in *2016 XXII International Conference on Electrical Machines (ICEM)*, 4-7 Sept. 2016 2016, pp. 2738-2744, doi: 10.1109/ICELMACH.2016.7732909.
- [70] P. Arumugam, Z. Xu, A. L. Rocca, G. Vakil, M. Dickinson, E. Amankwah, T. Hamiti, S. Bozhko, C. Gerada, and S. J. Pickering, "High-Speed Solid Rotor Permanent Magnet Machines: Concept and Design," *IEEE Transactions on Transportation Electrification*, vol. 2, no. 3, pp. 391-400, 2016, doi: 10.1109/TTE.2016.2592684.
- [71] V. Madonna, P. Giangrande, A. Walker, and M. Galea, "On the Effects of Advanced End-Winding Cooling on the Design and Performance of Electrical Machines," in *2018 XIII International Conference on Electrical Machines (ICEM)*, 3-6 Sept. 2018 2018, pp. 311-317, doi: 10.1109/ICELMACH.2018.8507170.
- [72] S. Nuzzo, M. Galea, C. Gerada, D. Gerada, A. Mebarki, and N. L. Brown, "Damper cage loss reduction and no-load voltage THD improvements in salient-pole synchronous generators," in *8th IET International Conference on Power Electronics, Machines and Drives (PEMD 2016)*, 19-21 April 2016 2016, pp. 1-7, doi: 10.1049/cp.2016.0203.
- [73] A. D. Gioia, I. P. Brown, Y. Nie, R. Knippel, D. C. Ludois, J. Dai, S. Hagen, and C. Altheld, "Design of a wound field synchronous machine for electric vehicle traction with brushless capacitive field excitation," in *2016 IEEE Energy Conversion Congress and Exposition (ECCE)*, 18-22 Sept. 2016 2016, pp. 1-8, doi: 10.1109/ECCE.2016.7855023.
- [74] S. Jacobs, E. Liebermann, and C. Babad, "Altitude Performance Test Results for Low Pressure Turbine Mounted Generator," SAE Technical Paper, 2006-11-07, 2006.
- [75] P. H. Mellor, D. Drury, R. Wrobel, J. Turner, B. Rolfe, R. Stevenson, and R. Collins, "Design Considerations for Aircraft Generator with Start Function," SAE Technical Paper, 2008-11-11, 2008.
- [76] J. Chen, X. Zhang, and C. Wen, "Harmonics Attenuation and Power Factor Correction of a More Electric Aircraft Power Grid Using Active Power Filter," *IEEE Transactions on Industrial Electronics*, vol. 63, no. 12, pp. 7310-7319, 2016, doi: 10.1109/TIE.2016.2590990.
- [77] D. Fallows, S. Nuzzo, A. Costabeber, and M. Galea, "Harmonic reduction methods for electrical generation: a review," *IET Generation, Transmission & Distribution*, vol. 12, no. 13, pp. 3107-3113, 2018, doi: 10.1049/iet-gtd.2018.0008.
- [78] U. Navy, "Aircraft Electric Power Characteristics," MIL-STD-704F, 2004.

References

- [79] S. Nuzzo, P. Bolognesi, G. Vakil, D. Fallows, C. Gerada, N. L. Brown, and M. Galea, "A methodology to remove Stator Skew in Small-Medium Size Synchronous Generators via innovative damper cage designs," *IEEE Transactions on Industrial Electronics*, pp. 1-1, 2018, doi: 10.1109/TIE.2018.2864699.
- [80] S. Nuzzo, P. Bolognesi, C. Gerada, and M. Galea, "Simplified Damper Cage Circuitual Model and Fast Analytical-Numerical Approach for the Analysis of Synchronous Generators," *IEEE Transactions on Industrial Electronics*, vol. 66, no. 11, pp. 8361-8371, 2019, doi: 10.1109/TIE.2018.2885737.
- [81] K. Edward Wilson, "Damper Windings and Damping," in *Power System Stability*: IEEE, 1995, pp. 241-246.
- [82] S. Nuzzo, M. Degano, M. Galea, C. Gerada, D. Gerada, and N. Brown, "Improved Damper Cage Design for Salient-Pole Synchronous Generators," *IEEE Transactions on Industrial Electronics*, vol. 64, no. 3, pp. 1958-1970, 2017, doi: 10.1109/TIE.2016.2619321.
- [83] S. Nuzzo, M. Galea, C. Gerada, and N. Brown, "A Fast Method for Modeling Skew and Its Effects in Salient-Pole Synchronous Generators," *IEEE Transactions on Industrial Electronics*, vol. 64, no. 10, pp. 7679-7688, 2017, doi: 10.1109/TIE.2017.2694378.
- [84] Y. Wang, G. Vakil, S. Nuzzo, M. Degano, M. Galea, C. Gerada, H. Zhang, and N. Brown, "Sensitivity analysis for performance and power density improvements in salient-pole synchronous generators," in *2017 IEEE Workshop on Electrical Machines Design, Control and Diagnosis (WEMDCD)*, 20-21 April 2017 2017, pp. 163-168, doi: 10.1109/WEMDCD.2017.7947741.
- [85] X. Chen and M. Kazerani, "Space Vector Modulation Control of an AC-DC-AC Converter With a Front-End Diode Rectifier and Reduced DC-link Capacitor," *IEEE Transactions on Power Electronics*, vol. 21, no. 5, pp. 1470-1478, 2006, doi: 10.1109/TPEL.2006.880236.
- [86] C. Gerada, M. Galea, and A. Kladas, "Electrical machines for aerospace applications," in *2015 IEEE Workshop on Electrical Machines Design, Control and Diagnosis (WEMDCD)*, 26-27 March 2015 2015, pp. 79-84, doi: 10.1109/WEMDCD.2015.7194513.
- [87] A. M. Abu-Jalala, T. Cox, C. Gerada, M. Rashed, T. Hamiti, and N. Brown, "Power Quality Improvement of Synchronous Generators Using an Active Power Filter," *IEEE Transactions on Industry Applications*, vol. 54, no. 5, pp. 4080-4090, 2018, doi: 10.1109/TIA.2018.2828789.
- [88] W. Lee and S. Sul, "DC-Link Voltage Stabilization for Reduced DC-Link Capacitor Inverter," *IEEE Transactions on Industry Applications*, vol. 50, no. 1, pp. 404-414, 2014, doi: 10.1109/TIA.2013.2268733.
- [89] H. E. Porte, "Application of VSCF Generators for Gas Turbine Accessories," SAE Technical Paper, 1969-02-01, 1969.
- [90] C. Liu, Z. Xu, D. Gerada, J. Li, C. Gerada, Y. C. Chong, M. Popescu, J. Goss, D. Staton, and H. Zhang, "Experimental Investigation on Oil Spray Cooling with Hairpin Windings," *IEEE Transactions on Industrial Electronics*, pp. 1-1, 2019, doi: 10.1109/TIE.2019.2942563.
- [91] Y. Liu, J. Ou, M. Schiefer, P. Breining, F. Grilli, and M. Doppelbauer, "Application of an Amorphous Core to an Ultra-High-Speed Sleeve-Free Interior Permanent-Magnet Rotor," *IEEE Transactions on Industrial Electronics*, vol. 65, no. 11, pp. 8498-8509, 2018, doi: 10.1109/TIE.2018.2807418.
- [92] S. Nagano, M. Takemoto, and S. Ogasawara, "An examination for improvement of constant output characteristics at high-speed region in a spoke-type IPMSM using ferrite permanent magnet by changing the shape of rotor surface," in *2016 IEEE Energy Conversion Congress and Exposition (ECCE)*, 18-22 Sept. 2016 2016, pp. 1-8, doi: 10.1109/ECCE.2016.7854843.
- [93] Z. Xu, A. L. Rocca, P. Arumugam, S. J. Pickering, C. Gerada, S. Bozhko, D. Gerada, and H. Zhang, "A semi-flooded cooling for a high speed machine: Concept, design and practice of an oil sleeve," in *IECON 2017 - 43rd Annual Conference of the IEEE Industrial Electronics Society*, 29 Oct.-1 Nov. 2017 2017, pp. 8557-8562, doi: 10.1109/IECON.2017.8217503.
- [94] A. Al-Timimy, M. Al-Ani, M. Degano, P. Giangrande, C. Gerada, and M. Galea, "Influence of rotor endcaps on the electromagnetic performance of high-speed PM machine," *IET*

- Electric Power Applications*, vol. 12, no. 8, pp. 1142-1149, 2018, doi: 10.1049/iet-epa.2017.0811.
- [95] N. Fernando, G. Vakil, P. Arumugam, E. Amankwah, C. Gerada, and S. Bozhko, "Impact of Soft Magnetic Material on Design of High-Speed Permanent-Magnet Machines," *IEEE Transactions on Industrial Electronics*, vol. 64, no. 3, pp. 2415-2423, 2017, doi: 10.1109/TIE.2016.2587815.
- [96] A. Al-Timimy, G. Vakil, M. Degano, P. Giangrande, C. Gerada, and M. Galea, "Considerations on the Effects That Core Material Machining Has on an Electrical Machine's Performance," *IEEE Transactions on Energy Conversion*, vol. 33, no. 3, pp. 1154-1163, 2018, doi: 10.1109/TEC.2018.2808041.
- [97] A. Saleem, Y. Zhang, H. Gong, and M. K. Majeed, "Fluoride doped SiC/Si₃N₄ composite as a high thermal conductive material with enhanced mechanical properties," *Ceramics International*, vol. 45, no. 16, pp. 21004-21010, 2019/11/01/ 2019, doi: <https://doi.org/10.1016/j.ceramint.2019.06.289>.
- [98] N. Jiao, W. Liu, T. Meng, J. Peng, and S. Mao, "Design and Control of a Two-Phase Brushless Exciter for Aircraft Wound-Rotor Synchronous Starter/Generator in the Starting Mode," *IEEE Transactions on Power Electronics*, vol. 31, no. 6, pp. 4452-4461, 2016, doi: 10.1109/TPEL.2015.2477456.
- [99] L. Guangjun, W. Xuefan, and X. Fei, "Design of a three-phase brushless exciter for static frequency converter-synchronous motor drive," in *2013 International Conference on Electrical Machines and Systems (ICEMS)*, 26-29 Oct. 2013 2013, pp. 72-76, doi: 10.1109/ICEMS.2013.6754532.
- [100] W. J. L. Shilling, OH), Baker, Donal E. (Elida, OH), "Starter generator system with two stator exciter windings," United States Patent Appl. 4743777, 1988.
- [101] B. Sarlioglu, "A Novel Control Scheme to Increase Electrical Torque of a Drive System for Aircraft Main Engine and APU Start," SAE Technical Paper, 2006-11-07, 2006.
- [102] S. Nuzzo, M. Galea, C. Gerada, and N. L. Brown, "Prediction of the voltage drop due to the diode commutation process in the excitation system of salient-pole synchronous generators," in *2016 19th International Conference on Electrical Machines and Systems (ICEMS)*, 13-16 Nov. 2016 2016, pp. 1-6.
- [103] D. C. Ludois, J. K. Reed, and K. Hanson, "Capacitive Power Transfer for Rotor Field Current in Synchronous Machines," *IEEE Transactions on Power Electronics*, vol. 27, no. 11, pp. 4638-4645, 2012, doi: 10.1109/TPEL.2012.2191160.
- [104] J. Dai, S. Hagen, D. C. Ludois, and I. P. Brown, "Synchronous Generator Brushless Field Excitation and Voltage Regulation via Capacitive Coupling Through Journal Bearings," *IEEE Transactions on Industry Applications*, vol. 53, no. 4, pp. 3317-3326, 2017, doi: 10.1109/TIA.2017.2681621.
- [105] F. P. Demello and C. Concordia, "Concepts of Synchronous Machine Stability as Affected by Excitation Control," *IEEE Transactions on Power Apparatus and Systems*, vol. PAS-88, no. 4, pp. 316-329, 1969, doi: 10.1109/TPAS.1969.292452.
- [106] J. Pyrhonen, *Design of rotating electrical machines / Juha Pyrhönen, Tapani Jokinen, Valéria Hrabovcová*, Second edition. ed. 2014.
- [107] I. Boldea, *Synchronous generators [electronic resource] / Ion Boldea*, 2nd ed. ed. Boca Raton: Boca Raton : CRC Press, Taylor & Francis Group, 2016.
- [108] N. Bianchi, *Electrical machine analysis using finite elements / Nicola Bianchi*. Boca Raton, Fla.: Boca Raton, Fla. : CRC Press, 2005.
- [109] A. Boglietti, A. Cavagnino, and D. Staton, "Determination of Critical Parameters in Electrical Machine Thermal Models," *IEEE Transactions on Industry Applications*, vol. 44, no. 4, pp. 1150-1159, 2008, doi: 10.1109/TIA.2008.926233.
- [110] J. P. Holman, *Heat transfer / J.P. Holman*, 9th ed. ed. New York: New York : McGraw-Hill, 2002.
- [111] M. Galea, G. Buticchi, L. Empringham, L. d. Lillo, and C. Gerada, "Design of a High-Force-Density Tubular Motor," *IEEE Transactions on Industry Applications*, vol. 50, no. 4, pp. 2523-2532, 2014, doi: 10.1109/TIA.2014.2300190.
- [112] K. Bersch, P. H. Connor, C. N. Eastwick, M. Galea, and R. Rolston, "CFD optimisation of the thermal design for a vented electrical machine," in *2017 IEEE Workshop on Electrical*

- Machines Design, Control and Diagnosis (WEMDCD)*, 20-21 April 2017 2017, pp. 39-44, doi: 10.1109/WEMDCD.2017.7947721.
- [113] M. Galea, C. Gerada, T. Raminosa, and P. Wheeler, "A Thermal Improvement Technique for the Phase Windings of Electrical Machines," *IEEE Transactions on Industry Applications*, vol. 48, no. 1, pp. 79-87, 2012, doi: 10.1109/TIA.2011.2175470.
- [114] C. Sciascera, P. Giangrande, L. Papini, C. Gerada, and M. Galea, "Analytical Thermal Model for Fast Stator Winding Temperature Prediction," *IEEE Transactions on Industrial Electronics*, vol. 64, no. 8, pp. 6116-6126, 2017, doi: 10.1109/TIE.2017.2682010.
- [115] F. Zhang, D. Gerada, Z. Xu, X. Zhang, C. Tighe, H. Zhang, and C. Gerada, "Back-Iron Extension Thermal Benefits for Electrical Machines With Concentrated Windings," *IEEE Transactions on Industrial Electronics*, vol. 67, no. 3, pp. 1728-1738, 2020, doi: 10.1109/TIE.2019.2903758.
- [116] I. Boldea, *Synchronous generators / Ion Boldea*, 2nd ed. ed. Boca Raton, FL: Boca Raton, FL : CRC Press, Taylor & Francis Group, 2016.
- [117] J. Al Tayie, C. Whitworth, and A. Biebighaeuser, "AC Generators with 2/3rd and 5/6th winding pitch," no. #WP105.
- [118] X. Liu, D. Gerada, Z. Xu, M. Corfield, C. Gerada, and H. Yu, "Effective Thermal Conductivity Calculation and Measurement of Litz Wire Based on the Porous Metal Materials Structure," *IEEE Transactions on Industrial Electronics*, vol. 67, no. 4, pp. 2667-2677, 2020, doi: 10.1109/TIE.2019.2910031.
- [119] E. F. Hammond, A. E. King, and A. L. Jokl, "Permanent Magnet Generators for Portable Military Power," SAE Technical Paper, 1971. [Online]. Available: <http://dx.doi.org/10.4271/710565>.
- [120] R. L. Mott, *Applied strength of materials / Robert L. Mott, Joseph A. Untener*, 6th ed. ed. Boca Raton: Boca Raton CRC Press, 2017.
- [121] A. M. E.-. Refaie, J. P. Alexander, S. Galioto, P. B. Reddy, K. Huh, P. d. Bock, and X. Shen, "Advanced High-Power-Density Interior Permanent Magnet Motor for Traction Applications," *IEEE Transactions on Industry Applications*, vol. 50, no. 5, pp. 3235-3248, 2014, doi: 10.1109/TIA.2014.2305804.
- [122] T. Miyachi, H. Okumura, and K. Ohtake, "An Analysis of the Effect of Centrifugal Force on the Impact Resistance of Composite Fan Blades for Turbo-Fan Engines," 1991. [Online]. Available: <https://doi.org/10.4271/912047>.
- [123] M. Kuosa, P. Sallinen, and J. Larjola, "Numerical and experimental modelling of gas flow and heat transfer in the air gap of an electric machine," *Journal of Thermal Science*, vol. 13, no. 3, p. 264, 2004/08/01 2004, doi: 10.1007/s11630-004-0041-4.
- [124] J. Nerg, M. Rilla, and J. Pyrhonen, "Thermal Analysis of Radial-Flux Electrical Machines With a High Power Density," *IEEE Transactions on Industrial Electronics*, vol. 55, no. 10, pp. 3543-3554, 2008, doi: 10.1109/TIE.2008.927403.
- [125] P. Zheng, R. Liu, P. Thelin, E. Nordlund, and C. Sadarangani, "Research on the Cooling System of a 4QT Prototype Machine Used for HEV," *IEEE Transactions on Energy Conversion*, vol. 23, no. 1, pp. 61-67, 2008, doi: 10.1109/TEC.2007.914356.
- [126] S. Nonaka, K. Murata, M. Yamamoto, and Y. Takeda, "Experimental Study on Cooling of Rotor in a Salient 4-Pole Synchronous Machine," *IEEE Transactions on Power Apparatus and Systems*, vol. PAS-98, no. 1, pp. 310-317, 1979, doi: 10.1109/TPAS.1979.319533.
- [127] Z. Hashin and S. Shtrikman, "A Variational Approach to the Theory of the Effective Magnetic Permeability of Multiphase Materials," *Journal of Applied Physics*, vol. 33, no. 10, pp. 3125-3131, 1962/10/01 1962, doi: 10.1063/1.1728579.
- [128] N. Simpson, R. Wrobel, and P. H. Mellor, "Estimation of Equivalent Thermal Parameters of Impregnated Electrical Windings," *IEEE Transactions on Industry Applications*, vol. 49, no. 6, pp. 2505-2515, 2013, doi: 10.1109/TIA.2013.2263271.
- [129] L. Idoughi, X. Mininger, F. Bouillault, L. Bernard, and E. Hoang, "Thermal Model With Winding Homogenization and FIT Discretization for Stator Slot," *IEEE Transactions on Magnetics*, vol. 47, no. 12, pp. 4822-4826, 2011, doi: 10.1109/TMAG.2011.2159013.